NANOCOMPOSITES FOR ELECTRONIC APPLICATIONS

Period January 1, 1990 thru December 31, 1991

FINAL REPORT

Volume I

OFFICE OF NAVAL RESEARCH

Contract No. N00014-90-J-1558

APPROVED FOR PUBLIC RELEASE – DISTRIBUTION UNLIMITED

L. Eric Cross

PENNSTATE

1855

THE MATERIALS RESEARCH LABORATORY

UNIVERSITY PARK, PA

REPORT DOCUMENTATION PAGE

Form Approved
OMB No. 0704-0188

1. AGENCY USE ONLY (Leave blank)	2. REPORT DATE	3. REPORT TYPE AND DATES COVERED
	06/14/93	FINAL REPORT 01/01/90 TO 12/31/91

4. TITLE AND SUBTITLE

NANOCOMPOSITES FOR ELECTRONIC APPLICATIONS

5. FUNDING NUMBERS

6. AUTHOR(S)

L. ERIC CROSS

7. PERFORMING ORGANIZATION NAME(S) AND ADDRESS(ES)

MATERIALS RESEARCH LABORATORY
THE PENNSYLVANIA STATE UNIVERSITY
UNIVERSITY PARK, PA 16802

8. PERFORMING ORGANIZATION REPORT NUMBER

N00014-90-J-1558

9. SPONSORING/MONITORING AGENCY NAME(S) AND ADDRESS(ES)

OFFICE OF NAVAL RESEARCH
CODE 1513:MBL
800 NORTH QUINCY STREET
ARLINGTON, VA 22217

DOUGLAS E. HEATON
DEPT. NAVY/ONR, RES. REP.
THE OHIO STATE UNIV. RES. CTR.
1960 KENNY ROAD
COLUMBUS, OH 43210-1063

10. SPONSORING/MONITORING AGENCY REPORT NUMBER

11. SUPPLEMENTARY NOTES

12a. DISTRIBUTION/AVAILABILITY STATEMENT

12b. DISTRIBUTION CODE

13. ABSTRACT (Maximum 200 words)

SEE FOLLOWING PAGES.

14. SUBJECT TERMS

15. NUMBER OF PAGES

16. PRICE CODE

17. SECURITY CLASSIFICATION OF REPORT	18. SECURITY CLASSIFICATION OF THIS PAGE	19. SECURITY CLASSIFICATION OF ABSTRACT	20. LIMITATION OF ABSTRACT

GENERAL INSTRUCTIONS FOR COMPLETING SF 298

The Report Documentation Page (RDP) is used in announcing and cataloging reports. It is important that this information be consistent with the rest of the report, particularly the cover and title page. Instructions for filling in each block of the form follow. It is important to ***stay within the lines*** to meet ***optical scanning requirements.***

Block 1. Agency Use Only *(Leave blank)*.

Block 2. Report Date. Full publication date including day, month, and year, if available (e.g. 1 Jan 88). Must cite at least the year.

Block 3. Type of Report and Dates Covered. State whether report is interim, final, etc. If applicable, enter inclusive report dates (e.g. 10 Jun 87 - 30 Jun 88).

Block 4. Title and Subtitle. A title is taken from the part of the report that provides the most meaningful and complete information. When a report is prepared in more than one volume, repeat the primary title, add volume number, and include subtitle for the specific volume. On classified documents enter the title classification in parentheses.

Block 5. Funding Numbers. To include contract and grant numbers; may include program element number(s), project number(s), task number(s), and work unit number(s). Use the following labels:

C	- Contract	PR	- Project
G	- Grant	TA	- Task
PE	- Program Element	WU	- Work Unit Accession No.

Block 6. Author(s). Name(s) of person(s) responsible for writing the report, performing the research, or credited with the content of the report. If editor or compiler, this should follow the name(s).

Block 7. Performing Organization Name(s) and Address(es). Self-explanatory.

Block 8. Performing Organization Report Number. Enter the unique alphanumeric report number(s) assigned by the organization performing the report.

Block 9. Sponsoring/Monitoring Agency Name(s) and Address(es). Self-explanatory.

Block 10. Sponsoring/Monitoring Agency Report Number. *(If known)*

Block 11. Supplementary Notes. Enter information not included elsewhere such as: Prepared in cooperation with...; Trans. of...; To be published in.... When a report is revised, include a statement whether the new report supersedes or supplements the older report.

Block 12a. Distribution/Availability Statement. Denotes public availability or limitations. Cite any availability to the public. Enter additional limitations or special markings in all capitals (e.g. NOFORN, REL, ITAR).

- **DOD** - See DoDD 5230.24, "Distribution Statements on Technical Documents."
- **DOE** - See authorities.
- **NASA** - See Handbook NHB 2200.2.
- **NTIS** - Leave blank.

Block 12b. Distribution Code.

- **DOD** - Leave blank.
- **DOE** - Enter DOE distribution categories from the Standard Distribution for Unclassified Scientific and Technical Reports.
- **NASA** - Leave blank.
- **NTIS** - Leave blank.

Block 13. Abstract. Include a brief *(Maximum 200 words)* factual summary of the most significant information contained in the report.

Block 14. Subject Terms. Keywords or phrases identifying major subjects in the report.

Block 15. Number of Pages. Enter the total number of pages.

Block 16. Price Code. Enter appropriate price code *(NTIS only)*.

Blocks 17. - 19. Security Classifications. Self-explanatory. Enter U.S. Security Classification in accordance with U.S. Security Regulations (i.e., UNCLASSIFIED). If form contains classified information, stamp classification on the top and bottom of the page.

Block 20. Limitation of Abstract. This block must be completed to assign a limitation to the abstract. Enter either UL (unlimited) or SAR (same as report). An entry in this block is necessary if the abstract is to be limited. If blank, the abstract is assumed to be unlimited.

ABSTRACT

This document is the final report of work on the DARPA sponsored University Research Initiative (URI) on the subject "Nanocomposites for Electronic Applications" funded under ONR Contract No. N00014-90-J-1558. Initial funding on the contract was for a three year period from 1987-1990. This document is the final report for the two year extension period finishing on December 31, 1991.

Work on this program and associated studies on the ONR program on "Piezoelectric and Electrostrictive Materials for Transducer Applications" has lead to a significantly improved understanding of the fundamental mechanisms in Relaxor Ferroelectrics. For the perovskite Lead Magnesium Niobate which is the prototype for many other relaxor perovskites, the self limiting nonstoichiometric ordering of Mg/Nb ions is shown to be the symmetry breaking key to the onset of micropolar regions at the Burns temperature well above the dielectric maximum. The simple paraelectric behavior at high temperature is shown to be modified by cooperation on cooling, leading to a Vogel:Fulcher type condensation into a glass like state at low temperature.

Many tungsten bronze structure ferroelectrics e.g. $Sr_{1-x}Ba_xNb_2O_6$ also show relaxor ferroelectric behavior, and in the lead barium niobate family of solid solutions there is a particularly rich panoply of behaviors. Depending on composition polarization may appear along the 4 fold axis, or along one of the orthogonal 2 fold axes of the prototypic 4/mmm prototype. In PBN a pseudo morphotropic phase boundary (PMPB) exists near the 60:40 Pb:Ba composition. The intriguing feature for the PBN compositions is that for the tetragonal symmetry, the permittivity increases for directions orthogonal to the 4 fold axis and there is a second freezing (in the polar state) near 100K. At the MPB the symmetry may be switched by electric field to that with macro-polarization along 2 (orthorhombic) and now the second freezing takes place for polarization along 4. The low temperature freezing occurs whether the initial phase is glassy or ferroelectric and gives rise to fascinating families of unusual dielectric, piezoelectric, elastic and optical properties.

A second important contribution on this program stemmed from the very careful preparative studies to make ultra find powders of simple perovskite ferroelectrics. The objective was to obtain understanding of the intrinsic size effects which must occur in ferroelectrics due to the cooperative nature of the phenomenon. From studies of spontaneous strain it was made clear that ferroelectricity in $BaTiO_3$ did not occur in powders with particular size less than 800°A whereas in $PbTiO_3$ ferroelectricity and spontaneous strain persists down to sizes of order 170°A.

In 0:3 type composites it is natural to have a major interest in the phenomenon of percolation, and of the critical concentrations for this phenomenon. Practical aspects of this work occur in the PTC polymer:carbon composites and in other systems.

Fundamental studies on silicon, germanium and silica germania composites using wavelength scanning ellipsometry have lead to the evolution of effective techniques for the evaluation of inhomogeneity in highly transparent oxides, in systems with uniaxial anisotropy and have validated spectroscopic ellipisometry as one of the most valuable nondestructive techniques for the study of ferroelectric surfaces and thin films.

NANOCOMPOSITES FOR ELECTRONIC APPLICATIONS

Period January 1, 1990 thru December 31, 1991

FINAL REPORT

Volume I

OFFICE OF NAVAL RESEARCH

Contract No. N00014-90-J-1558

APPROVED FOR PUBLIC RELEASE – DISTRIBUTION UNLIMITED

L. Eric Cross

PENNSTATE

1855

THE MATERIALS RESEARCH LABORATORY

UNIVERSITY PARK, PA

TABLE OF CONTENTS

APPENDICES

APPENDICES *(continued)*

7. A. S. Bhalla, R. Guo, L. E. Cross, G. Burns, F. H. Dacol, and R. R. Neurgaonkar. "Glassy Polarization in the Ferroelectric Tungsten Bronze (BaSr)Nb_2O_6," J. Appl. Phys. 71 (11), 5591 (1992).

8. C. A. Randall, R. Guo, A. S. Bhalla, and L. E. Cross. "Microstructure-Property Relations in Tungsten Bronze Lead Barium Niobate $Pb_{1-x}Ba_xNb_2O_6$," J. Mat. Res. 6 (8), 1720 (1991).

9. R. Guo, A. S. Bhalla, and L. E. Cross. "Pyroelectric Properties of Lead Barium Niobate Single Crystals," Ferroelectrics 118, 77 (1991).

10. D. Viehland, S. J. Jang, L. E. Cross, and M. Wuttig. "The Dielectric Relaxation of Lead Magnesium Niobate Relaxor Ferroelectrics," Phil Mag B 64 (3), 335 (1991).

11. D. Viehland, S. J. Jang, L. E. Cross, and M. Wuttig. "Anelastic Relaxation and Internal Strain in Lead Magnesium Niobate Relaxors," Phil Mag A 64 (4), 835 (1991).

12. D. Viehland, S. J. Jang, L. E. Cross, and M. Wuttig. "Local Polar Configurations in Lead Magnesium Niobate Relaxors," J. Appl. Phys. 69 (1), 414 (1991).

13. D. Viehland, M. Wuttig, and L. E. Cross. "The Glassy Behavior of the Relaxor Ferroelectrics," Ferroelectrics 120, 71 (1991).

14. D. Viehland, S. J. Jang, L. E. Cross, and M. Wuttig. "Freezing of the Polarization Fluctuations in Lead Magnesium Niobate Relaxors," J. Appl. Phys. 68 (6), 2916 (1990).

15. J. R. Giniewicz, A. S. Bhalla, and L. E. Cross. "Lead Scandium Tantalate – Lead Titanate Materials for Field Stabilized Pyroelectric Device Applications," Ferroelectrics Letters 14, 21 (1992).

16. J. R. Giniewicz, D. A. McHenry, T. R. Shrout, S. J. Jang, A. S. Bhalla, and F. Ainger. "Characterization of (1-x) $PbMg_{1/3}Nb_{2/3}O_3$-$xPbTiO_3$ and $PbSc_{1/2}Ta_{1/2}O_3$ Transparent Ceramics Prepared by Uniaxial Hot Pressing," Ferroelectrics 109, 167 (1990).

17. J. R. Giniewicz, A. S. Bhalla, and L. E. Cross. "Pyroelectric Response and Depolarization Behavior of (1-x) $PbSc_{1/2}Ta_{1/2}O_3$-$xPbTiO_3$ Materials," Ferroelectrics 118, 157 (1991).

18. D. A. McHenry, J. R. Giniewicz, T. R. Shrout, S. J. Jang, and A. S. Bhalla. "Electrical and Optical Properties of Relaxor Ferroelectrics," Ferroelectrics 102, 161 (1990).

19. D. A. McHenry, J. R. Giniewicz, S. J. Jang, T. R. Shrout, and A. S. Bhalla. "Optical and Electro-optical Properties of Lead Magnesium Niobate:Lead Titanate," Ferroelectrics 107, 45, (1990).

APPENDICES ***(continued)***

20. D. A. McHenry, J. Giniewicz, S. J. Jang, A. S. Bhalla, and T. R. Shrout. "Optical Properties of Hot Pressed Relaxor Ferroelectrics," Ferroelectrics 93, 351 (1989).

21. G. R. Fox, J. K. Yamamoto, D. V. Miller, L. E. Cross, and S. K. Kurtz. "Thermal Hysteresis of Optical Second Harmonic in Paraelectric $BaTiO_3$," Materials Letters 9 (7, 8), 284 (1990).

Micro Composites Studies

22. G. R. Harshe. "Magnetoelectric Effect in Piezoelectric-Magnetostrictive Composites," PhD Thesis, Solid State Science, The Pennsylvania State University (August 1991).

23. G. Harshe, J.Dougherty, and R. E. Newnham. "Magnetoelectric Effect in Composite Materials," Proceedings Conference on Smart Materials and Structures, SPIE, Albuquerque, NM (February 1-4, 1993).

24. G. Harshe, J. P. Dougherty, and R. E. Newnham. "Theoretical Modelling of 3-0/0-3 Magnetoelectric Composites," Submitted, Int. J. of Appl. Electromagnetics in Materials.

25. G. Harshe, J. P. Dougherty, and R. E. Newnham. "Theoretical Modelling of Multilayer Magnetoelectric Composites," Submitted, Int. J. of Appl. Electromagnetics in Materials.

26. R. J. Sullivan and R. E. Newnham. "Composite Thermistors," Chemistry of Advanced Materials, Edited by C. N. R. Rao, Blackwell Scientific Publications (1992).

27. G. R. Ruschau, S. Yoshikawa, and R. E. Newnham. "Percolation Constraints in the Use of Conductor-Filled Polymers for Interconnects," Proc. Elect. and Comp. Tech., IEEE, San Diego (May 18-20, 1992).

28. M. Blaszkiewicz, D. S. McLachlan, and R. E. Newnham. "The Volume Fraction and Temperature Dependence of the Resistivity in Carbon Black and Graphite Polymer Composites: An Effective Media Percolation Approach."

29. G. R. Ruschau, S. Yoshikawa, and R. E. Newnham. "Resistivities of Conductive Composites," J. Appl. Phys. 72 (3), 953 (1992).

30. D. M. Moffatt, J. Runt, W. Huebner, S. Yoshikawa, and R. E. Newnham. "PTC Effects in Conductor Filled Amorphous Polymer Composites," PTC Effects in Polymer Composites, Chapter 3, pp. 51.

Intrinsic Size Effects in Ferroelectrics

31. R. E. Newnham, K. R. Udayakumar, and S. Trolier-McKinstry. "Size Effects in Ferroelectric Thin Films," Book Chapter, Chemical Processing of Advanced Materials, Editor L. Hench, J. K. West, John Wiley & Sons Inc. (1992).

Spectroscopic Ellipsometry

32. N. Van Nguyen. "Spectroscopic Ellipsometry of Interfaces," PhD Thesis, Physics, The Pennsylvania State University (November 1989).

APPENDICES *(continued)*

33. P. Chindaudom. "Characterization of Inhomogeneous Transparent Thin Films on Transparent Substrates by Spectroscopic Ellipsometry," PhD Thesis, Physics, The Pennsylvania State University (August 1991).

34. N. V. Nguyen, K. Vedam, and J. Narayan. "Characterization of the Interface Between Ge^+ –Implanted Crystalline Silicon and Its Thermally Grown Oxide by Spectroscopic Ellipsometry," J. Appl. Phys. 67 (2) (1990).

35. S. Trolier-McKinstry, H. Hu, S. B. Krupanidhi, P. Chindaudom, K. Vedam, and R. E. Newnham. "Spectroscopic Ellipsometry Studies on Ion Beam Sputter Deposited $Pb(ZrTi)O_3$ Films on Sapphire and on PT Coated Silicon Substrates," Submitted, J. Appl. Phys.

36 J. Chen, K. R. Udayakumar, K. G. Brooks, and L. E. Cross. "Dielectric Behavior of Ferroelectric Thin Films at High Frequencies," pp. 182, Proc. ISAF 92, Greenville, South Carolina.

37. K. R. Udayakumar, J. Chen, K. G. Brooks, L. E. Cross, A. M. Flynn and D. J. Ehrlich. "Piezoelectric Thin Film Ultrasonic Micromotors," Mat. Res. Soc. Symp. Proc., Vol. 243, pp. 49-54 (1992 Materials Research Society).

ABSTRACT

This document is the final report of work on the DARPA sponsored University Research Initiative (URI) on the subject "Nanocomposites for Electronic Applications" funded under ONR Contract No. N00014-90-J-1558. Initial funding on the contract was for a three year period from 1987-1990. This document is the final report for the two year extension period finishing on December 31, 1991.

Work on this program and associated studies on the ONR program on "Piezoelectric and Electrostrictive Materials for Transducer Applications" has lead to a significantly improved understanding of the fundamental mechanisms in Relaxor Ferroelectrics. For the perovskite Lead Magnesium Niobate which is the prototype for many other relaxor perovskites, the self limiting nonstoichiometric ordering of Mg/Nb ions is shown to be the symmetry breaking key to the onset of micropolar regions at the Burns temperature well above the dielectric maximum. The simple paraelectric behavior at high temperature is shown to be modified by cooperation on cooling, leading to a Vogel:Fulcher type condensation into a glass like state at low temperature.

Many tungsten bronze structure ferroelectrics e.g. $Sr_{1-x}Ba_xNb_2O_6$ also show relaxor ferroelectric behavior, and in the lead barium niobate family of solid solutions there is a particularly rich panoply of behaviors. Depending on composition polarization may appear along the 4 fold axis, or along one of the orthogonal 2 fold axes of the prototypic 4/mmm prototype. In PBN a pseudo morphotropic phase boundary (PMPB) exists near the 60:40 Pb:Ba composition. The intriguing feature for the PBN compositions is that for the tetragonal symmetry, the permittivity increases for directions orthogonal to the 4 fold axis and there is a second freezing (in the polar state) near 100K. At the MPB the symmetry may be switched by electric field to that with macro-polarization along 2 (orthorhombic) and now the second freezing takes place for polarization along 4. The low temperature freezing occurs whether the initial phase is glassy or ferroelectric and gives rise to fascinating families of unusual dielectric, piezoelectric, elastic and optical properties.

A second important contribution on this program stemmed from the very careful preparative studies to make ultra find powders of simple perovskite ferroelectrics. The objective was to obtain understanding of the intrinsic size effects which must occur in ferroelectrics due to the cooperative nature of the phenomenon. From studies of spontaneous strain it was made clear that ferroelectricity in $BaTiO_3$ did not occur in powders with particular size less than 800°A whereas in $PbTiO_3$ ferroelectricity and spontaneous strain persists down to sizes of order 170°A.

In 0:3 type composites it is natural to have a major interest in the phenomenon of percolation, and of the critical concentrations for this phenomenon. Practical aspects of this work occur in the PTC polymer:carbon composites and in other systems.

Fundamental studies on silicon, germanium and silica germania composites using wavelength scanning ellipsometry have lead to the evolution of effective techniques for the evaluation of inhomogeneity in highly transparent oxides, in systems with uniaxial anisotropy and have validated spectroscopic ellipisometry as one of the .nost valuable nondestructive techniques for the study of ferroelectric surfaces and thin films.

1. INTRODUCTION

This document reports work on the final two years of the DARPA sponsored University Research Initiative (URI) on the subject of "Nanocomposites for Electronic Applications." Initial funding on the program was for a three year period, the new contract from ONR Contract No. N00014-90-J-1558 carried the program for the final two years which are the subject of this report.

Work on the program has produced major progress in four topic areas.

I. *Relaxor Ferroelectrics:* Where studies have explored the phenomena associated with these interesting high permittivity relaxation dielectrics in both perovskite and tungsten bronze structure families. For these materials dielectric and electrostrictive studies proceeded in parallel with similar work on our ONR Transducer program. Optical and electro-optic studies were solely on this program.

II. *Micro-Composites Studies:* Topics of interest were the magneto-electric effects which can be achieved through elastic mediation between strongly piezoelectric and strongly magnetostrictive oxides and the interesting percolation problems associated with the PTC effects in polymer:conductor 0:3 particulate composites.

III. *Intrinsic Size Effects in Ferroelectrics:* Here the effort was to complete earlier studies on the previous contract showing the size limitations on ferroelectricity in fine particles of $BaTiO_3$ and $PbTiO_3$ using the coupled electrostrictive distortion to monitor polarization.

IV. *Spectroscopic Ellipsometry:* Early work was focused upon silica: germania systems whilst the tools were developed to handle ellipsometric exploration of uniaxially anisotropic highly transparent interfaces. This early work lead to the focused use of the wavelength scanning ellipsometer to explore ferroelectric surfaces and thin films.

As is the intent of the URI programs the funding has provided the vehicle for the education of six PhD candidates in Solid State Science and in Physics. Abstracts of these thesis researchers are included in the appendices. The work by Dr. Ruyan Guo for the thesis which was presented in December 1990 was recognized by the University with the Xerox Research Award, presented for the best PhD work on Materials for 1991. More recently the studies leading up to our current understanding of the fascinating self-assembling self-limiting character of the heterogeneity in the perovskite relaxor ferroelectrics was recognized by the award of the MRS Medal and Award for innovation in 1992.

In 1992, Professors Cross and Newnham were honored to present the Orton and Sosman Lectures at the annual Meeting of the American Ceramic Society and Professor Newnham was honored by the International Ceramics Meeting in Assissi, Italy with their prestigious award.

The following report uses the format established earlier of giving a brief narrative account of the topics covered and appending the formal published results for more detailed reference. The papers are assembled under five general headings:

GENERAL PAPERS.
RELAXOR FERROELECTRICS.
MICRO-COMPOSITES STUDIES.
INTRINSIC SIZE EFFECTS IN FERROELECTRICS.
SPECTROSCOPIC ELLIPSOMETRY.

2. GENERAL PAPERS

It has always been an element of the research philosophy in MRL that practical "demand pull" should be factored into the choice of research topics in the Laboratory. The paper by Cross on "Ferroelectric Ceramics: Tailoring Properties for Specific Applications" (Appendix 1) highlights some of the steps towards fundamental understanding which can be useful in property control. The sections on relaxor ferroelectrics applied to capacitor and actuator systems draws on work sponsored on this program.

In the general paper on Electronic Ceramics by Newnham and Shrout (Appendix 2), the focus is upon processing of electronic compositions particularly the requirements for the newer evolving multilayer tape cast systems. The paper considers the diverse needs of high density packaging and the drive towards incorporationg functional ceramics directly into the package.

3. RELAXOR FERROELECTRICS

Developing understanding of the key phenomena in the perovskite and tungsten bronze structure relaxor ferroelectrics has been the driving force behind the PhD studies of Dwight Viehland (Appendix 3), Ruyan Guo (Appendix 4), D. A. McHenry (Appendix 5) and Jayne R. Giniewicz (Appendix 6).

Ruyan Guo's studies were focused upon tungsten bronze structure relaxors in the lead barium niobate solid solution family. PBN is of major interest since it has been known for some time that the system embraces a morphotropic phase boundary near the $Pb_{0.6}Ba_{0.4}Nb_2O_6$ composition which separates tetragonal and orthorhombic ferroelectric variants. With good single crystal samples Ruyan was able to demonstrate for this first time direct evidence of ferroelectric:ferroelectric switching in this MPB system. It was intriguing to find that in both tetragonal and rhombohedral variants, the polarizability orthogonal to the major polarization

diverges at low temperature then shows a Vogel:Fulcher type freezing. This is perhaps the first evidence of an "orientational" glassy state in a polar domain structure. The work is summarized effectively in Appendices 7-9.

Viehland's work which was carried out jointly with our Transducer Program is summarized in Appendices 10-14. Detailed study of the dielectric and elastic properties of lead magnesium niobate carried out in association with Dr. Manfred Wuttig's group at University of Maryland showed up the inadequacy of the earlier super paraelectric model at lower temperatures and the Vogel:Fulcher like freezing of the polarization fluctuations into a glass like state at lower temperature. The large local dipole moments however allow the glassy state to be "reorganized" into ferroelectric macrodomains under high electric field following Almeida:Thouless type behavior as in a spin glass. Again the glassy state exhibits high local strains associated with the local polarizations, which soften the elastic properties giving a much richer and more useful mix of properties as compared to the magnetic spin glass systems.

Jayne Giniewicz studies concerned the order:disorder phenomenon in the lead scandium tantalate based perovskites which gives rise to controlled relaxor behavior, and the manner in which this is modified on solid solutions with lead titanate (Appendices 15-17).

It is interesting to note that only 7 mole% of lead titanate in solid solution will frustrate the possibility of doing order:disorder in the system, yet some 35% is required to get to the rhombohedral:tetragonal morphotropic phase boundary.

Optical and Electro-optic properties of relaxors which were a primary concern on this contract are delineated in Appendices 18, 19, 20, 21. From the temperature dependence of the refractive index it is possible to monitor the onset of RMS Polarization (The Burns Temperature) and to show that though the electro-optic g constant are dispersive, the behavior gives a coherent description of the fluctuating polarization levels. Just as in the electrostrictive response field biasing gives rise to a linear electrooptic effect so that the induced R constants may be derived. In general the polarization related linear and quadratic constants are very similar to those in other lead containing perovskites.

Appendix 21 reports interesting data on the persistence of the optical second harmonic generation above the accepted Curie temperature in $BaTiO_3$. Relaxation times for the response suggest that in Remeika $BaTiO_3$ the phenomenon is related to defect ordering which provides a "pseudo" bias field in the domain above T_c.

4.0 MICRO COMPOSITES STUDIES

During the contract period a number of approaches were tried to realize closely coupled phases of $BaTiO_3$ (piezoelectric) and $CoFe_2O_4$ (Magnetostrictive) so as to be able to explore elastically coupled magneto-electricity (Appendices 22-25). Both micro 0-3/3-0 composites and

macroscopic layer structure 2:2 composites were fabricated and explored. The best macro-composites had values of α the magneto-electric coefficient from 25 to 500 times that of single phase Cr_2O_3. Theoretical models however suggest that even these improved materials are far from optimum and that even higher α should be possible if processing can be improved.

Composites composed of a high conductivity ceramic or metal phase distributed in a nonconductive matrix have many practical and theoretically interesting properties. Practical interest in PTC thermistors is explored in Appendix 26. Percolation constraints which give the interesting sharp resistance changes with temperature in the PTC are discussed in Appendix 27 and the possible use in interconnect systems considered. Appendix 28 gives a more quantitative general treatment for the resistivity:volume fraction relations in polymer:carbon black composites using a general effective medium approach.

An alternative series, parallel connectivity approach useful for coated power filler phases is examined in Appendix 29. For filler phases with more complex resistivity temperature characteristics such at V_2O_3 have been shown to give the possibility of engineering composites with conductive "windows" in the conductivity temperature curves (Appendix 30).

5.0 INTRINSIC SIZE EFFECTS IN FERROELECTRICS

The phenomena of size effects in ferroelectric crystal powders and ceramics is neatly summarized in Appendix 31. The data from clean powders is shown to be very important predicting size effects which strongly limit scale in $BaTiO_3$ but are much less constraining in $PbTiO_3$. The consequences of these limitation are discussed for thin film ferroelectrics.

6.0 SPECTROSCOPIC ELLIPSOMETRY

The run "up to" the use of spectroscopic ellipsometry in characterizing oxide ferroelectric surfaces and films is given in the PhD theses of Nguyen and Chindaudom (Appendices 32 and 33), and in the paper by Nguyen, Vedam and Narayan (Appendix 34).

The "payoff" for ferroelectricians is discussed in the application to PZT films on buffered silicon (appendix 35) where the full power of the method for evaluating the inhomogeneity in the fractal structure of the films is abundantly clear.

The importance of this understanding is clear from the remarkable changes in the dielectric dispersion in PZT thin films which can occur due to improper control of processing parameter (Appendix 36). An interesting application of the piezoelectric effect in PZT films to the fabrication of mini-piezoelectric surface flexure wave motors is discussed in Appendix 37.

7.0 INVITED LECTURES

1. Cross, L. Eric, "Ferroelectric Materials for Applications in the 1990's," The Science Behind Materials Synthesis, Materials Research Laboratory, University Park, PA (June 10-13, 1990).

2. Cross, L. E., "High Performance Ceramics," MRS International 1990, Beijing, China (June 18-22, 1990).

3. Iijima, S., T. Ota, Iyamai, R. Newnham and S. Yoshikawa, "Electrical Resistivity of Conductive Ceramic-Polymer Composites," The 28th Ceramics Basic Science Conference, Fukuoka, Japan (January 24, 1990).

4. Newnham, R. E., "Structure-Property Relations in Nanocomposites," American Crystallographic Association Annual Meeting, New Orleans, Louisana (April 8-13, 1990).

5. Ruschau, G. R., R. E. Newnham and J. Runt, "Conductive Composites as Chemical Sensors," Materials Research Society Meeting, San Francisco, CA (April 16-21, 1990).

6. Smith, D. J., R. E. Newnham and S. Yoshikawa, "Ultraviolet System for Ceramic Tap Casting," American Ceramic Society Meeting, Dallas, TX (April 21-24, 1990).

7. Newnham, R. E., "How Smart is a Ceramic?," Swedish Royal Academy, Stockholm, Sweden (May 30, 1990).

8. Newnham, R. E., "Global Perspectives on the Applications of Ferroelectrics," International Symposium on Application of Ferroelectrics (ISAF), University of Illinois, Urbana, IL (June 6-8, 1990).

9. Shrout, T. R. and J. Fielding, Jr., "Relaxor Ferroelectric Materials," IEEE Ultrasonics Symposium (December 1990).

10. Newnham, R. E., "Size Effects in Ferroelectric Films," 5th International Congress on Ultra Structure Processing," Orlando, Florida (February 14, 1991).

11. Newnham, R. E., "Biomimitic Sensors and Actuators," Materials Research Society, Boston (December 1991).

12. Udayakumar, K. R., A. M. Flynn, J. Chen and L. E. Cross, "Ferroelectric PZT Thin Films for Microelectromechanical Applications," MEMS 91, Narita, Japan (January 31, 1991).

13. Cross, L. E., "A Dipolar Glass Model for Relaxor Ferroelectrics," EMF7 European Meeting on Ferroelectrics, Dijon, France (July 1991).

14. Cross, L. E., "Possibility of Super Responses in Ceramics," Gordon Conference on Ceramics, Holderness, Plymouth (July 29, 1991).

15. Cross, L. E., "Ferroelectric Thin Films - Current Status and Future Prospects (Overview)," 93rd American Ceramic Society National Meeting, Cincinnati, Ohio (April 29, 1991).

8.0 CONTRIBUTED PAPERS

1. Blaszkiewicz, M., D. A. McLachlan and R. E. Newnham, "A Study of the Volume Fraction, Temperature, and Pressure Dependence of the Resistivity in a Ceramic-Polymer Composite Using a General Effective Media Theory Equation," American Ceramic Society Annual meeting, Dallas, Texas (April 1990).

2. Mulvihill, M. L., A. Das, P. Fuierer, W. K. Kim and W. Huebner, "Low Dielectric Planarization Coatings for Electronic Packaging," American Ceramic Society Annual Meeting, Dallas, Texas (April 1990).

3. McLachlan, D. S., M. Blaszkiewicz, S. Yoshikawa and R. E. Newnham, "A Study of the Volume Fraction, Temperature, and Pressure Dependence of the Resistivity in a Ceramics-Polymer Composite using a General Effective Media Theory Equation," Materials Research Society, Spring Meeting Symposium, San Francisco, CA (April 16-21, 1990).

4. Viehland, D., S. Jang and L. E. Cross, Materials Research Laboratory, Pennsylvania State University, University Park, PA; and M. Wuttig, University of Maryland, College Park, MD, "Local Interactions in Relaxor Ferroelectrics," Seventh International Symposium on the Application of Ferroelectrics (ISAF 1990), University Illinois, Champaign, Illinois (June 6-8, 1990).

5. Udayakumar, K. R., J. Chen, S. B. Krupanidhi and L. E. Cross, "Fabrication and Characterization of Morphotropic Phase Boundary PMN-PT Sol-Gel Thin Films," Seventh International Symposium on the Application of Ferroelectrics (ISAF 1990), University Illinois, Champaign, Illinois (June 6-8, 1990).

6. Reed, D. M., T. T. Srinivasan, Q. C. Xu and R. E. Newnham, "Effect of Particle Size on Dielectric and Piezoelectric Properties in Various Volume Percent Loaded Sm and Mn Doped Polymer - $PbTiO_3$ Composites," Seventh International Symposium on the Application of Ferroelectrics (ISAF 1990), University Illinois, Champaign, Illinois (June 6-8, 1990).

7. Xu, Q. C., R. Flannigan, T. T. Srinivasan and R. E. Newnham, "Aging of Ferroelectric Ceramic/Polymer 0-3 Composites," Seventh International Symposium on the Application of Ferroelectrics (ISAF 1990), University Illinois, Champaign, Illinois (June 6-8, 1990).

8. Newnham, R. E., M. Blaszkiewicz, Q. C. Xu, T. T. Fang, T. T. Srinivasan and S. Yoshikawa, "Nonlinear Ceramic-Polymer 2-2 Piezoelectric Composites," Seventh International Symposium on the Application of Ferroelectrics (ISAF 1990), University Illinois, Champaign, Illinois (June 6-8, 1990).

9. Harshe, G., T. T. Srinivasan, J. P. Dougherty and R. E. Newnham, "Magnetoelectric Multilayer Composites," Seventh International Symposium on the Application of Ferroelectrics (ISAF 1990), University Illinois, Champaign, Illinois (June 6-8, 1990).

10. Troiler-McKinstry, S. and R. E. Newnham, "Spectroscopic Ellipsometry Study of Ferroelectric Surfaces," Seventh International Symposium on the Application of Ferroelectrics (ISAF 1990), University Illinois, Champaign, Illinois (June 6-8, 1990).

11. Yoshikawa, S., G. R. Ruschau and R. E. Newnham, "Conductor-Polymer Composite for Electronic Connectors," Second International Ceramic Science and Technology Congress, Orlando, Florida (November 12-15, 1990).

8.0 CONTRIBUTED PAPERS *(continued)*

12. Mulvihill, M. L., A. Das, J. P. Dougherty and R. E. Newnham, "Low Dielectric Constant Planarization Coating for Electronic Packaging," Second International Ceramic Science and Technology Congress, Orlando, Florida (November 12-15, 1990).

13. Ota, T., I. Yamai, J. Takahashi, R. E. Newnham and S. Yoshikawa, "Effects of Filler Particle Size on the Electrical Resistance of Conductor-Polymer Composites," Second International Ceramic Science and Technology Congress, Orlando, Florida (November 12-15, 1990).

14. Ravindranathan, P., S. Komarneni, A. S. Bhalla and R. Roy, "Effect of Seeding on the Crystallization of Lead Magnesium Niobate (PMN) Gels," 93rd American Ceramic Society National Meeting, Cincinnati, Ohio (April 29, 1991).

15. McHenry, D. A., S. J. Jang and A. S. Bhalla, "Electrooptic Effects in the Ceramic $Pb(Mg_{1/3}Nb_{2/3})O_3$, $PbTiO_3$ System," 93rd American Ceramic Society National Meeting, Cincinnati, Ohio (April 29, 1991).

16. Kim, N., J. T. Fielding, S. J. Jang and T. R. Shrout, "Grain Size Effects in PZT Based Ceramics," 93rd American Ceramic Society National Meeting, Cincinnati, Ohio (April 29, 1991).

17. Troiler-McKinstry, S. E., P. Chindaudom and R. E. Newnham, "Characterization of Ferroelectric Surfaces and Thin Films by Spectroscopic Ellipsometry," 93rd American Ceramic Society National Meeting, Cincinnati, Ohio (April 29, 1991).

18. Viehland, D., S. J. Jang and L. E. Cross, Pennsylvania State University, University Park, PA; and M. Wuttig, University of Maryland, College Park, MD, "The Dielectric Dispersion of Relaxor Ferroelectrics," 93rd American Ceramic Society National Meeting, Cincinnati, Ohio (April 29, 1991).

19. Kumar, U. and J. P. Dougherty, "Low Temperature Conventional Preparation of Ultra-Fine Grained $BaTiO_3$ Ceramic," 93rd American Ceramic Society National Meeting, Cincinnati, Ohio (April 29, 1991).

20. Guo, R., D. A. McHenry, A. S. Bhalla and L. E. Cross, "Optical and Electrooptic Properties of Lead Barium Niobate (PBN) Single Crystals," 93rd American Ceramic Society National Meeting, Cincinnati, Ohio (April 29, 1991).

21. Brooks, Keith G., Jiayu Chen, K. R. Udayakumar and L. Eric Cross, "Properties of PZT Thin Films with Glass Additives Prepared by the Sol-Gel Process," Materials Research Society Meeting, Boston, Massachusetts (December 1991).

22. Brooks, Keith G., Jiayu Chen, K. R. Udayakumar and L. Eric Cross, "Modified Tetragonal Lead Zirconate Titanate Stannate Thin Films Prepared by Sol-Gel Process Large Strain Microactuator Applications," Materials Research Society Meeting, Boston, Massachusetts (December 1991).

9.0 HONORS TO MRL FACULTY AND STUDENTS

Name of Person Receiving the Award	Name of Award	Sponsor
A. S. Bhalla	Fellow	American Ceramic Society
L. E. Cross	Chairman	IEEE Ferroelectrics Section of UFFC
L. E. Cross	National Representative	IUPAP International Committee on Ferroelectrics
Ruyan Guo	Xerox Award for Best Materials PhD in 1991	Xerox Corporation
R. E. Newnham	Educator of the Year	Ceramic Education Council
R. E. Newnham	John Jeppson Medal and Award	American Ceramic Society
R. E. Newnham	Centennial Award of Ceramic Society of Japan	Japan Ceramic Society

GENERAL PAPERS

APPENDIX 1

FERROELECTRIC CERAMICS: TAILORING PROPERTIES FOR SPECIFIC APPLICATIONS

L. Eric Cross

1 Introduction

Ferroelectric oxide ceramics are used in a very broad range of functional ceramics and form the materials base for the majority of electronic applications. These electronic applications account for more than 60% of the total high technology ceramics market worldwide (High Technology Ceramic News, 1990). It is the purpose of this tutorial paper to examine the range of physical properties which make the ferroelectrics attractive for electronic applications and the techniques which can be used to modify, control and optimize these families of properties.

Major applications can be divided into five distinct areas which draw upon different combinations of properties:

Dielectric applications make use of the very high dielectric permittivity ε_{ij}, low dispersion and wide frequency range of response for compact capacitors in multilayers, thick and thin film forms (Herbert, 1985a). Nonlinear hysteritic response is of interest also for thin film nonvolatile semiconductor memory (Myers and Kingon, 1990), and high permittivity films are of interest for local capacitance in high count DRAMs and both on and off chip in packaging (Tummala and Rymaszewski, 1989).

Piezoelectric and electrostrictive responses in poled and unpoled ferroelectric and relaxor ferroelectric compositions are of importance in Transducers (Levinson, 1988) for converting electrical to mechanical response (Rosen, 1959) and vice versa (Herbert, 1985b). Sensor applications make use of the very high piezoelectric constants d_{ijk} of the converse effect, which also permit efficient conversion of electrical to mechanical response (Jaffe and Berlincourt, 1965). For actuation the strong basic electrostrictive coupling can be exploited for very high precision position control (Aldrich, 1980) and the possibility of phase and domain switching with shape memory is used in polarization controlled actuation (Pan et al., 1989).

Pyroelectric systems rely upon the strong temperature sensitivity of electric polarization (dP_S/dT) (Porter, 1981), the pyroelectric effect in ferroelectrics, for the bolometric detection of

long wavelength infra red (IR) radiation (Whatmore et al., 1980). Simple point detectors are widely used in domestic and industrial applications (Liu, 1976) and there is now a strong focus upon imaging systems which may be used for nigh vision (Watton, 1986) and for thermal-medical diagnostics (Kazan, 1977).

P.T.C. semiconductors are a specialized area of application in which the barrier to charge transport at the ceramic grain boundary in specially processed barium titanate based ceramics is controlled by the polarization state of the ferroelectric (Daniels and Haerdtl, 1976), giving rise to an extremely strong positive temperature coefficient of resistivity (PTCR effect) controlled by the Curie point of the ferroelectric composition (Hanke, 1979).

In Electro-optic applications the properties of interest are the high quadratic (DiDomenico and Wemple, 1969) and linear (Günter, 1980) electro-optic coefficients (r_{ijk}, g_{ijkl}) which occur in ferroelectrics and the manner in which these can be controlled in modulators (Salvo, 1971), switches (Alfness, 1986), guided wave structures and photo-refractive devices (VanderLinde and Glass, 1975).

In this tutorial, the dielectric, piezoelectric and electrostrictive applications will be the focus, but the techniques examined to modify and improve properties will also be valid for many of the other material needs.

Considering the nature of the properties to be optimized, two important features will be stressed. Firstly the interest is in bulk, lattice properties controlled largely by the crystal structure of the ceramic. Secondly in every case it is augmented compliance (softness) which is of interest, in contrast often to the structural ceramics where it is stiffness which must be augmented. It follows then that instability of the lattice will be of importance, since this engenders compliance, and thus phase changes which are the finger prints of instability will be of major importance. Frequently to improve properties then, we are looking to exploit and control solid state phase transitions.

Clearly a bounding condition is that the crystal structure must permit ferroelectricity in a useful region of temperature and pressure, and must be of a type which can be exploited in the simple polycrystal ceramic form. In fact, all of the structures of interest are based on regular arrays of oxygen octahedra, and the simple perovskite structure is certainly the most widely used.

2 Structure Types of Interest

The interesting oxygen octahedron structures which show strong ferroelectric properties with high usable temperature ranges are all based upon corner linking of oxygen octahedra. The simplest arrangement is the very well known perovskite structure Figure 2.1 where the octahedra are linked in a regular cubic array forming the high symmetry m3m prototype for many ferroelectric forms.

he small 6 fold coordinated site in the center of the octahedron is filled by a small highly charged (3,4,5 or 6 valent) cation and the larger 12 fold coordinated 'interstitial' site between octahedra carries a larger mono, di or trivalent cation, or is empty as in WO_3.

The perovskite structure is a common stable form for many double oxides, but ferroelectricity was not discovered in the family until the early 1940s, when Wainer and Soloman (1942) in the USA, Ogawa (1946) in Japan and Wul and Goldman (1945) in the USSR made almost simultaneous discovery of ferroelectricity in barium titanate $BaTiO_3$. The US study was part of a 'crash' program during World War II to discover a ceramic substitute for mica which was being exhausted by rapidly escalating military needs. It is perhaps interesting to note that $BaTiO_3$ which was the highlight of these early studies is still the base for the composition of most of the world's ceramic capacitors.

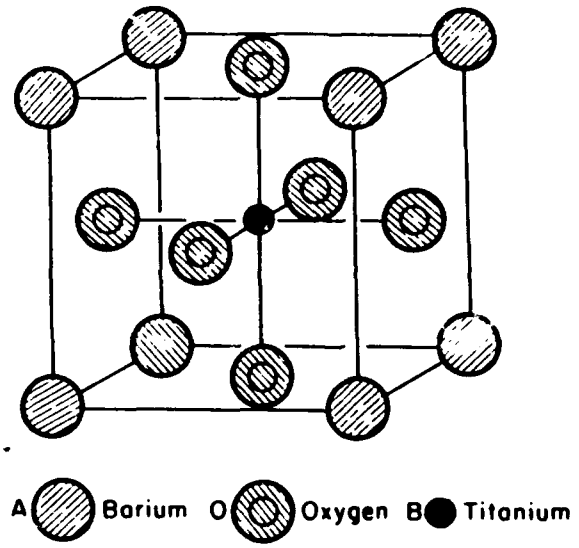

Figure 2.1: The unit cell for a typical cubic perovskite barium titanate in the cubic Pm3m prototypic phase above T_C.

An interesting documentation of early work in Japan has been carried forward by Murata Company and is now available in book form (Wakino, 1990) for those well versed in the language. Perhaps now it may be possible to catalogue more completely the Soviet contribution to complete the early history of the titanates. Structural information for a very broad range of perovskites is available in the early book by Galasso (1969) which is now being revised and updated. Certainly the most complete trustworthy cataloguing of ferroelectric oxide perovskites is given in the Landolt Bornstein Vol. 16a on oxide ferroelectrics (Landolt Bornstein, 1981). This

tabulates more than 100 perovskite compounds and innumerable solid solutions between compounds.

Of major importance in ceramic dielectric applications are $BaTiO_3$ and solid solutions with $SrTiO_3$, $PbTiO_3$, $BaZrO_3$, $BaSnO_3$, $CaTiO_3$..... and a range of bismuth oxide based modifiers. In piezoelectrics the higher Curie points in the $PbTiO_3$:$PbZrO_3$ solid solutions and the unusual ferroelectric phase makeup are vital and in both dielectric and electrostrictive application the $Pb(B_1B_2)O_3$ mixed cation compositions are becoming of increasing interest where B_1 may be Fe, Ni, Mg, Zn..... and B_2, Ti, Zr, Nb, Ta, W.... etc.

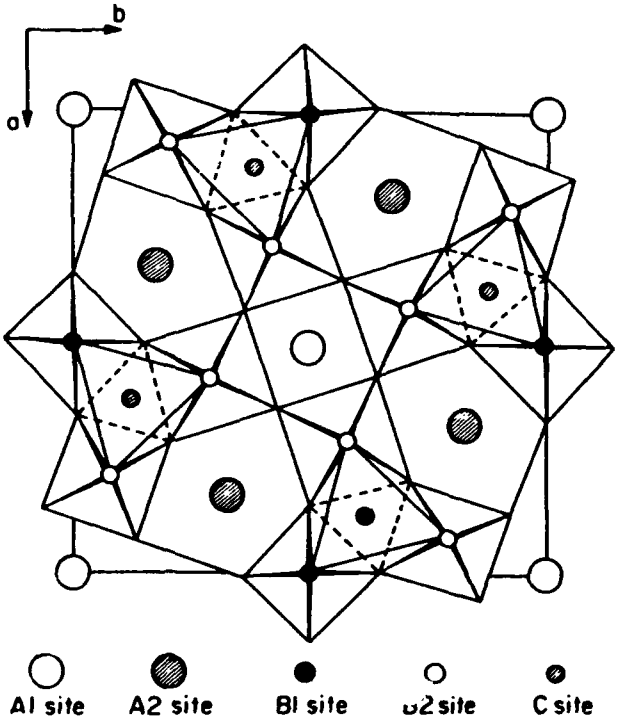

$$(A1)_2^{XII}(A2)_4^{XV}(C)_4^{IX}(B1)_2^{VI}(B2)_8^{VI}O_{30}^{VI}$$

Figure 2.2: Projection down the c(3) axis of a unit cell in the tungsten bronze structure. Site locations are marked and the structure related formula is given. Roman superscripts mark the coordination of the ions at each site location.

In current electronic ceramic applications only perovskite structure compositions are used, however with increasing sophistication in ceramic processing it is probably that strongly grain oriented structures may become practicable. The newer thin film structures also provide avenues

for orientation using topotactic configurations on suitable substrates, so that ferroelectrics from lower prototypic symmetries may become of interest in ceramics.

The next most versatile structure family are the Tungsten Bronze structure ferroelectrics with the octahedron arrangement in Figure 2.2. The rotations of the octahedra evident in the ab plane of the structure in 2.2 reduce the point symmetry to tetragonal (4/mmm) with layers stacked in regular sequence along the 4 fold (c) axis. The arrangement distinguishes two inequivalent 6 fold coordinated B sites at the centers of inequivalent octahedra with 5, 4 and 3 sided tunnels for the A site cations extending along the c axis giving the structure related formula for the bronzes:

$$(A_1)_2^{XII}(A_2)_4^{XV}(C_4)_4^{IV}(B_1)_2^{VI}(B_2)_8^{VI}O_{30}\ .$$

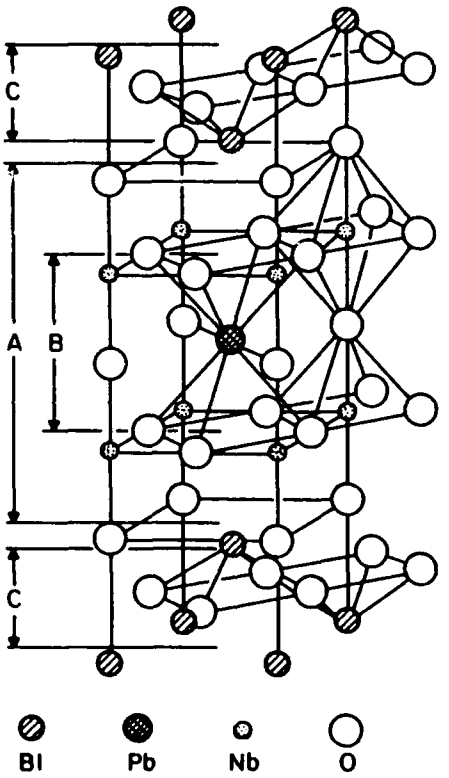

Figure 2.3: One half of the tetragonal (4/mmm) unit cell of $PbBi_2Nb_2O_9$. A denotes the perovskite double layer $(PbNb_2O_7)^{2-}$; B denotes a hypothetical $PbNbO_3$; C denotes the $(Bi_2O_2)^{2+}$ layers.

The bronzes are a very rich family of oxide ferroelectrics with Curie temperatures reaching up to 560°C and more than 85 compounds in the most recent survey (Oliver et al., 1989). Again there

is very extensive solid solution between end members (Landolt Bornstein, 1981) and the open nature of the structure as compared to the perovskite permits a very wide range of cation and anion substitutions without loss of ferroelectricity.

The bismuth oxide layer structures for which $Bi_4Ti_3O_{12}$ is the prototype are depicted in Figure 2.3 and have structures based on corner linked perovskite-like sheets, separated by bismuth oxide $(Bi_2O_2)^{2+}$ layers (Cummins and Cross, 1967). Compositions with 1, 2, 3, 4 and 5 layers are known and there is limited mutual solid solubility (Subbarao, 1962).

The lithium niobate structure is really a variant of the perovskite Figure 2.4 and a much more restrictive arrangement, so that only $LiNbO_3$, $LiTaO_3$ and a very limited range of solid solutions based on these compounds have this form.

In what follows, the discussion is centered on systems with the perovskite structure.

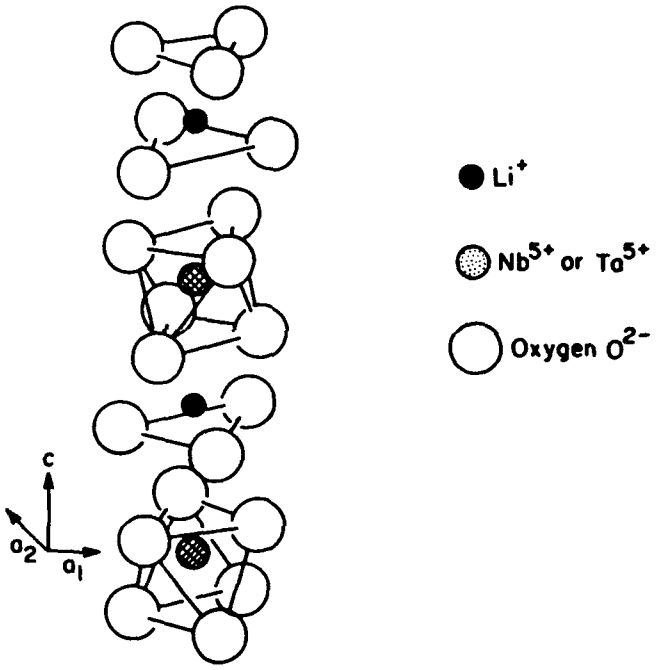

Figure 2.4: Structure of ferroelectric $LiNbO_3$ and $LiTaO_3$ (40).

3 Phase Transitions in Perovskites

Three different types of phase transitions are of interest in the perovskites, starting from the highest symmetry cubic form:

Simple proper ferroelectric transitions leading to fully ferroelectric partially ferroelastic species.

Antiferroelectric transitions close in free energy to the ferroelectric forms, giving rise to interesting dielectric and to improper ferroelastic species.

Oxygen octahedron tilting transitions which can occur independently, or in association with either ferroelectric or antiferroelectric forms.

3.1 Ferroelectric Phase Transitions

Most important for their profound influence on the dielectric polarizability and the resultant sequence of polar variants are the simple proper ferroelectric transitions. In the symmetry classification of Aizu (1966, 1970, 1967) and of Shuvalov (1970) the high symmetry cubic m3m prototype can give rise to six different polar species (Table 3.1). The vector directions of polarization which are specified with respect to elements of the prototype symmetry form the domain states of the ferroelectric form in each case giving 6, 12, 8, 24, 24 and 48 domain polarization directions respectively.

Table 3.1: Ferroelectric phase transitions possible from the cubic m3m prototype following the symbolism of Shuvalov.

Phase	Symmetry	Polarization Components	Shuvalov Species
Cubic	m3m	$P_1 = P_2 = P_3 = 0$	Prototype
Tetragonal	4mm	$P_1^2 \neq 0 \quad P_1^2 \approx P_3^2 = 0$	m3m(3)D4F4mm
Orthorhombic	mm2	$P_1^2 = P_2^2 \neq 0 \quad P_3^2 = 0$	m3m(6)D2Fmm2
Rhombohedral	3m	$P_1^2 = P_2^2 = P_3^2 \neq 0$	m3m(4)D3F3m
Monoclinic	m	$P_1^2 \neq P_2^2 \neq 0 \quad P_3^2 = 0$	m3m(12)A4Fm
Monoclinic	m	$P_1^2 = P_2^2 \neq 0 \quad P_3^2 \neq 0$ $P_1^2 \neq P_3^2$	m3m(12)A2Fm
Triclinic	1	$P_1^2 \neq P_2^2 \neq P_3^2 \neq 0$	m3m(24)A1F

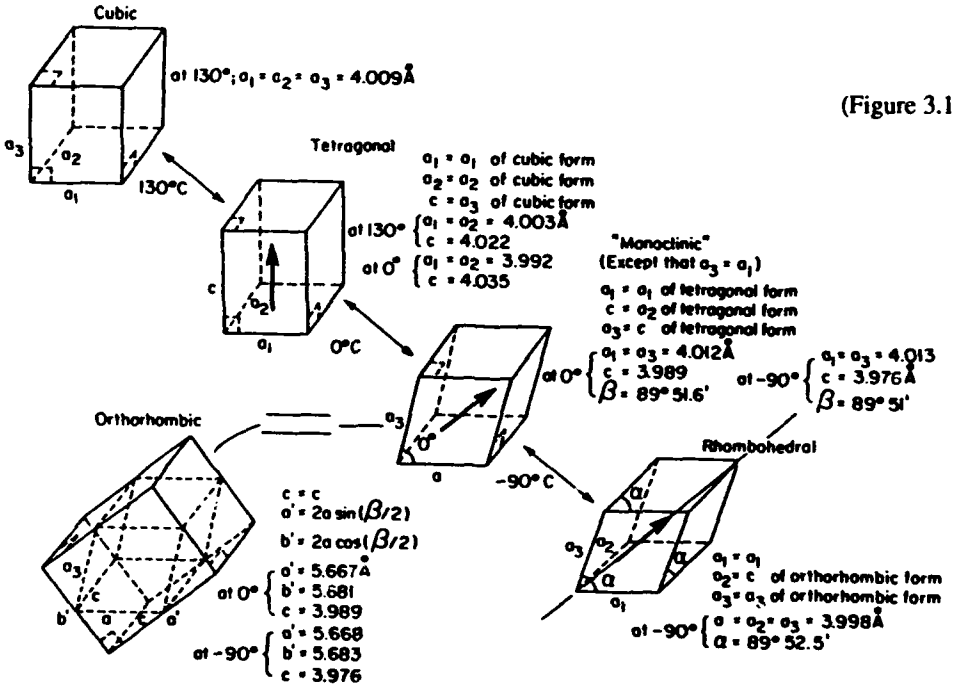

(Figure 3.1a)

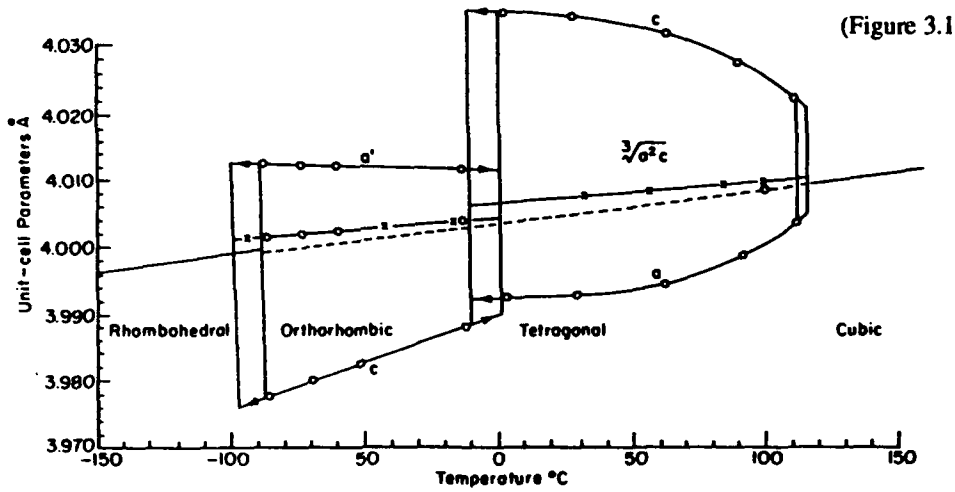

(Figure 3.1b)

Figure 3.1: Sequence of phases which occur on cooling a $BaTiO_3$ crystal from high temperature. (Figure 3.1a) Unit cell dimensions and orientation of Ps vector in each phase. (Figure 3.1b) Unit cell dimensions as a function of temperature across the three ferroelectric phases.

Clearly for a randomly axed polycrystalline ceramic form, the more switchable domain states, the easier it will be to "thread" polarization through the sample. Surprisingly however, even though permitted by symmetry, there have been no cases reported of transitions into monoclinic or triclinic symmetries in the perovskites even though such states would be highly advantageous for ceramics.

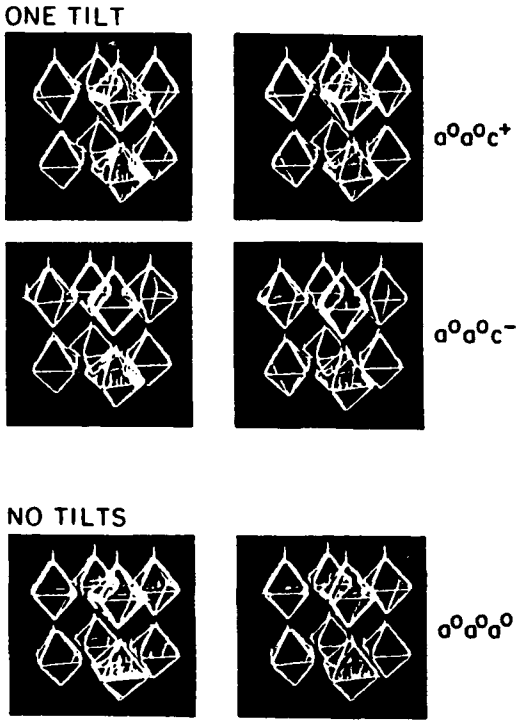

Figure 3.2: Oxygen octahedral arrangements in an untilted structure $a^0a^0a^0$: Oxygen tilts in a co-tilted c axis rotated structure $a^0a^0c^+$ and in a contra-rotated layer structure $a^0a^0c^-$. Notation due to Glaser.

In many instances the ferroelectric variant is not stable over the whole temperature range below the first ferroelectric Curie point transition and the structure may go successively into lower symmetry species. The sequence of transitions in barium titanate, which is the base composition for most dielectric applications is shown in Figure 3.1a. Successive transitions on cooling take the domain symmetry to tetragonal, orthorhombic and rhombohedral. A very simple Landau type theory has been given by Devonshire (1949, 1951) which gives an elegant phenomenological description of the phase transitions, polarization states, dielectric and elastic properties and the shape changes depicted in Figure 3.1b.

Complete list of possible simple tilt systems

Serial number	Symbol	Lattice centring	Multiple cell	Relative pseudocubic subcell parameters	Space group
3-tilt systems					
(1)	$a^+b^+c^+$	I	$2a_p \times 2b_p \times 2c_p$	$a_p \neq b_p \neq c_p$	$Immm$ (No. 71)
(2)	$a^+b^+b^+$	I		$a_p \neq b_p = c_p$	$Immm$ (No. 71)
(3)	$a^+a^+a^+$	I		$a_p = b_p = c_p$	$Im\bar{3}$ (No. 204)
(4)	$a^+b^+c^-$	P		$a_p \neq b_p \neq c_p$	$Pmmn$ (No. 59)
(5)	$a^+a^+c^-$	P		$a_p = b_p \neq c_p$	$Pmmn$ (No. 59)
(6)	$a^+b^+b^-$	P		$a_p \neq b_p = c_p$	$Pmmn$ (No. 59)
(7)	$a^+a^+a^-$	P		$a_p = b_p = c_p$	$Pmmn$ (No. 59)
(8)	$a^+b^-c^-$	A		$a_p \neq b_p \neq c_p \alpha \neq 90°$	$A2_1/m11$ (No. 11)
(9)	$a^+a^-c^-$	A		$a_p = b_p \neq c_p \alpha \neq 90°$	$A2_1/m11$ (No. 11)
(10)	$a^+b^-b^-$	A		$a_p \neq b_p = c_p \alpha \neq 90°$	$Pnma$ (No. 62)*
(11)	$a^+a^-a^-$	A		$a_p = b_p = c_p \alpha \neq 90°$	$Pnma$ (No. 62)*
(12)	$a^-b^-c^-$	F		$a_p \neq b_p \neq c_p \alpha \neq \beta \neq \gamma \neq 90°$	$F\bar{1}$ (No. 2)
(13)	$a^-b^-b^-$	F		$a_p \neq b_p = c_p \alpha \neq \beta \neq \gamma \neq 90°$	$I2/a$ (No. 15)*
(14)	$a^-a^-a^-$	F		$a_p = b_p = c_p \alpha = \beta = \gamma \neq 90°$	$R\bar{3}c$ (No. 167)
2-tilt systems					
(15)	$a^0b^+c^+$	I	$2a_p \times 2b_p \times 2c_p$	$a_p < b_p \neq c_p$	$Immm$ (No. 71)
(16)	$a^0b^+b^+$	I		$a_p < b_p = c_p$	$I4/m$ (No. 87)
(17)	$a^0b^+c^-$	B		$a_p < b_p \neq c_p$	$Bmmb$ (No. 63)
(18)	$a^0b^+b^-$	B		$a_p < b_p = c_p$	$Bmmb$ (No. 63)
(19)	$a^0b^-c^-$	F		$a_p < b_p \neq c_p \alpha \neq 90°$	$F2/m11$ (No. 12)
(20)	$a^0b^-b^-$	F		$a_p < b_p = c_p \alpha \neq 90°$	$Imcm$ (No. 74)*
1-tilt systems					
(21)	$a^0a^0c^+$	C	$2a_p \times 2b_p \times c_p$	$a_p = b_p < c_p$	$C4/mmb$ (No. 127)
(22)	$a^0a^0c^-$	F	$2a_p \times 2b_p \times 2c_p$	$a_p = b_p < c_p$	$F4/mmc$ (No. 140)
Zero-tilt system					
(23)	$a^0a^0a^0$	P	$a_p \times b_p \times c_p$	$a_p = b_p = c_p$	$Pm\bar{3}m$ (No. 221)

* These space group symbols refer to axes chosen according to the matrix transformation

$$\begin{pmatrix} 1 & 0 & 0 \\ 0 & \frac{1}{2} & -\frac{1}{2} \\ 0 & \frac{1}{2} & \frac{1}{2} \end{pmatrix}.$$

Figure 3.3: Classification for zero, one, two and three tilt systems after Glaser.

3.2 Octahedral Tilting Phase Transitions

In many perovskites, particularly those with smaller A site cations, the net of orthogonal corner linked oxygen octahedra "crumples" at lower temperatures. The octahedra remain corner linked and adjacent octahedra thus must contra rotate, Figure 3.2. Rotations can take place around any of the three 4-fold axes so that formally the tilt structures may be treated phenomenologically (using the tilt angle θ as the appropriate order parameter) (Axe, 1972). Since the tilts necessarily carry strongly coupled anti-polar oxygen displacement, effects on the polarizability of the lattice are not strong, however the displacements are shape changing and thus give rise to improper ferroelastic domain structures. Excellent compact classifications of the possible tilt system have been given by Glazer (1975) (see Figure 3.3) and by Alexandrov (1976, 1978).

Compound	Formula	Phase-transition temperature °C
1	2	3
	Displacive antiferroelectrics	
	A. Perovskite structure	
Lead zirconate	$PbZrO_3$	230, ~228
Sodium niobate	$NaNbO_3$	~480, 354, ~200
Lead hafnate	$PbHfO_3$	215, 160
Bismuth ferrite?	$BiFeO_3$	~850, ~400, ~200
Silver niobate?	$AgNbO_3$	325, 550
Lead stannate?	$PbSnO_3$	~400
Lead magnesium tungstate	$PbMg_{1/2}W_{1/2}O_3$	~38
Lead nickel tungstate	$PbNi_{1/2}W_{1/2}O_3$	17-160
Lead cobalt tungstate	$PbCo_{1/2}W_{1/2}O_3$	~30, ~20, ~206
Lead cadmium tungstate?	$PbCd_{1/2}W_{1/2}O_3$	~400, 100
Lead ytterbium niobate	$PbYb_{1/2}Nb_{1/2}O_3$	~310, ~160
Lead ytterbium tantalate?	$PbYb_{1/2}Ta_{1/2}O_3$	~290
Lead lutecium niobate?	$PbLu_{1/2}Nb_{1/2}O_3$	~280
Lead lutecium tantalate?	$PbLu_{1/2}Ta_{1/2}O_3$	~270
Lead indium niobate?	$PbIn_{1/2}Nb_{1/2}O_3$	~90
Sodium bismuth titanate?	$Na_{1/2}Bi_{1/2}TiO_3$	200, 320, 520
Lead ferrouranate?	$PbFe_{2/3}U_{1/3}O_3$	~-100
Lead manganese tungstate?	$PbMn_{1/2}W_{1/2}O_3$	~150
Lead manganese tungstate?	$PbMn_{2/3}W_{1/3}O_3$	200, ~70
Lead gallium niobate?	Pb_2GaNbO_6	~100
Lead bismuth niobate?	Pb_2BiNbO_6	~-235
Lead manganese rhoenate?	$PbMn_{1/2}Re_{1/2}O_3$	~120, ~170
Lead cobalt rhoenate?	$PbCo_{1/2}Re_{1/2}O_3$	~130

Figure 3.4: Antiferroelectric perovskites.

3.3 Antiferroelectric Phase Transitions

In certain perovskites the dielectric "fingerprints" in the prototypic high temperature phase suggest increasing compliance with decreasing temperature, the signal for a lower temperature ferroelectricity. However the phase transition is into a nonpolar form with antipolar displacements of the normal ferroactive cations at the unit cell level. As with the polar forms, the antipolar displacements are strongly coupled to the crystal shape so that in symmetry, the domain states are a sub-group of the improper ferroelastics. For electrical purposes only those antiferroelectrics which are close in free energy to alternative ferroelectric forms are of interest especially in the special case where the energy difference can be over ridden by a realizable electric field.

Sodium niobate and lead zirconate are two well documented antiferroelectrics where high field switching to the ferroelectric form has been well authenticated (Cross and Nicholson, 1955; Fesenko et al., 1978). However the list of "card carrying" perovskite antiferroelectrics is still short

and the subject merits additional study. It would be indeed useful to remove some of the question marks which 'dog' current lists of antiferroelectric compositions (Figure 3.4).

4 Engineering of Ferroelectric Phase Transitions

The extrema which occur in the dielectric, pyroelectric, elasto-electric and opto-electric properties of ferroelectrics at temperatures close to the phase transitions take the properties into exceedingly interesting and practically important ranges. It is thus important to explore the mechanisms which can be used to modify and control the transition behaviour.

In the perovskite system, five types of control are important:

• For solid solutions, the phase transition temperatures often change continuously with composition so that in homogeneous compositions the transitions may be placed at optimum temperatures. Further, by controlling a deliberate heterogeneity a range of transitions can be engendered spreading and smoothing the sharp extrema.

• In some solid solutions, ferroelectric:ferroelectric phase transitions occur at fixed compositions and are nearly independent of temperature. These so called morphotropic phase boundaries are extremely important in piezoelectric ceramics.

• Elastic stress can have a marked effect on the transition behaviour and the property extrema near the transition so that self generated stresses in ceramics may be engineered to improve the properties.

• For ceramic compositions the grain:grain boundary heterogeneity can be invoked to modify extrema and to control the field distribution in the ceramic.

• Since ferroelectricity is a cooperative phenomenon the scale of the ferroelectric region is of critical importance. Nano-scale heterogeneity can engender completely new properties and give rise to spin glass behaviour which can be exploited in both capacitors and transducers.

4.1 Engineering Transitions for Dielectric Applications

Many practical ferroelectric capacitor dielectrics are based upon barium titanate, $BaTiO_3$. The key feature of any ferroelectric is that is some accessible range of temperature and pressure it has a

ferroelectric phase, and that in that phase a spontaneous electric polarization can be switched between two or more equilibrium orientations by a realizable electric field.

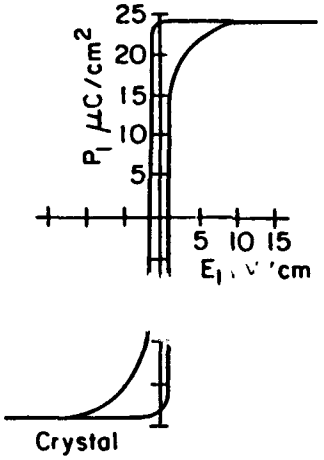

Figure 4.1: Hysteresis in single crystal $BaTiO_3$ selected to be without 90° domains.

As has been shown in Figure 3.1, $BaTiO_3$ at room temperature is ferroelectric with six alternative domain states polarized along any one of the six equivalent <100> directions of the original cubic prototypic form.

For a 100 oriented single crystal the hysteresis loop is very square, Figure 4.1, the end states may be shown to be single domain yielding in the most perfect crystals a value P_S - 26 μc/cm^2 at 20°C (Merz, 1953). In a polycrystaline ceramic, the domain structure is much more complex, Figure 4.2, the hysteresis loop very rounded so that both maximum and remanent polarizations are much lower than the single crystal values Figure 4.3 (Jaffe et al., 1971).

For the more perfect crystal which can be converted to single domain state, the paraelectric and the single domain intrinsic polarizability can be measured, Figure 4.4, 4.5. Unlike ferromagnets very high permittivity persists for a wide temperature range above the Curie Point T_C following a Curie Weiss law $\mathcal{E} = \frac{C}{T-\Theta}$.

In this case however $C \simeq 1.5\ 10^5$°K as compared to $C \sim 10^{-2}$°K in a corresponding ferro- or ferrimagnet (Figure 4.6).

Above T_C, the cubic m3m symmetry dictates that the weak field dielectric susceptibility (permittivity) be spherically symmetrical so the ε_W can be completely characterized.

$$\begin{matrix} \varepsilon_w & 0 & 0 \\ 0 & \varepsilon_w & 0 \\ 0 & 0 & \varepsilon_w \end{matrix}$$

Figure 4.2: Microstructure of 90° twin domains in a coarse grained $BaTiO_3$ ceramic.

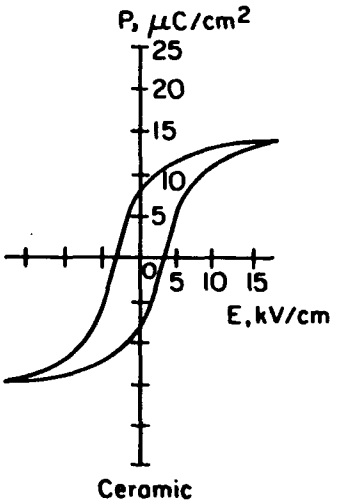

Figure 4.3: Dielectric hysteresis in a coarse grain $BaTiO_3$ ceramic.

In ceramic form, the first question must be whether the grain boundary acts as a high impedance layer strongly limiting utility as a capacitor. The cubic form above T_C permits an unequivocal answer. Extensive experiments on very carefully prepared $BaTiO_3$ ceramics with average grain size from 0.75 to 53 μ meters by Yamagi et al. (1976) show no significant change either in C or in Θ as compared to the crystal (Figure 4.7), confirming that ceramics can be made with low impedance grain boundary structures

The absence of major grain boundary impedance suggests that the high permittivity near T_C could be exploited in capacitors if T_C could be moved near room temperature and the response

broadened. In solid solutions, all of the phase transitions move continuously with composition as shown in Figure 4.8 for solutions with $PbTiO_3$, $SrTiO_3$, $BaZrO_3$, $CaTiO_3$ and $BaSnO_3$.

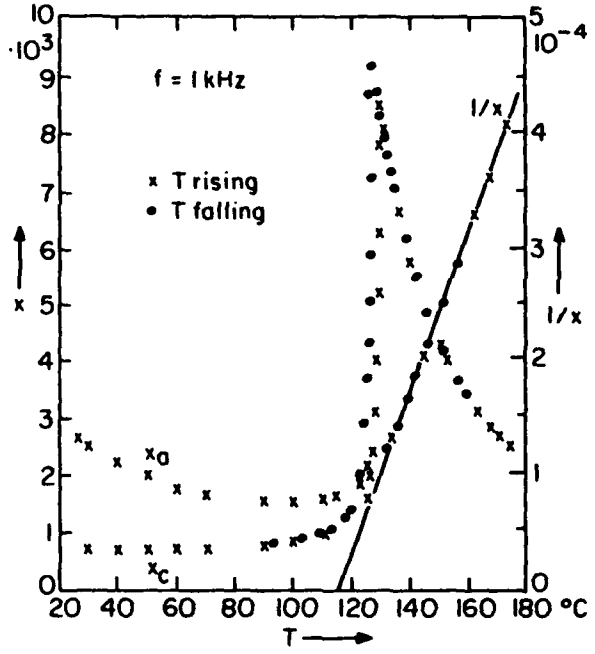

Figure 4.4: Dielectric permittivity (weak field) near the Curie temperature in a single domain $BaTiO_3$ crystal.

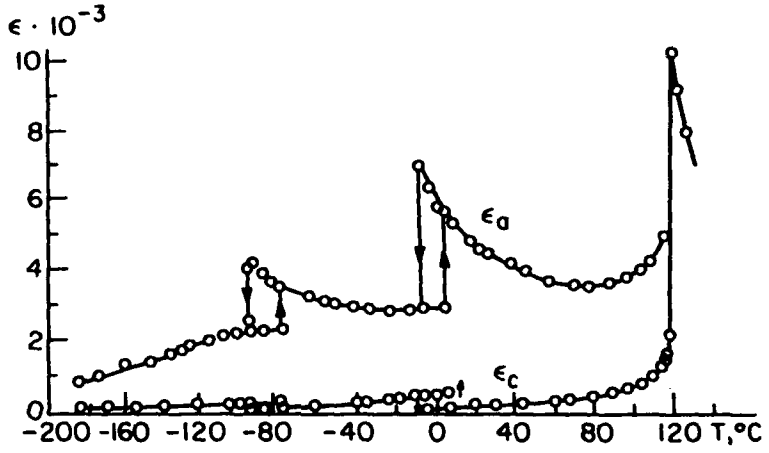

Figure 4.5: Lower temperature weak field dielectric permittivity in a single domain $BaTiO_3$ crystal. Note that below 0°C the crystal breaks up into domains and below -90°C the domain structure imparts an anisotropy which should not occur in the single domain state.

In both $BaZrO_3$ and $BaSnO_3$ systems there is an interesting "pinch off" region in the phase diagram where for temperatures close to room temperature tetragonal, orthorhombic and rhombohedral states are becoming of similar energy i.e., it becomes easy to thread the polarization vector through a randomly axed ceramic.

For the dielectric response, two desirable effects are evident as for example in the $Ba(T_{1-x}Zr_x)O_3$ system. At low level additions the dielectric peak rises sharply (Figure 4.9) and with further addition broadens markedly. Broadening may be traced to macroscopic heterogeneity in the composition giving rise to a distribution of Curie temperatures and thus a broadened peak. This principle is widely used in commercial dielectrics, which often use several additives to trim the properties. Some commercial formulations taken from the book by Herbert (1985a) are shown in Table 4.1.

To provide capacitors with high K but greater temperature stability, two additional features are used to control and enhance permittivity in almost pure $BaTiO_3$ ceramics:

1 Control of the permittivity in fine grained $BaTiO_3$ ceramic.

2 Control of the grain boundary impedance to suppress the Curie peak at T_C.

Both effects are illustrated in Figure 4.10 which contrasts this behaviour vis-a-vie the Curie point adjusted compositions.

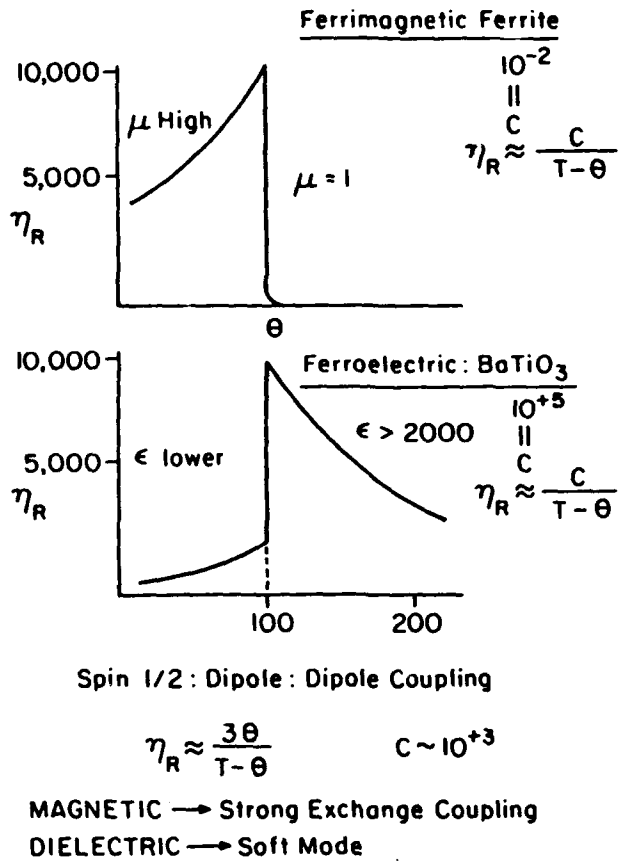

Figure 4.6: Contrast between the dielectric behaviour of a $BaTiO_3$ perovskite type ferroelectric and the magnetic behaviour of a normal soft ferrite ferrimagnet.

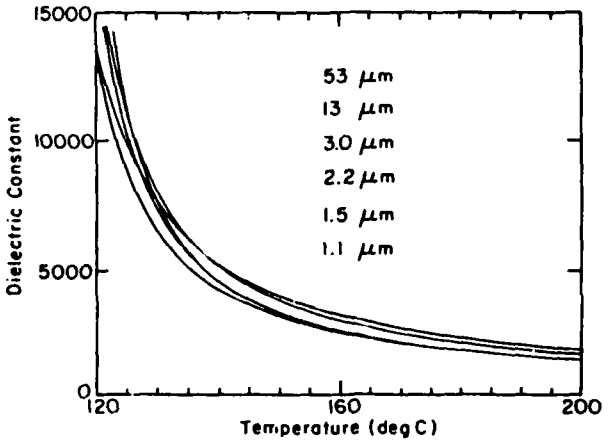

Figure 4.7: Dielectric permittivity above the Curie temperature in very carefully prepared $BaTiO_3$ ceramics as a function of grain size. Note there is no significant grain size dependence.

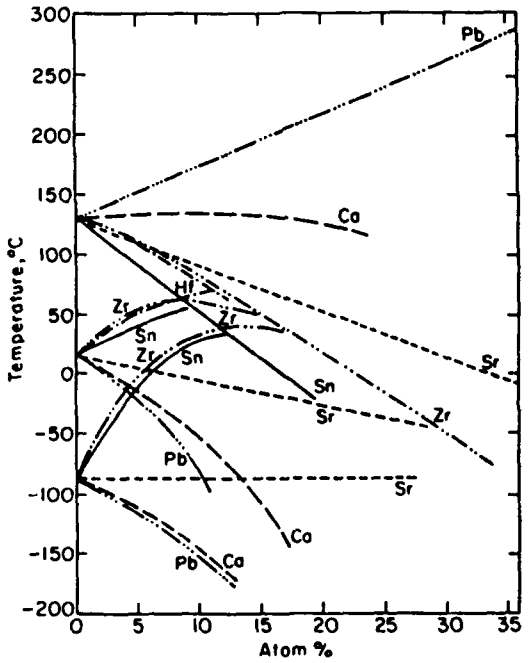

Figure 4.8: Behaviour of the phase transitions as a function of composition in a sequence of $BaTiO_3$:ABO_3 solids solutions.

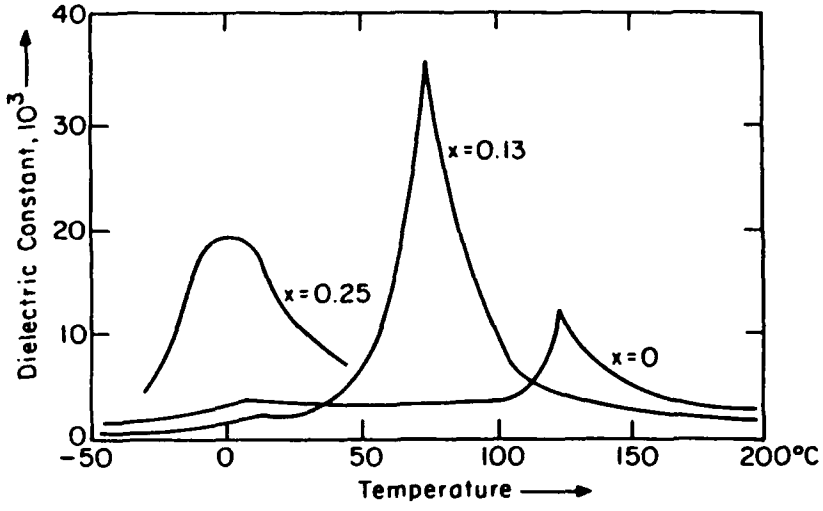

Figure 4.9: Permittivity temperature curves for solid solutions in the BaTiO3:BaZrO3 composition system.

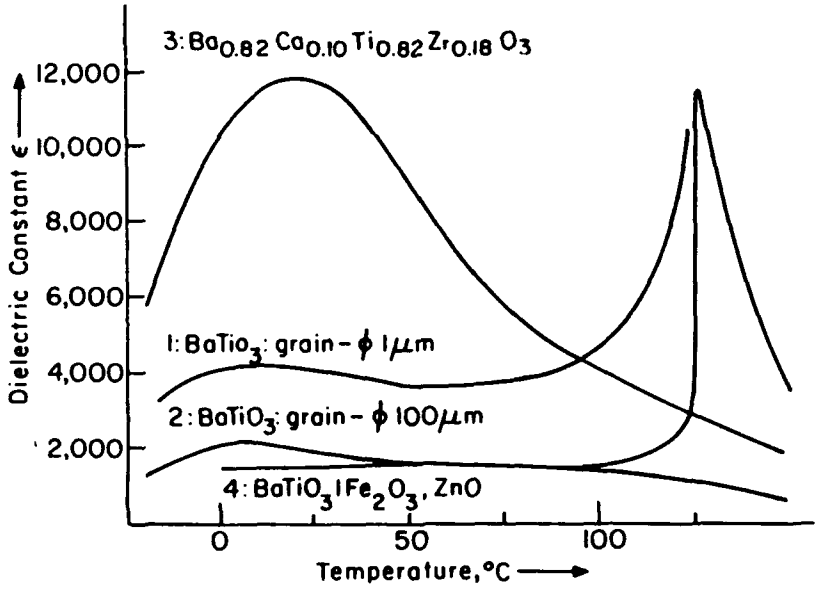

Figure 4.10: Comparison of Curie point shifted high-K dielectrics, with grain size and grain boundary controlled "pure" BaTiO3 compositions.

Table 4.1: Typical practical $BaTiO_3$ based dielectric formations taken from Herbert.

Item	K_{max}	Temp. range for K_{max} -20%	AO/BO_2	Ba	Sr	Ca	Mg	Ti	Zr	Sn
				Composition in cation%						
A	22500	-20 to +100	0.98	48.5	0.73	-	-	49.5	-	0.73
B	12600	0 to 120	1.03	45.1	-	4.8	1.08	44.0	4.8	-
C	3450	-10 to 72	1.01	44.2	-	5.7	0.75	42.9	6.4	-
D	5000	12 to 75	1.02	47.6	2.5	-	0.45	45.3	0.45	3.38
E	8200	42 to 70	1.005	35.5	12.5	1.8	0.8	46.9	2.6	-

4.1.1 Grain Size Effects in $BaTiO_3$ Ceramics

It was known from the early 1950s, that small additions of TiO_2 together with controlled firing could give rise to $BaTiO_3$ ceramic capacitors with permittivity close to 3,000 over a broad temperature range. Over time the beneficial effects were traced to a liquid phase densification which inhibited grain growth in the ceramic and left a residual boundary phase, which reduced the Curie peak permittivity. More recently these effects have been achieved by other means and both effects studied separately.

Probably the best measurements of the pure grain size effect are due to Kinoshita (1976) who used hot pressing of a weakly dysprosium doped $BaTiO_3$ to produce samples with controlled grain size from 1.1 μm to 53 μm which showed no suppression of the Curie peak. In his samples there is a continuous increase of weak field permittivity $\bar{\varepsilon}$ near room temperature with reduction in grain size to values above 5,000 at 1.1 μ meter (Figure 4.11).

Concomitant with the reduction in grain size, the group at NTT also observed a reduction in the frequency of occurrence of 90° domains with reducing grain size. Earlier, Buessem et al. (1966) had suggested that a reduction in the twin density would give rise to internal stress of the type depicted in Figure 4.12 which would strongly enhance the intrinsic permittivity, markedly raising $\bar{\varepsilon}$ and shifting the orthorhombic tetragonal transition to higher temperature (Figure 4.12). Some additional support for this model come on studies of the mechanical strength in hot pressed $BaTiO_3$ by Pohanka et al (1976) who measured the flexural strength above and below T_C and noted a reduction in strength in the ferroelectric phase which could be accounted for by the internal tensile stresses required in the Buessem model.

It must be noted however that an alternative model for the grain size effect has been proposed by Arlt and co workers (1985) which would require that the fine grain ceramic have a higher density of twins and some experimental evidence is advanced for this hypothesis. The advantage of the twin (domain) model is that is does account well for the higher $\tan\delta$ in the fine grain system, but it does not explain the phase transition shift. Clearly more work is needed to resolve this important question.

One possible avenue for study would be to suppress the 0°C transition as for example by calcium titanate doping. For the internal stress model, the grain size effect should diminish rapidly

as ε_a intrinsic is lowered. For the domain wall model, the proximity of the tetragonal:orthorhombic transition is not necessary provided the lattice strain and wall energy are not too strongly effected.

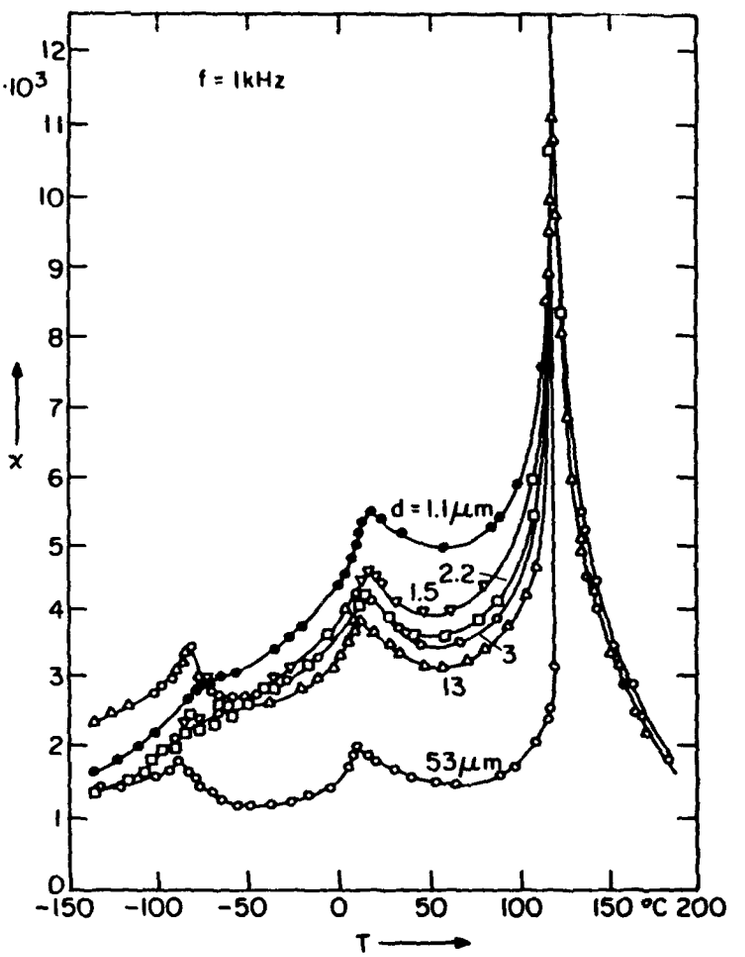

Figure 4.11: Dielectric permittivity of $BaTiO_3$ as a function of grain size.

4.2 Manipulation of Grain Boundary Impedance

In $BaTiO_3$ ceramics, it is remarkably easy to produce "dirty" grain boundaries, and most ceramics like the Seimens C40 material show Curie maximum suppression to greater or lesser degree, and it is often advantageous for practical application. To demonstrate the phenomenon quantitatively, and in the process to produce a useful high voltage dielectric, Payne and Cross (1973, 1984)

explored fast fired $BaTiO_3$:$NaNbO_3$ composites. Using the fact that there is a pseudo eutectic in the solid solution system, it is possible to generate a rapid liquid phase densification which leaves a thin $NaNbO_3$ coating over the $BaTiO_3$ grains whose thickness can be controlled by the volume of $NaNbO_3$ used. Since $NaNbO_3$ has a flat permittivity:temperature behaviour, it is possible to use Curie Weiss analysis to derive the impedance of the boundary phase directly and to verify the predictions of the simple "brick wall" model for the ceramic. The argument is presented pictorially in figures 4.13, 4.14, 4.15, 4.16, 4.17, 4.18. A comparison of the characteristics of a 5% $NaNbO_3$:$BaTiO_3$ versus a pure $BaTiO_3$ capacitor is given in Table 4.2.

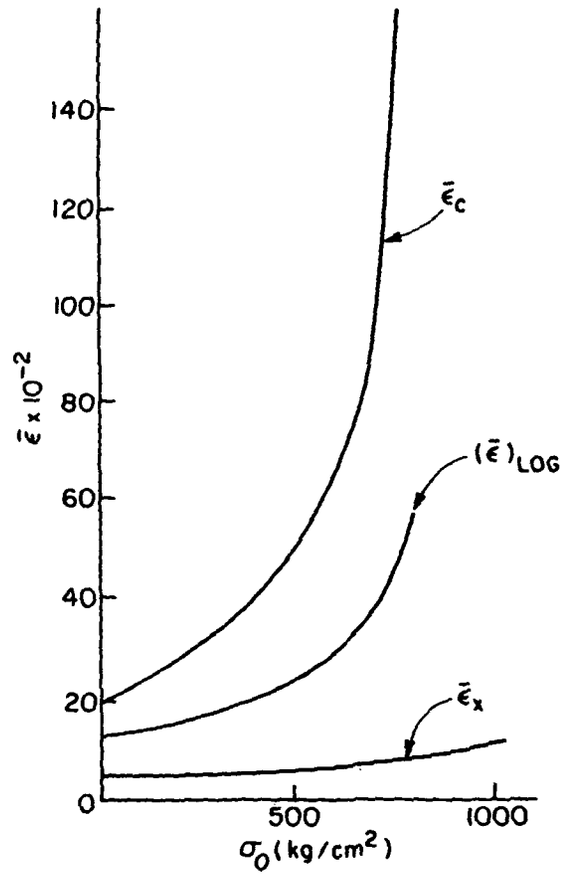

Figure 4.12: Calculated mean permittivity as a function of combined uniaxial compressive and orthogonal two dimensional tensile stress: the self generated stress system expected in untwinned fine grain $BaTiO_3$.

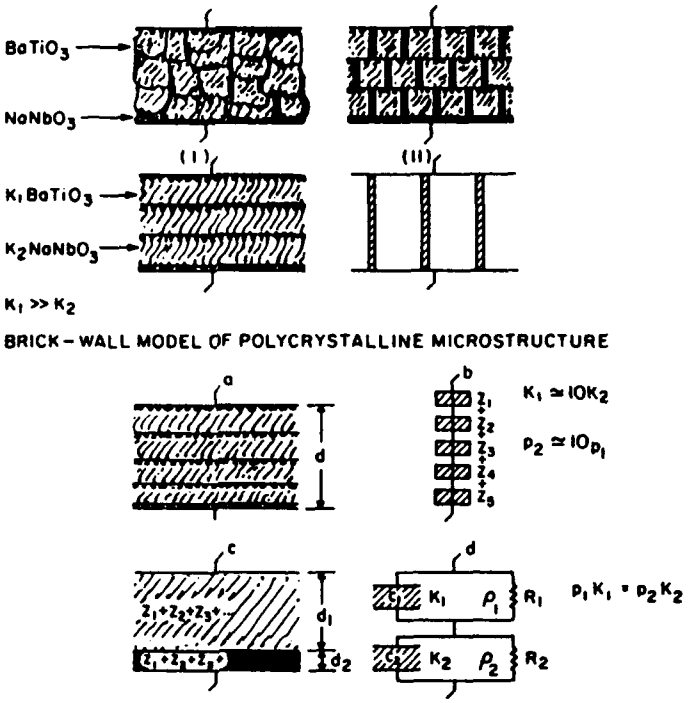

Figure 4.13: Derivation of the simple brick wall model for a diphasic ceramic and the reduction to a simple RC parallel circuit combination.

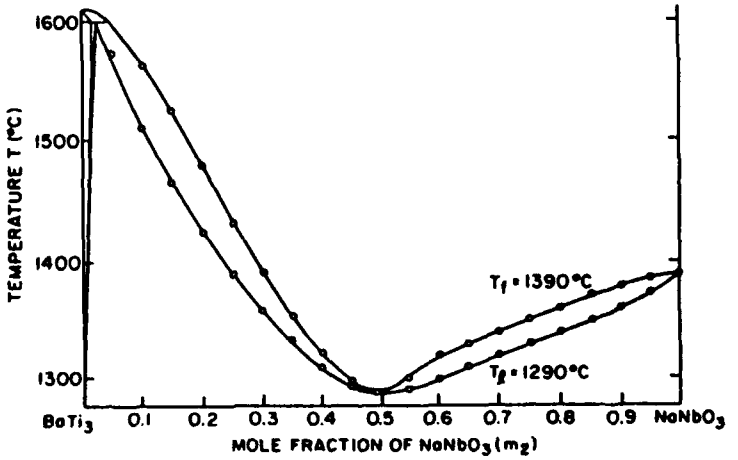

Figure 4.14: Pseudo eutectic in the phase diagram of BaTiO3:NaNbO3 solid solutions.

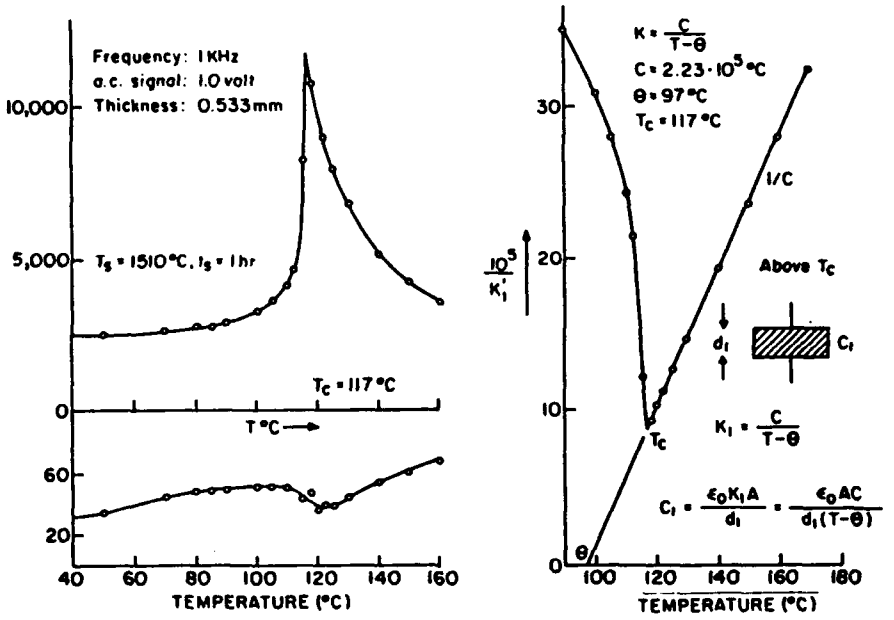

Figure 4.15: Weak field dielectric permittivity of $BaTiO_3$ as function of temperature.

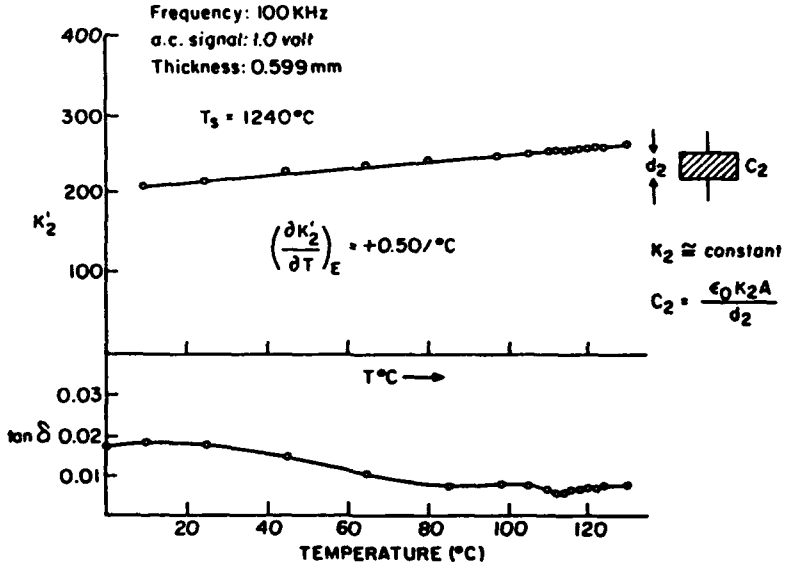

Figure 4.16: Weak field permittivity of $NaNbO_3$ as function of temperature showing near constant behaviour.

Table 4.2: Practical advantage of a $BaTiO_3$:$NaNbO_3$ composite dielectric for a high voltage capacitor.

Dielectric	Permittivity K at O Volts	Permittivity K at 60 KV/cm	Aging %/Decade	Breakdown Strength
$BaTiO_3$	2,100	400	2.8	100 Kv/cm
$BaTiO_3$ 5% $NaNbO_3$	2,100	750	1.25	200 Kv/cm

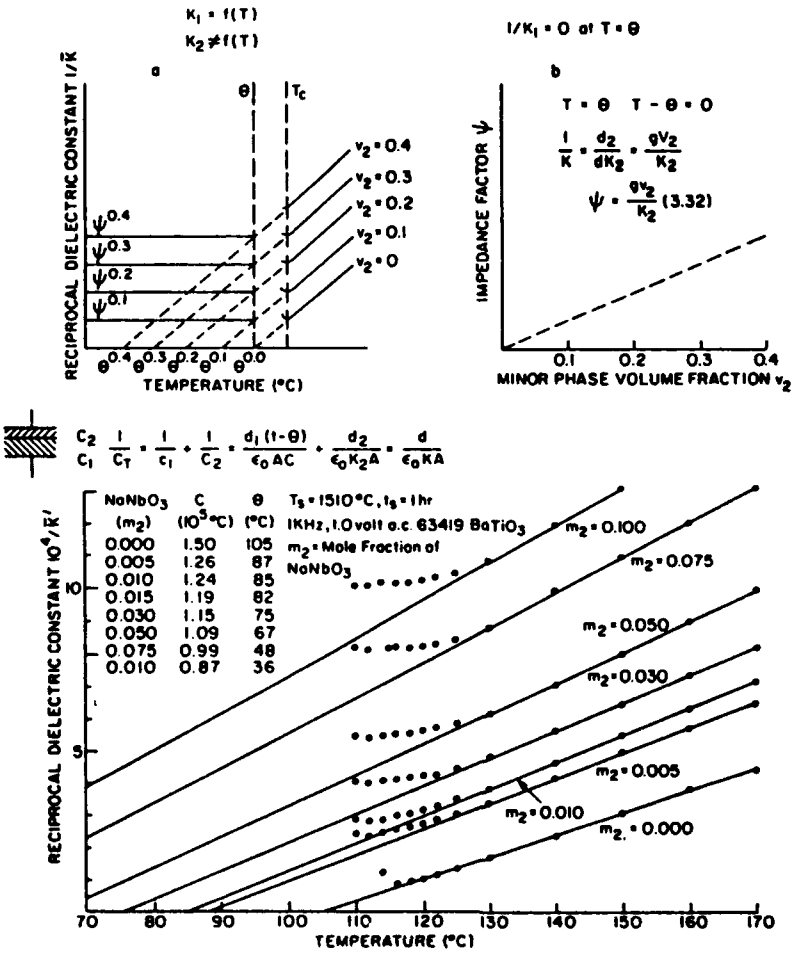

Figure 4.17: Expectation for Curie Weiss behaviour in a diphasic $BaTiO_3$ ceramic, and confirmation of the behaviour in fast fired ceramics.

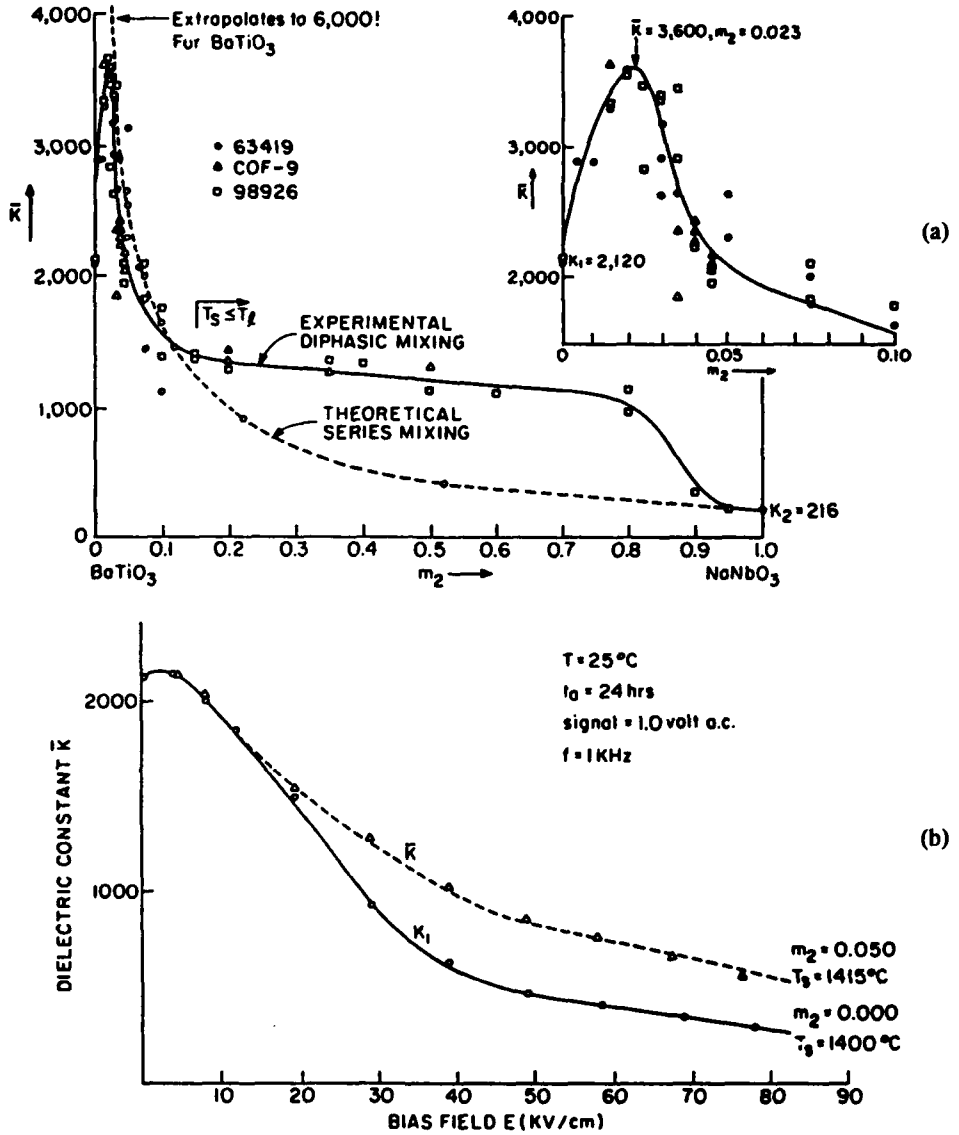

Figure 4.18: (a) Permittivity levels as a function of $NaNbO_3$ mole fraction in the diphasic system. (b) Improvement in the high field performance due to field splitting by the diphasic system.

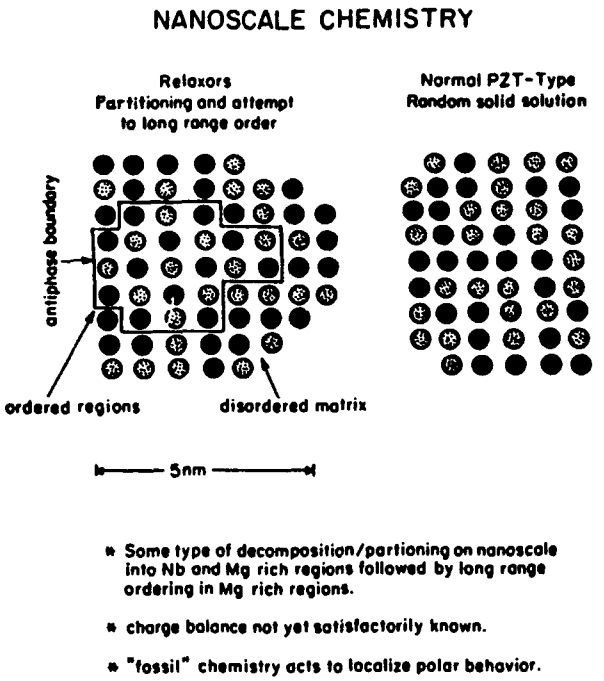

Figure 4.19: Nanoscale ordering in Lead Magnesium niobate compared to a disordered PZT solid solution.

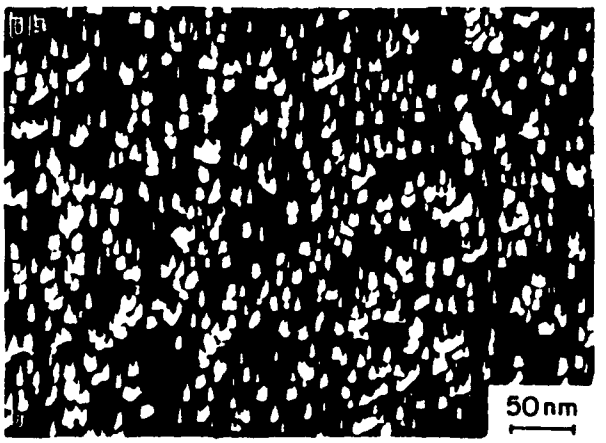

Figure 4.20: Dark field image of the chemically ordered domains in Lead Magnesium Niobate.

4.3 Scale Effects in Heterogeneous Ferroelectric Dielectrics

It was shown earlier in this section 4 that a measure of compositional heterogeneity is essential in very high K dielectrics so that the dielectric extrema at the Curie temperature is spread over a practically useful range. For most widely used $BaTiO_3$ based formula, this heterogeneity is on a scale comparable to the grain structure and is often induced by processing to a non equilibrium phase distribution.

As the dielectric thickness gets smaller, particularly in ultra high capacitance density multilayer capacitors, it becomes difficult to control macroscopic heterogeneity because of short diffusion distances, and a finer scale composite would be desirable.

In the $Pb(B_1B_2)O_3$ perovskites for which $PbMg_{1/3}Nb_{2/3}O_3$ (PMN) is a useful prototype, it has become clear that there is a new mechanism which establishes a truly nanometer scale heterogeneity in the composition in such materials. Extensive studies by transmission electron microscopy have revealed that ordering takes place between Mg:Nb cations but not as might be expected in a 2:1 ordered sheet structure as occurs in $BaMg_{1/3}Ta_{2/3}O_3$, but on a local 1:1 ordering in an NaCl type lattice (Harmer et al., 1984; Randall, 1987).

A crude two dimensional picture is given in Figure 4.19 which compares the atomic arrangement in PMN with that in a conventional PZT ceramic. A feature which is immediately evident in the PMN is that the 1:1 ordering is non stoichiometric and must give rise to massive short range chemical heterogeneity. The ordered regions are highly Mg rich and must give rise to a local charge imbalance which presumably stops the ordering process at this ~5nm scale.

The ordering which is within a coherent crystal lattice occurs in both single crystal and ceramic samples and can be imaged using TEM (Figure 4.20) (Chen, 1991). This fossil chemistry which is formed at very high temperature leads to a nanoscale chemical heterogeneity which influences the manner in which these materials exhibit ferroelectricity. This family of lead based complex perovskites has been called relaxor ferroelectrics. The outstanding features of the dielectric and ferroelectric response are summarized in Figure 4.21 and the most salient features tabulated in Table 4.3. Earlier studies (Cross, 1987) based on the very small scale of the polar regions in PMN had suggested a super paraelectric model for the high temperature behaviour and measurements on the SBN bronze had been adduced to demonstrate the mobility of the polar phase (Asadipour, 1986). A recent natural extension has been to explore a spin glass model for the behaviour (Viehland, 1991a).

Viehland (1991b) has authenticated a Vogel-Fulcher model for the dielectric relaxation (Figure 4.22) which postulates local cooperation between polar micro regions leading to a freezing temperature T_f. It was noted also, that for the field forced low temperature ferroelectric phase, the collapse of remanent polarization leads to a thawing temperature in close agreement with T_f. By looking at the manner in which different levels of DC electric field force a spin-glass to

ferroelectric phase change Viehland (1991c) (Figure 4.23) was able to use the De Almedia-Thouless relation (1978) to deduce a size for the uncoupled polar entities in close agreement with the scale of the heterogeneity observed by transmission microscopy (Figure 4.24).

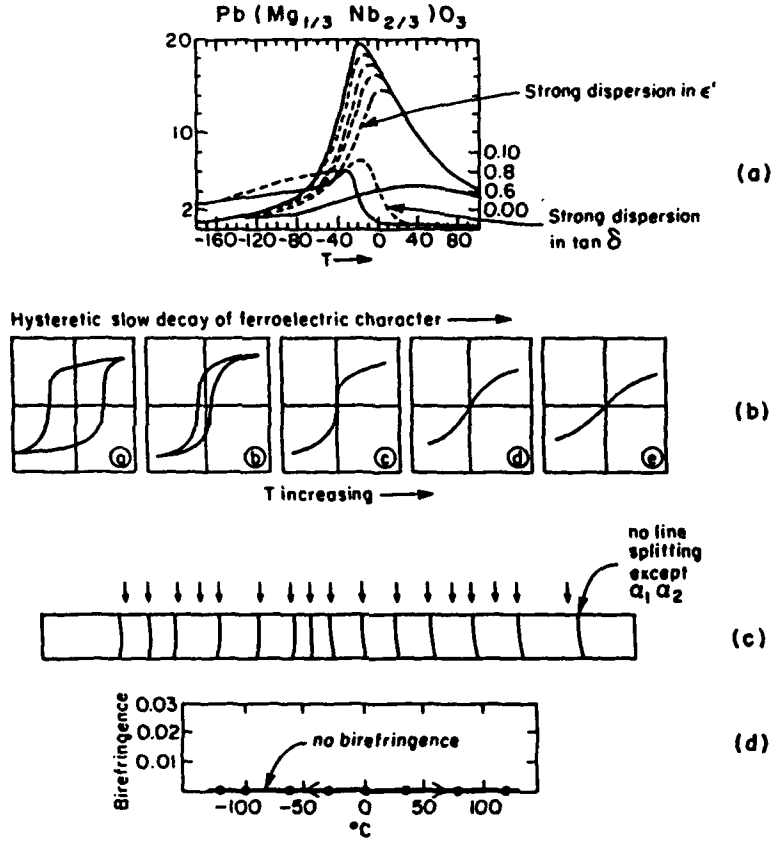

Figure 4.21: Special properties of the relaxor type perovskite dielectrics.

(a) Weak field dielectric permittivity vs. T.

(b) High field hysteritic behaviour vs. T.

(c) Low temperature X-ray spectrum showing no departure from cubic structure.

(d) Optical anisotropy in a zero field cooled single crystal of PMN.

In a number of ways, the dielectric spin glass is more complex than the magnetic because of the strong electrostriction which couples nano scale polarization to nano scale distortion of the lattice. Many of the expected consequences have now been explored (Figures 4.25 to 4.30). It must be stated however that the current work has not yet proven spin glass behaviour in PMN, however the list of confirmed glass like features is indeed impressive as tabulated in Table 4.4.

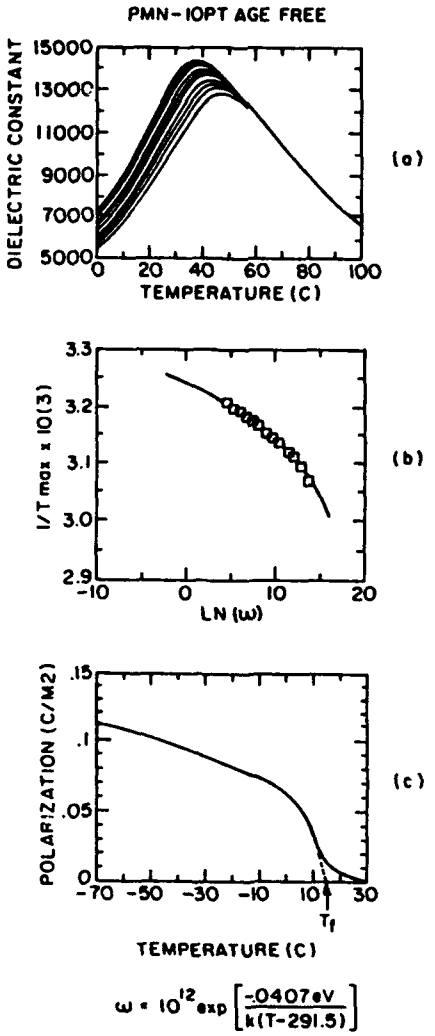

Figure 4.22: Vogel:Fulcher type freezing of the dielectric response in PMN:10%PT.

(a) Dielectric response as a function of frequency and temperature.

(b) Plot of 1/Tmax the temperature of maximum response vs. frequency. Square dots are experimental points, line is a fit to the equation yielding pre-exponential $vo = 10^{12}$ Hz.

(c) Release of polarization on heating for a field cooled (poled) sample: the thawing temperature $Tf = 291$ °K.

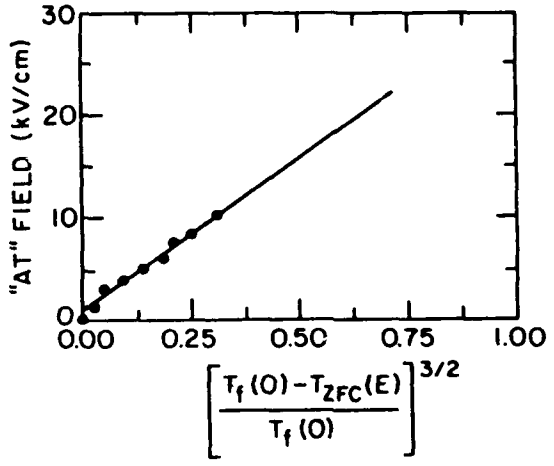

$$E = A\left[\frac{T_f(0)-T_{zfc}(E)}{T_f(0)}\right]^{\frac{3}{2}}$$

Figure 4.23: Plot of the applied bias ("AT" field) as a function of the temperature of maximum charging current, where Tf(0) is the freezing temperature of the ZFC state and the solid line is the curve fitting to the deAlmedia Thouless relationship.

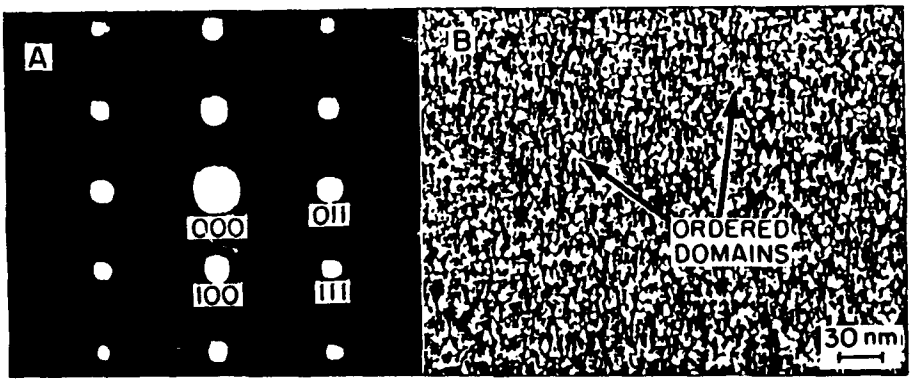

Figure 4.24: (a) Diffraction pattern of PMN showing superlattice reflections [011] zone.(b) CDF image of ordered microdomains (3-5 n meter) in PMN using $(\frac{111}{222})$ *reflection.*

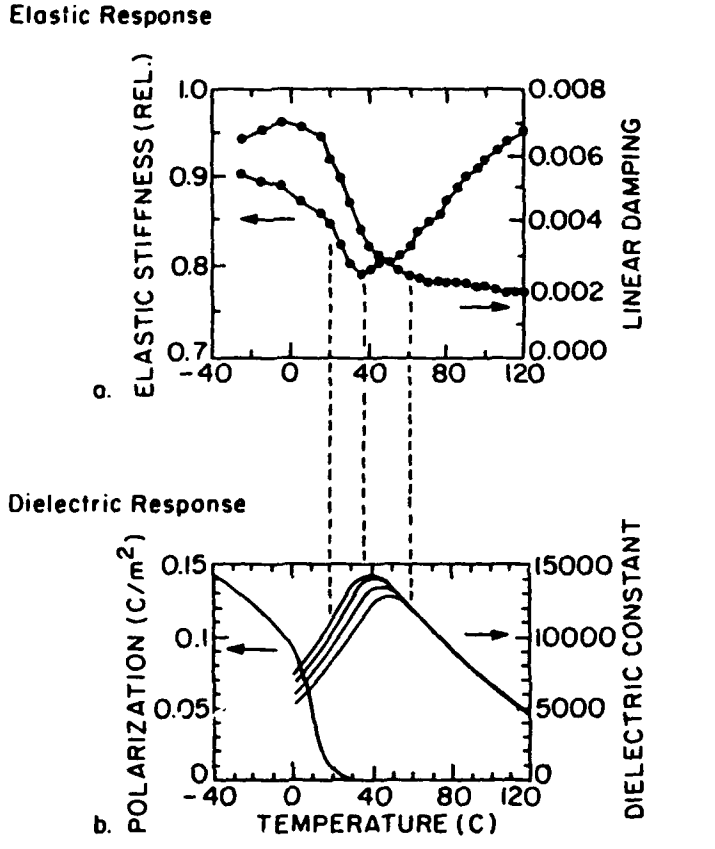

Figure 4.25: Comparison of dielectric and elastic response in PMN. Maximum softening for both responses occurs at the same temperature - suggesting a common origin, reflecting the kinetics of polarization fluctuations coupled to the lattice via electrostriction.

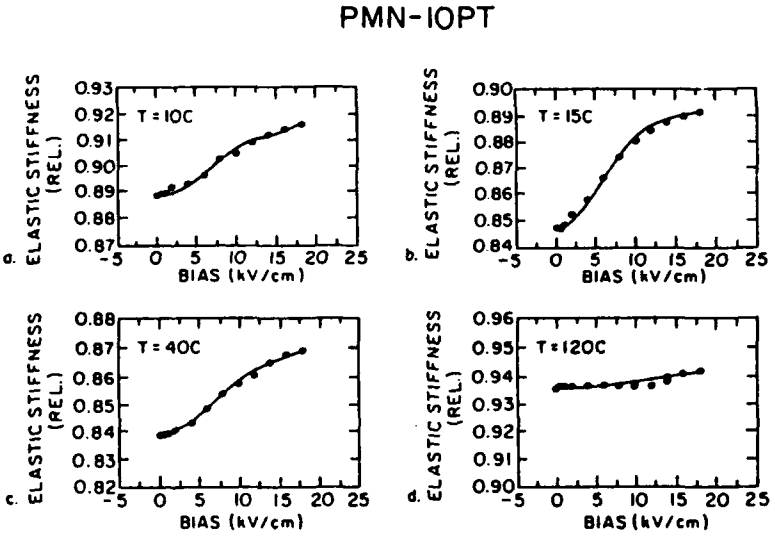

Figure 4.26: Elastic stiffness as a function of applied electric field at various temperatures.

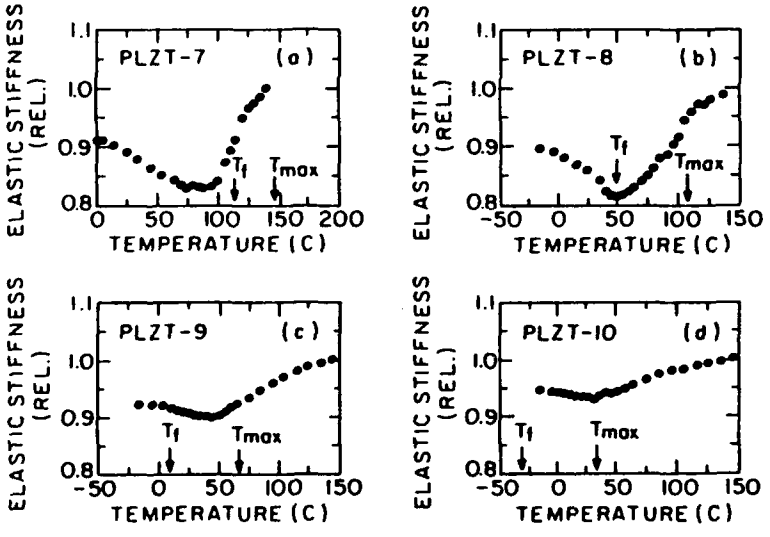

Figure 4.27: The 100 Hz elastic stiffness as a function of temperature for various compositions of PLZT; where Tf is the freezing temperature, and Tmax the temperature of the 100 Hz permittivity maximum. (a) PLZT-7, (b) PLZT-8, (c) PLZT-9, and (d) PLZT-10.

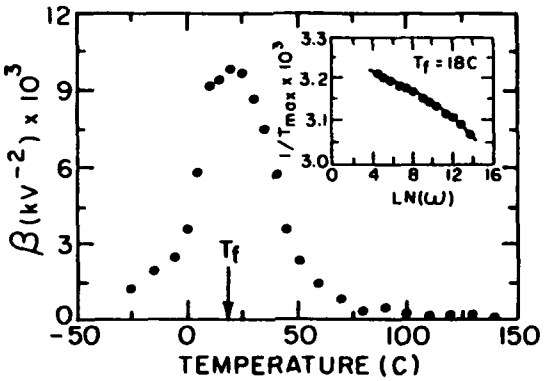

Figure 4.28: For the elastic constant vs. electric field $C(E) = c(o) + \beta E^2 + \eta E^4$. Plot shows β as a function of temperature. Note that maximum β occurs near the freezing temperature Tf of the polarization fluctuations.

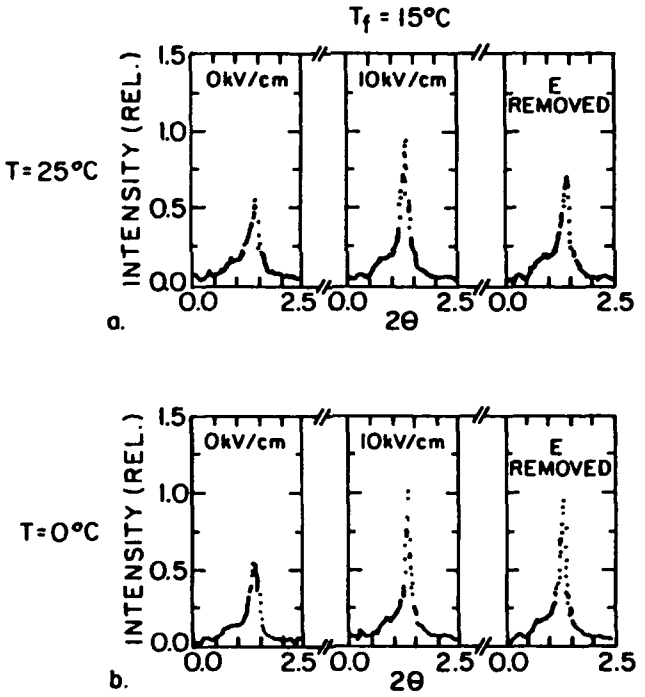

Figure 4.29: X-ray line broadening as a function of applied electric field in PMN at a temperature above (25°C) and below (0°) the freezing temperature. Note that the narrowing and peak shift is transient after field application above Tf, but persists after field application below Tf.

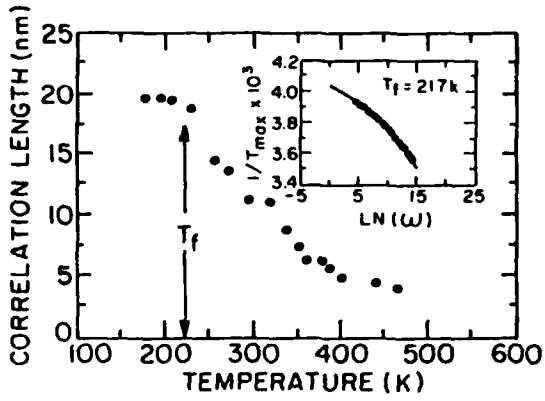

Figure 4.30: Correlation length in single crystal PMN as a function of temperature, as deduced from neutron scattering. Correlation length saturates near T_f at 200Å. At T_{Burns} the length ~30-40Å close to the uncoupled cluster size.

Table 4.3: Common features in the behaviour of relaxor ferroelectric crystals and ceramics.

COMMON FEATURES

- **Compositions: Structures.**
  Common in lead containing perovskite structures of complex composition: Prototype lead magnesium niobate $Pb(Mg_{1/3}Nb_{2/3})O_3$.
  Occurs in many tungsten bronze compositions: Prototype strontium barium niobate $Sr_{0.75}Ba_{0.25}Nb_2O_6$.

- **Dielectric Response.**
  High dispersive peak permittivity ε_R ~ 30,000.
  Ferroelectric response under high fields at low temperatures.

- **Compositional Heterogeneity.**
  Nano-scale heterogeneity on a coherent crystal lattice.

- **Polarization Fluctuations.**
  Large values of RMS polarization at temperatures well above that of the dielectric maximum.
  Evidence that the fluctuations are dynamical.

- **Evidence from TEM.**
  Local compositional (chemical) ordering.
  Local polar regions at low temperature nano to macro domain transitions.

Table 4.4: Summary table of similarities between the relaxor ferroelectric PMN and the Magnetic spin glass (Y in the table indicates [yes] that the phenomenon has been confirmed.)

PROPERTY	RELAXOR	SPIN GLASS
Dispersion of Susceptibility	Y	Y
Dispersion of Tmax	Y	Y
Freezing Temperature (Tf)	Y	Y
Imaginary Component Frequency Independent below Tf	Y	Y
Strong Nonlinear Response	Y	Y
Maximum Nonlinearities near Tf	Y	Y
Frustration	Y	Y
Susceptibility "Diffuse"	Y	Y
Deviations from Curie-Weiss Behavior	Y	Y
Analysis of Deviation for Local Order Parameter	Y	Y
Broadening of Relaxation Time Distribution on Cooling	Y	Y
Hysteresis, Irreversibility, and Remance below Tf	Y	Y
Local polarization or magnetization	Y	Y
Local correlations between moments	Y	Y
Long range ordering in the Field Cooled State	Y	Y
Lack of anisotropy in the Zero Field Cooled State	Y	Y
De-Almedia Thouless Analysis	Y	Y
Polarization or Magnetization Viscosity	Y	Y
Chemical or Structural Inhomogeneity	Y	Y

5 Multilayer Ceramic Capacitors

The major sector of the high K ceramic capacitor market addresses ultra compact high capacitance miniature units which are required for power line stabilization in the packaging of silicon semiconductor integrated circuits. These units are fabricated using a co-firing technology which integrates the electrode into a monolithic multilayer ceramic. The normal construction is shown in schematic form in Figure 5.1. The alternating electrode layers which are fired into the ceramic are picked up on a modified silver termination which is added in a post firing operation.

For the early $BaTiO_3$ formulations, the necessary high firing temperatures forced the use of platinum or gold-platinum alloy electrodes which become the major cost in the unit. Over time an essential component of the evolution has been the development of lead and bismuth oxide based fluxes which permit co-firing at temperatures down to 1150°C and thus the use of less expensive palladium-silver alloy electrodes (Hagemann et al., 1983). Basic principles of the design of the dielectrics are essentially unchanged from before, and the effort has been to find fugitive fluxes or fluxes which incorporate into the dielectric with minimum damage to the permittivity properties.

Alternative to the $BaTiO_3$ based compositions, the lead based relaxor (spin glass) compositions appear to be attracting increasing attention from the major MLC producers. A recent survey of the patent literature, Table 5.1, highlights some of the activity. It would be nice to report that it is the intrinsically superior dielectric properties (Figure 5.2) which are the major drawing force, however what must be also factored in is the important fact that the lead based formulation can be designed to fire at temperatures below 900°C so that with them there is the possibility of using high 70:30 silver palladium alloy electrodes, in some cases pure silver (Table 5.2) and with appropriate doping, base metal copper electrodes (Kato et al., 1987).

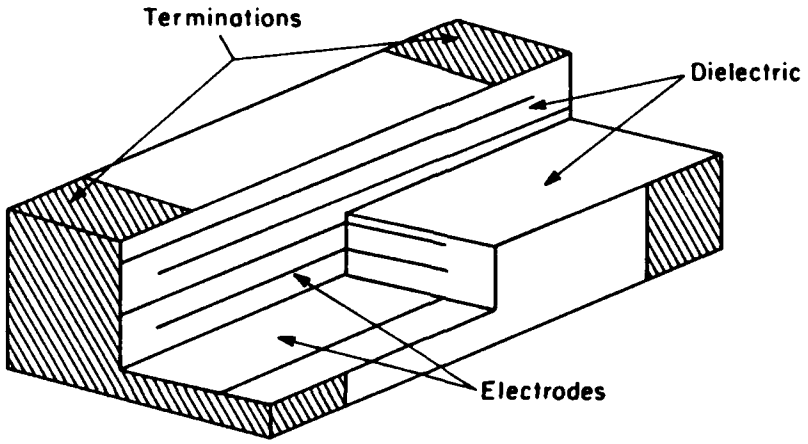

Figure 5.1: Construction of a typical ceramic MLC.

Table 5.1: Compositions being explored and recent patent filings for relaxor based dielectric formulations.

Complex Perovskites	$^{+}T_c$ (°C)	$^{++}$ Behavior	Simple Perovskites	T_c (°C)	Behavior
[PMN]	-10	Relaxor-FE	$PbTiO_3$	490	FE
[PZN]	140	Relaxor-FE	$PbZrO_3$	230	AF
[PNN]	-120	Relaxor-FE	$BaTiO_3$	130	FE
[PFN]	110	Normal-FE	$SrTiO_3$		Para
[PFW]	-95	Relaxor-FE			
[PMW]	38	AF			
[PNW]	17	AF			

$^{+}$ Transition temperatures for relaxors are averages or at 1 kHz.

$^{++}$ FE - Ferroelectric, AF - Antiferroelectric, Para - Paraelectric.

[PMN]: $Pb(Mg_{1/3}Nb_{2/3})O_3$ [PFW]: $Pb(Fe_{2/3}W_{1/3})O_3$

[PZN]: $Pb(Zn_{1/3}Nb_{2/3})O_3$ [PMW]: $Pb(Mg_{1/2}W_{1/2})O_3$

[PNN]: $Pb(Ni_{1/3}Nb_{2/3})O_3$ [PNW]: $Pb(Ni_{1/2}W_{1/2})O_3$

[PFN]: $Pb(Fe_{1/2}Nb_{1/2})O_3$

Compositional Families for Relaxor-Based MLCs

Composition	EIA Temp Specification	Manufacturer (Assignee)	Patents and Refs.
PLZT-Ag	X7R	Sprague	U.S. Pat. 4,027,209 (1973) Ref. 9
PMW-PT-ST	X7R	DuPont	U.S. Pat. 4,048,546 (1973)
PFN-PFW	Y5V	NEC	U.S. Pat. 4,078,938 (1978)
PFN-PFW-PZN	Y5V	NEC	U.S. Pat. 4,236,928 (1980)
PFN-PMT		TDK	U.S. Pat. 4,216,103 (1980)
PMN-PT	Y5V	TDK	U.S. Pat. 4,265,668 (1981)
PMN-PFN	Y5V	TDK	U.S. Pat. 4,216,102 (1980)
PMN-PFN-PMW	Y5V	TDK	U.S. Pat. 4,287,075 (1981)
PFW-PZ	Z5U	TDK	U.S. Pat. 4,235,635 (1980)
PFW-PT-MN	Z5U	Hitachi	U.S. Pat. 4,308,571 (1981)
PMN-PZN-PT	Z5U	Murata	U.S. Pat. 4,339,544 (1982)
PFN-PFW-PbGe (MSC)	X7R		Ref. 10
PFN-PFM-PNN	Z5U, Y5V	Ferro	U.S. Pat. 4,379,319 (1983)
PMW-PT-PNN	Z5U	NEC	U.S. Pat. 4,450,240 (1984) Ref. 11
PFN-BaCa(CuW)-PFW	Y5V	Toshiba	U.S. Pat. 4,544,644 (1985) Ref. 12
PMN-PZN	Z5U	STL	U.K. Pat. 2,127,187A (1984)
PMN-PFN-PT	Z5U	STL	U.K. Pat. 2,126,575 (1984)
PMN-PZN-PFN	Z5U	Matsushita	Japan Pat. 59-107959 (1984)
PMN-PFW-PT		Matsushita	Japan Pat. 59-203759 (1984)
PNN-PFN-PFW	Y5V	Matsushita	Japan Pat. 59-111201 (1984)
PZN-PT-ST		Toshiba	Ref. 13
PMN-PFN-PbGe	Z5U	Union Carbide	U.S. Pat. 4,550,088 (1985)
PFN-PNN	Y5V		Ref. 14
PFW-PFN (MSC)		NIT	Refs. 15-17
PMN-PT-PNW	Z5U	Matsushita	Ref. 18
PMW-PT-PZ	X7R	NEC	Ref. 19
PZN-PMN-PT-BT-ST	Z5U	Toshiba	Japan Pat. 61-155245 (1986)
PZN-PT-BT-ST	X7R	Toshiba	Japan Pat. 61-250904 (1986)
PZN-PMN-BT	Y5U, Y5S	Toshiba	Ref. 20
PMN-PLZT	Z5U	MMC	U.S. Pat. 4,716,134 (1987)
PMN-CT, ST, BT	Z5U	Matsushita	Japan Pat. 62-115817 (1986)
PFW-PFN-PT	Y5V		Ref. 21
BT-PMN-PZN (MSC)	X7R, X7S	Toshiba	U.S. Pat. 4,767,732 (1988)
PMN-PS-PNW-Ca (Base Metal)	Z5U	Matsushita	Refs. 22-23

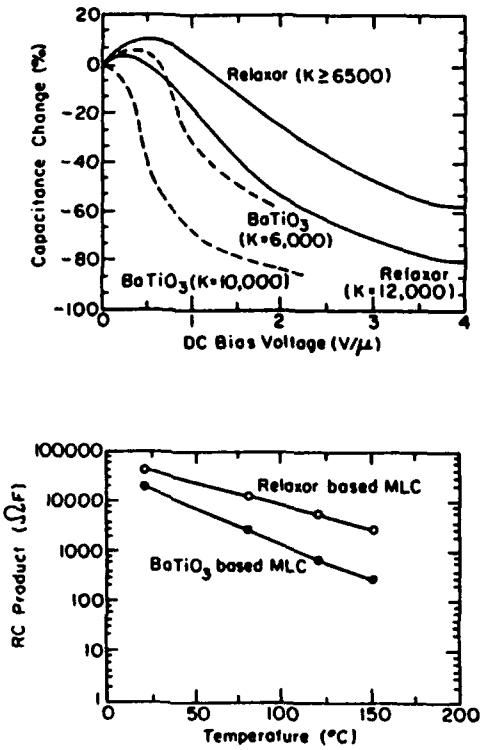

Figure 5.2: Comparison of dielectric saturation and RC time constant behaviour between relaxor based and $BaTiO_3$ based MLC dielectrics.

Table 5.2: Firing conditions for and appropriate electrodes to use with $BaTiO_3$ and relaxor based formulations.

Dielectric	Firing Condition		Electrode	
HF-BT	>1250 °C	(air) (reducing)	Pb Ni*	(100%)
MF-BT	1100-1250 °C	(air) (reducing)	Ag:Pd Cu, Ni	(70/30 to 30/70)
LF-BT (R&D only)	<1100 °C	(air)	Ag:Pd	(70/30)
HF-Relaxor	>1000 °C	(air) (reducing)	Ag:Pd Cu	(70/30)
LF-Relaxor	<1000 °C	(air) (reducing)	Ag:Pd (85/15), Ag (100%) Cu	

*The partial pressure pO_2 at which $Ni \rightarrow NiO$ occurs is such that $PbO \rightarrow Pb_{metal}$ results, hence Ni-based electrodes are thermodynamically not feasible for relaxors

6 Ferroelectric Thin Films

6.1 Introduction

Over the last four years (1987 to 1991) there has been a rapid increase in interest in ferroelectric thin films deposited onto semiconductor substrates for uses in nonvolatile radiation hard random access memory. The effort which has been driven in the USA primarily by major funding from the department of defense has lead to a strong revival of interest in ferroelectric switching behaviour and the evolution of a very broad range of deposition methods for a large variety of ferroelectric compositions. Since the summer school will have talks which focus upon the preparation methods for films and the switching behaviour, these will only be briefly mentioned and the primary focus will be upon those properties which are likely to make the films important for more conventional capacitors and for piezoelectric transducer and sensor applications.

6.2 Material Systems of Interest

The majority of studies are being carried forward upon randomly axed polycrystalline films so that it is not surprising to find major interest in the perovskite structure composition. Considerable early work on $BaTiO_3$ films (Schwarz and Tourtellotte, 1969; Dudkevich et al., 1981) never showed convincing evidence that strong ferroelectricity could be retained in sub micron thick films, and this is perhaps not surprising in the light of the very slim loops observed even in bulk $BaTiO_3$ when the grain size approaches sub micron levels.

Most important steps in forward progress were the demonstrations of convincing dielectric hysteresis by Sayer (1983) in sputter deposited PZT films and the confirmation of excellent hysteretic behaviour in sol-gel deposited PZT films by Dey, Payne and Budd (1988).

More recently the list of compositions for which useful ferroelectric behaviour has been convincingly demonstrated in thin films has increased markedly. A recent survey is given in Tab. 6.1.

6.3 Preparation Techniques

The very broad range of techniques which have already been applied to the fabrication of ferroelectric thin films are summarized in Table 6.2. The majority are vapour phase methods but sol-gel and metal organic deposition are widely used. Attempts are also being made to use true metal organic chemical vapour deposition, but this approach is strongly handicapped by the low volatility and the hazardous nature of the suitable organic vehicles for the required chemical constituents.

Table 6.1: Compositions which are under study as thin films.

CHOICE OF MATERIAL SYSTEMS

Non Volatile Memory

Multiaxial Ferroelectrics for Randomly Axed Films

Lead Zirconate Titanate	PZT
Lead Lanthanum Zirconate Titanate	PLZT
Lead Titanate	PT
Lead Lanthanum Titanate	PLT
Lead Bismuth Titanate	PBiT
Lead Barium Niobate	PBN

Uniaxial Ferroelectrics for Grain Orientated/ Epitaxial Films

Potassium Lithium Niobate	KLN
Strontium Barium Niobate	SBN
Lead Germanate	PG
Potassium Magnesium Fluoride	KMgF

All methods currently have the common feature that they deposit an amorphous or micro crystalline ensemble of the required chemical constituents which must be architected into the required perovskite structure form by a subsequent heat treatment. These post deposition annealing treatments have received a lot of attention and it is clear that they can radically change the character of the resultant film. There appears to be a strong movement towards rapid thermal annealing methods, but again much care is needed to optimize the conditions.

In vapour phase methods substrate heating and low energy add atom assist are being used to improve quality, but the need for a sub film electrode metal precludes the possibility of precise epitaxy for perovskite type films, though topotactic grain orientation is frequently observed.

Table 6.2: Growth techniques for ferroelectric thin films.

* Magnetron Sputtering from Oxide Targets.
* Mult-magnetron Sputtering (MMS).
* Multi-ion Beam Reactive Sputtering.
* Electron-Cyclotron Resonant (ECR) Plasma Assisted Growth.
* Chemical Vapor Deposition (Photo-Assist).
* Excimer Laser Ablation.
* Sol-Gel Methods.
* MOD Techniques.

Substrate Heating.
Post Deposition Annealing.
Rapid Thermal Annealing (RTA).
Low Energy Ad Atom Assist.

There are numerous reports that the phase makeup of $PbZrO_3$:$PbTiO_3$ thin films differs markedly from bulk values, however, data from S. Dey (1991a) on carefully annealed films (Figure 6.1) suggests that the morphotropic phase boundary separating tetragonal and rhombohedral phases is close to that observed in the bulk composition.

6.4 Important Properties of High K Films

In PZT films at the 52/48 Zr/Ti composition weak field dielectric permittivity ε_w at room temperature as measured by many investigator on films made by different techniques is of order 1,200 and independent of thickness down to 3,500Å. Typical data from Dey (1991b) (Figure 6.2) indicates the films are dispersion free to over 10^7 Hz. Improper thermal annealing either at too elevated a temperature or for too long a time (Figure 6.3) indicates that massive dispersion can be induced at frequencies as low as 10^4 Hz. Under cyclic DC bias again films behave exactly as would be expected for proper ferroelectrics (Figure 6.4).

That the 52/48 composition is properly ferroelectric is evident from the 60 Hz hysteresis curve in Figure 6.5 with $P_r = 30\ \mu c/cm^2$ and $E_c \simeq 31$ KV/cm. That the ferroelectric polarization can be switched fast enough to be of interest in memory application is evident from the data taken by Dey (Figure 6.6) which shows switching times of ~ nano seconds in a 30 μ x 30 μ square capacitor.

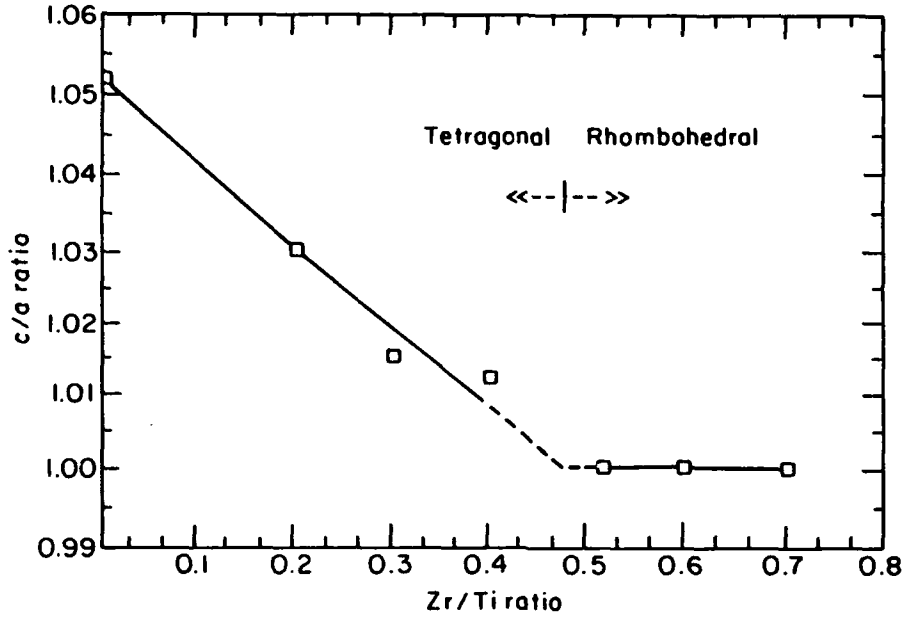

Figure 6.1: Structure vs. composition in well annealed PZT thin films (after Dey).

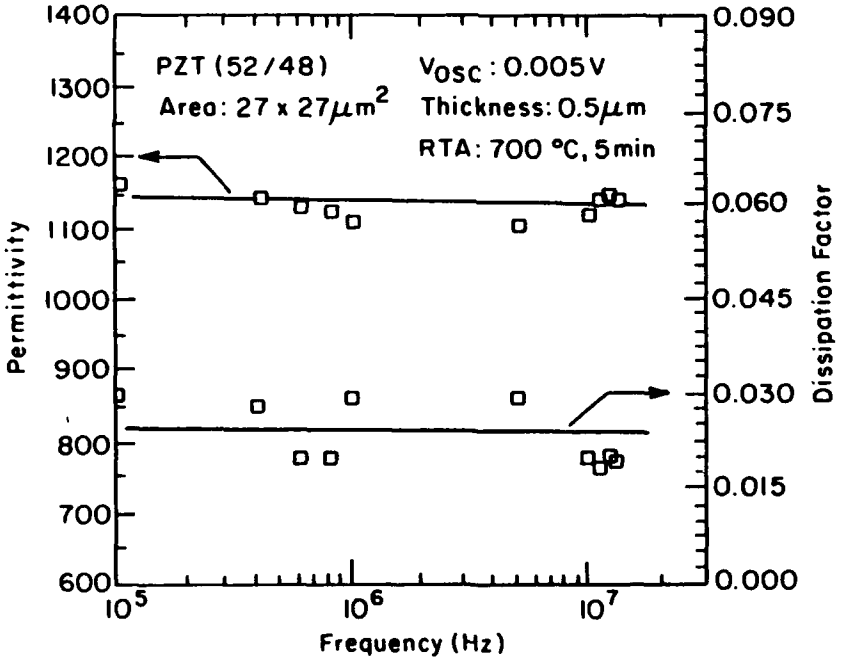

Figure 6.2: Weak field dielectric permittivity vs. frequency typical for PZT 52:48 compositions (after Dey).

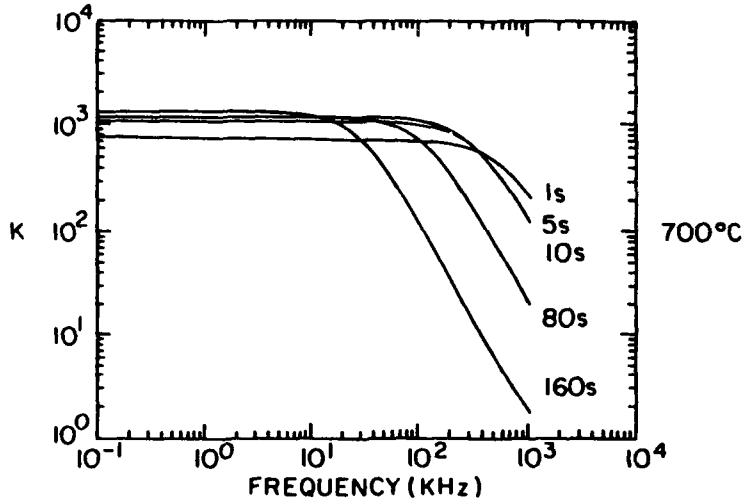

Figure 6.3: Dielectric response vs. frequency for PZT 52:48 compositions as a function of 'over' annealing.

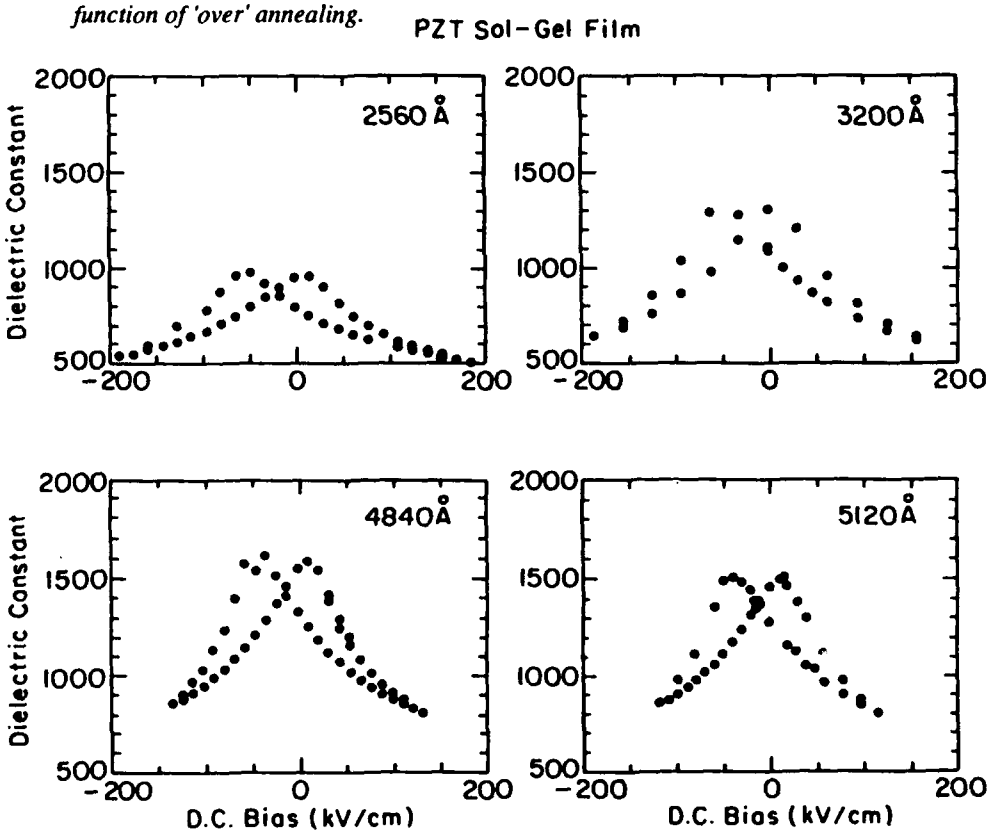

Figure 6.4: Permittivity ε_W as a function of applied electrical bias in PZT 52:45 films

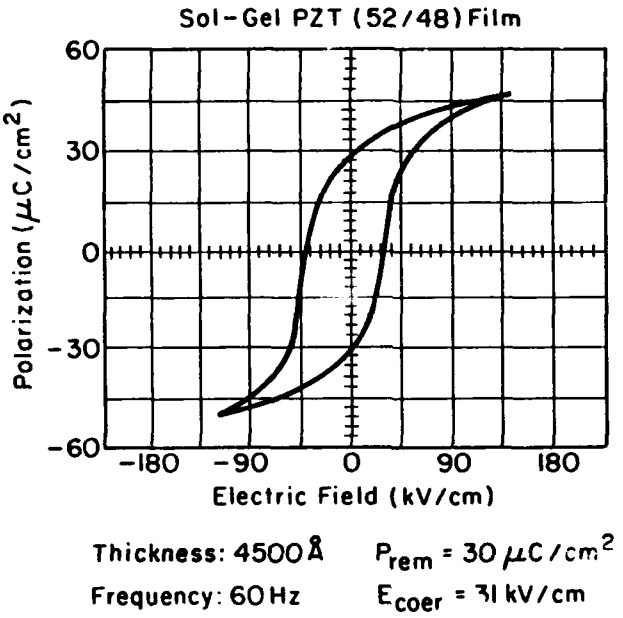

Figure 6.5: Polarization:field hysteresis in a PZT 52:48 film 4,500A thick taken at 60Hz.

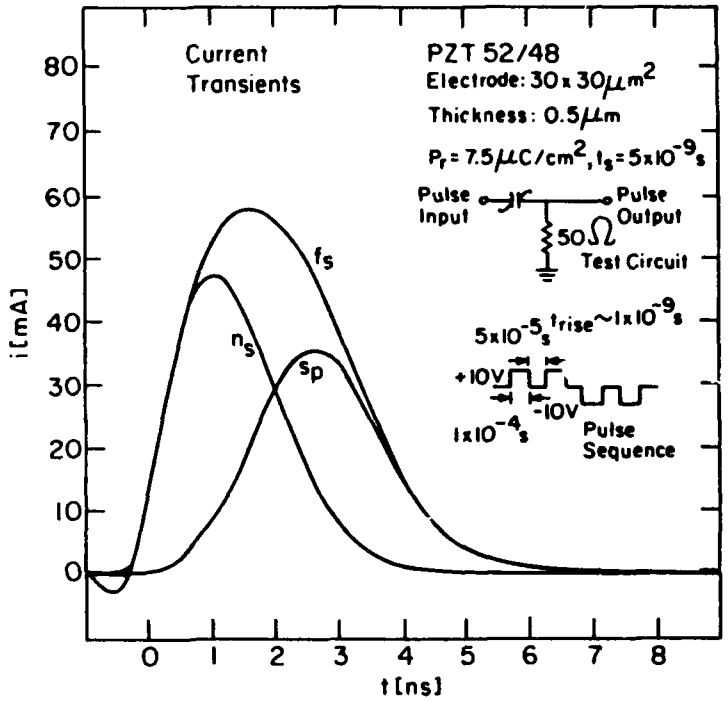

Figure 6.6: Polarization switching using very high current pulses in PZT 52/48 (after Dey).

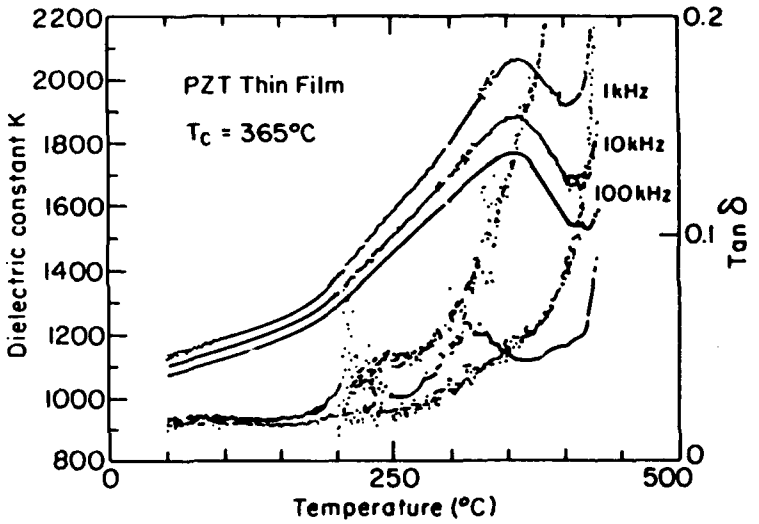

Figure 6.7: Weak field permittivity as a function of temperature in PZT 52/48.

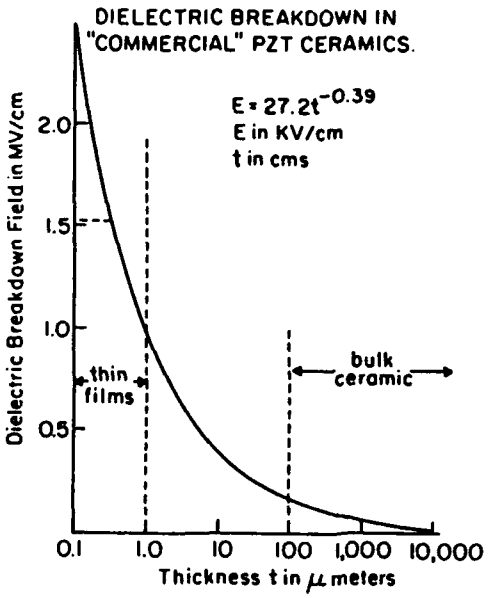

Figure 6.8: Breakdown field E_B as a function of thickness from the empirical equation by Gerson and Marshal.

Perhaps the most startling difference from bulk PZT comes in examination of the weak field dielectric permittivity vs. temperatures (Figure 6.7). The peak is roughly at the right temperature, but the value is low and the peak is highly rounded. In all our own studies the best ratio $\varepsilon_{peak}/\varepsilon_{room} < 3:1$, where in a well prepared bulk material the peak is very sharp, non dispersive and the ratio ~ 15:1.

A significant positive aspect of film behaviour is the manner in which the dielectric strength increases at low film thickness (Figure 6.8). Values of E_B as large as 4 MV/cm are not uncommon. It is interesting to note that the empirical curve predicted by Gerson and Marshall (1959) based only on bulk measurements predicts breakdown fields for submicron thick films above 1 MV/cm.

For simple high K applications where hysteresis would be a marked disadvantage, two alternative lead based compositions are being explored. In the high lanthanum Lead Lanthanum titanates Dey has explored a 28:0:100 PLT which shows good linearity (P vs. E) some dispersion with a K ~ 1,600 at 100 Hz and 1,400 at 10 MHz. Udayakumar (1992) has explored PMN:PT compositions which show K values up to 2,800 and only weak dispersion to 10 MHz.

Clearly there are claimant needs for very compact film capacitors in high density silicon and ultra high speed GaAs circuits and there are many options yet to explore for high K systems.

7 Piezoelectric Ceramics

7.1 Phenomenological and Pictorial Descriptions of Piezoelectricity in Crystals

The phenomenological master equation which describes the deformations of an insulating crystal subject to both elastic and electric stress takes the form

$x_{ij} = s_{ijkl} X_{kl} + d_{mij} E_m + M_{mnij} E_m E_n$

where

x_{ij}	are the components of elastic strain
X_{ij}	the stress components
s_{ijkl}	the elastic compliance tensor
$E_m E_n$	are components of electric field
d_{mij}	the piezoelectric tensor components
M_{mnij}	the electrostriction tensor in field notation

and the Einstein summation convention is assumed.

For crystals in which some components of the d_{mij} tensor are non zero, when $X_{kl} \equiv 0$ the elastic strain is given by

$$x_{ij} = d_{mij} E_m \tag{7.1}$$

which is the equation for the converse piezoelectric effect, relating induced strain directly to the first power of the field, i.e. x_{ij} changes sign with E_m.

In the thermodynamically equivalent direct effect

$$P_m = d_{mij} X_{ij} \tag{7.2}$$

Clearly 7.1 describes the actuating function of a piezoelectric, changing shape under electric field control. Equation 7.2 describes the sensing function, a change in polarization under stress charges the capacitance of the sensing crystal giving a voltage proportional to the stress applied.

If the d_{mij} constants are zero due to symmetry as for example in a centric crystal, the residual effect is electrostrictive and at zero stress

$$x_{ij} = M_{mnij} E_m E_n .$$

Now the strain is a quadratic function of the applied stress.

The thermodynamically converse effect is now given by

$$\eta_{mn} = M_{mnij} X_{ij}$$

i.e. the elastic stress dependence of the dielectric susceptibility.

Pictorially, the piezoelectric effect is illustrated by the two dimensional sketches in Figure 7.1 which models a polar crystal of the perovskite lead titanate in its single domain ferroelectric form. To simplify the description it is assumed that the polarization resides in the Ti^{4+} ion as in

$BaTiO_3$ and the lead ion displacements are neglected. In the base state, the titanium ion is displaced along the 3 directions a distance corresponding to the spontaneous polarization P_3 and the resulting symmetry is tetragonal 4mm.

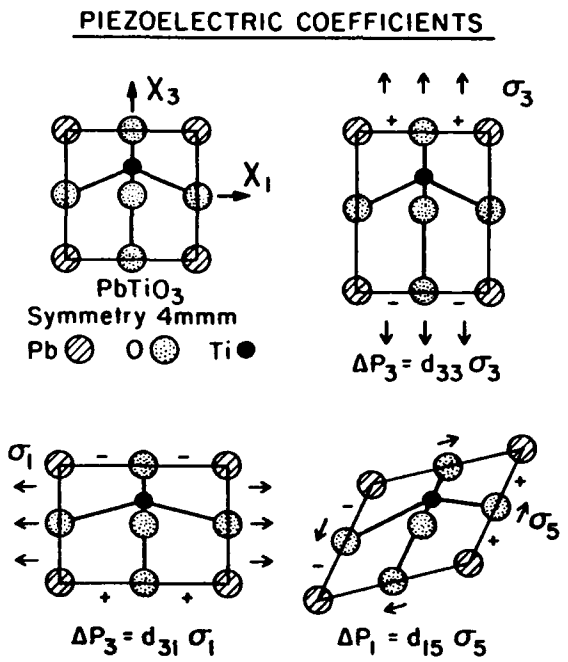

Figure 7.1: Two dimensional description of the origin of the piezoelectric response in a single domain $PbTiO_3$ crystal. (a) Situation under no field. (b) Shift of the Ti cation away from the equilibrium position under stress τ_3. (c) Shift of the Ti cation back towards the cell center under stress τ_1. (d) Tilting of the Ti position giving ΔP, under a shear stress τ_5.

If a tensile stress σ_3 is now applied in the X_3 direction(Figure 7.1b), the upper and lower oxygen ions pull out the equatorial ions squash in forcing the Ti^{4+} farther away from the cell center and generating an enhancement of P_S by ΔP. Since the displacement are very small $\Delta P \alpha \sigma_3$ and the constant of proportionality d_{33} is positive, i.e. a positive (tensile stress) gives a positive change in ΔP.

For a transverse tensile stress σ_1 however (Figure 7.1c) the equatorial oxygens are pulled out, the Ti^{4+} brought back more towards the center of the cell, giving a negative increment ΔP_3 so that

$$\Delta P_3 = d_{31}\,\sigma_1$$

and d_{31} must be a negative quality.

Similarly a shear stress σ_5 (σ_{31}) leads to a canting of the Ti^{4+} and a displacement direction normal to P_3 i.e. a ΔP_1 so that Figure 7.1d.

$$\Delta P_1 = d_{15}\,\tau_5$$

For the point group 4mm clearly the action of the 4 fold axis makes 2 equivalent to 1 so that

$$d_{31} = d_{32} \quad \text{and} \quad d_{15} = d_{24}$$

and the complete piezoelectric tensor takes the form

$$\begin{bmatrix} 0 & 0 & 0 & 0 & d_{15} & 0 \\ 0 & 0 & 0 & d_{15} & 0 & 0 \\ d_{31} & d_{31} & d_{33} & 0 & 0 & 0 \end{bmatrix}$$

7.2 Piezoelectricity in Ceramics

In a randomly axed polycrystal ceramic, even if the grains are polar or ferroelectric as in Figure 7.2 under normal circumstance the random orientation will cancel out any anisotropy engendering a macroscopic center of symmetry which forbids piezoelectricity. For the ferroelectric ceramic however a new anisotropy can be induced since the domain polar vectors can be switched under realizable field. Thus the poling operation which develops a high remanent polarization P_R in the ceramic is essential to destroy the macro center of symmetry taking the material into the texture symmetry group ∞ mm.

Theoretically it is quite straightforward to derive the possible P_r which may be induced in a ferroelectric ceramic if all domains of a given type may switch under the poling field. In a ferroelectric with only 2 antipolar domain states, only 180° switching would be possible and $\bar{P}_{r\ max} = 0.25\,P_s$. In a tetragonal ferroelectric perovskite there are 6 axial orientation for the domains and $\bar{P}_{r\ max} = .83\,P_s$, and for the rhombohedral case with 8 body diagonal orientations $\bar{P}_{r\ max} = 0.87\,P_s$. Unfortunately the ability to pole in practical ceramics is more restricted, so that a high count of available orientation states becomes essential. This is illustrated for $BaTiO_3$ at room temperature in Figure 7.3. In the single domain single crystal $P_S = 26\ \mu c/cm^2$ (Figure 7.3a). Even in a very large grain ceramic $P_{r\ max} \simeq 8\ \mu c/cm^2$, Figure 7.3b and in a practical fine (1 μ meter grain) ceramic P_r almost vanishes (Figure 7.3c).

7.3 Lead Zirconate Titanate Piezoceramics

The uniquely advantageous feature of the lead zirconate lead titanate ferroelectric phase diagram

Figure 7.4 is the almost vertical phase boundary near the 50:50 Zr/Ti composition, the so called morphotropic phase boundary which separates a tetragonal and a rhombohedral ferroelectric phases. All ferroelectric:ferroelectric phase transitions are first order so that the boundary encompasses a finite two phase region where the 6 domain states of the tetragonal variant coexist with the 8 domain states of the rhombohedral. The advantage in terms of polability for ceramics near this composition is compared to other perovskite possibilities in Figure 7.5 showing the clear superiority of the PZT.

The maximum polability for compositions near the MPB is shown clearly in Figure 7.6, and the consequent advantage in piezoelectric constants in Figure 7.7, both taken from the book by Jaffe Cooke and Jaffe (1971).

7.3.1 Phenomenology of Piezoelectricity in PZTs

It is clear from the earlier consideration of dielectric applications that the instability at the paraelectric:ferroelectric phase transition contributes an intrinsic compliance in the dielectric property which can be manipulated to great practical advantage. For $BaTiO_3$, it is easy to trace this enhanced compliance as excellent single crystals can be grown and by simple poling procedures converted into single domain states. Thus the properties of a single domain can be measured at any temperature or stress of interest and a full Landau:Ginsburg:Devonshire phenomenology developed which will mimic the intrinsic properties of $BaTiO_3$ domains under any set of electric/elastic boundary conditions (Devonshire, 1954; Cross, 1956; Cross, 1967).

In the lead zirconate titanate solid solution system however, the situation is significantly more complex. Different composition across the phase field exhibit antiferroelectric, oxygen octahedral tilted, and simple proper ferroelectric phases. An even more important constraint is that in spite of almost 30 years of continuous effort there are still no reputable single crystals available with compositions near to the critical 50/50 Zr/Ti ratio of the MPB and thus no direct measurements of single domain properties. Only compositions close to pure $PbZrO_3$ and pure $PbTiO_3$ have been grown with adequate quality and for other compositions it is necessary to use indirect methods to deduce the thermodynamic constants.

Over some 10 years the ferroelectric group at Penn State has dedicated a continuing effort to formulating an adequate phenomenology. Faculty and students involved have included B. Gadger, A. Amin, H. McKinstry, T. Halemane, M. Haun, G. Rossetti and L. E. Cross and their work is documented in a sequence of papers (Amin and Cross, 1983; Halemane et al., 1985; Amin et al., 1985; Haun et al., 1985; Haun et al., 1989a-e). The papers of Haun et al. (1985, 1989a-e) provide an excellent summary of the pure PZT work.

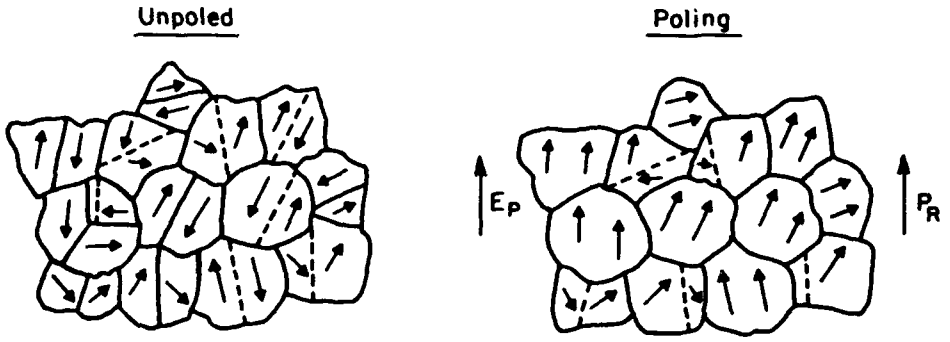

Figure 7.2: Two dimension schematic of the polarization vectors in unpoled and in poled PZT. In (a) the symmetry is ∞∞∞ which is centric and forbids piezoelectricity. In (b) the symmetry is ∞ mm which is non centric (polar) and permits piezoelectricity.

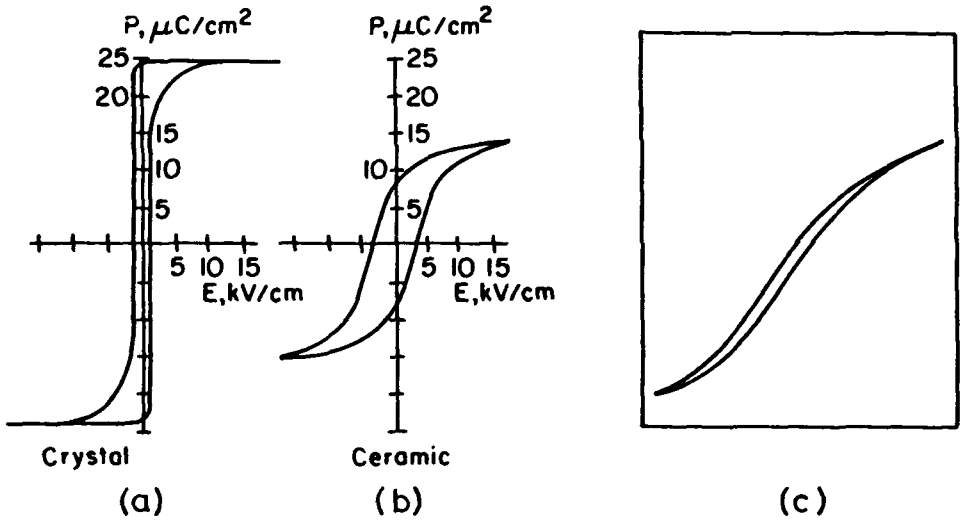

Figure 7.3: Contrasting polarization hysteresis in (a) single crystal ; (b) ceramic polycrystal ; (c) fine grain ceramic $BaTiO_3$ samples.

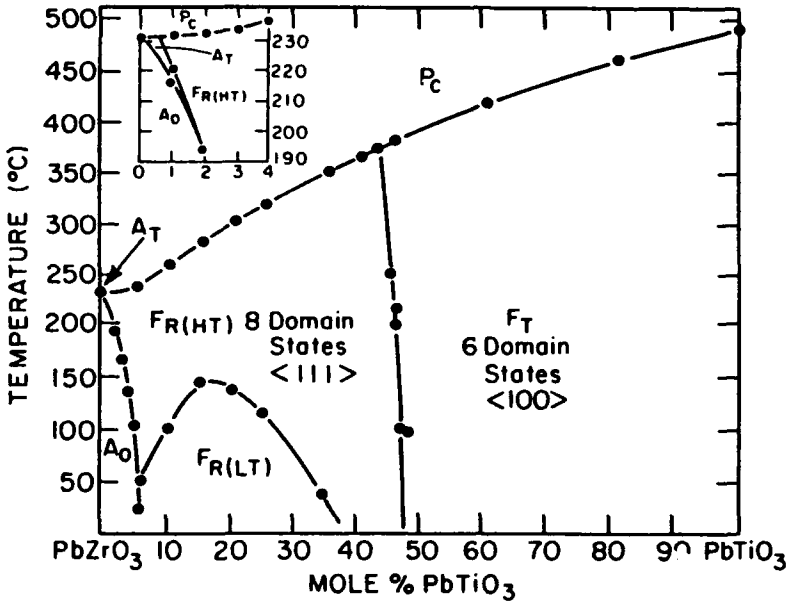

Figure 7.4: Phase diagram of the Lead zirconate:lead titanate solid solution system, highlighting the important morphotropic phase boundary (MPB).

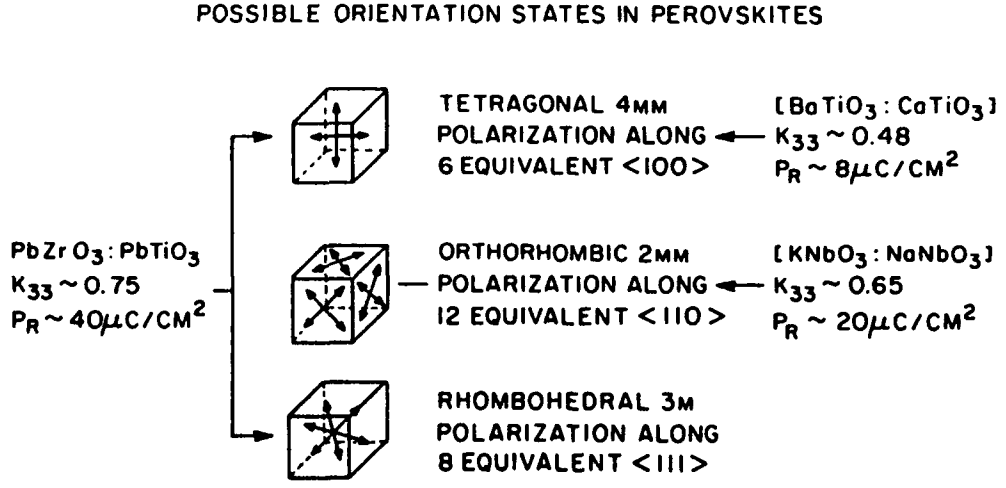

Figure 7.5: Indicating from examples in different perovskite ceramic compositions the importance of number of equivalent domain states in realizing poling and high piezoelectric activity.

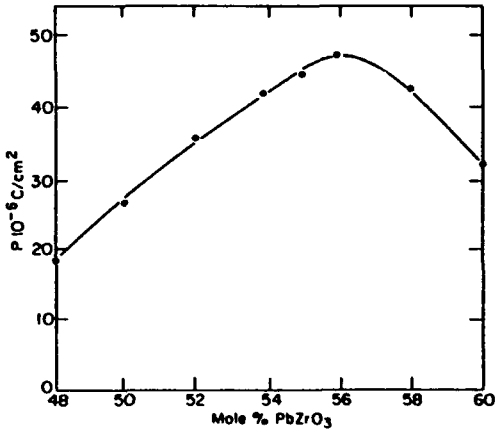

Figure 7.6: Remanent polarization in PZT ceramics of comparable grain size as a function of Zr:Ti ratio

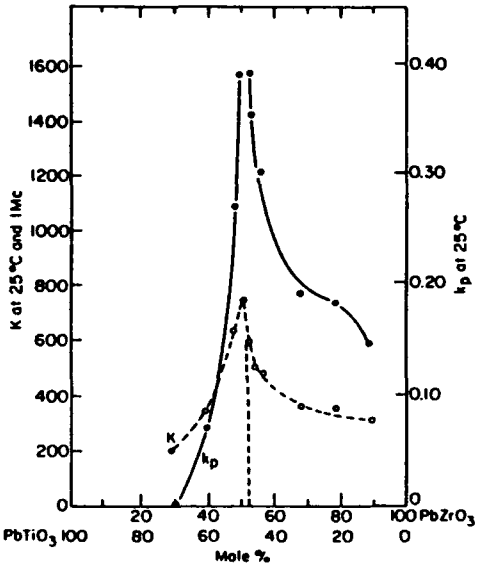

Figure 7.7: Dielectric and piezoelectric response in poled PZT as a function of Zr:Ti ratio.

Table 7.1: Coefficients of the PZT Energy Function

α_i, α_{ij}, α_{ijk}	ferroelectric dielectric stiffness at constant stress
σ_i, σ_{ij}, σ_{ijk}	antiferroelectric dielectric stiffness at constant stress
μ_{ij}	coupling between the ferroelectric and antiferroelectric polarizations
β_i, β_{ij}	octahedral torsion coefficients
γ_{ij}	coupling between the ferroelectric polarization and tilt angle
s_{ij}	elastic compliances at constant polarization
Q_{ij}	electrostrictive coupling between the ferroelectric polarization and stress
Z_{ij}	electrostrictive coupling between the antiferroelectric polarization and stress
R_{ij}	rotostrictive coupling between the tilt angle and stress

In developing the "master equation" for the free energy in terms of the extensive variables, it is necessary to start with a two sub lattice model to encompass the antiferroelectric states, however, since these are confined to compositions very close to lead zirconate it is advantageous to use linear combination of the sub lattice polarization P_A and P_B in the form

$$P = P_A + P_B$$

$$p = P_A - P_B$$

Thus when $P_A = +P_B$ $P \neq 0$ and represents the effective ferroelectric polarization, and when $P_A = -P_B$ $p \neq 0$ and represents the magnitude of the antipolarization in the antiferroelectric phase.

Polarization and antipolarization have the axial components $P_1P_2P_3$ and $p_1p_2p_3$ respectively. The oxygen octahedra have tilt angle q with components about the axial direction $\theta_1\theta_2\theta_3$. Elastic stress and strain are designated X_{ij} x_{ij}. The full family of coupling variables are delineated in Table 7.1 and the resulting Equation 7.3.

$$
\begin{aligned}
\Delta G = {} & \alpha_1[P_1^2 + P_2^2 + P_3^2] + \alpha_{11}[P_1^4 + P_2^4 + P_3^4] \\
& + \alpha_{12}[P_1^2P_2^2 + P_2^2P_3^2 + P_3^2P_1^2] + \alpha_{111}[P_1^6 + P_2^6 + P_3^6] \\
& + \alpha_{112}[P_1^4(P_2^2 + P_3^2) + P_2^4(P_1^2 + P_3^2) + P_3^4(P_1^2 + P_2^2)] \\
& + \alpha_{123}P_1^2P_2^2P_3^2 + \sigma_1[p_1^2 + p_2^2 + p_3^2] + \sigma_{11}[p_1^4 + p_2^4 + p_3^4] \\
& + \sigma_{12}[p_1^2p_2^2 + p_2^2p_3^2 + p_3^2p_1^2] + \sigma_{111}[p_1^6 + p_2^6 + p_3^6] \\
& + \sigma_{112}[p_1^4(p_2^2 + p_3^2) + p_2^4(p_1^2 + p_3^2) + p_3^4(p_1^2 + p_2^2)] \\
& + \sigma_{123}p_1^2p_2^2p_3^2 + \mu_{11}[P_1^2p_1^2 + P_2^2p_2^2 + P_3^2p_3^2] \\
& + \mu_{12}[P_1^2(p_2^2 + p_3^2) + P_2^2(p_1^2 + p_3^2) + P_3^2(p_1^2 + p_2^2)] \\
& + \mu_{44}[P_1P_2p_1p + P_2P_3p_2p_3 + P_3P_1p_3p_1] + \beta_1[\theta_1^2 + \theta_2^2 + \theta_3^2] \\
& + \beta_{11}[\theta_1^4 + \theta_2^4 + \theta_3^4] + \gamma_{11}[P_1^2\theta_1^2 + P_2^2\theta_2^2 + P_3^2\theta_3^2] \\
& + \gamma_{12}[P_1^2(\theta_1^2 + \theta_2^2) + P_2^2(\theta_1^2 + \theta_3^2) + P_3^2(\theta_1^2 + \theta_2^2)] \\
& + \gamma_{44}[P_1P_2\theta_1\theta_2 + P_2P_3\theta_2\theta_3 + P_3P_1\theta_3\theta_1] \\
& - \tfrac{1}{2}S_{11}[X_1^2 + X_2^2 + X_3^2] - S_{12}[X_1X_2 + X_2X_3 + X_3X_1] \\
& - \tfrac{1}{2}S_{44}[X_4^2 + X_5^2 + X_6^2] - Q_{11}[X_1P_1^2 + X_2P_2^2 + X_3P_3^2] \\
& - Q_{12}[X_1(P_2^2 + P_3^2) + X_2(P_1^2 + P_3^2) + X_3(P_1^2 + P_2^2)] \\
& - Q_{44}[X_4P_2P_3 + X_5P_1P_3 + X_6P_1P_2] - Z_{11}[X_1^2p_1 + X_2^2p_2 + X_3^2p_3] \\
& - Z_{12}[X_1(p_2^2 + p_3^2) + X_2(p_1^2 + p_3^2) + X_3(p_1^2 + p_2^2)] \\
& - Z_{44}[X_4p_2p_3 + X_5p_1p_3 + X_6p_1p_2] - R_{11}[X_1\theta_1^2 + X_2\theta_2^2 + X_3\theta_3^2] \\
& - R_{12}[X_1(\theta_2^2 + \theta_3^2) + X_2(\theta_1^2 + \theta_3^2) + X_3(\theta_1^2 + \theta_2^2)] \\
& - R_{44}[X_4\theta_2\theta_3 + X_5\theta_1\theta_3 + X_6\theta_1\theta_2]
\end{aligned}
\tag{7.3}
$$

7.3.2 Solutions to the Energy Function

Considering zero stress conditions the following solutions to the energy function (Equation 7.3) are of interest in the PZT system:

Paraelectric Cubic (P_C)

$$P_1 = P_2 = P_3 = 0, \quad p_1 = p_2 = p_3 = 0, \quad \theta_1 = \theta_2 = \theta_3 = 0 \tag{7.4}$$

Ferroelectric Tetragonal (F_T)

$$P_1 = P_2 = 0, \quad P_3^2 \neq 0, \quad p_1 = p_2 = p_3 = 0, \quad \theta_1 = \theta_2 = \theta_3 = 0 \tag{7.5}$$

Ferroelectric Orthorhombic (F_O)

$$P_1 = 0, \quad P_2^2 = P_3^2 \neq 0, \quad p_1 = p_2 = p_3 = 0, \quad \theta_1 = \theta_2 = \theta_3 = 0 \tag{7.6}$$

Ferroelectric High-temperature Rhombohedral ($F_{R(HT)}$)

$$P_1^2 = P_2^2 = P_3^2 \neq 0, \quad p_1 = p_2 = p_3 = 0, \quad \theta_1 = \theta_2 = \theta_3 = 0 \tag{7.7}$$

Ferroelectric Low-temperature Rhombohedral ($F_{R(LT)}$)

$$P_1^2 = P_2^2 = P_3^2 \neq 0, \quad p_1 = p_2 = p_3 = 0, \quad \theta_1^2 = \theta_2^2 = \theta_3^2 \neq 0 \tag{7.8}$$

Antiferroelectric Orthorhombic (A_O)

$$P_1 = P_2 = P_3 = 0, \quad p_1 = 0, \quad p_2^2 = p_3^2 \neq 0, \quad \theta_1 = \theta_2 = \theta_3 = 0 \tag{7.9}$$

All of these solutions, except for the ferroelectric orthorhombic solution, are stable in the PZT system. The ferroelectric orthorhombic solution was also included here, because the coefficients necessary to calculate the energy of this phase can be determined. An independent check of the calculated coefficients can then be made by confirming that this phase is metastable across the PZT system.

Applying these solutions to Equation 7.3 under zero stress conditions results in the following relations for the energies of each solution

$$P_C \quad \Delta G = 0 \tag{7.10}$$

$$F_T \quad \Delta G = \alpha_1 P_3^2 + \alpha_{11} P_3^4 + \alpha_{111} P_3^6 \tag{7.11}$$

$$F_O \quad \Delta G = 2\alpha_1 P_3^2 + (2\alpha_{11} + \alpha_{12}) P_3^4 + 2(\alpha_{111} + \alpha_{112}) P_3^6 \tag{7.12}$$

$$F_{R(HT)} \quad \Delta G = 3\alpha_1 P_3^2 + 3(\alpha_{11} + \alpha_{12}) P_3^4 + (3\alpha_{111} + 6\alpha_{112} + \alpha_{123}) P_3^6 \tag{7.13}$$

$$F_{R(LT)} \quad \Delta G = 3\alpha_1 P_3^2 + 3(\alpha_{11} + \alpha_{12}) P_3^4 + (3\alpha_{111} + 6\alpha_{112} + \alpha_{123}) P_3^6 + 3\beta_1 \theta_3^2 + 3\beta_{11} \theta_3^4 + 3(\gamma_{11} + 2\gamma_{12} + \gamma_{44}) P_3^2 \theta_3^2 \tag{7.14}$$

$$A_O \quad \Delta G = 2\sigma_1 p_3^2 + (2\sigma_{11} + \sigma_{12}) p_3^4 + 2(\sigma_{111} + \sigma_{112}) p_3^6 \tag{7.15}$$

The spontaneous ferroelectric and antiferroelectric polarizations (P_3 and p_3) and tilt angle (θ_3) in the above equations can be found from the first partial derivative stability conditions ($\partial\Delta G/\partial P_3$, $\partial\Delta G/\partial p_3$, and $\partial\Delta G/\partial\theta_3$) as shown below.

$$F_T \quad \partial\Delta G/\partial P_3 = 0 = 3\alpha_{111}P_3^4 + 2\alpha_{11}P_3^2 + \alpha_1 \tag{7.16}$$

$$F_O \quad \partial\Delta G/\partial P_3 = 0 = 3(\alpha_{111} + \alpha_{112})P_3^4 + (2\alpha_{11} + \alpha_{112})P_3^2 + \alpha_1 \tag{7.17}$$

$$F_{R(HT)} \quad \partial\Delta G/\partial P_3 = 0 = (3\alpha_{111} + 6\alpha_{112} + \alpha_{123})P_3^4 + 2(\alpha_{11} + \alpha_{12})P_3^2 + \alpha_1 \tag{7.18}$$

$$F_{R(LT)} \quad \partial\Delta G/\partial P_3 = 0 = (3\alpha_{111} + 6\alpha_{112} + \alpha_{123})P_3^4 + 2(\alpha_{11} + \alpha_{12})P_3^2 + \alpha_1 + \gamma_{11}\theta_3^2 \tag{7.19}$$

$$\partial\Delta G/\partial\theta_3 = 0 = \beta_1 + 2\beta_{11}\theta_3^2 + \gamma_{11}P_3^2 \tag{7.20}$$

$$A_O \quad \partial\Delta G/\partial p_3 = 0 = 3(\sigma_{111} + \sigma_{112})p_3^4 + (2\sigma_{11} + \sigma_{12})p_3^2 + \sigma_1 \tag{7.21}$$

The polarizations and tilt angle can be calculated by solving these quadratic equations. Equations 7.10 - 7.15 relate the energies of each solution to the coefficients of the energy function. Thus by determining these coefficients, the energies of each phase can be calculated.

7.3.3 Spontaneous Elastic Strains

The spontaneous elastic strains x_i ($\partial\Delta G/\partial X_i$) under zero stress conditions can be derived from Equation 7.3 as follows:

$$P_C \quad x_1 = x_2 = x_3 = x_4 = x_5 = x_6 = 0 \tag{7.22}$$

$$F_T \quad x_1 = x_2 = Q_{12}P_3^2, \quad x_3 = Q_{11}P_3^2, \quad x_4 = x_5 = x_6 = 0 \tag{7.23}$$

$$F_O \quad x_1 = 2Q_{12}P_3^2, \quad x_2 = x_3 = (Q_{11} + Q_{12})P_3^2, \quad x_4 = Q_{44}P_3^2, \quad x_5 = x_6 = 0 \tag{7.24}$$

$$F_{R(HT)} \quad x_1 = x_2 = x_3 = (Q_{11} + 2Q_{12})P_3^2, \quad x_4 = x_5 = x_6 = Q_{44}P_3^2 \tag{7.25}$$

$$F_{R(LT)} \quad x_1 = x_2 = x_3 = (Q_{11} + 2Q_{12})P_3^2 + (R_{11} + 2R_{12})\theta_3^2, \quad x_4 = x_5 = x_6 = Q_{44}P_3^2 + R_{44}\theta_3^2 \tag{7.26}$$

$$A_O \quad x_1 = 2Z_{12}p_3^2, \quad x_2 = x_3 = (Z_{11} + Z_{12})p_3^2, \quad x_4 = Z_{44}p_3^2, \quad x_5 = x_6 = 0 \tag{7.27}$$

These spontaneous strain relations can be shown to be very important in determining the coefficients of the energy function. Spontaneous strain data will be determined from x-ray diffraction of PZT powders, and used with the electrostrictive constants to calculate the spontaneous polarization, which is needed to determine coefficients of the energy function.

7.3.4 Intrinsic Dielectric Properties

Relations for the relative dielectric stiffness χ_{ij} ($= \partial^2 \Delta G / \partial P_i \partial P_j$) were derived from Equation 7.3 for the six solutions:

$$P_C \quad \chi_{11} = \chi_{22} = \chi_{33} = 2\varepsilon_0\alpha_1, \quad \chi_{12} = \chi_{23} = \chi_{31} = 0 \tag{7.28}$$

$$F_T \quad \chi_{11} = \chi_{22} = 2\varepsilon_0[\alpha_1 + \alpha_{12}P_3^2 + \alpha_{112}P_3^4],$$
$$\chi_{33} = 2\varepsilon_0[\alpha_1 + 6\alpha_{11}P_3^2 + 15\alpha_{111}P_3^4], \quad \chi_{12} = \chi_{23} = \chi_{31} = 0 \tag{7.29}$$

$$F_O \quad \chi_{11} = 2\varepsilon_0[\alpha_1 + 2\alpha_{12}P_3^2 + (2\alpha_{112} + \alpha_{123})P_3^4],$$
$$\chi_{22} = \chi_{33} = 2\varepsilon_0[\alpha_1 + (6\alpha_{11} + \alpha_{12})P_3^2 + (15\alpha_{111} + 7\alpha_{112})P_3^4],$$
$$\chi_{12} = \chi_{31} = 0, \quad \chi_{23} = 4\varepsilon_0[\alpha_{12}P_3^2 + 4\alpha_{112}P_3^4] \tag{7.30}$$

$$F_{R(HT)} \quad \chi_{11} = \chi_{22} = \chi_{33} = 2\varepsilon_0[\alpha_1 + (6\alpha_{11} + 2\alpha_{22})P_3^2$$
$$+ (15\alpha_{111} + 14\alpha_{112} + \alpha_{123})P_3^4,$$
$$\chi_{12} = \chi_{23} = \chi_{31} = 4\varepsilon_0[\alpha_{12}P_3^2 + (4\alpha_{112} + \alpha_{123})P_3^4] \tag{7.31}$$

$$F_{R(LT)} \quad \chi_{11} = \chi_{22} = \chi_{33} = 2\varepsilon_0[\alpha_1 + (6\alpha_{11} + 2\alpha_{12})P_3^2$$
$$+ (15\alpha_{111} + 14\alpha_{112} + \alpha_{123})P_3^4 + (\gamma_{11} + 2\gamma_{12})\theta_3^2],$$
$$\chi_{12} = \chi_{23} = \chi_{31} = 4\varepsilon_0[\alpha_{12}P_3^2 + (4\alpha_{112} + \alpha_{123})P_3^4 + \gamma_{44}\theta_3^2] \tag{7.32}$$

$$A_O \quad \chi_{11} = 2\varepsilon_0[\alpha_1 + 2\mu_{12}p_3^2], \quad \chi_{22} = \chi_{33} = 2\varepsilon_0[\alpha_1 + (\mu_{11} + \mu_{12})p_3^2],$$
$$\chi_{12} = \chi_{31} = 0, \quad \chi_{23} = \varepsilon_0\mu_{44}p_3^2 \tag{7.33}$$

The multiplication by permittivity of free space ε_0 in these equations was required to convert from absolute to relative dielectric stiffness. Equations 7.28 - 7.33 can be used to calculate the relative dielectric stiffness for each phase based on the original cubic axes.

In the orthorhombic state the polarization can be along any of the <110> directions of the original cubic axes. The polarization of the rhombohedral state can be along any of the <111> directions. By rotating these axes so that for both states the new x3 axis is along the polar directions, diagonalized matrices will result. The new dielectric stiffness coefficients (indicated by a prime) can be related to the old coefficients [defined by Equations 7.28 - 7.33] with the following relations:

$$F_O \text{ and } A_O \quad \chi'_{11} = \chi_{11}, \quad \chi'_{22} = \chi_{33} - \chi_{23}$$
$$\chi'_{33} = \chi_{33} + \chi_{23}, \quad \chi'_{12} = \chi'_{23} = \chi'_{31} = 0 \tag{7.34}$$

$$F_{R(HT)} \text{ and } F_{R(LT)} \quad \chi'_{11} = \chi'_{22} = \chi_{11} - \chi_{12}, \quad \chi'_{33} = \chi_{11} + 2\chi_{12}$$
$$\chi'_{12} = \chi'_{23} = \chi'_{31} = 0 \tag{7.35}$$

These equations can be used to calculate the dielectric stiffness of the orthorhombic and rhombohedral phases parallel and perpendicular to the polar axes.

The dielectric susceptibility coefficients (η_{ij}) can be determined from the reciprocal of the dielectric stiffness matrices (χ_{ij}) using the following relation:

$$\eta_{ij} = A_{ij}/\Delta \tag{7.36}$$

where A_{ji} and Δ are the cofactor and determinant of the χ_{ij} matrix. Using this relation results in the following relations for the dielectric susceptibility coefficients (η_{ij}):

P_C $\eta_{11} = \eta_{22} = \eta_{33} = 1/\chi_{11}, \quad \eta_{12} = \eta_{23} = \eta_{31} = 0$ (7.37)

F_T $\eta_{11} = \eta_{22} = 1/\chi_{11}, \quad \eta_{33} = 1/\chi_{33}$ (7.38)

F_O and A_O $\eta_{11} = 1/\chi_{11}, \quad \eta_{22} = \eta_{33} = \chi_{33}/(\chi_{33}^2 - \chi_{23}^2),$

$\eta_{12} = \eta_{31} = 0, \quad \eta_{23} = -\chi_{23}/(\chi_{33}^2 - \chi_{23}^2)$ (7.39)

$\eta'_{11} = 1/\chi'_{11}, \quad \eta'_{22} = 1/\chi'_{22}, \quad \eta'_{33} = 1/\chi'_{33}$

$\eta'_{12} = \eta'_{23} = \eta'_{31} = 0$ (7.40)

$F_{R(HT)}$ and $F_{R(LT)}$ $\eta_{11} = \eta_{22} = \eta_{33} = (\chi_{11}^2 - \chi_{12}^2)/(\chi_{11}^3 - 3\chi_{11}\chi_{12}^2 + 2\chi_{12}^3)$

$\eta_{12} = \eta_{23} = \eta_{31} = (\chi_{12}^2 - \chi_{11}\chi_{12})/(\chi_{11}^3 - 3\chi_{11}\chi_{12}^2 + 2\chi_{12}^3)$

$\eta'_{11} = \eta'_{22} = 1/\chi'_{11}, \quad \eta'_{33} = 1/\chi'_{33}$ (7.41)

$\eta'_{12} = \eta'_{23} = \eta'_{31} = 0$ (7.42)

These equations can be used to calculate the dielectric susceptibilities of each phase from the coefficients of the energy function.

7.3.5 Piezoelectric Properties

Relations for the piezoelectric b_{ij} coefficients ($= \partial^2\Delta G/\partial P_i \partial X_j$) were derived from Equation 7.3 for the tetragonal and rhombohedral states as shown below:

F_T $b_{33} = 2Q_{11}P_3, \quad b_{31} = b_{32} = 2Q_{12}P_3,$

$b_{15} = b_{24} = Q_{44}P_3, \quad b_{11} = b_{12} = b_{13} = b_{14} = b_{16} = 0,$

$b_{21} = b_{22} = b_{23} = b_{25} = b_{26} = b_{34} = b_{35} = b_{36} = 0$ (7.43)

$F_{R(HT)}$ and $F_{R(LT)}$ $b_{11} = b_{22} = b_{33} = 2Q_{11}P_3, \quad b_{14} = b_{25} = b_{36} = 0$

$b_{12} = b_{13} = b_{21} = b_{23} = b_{31} = b_{32} = 2Q_{12}P_3,$

$b_{15} = b_{16} = b_{24} = b_{26} = b_{34} = b_{35} = Q_{44}P_3,$ (7.44)

Since a coupling term of type $X_iP_i\theta_i$ was not included in Equation 7.3, the b_{ij} relations [Equation 7.44] for the high and low temperature rhombohedral phases are of the same form. However, the spontaneous polarizations P_3 are defined by different relations for the high and low temperature rhombohedral phases, and thus different values would result for these coefficient.

The piezoelectric d_{ij} coefficients are defined by:

$$d_{ij} = b_{kj}\,\eta_{ik} \tag{7.45}$$

Using this relation for the tetragonal and rhombohedral states results in the following relations:

F_T

$$d_{33} = 2\varepsilon_0\eta_{33}Q_{11}P_3, \quad d_{31} = d_{32} = 2\varepsilon_0\eta_{33}Q_{12}P_3,$$
$$d_{15} = d_{24} = \varepsilon_0\eta_{11}Q_{44}P_3, \quad d_{11} = d_{12} = d_{13} = d_{14} = d_{16} = 0,$$
$$d_{21} = d_{22} = d_{23} = d_{25} = d_{26} = d_{34} = d_{35} = d_{36} = 0$$

$F_{R(HT)}$ and $F_{R(LT)}$

$$d_{11} = d_{22} = d_{33} = 2\varepsilon_0(\eta_{11}Q_{11} + 2\eta_{12}Q_{12})P_3, \tag{7.46}$$
$$d_{12} = d_{13} = d_{21} = d_{23} = d_{31} = d_{32}$$
$$= 2\varepsilon_0[\eta_{11}Q_{12} + \eta_{12}(Q_{11} + Q_{12})]P_3,$$
$$d_{14} = d_{25} = d_{36} = 2\varepsilon_0\eta_{12}Q_{44}P_3,$$
$$d_{15} = d_{16} = d_{24} = d_{26} = d_{34} = d_{35} = \varepsilon_0(\eta_{11} + \eta_{12})Q_{44}P_3, \tag{7.47}$$

The multiplication by the permittivity of free space ε_0 in these three equations was required to convert the dielectric susceptibilities from relative to absolute. Equations 7.43, 7.44, 7.45, and 7.46 can be used to calculate the piezoeleectric b_{ij} and d_{ij} coefficients of the tetragonal and rhombohedral phases from the coefficients of the energy function.

7.3.6 Delineation of the Phenomenological Constants

The initial basic assumption applied was that all temperature dependence was carried the lowest order stiffness constants α_1 and τ_1 which were made linear functions of temperature. The Curie temperature Tc was taken from the phase diagram and the Curie constant C used measured values taken from high density ceramic samples. The temperature dependence of P_S required to model the higher order α_{ij}, Curie was determined by assuming quadratic electrostriction and measuring the X-ray spontaneous strain in carefully prepared chemically coprecipated powders. The MPB imposes a major constraint upon the α's since it requires that near the 50/50 Zr/Ti composition the tetragonal and rhombohedral phases have similar energies across a very wide temperature range.

Full details of the procedures, and of the most recent families of constants can be found in Haun (1989a-e). A tabulation of the room temperature values is given in Table 7.2.

Table 7.2: Values of the coefficients used in the energy function (eq. 7.3) at 25°C, as a function of Zr:Ti ratio.

	Mole Fraction $PbTiO_3$ in PZT										
	0.0	0.1	0.2	0.3	0.4	0.5	0.6	0.7	0.8	0.9	1.0
T_C (°C)	231.5	256.5	300.6	334.4	364.3	392.6	418.4	440.2	459.1	477.1	492.1
$C(10^5$ °C)	2.027	2.050	2.083	2.153	2.424	4.247	2.664	1.881	1.642	1.547	1.500
$Q_{11}(10^{-2}$ m^4/C^2)	4.620	5.080	5.574	6.175	7.260	9.660	8.116	7.887	8.142	8.504	8.900
$Q_{12}(10^{-2}$ m^4/C^2)	-1.391	-1.540	-1.720	-1.997	-2.708	-4.600	-2.950	-2.480	-2.446	-2.507	-2.600
$Q_{44}(10^{-2}$ m^4/C^2)	4.664	4.900	5.165	5.522	6.293	9.190	6.710	6.356	6.417	6.569	6.750
α_1 (10^7 m/F) at 25 °C	-4.582	-6.376	-7.470	-8.116	-7.904	-4.887	-8.340	-12.47	-14.84	-16.17	-17.05
α_{11} (10^7 m^5/C^{2}F)	62.35	41.25	31.29	22.30	13.62	4.764	3.614	0.6458	-3.050	-5.845	-7.253
α_{12} (10^8m^5/C^{2}F)	-16.71	-4.222	-0.0345	1.688	2.391	1.735	3.233	5.109	6.320	7.063	7.500
$\zeta(10^8$m^5/C^{2}F)	-34.42	-0.2897	9.284	11.75	11.26	6.634	10.78	15.52	18.05	19.44	20.32
α_{111} (10^8 m^9/C^{4}F)	5.932	5.068	4.288	3.560	2.713	1.336	1.859	2.348	2.475	2.518	2.606
α_{112} (10^8 m^9/C^{4}F)	311.2	34.45	18.14	15.27	12.13	6.128	8.503	10.25	9.684	8.099	6.100
α_{123} (10^8 m^9/C^{4}F)	-104.1	-8.797	-7.545	-7.052	-5.690	-2.894	-4.063	-5.003	-4.901	-4.359	-3.660
$\zeta(10^9$m^9/C^{4}F)	84.41	13.39	4.627	3.176	2.402	1.183	1.596	1.851	1.652	1.256	0.7818

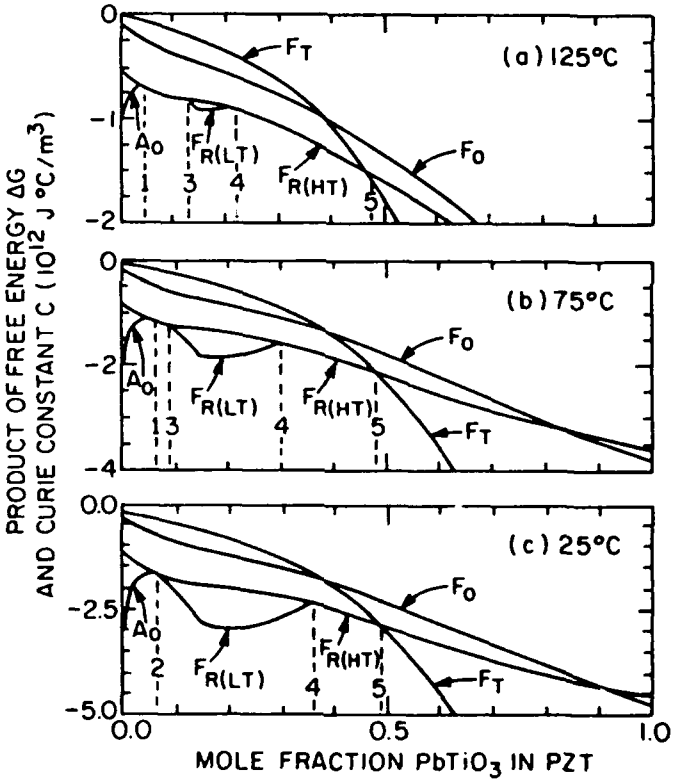

Figure 7.8: Calculated Free Energy profiles for each realizable phase as a function of Zr:Ti ratio at (a) 25°C, (b) 75°C, (c) 125°C.

7.3.7 Intrinsic Properties of PZT

Plots of the free energy vs. compositions, using the fitted parameters are given in Figure 7.8 for temperatures of 25°C, 75°C and 125°C. The resulting phase diagram deduced from the crossing points of the phase stability lines for the whole composition temperature field is given in Figure 7.9 and is shown to be in good agreement with the accepted phase diagram.

Indications of the capability to delineate single domain properties are given in Figure 7.10 for the susceptibility as a function of temperature in the PZT 60:40, and in the susceptibility as a function of composition at room temperature, given in Figure 7.11. Examples of the full family of elasto-dielectric properties which can be deduced are given in the original references.

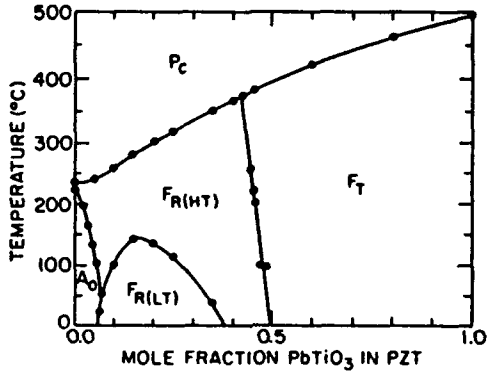

Figure 7.9: Comparison of calculated and measured phase diagram for PZT.

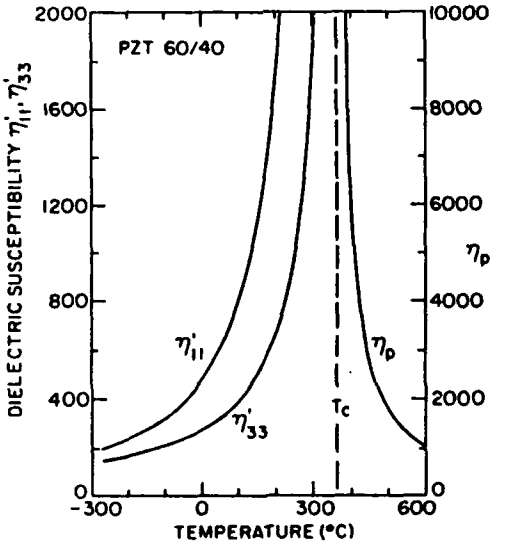

Figure 7.10: Single domain dielectric susceptibility calculated for a PZT 60:40 composition.

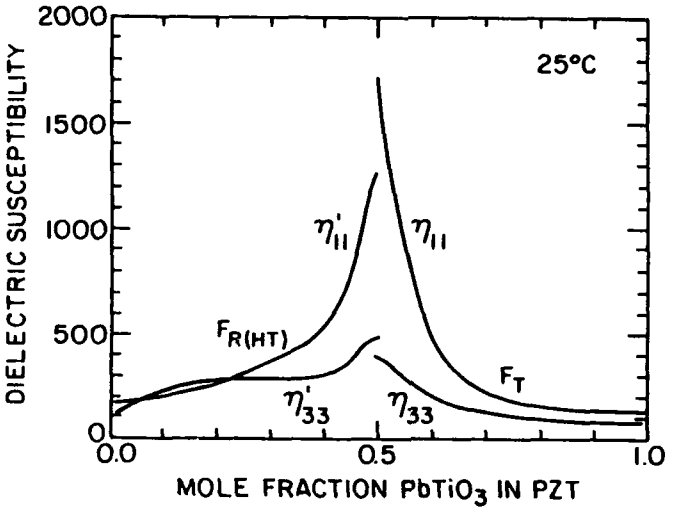

Figure 7.11: Dielectric susceptibility of single domain states as a function of Zr:Ti ratio.

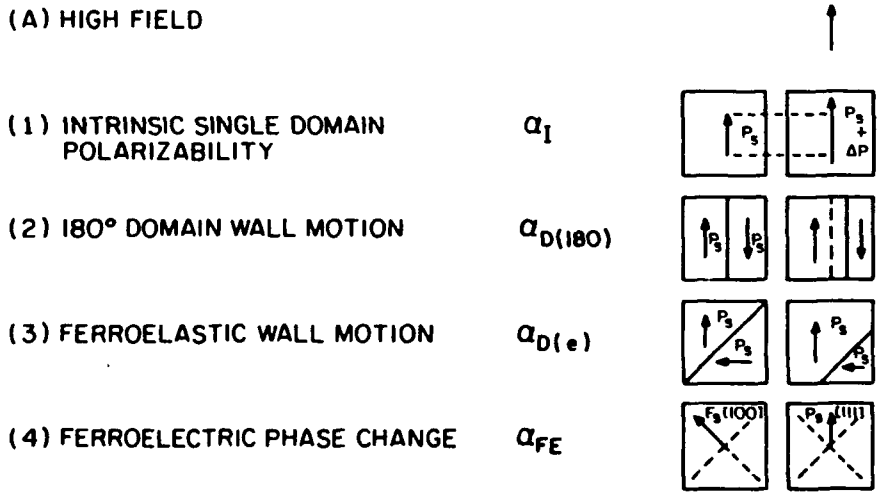

Figure 7.12: Possible mechanisms which can contribute to the dielectric polarizability in a ferroelectric PZT at the MPB composition.

7.4 Extrinsic Contributions to Response in PZT Type Piezoceramics

Even in the best poled PZT ceramic, because of the random orientation and the internal stresses generated by switching the large spontaneous strains during poling, the sample does not come to an ensemble of single domain grains. Thus in considering the polarizability of the ceramic in its ferroelectric phases, we must consider the extrinsic contributions due to changes in the polar domain structure and phase makeup brought about by the field. The type of changes occurring which could contribute to the polarizability are shown schematically in two dimensions in Figure 7.12.

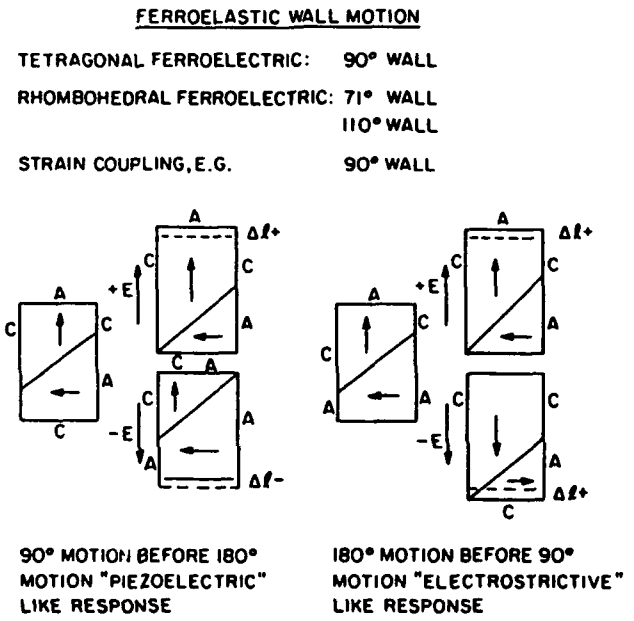

Figure 7.13: Shape changing effects of 180° pure ferroelectric and ferroelectric:ferroelastic domain wall motion, depicted in schematic two dimensional models.

For the piezoelectric response, only extrinsic actions which are shape changing will contribute so that simple 180° domain wall motion does not contribute, and is in fact deleterious to piezo response since it contributes polarization without any shape changes e.g.

$x_3 = Q_{11} P_3^2$, $x_1 = Q_{12} P_3^2$ and $\pm P_3$ give rise to identical strains x_3 and x_1

Non 180° wall motion, that is motion of 90° walls in the tetragonal phase, and motion of 71° and 110° walls in the rhombohedral phases will give rise to shape change, however, the nature of the shape change will depend on the relation between ferroelectric: ferroelastic wall motion and pure ferroelectric wall motion. From Figure 7.13, if 90° motion occurs before 180° motion the effective shape change reverses sign with the field, if however 180° motion precedes 90° wall motion the shape change does not reverse sign with the field and is effectively electrostrictive. A similar situation exists for phase boundary motion (Figure 7.14) where again the relation to pure ferroelectric 180° wall switching is quite critical.

It must be stressed that in all these considerations it is that component of wall motion which is reversible with the field and which persists down to almost zero field which is of important.

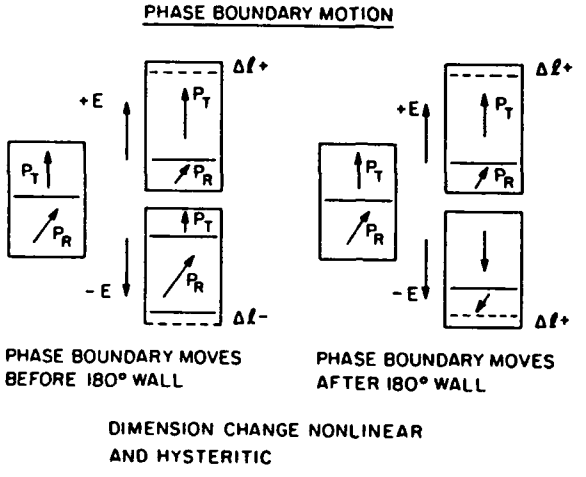

Figure 7.14: Shape changing effects of 180° pure ferroelectric domain motion and of phase boundary motion in a PZT ferroelectric at a composition near the MPB.

7.4.1 Control of Extrinsic Contributions to Response

During the course of many years of empirical development a wide range of low level additives (0-5 mole%) have been found to have a marked influence upon dielectric and piezoelectric properties in PZT compositions. In general, the aliovalent oxides fall into two distinct groups. Electron donor additions where the charge on the cation is larger than that which it replaces in the PZT structure and electron acceptor additives where the charge on the cation is smaller than that of the ion which it replaces (Table 7).

The donor additions enhance both dielectric and piezoelectric response at room temperature and under high fields show symmetrical unbiased hysteresis loops with good "squareness" and lower coercivity (Gerson and Jaffe, 1963; Gerson, 1960). The acceptor additives in general reduce both dielectric and piezoelectric responses, they give rise to highly asymmetric hysteresis

response, larger coercivity and higher electrical and mechanical Q. That the effects of the dopants are mostly upon the extrinsic components of response is expected from their marked influence on the hysteresis and is confirmed by the very low temperature behaviours (Figure 7.15). For the Navy type I to V the compositions range from a strongly donor doping (type V) to a strongly acceptor doping in type III but all are at the same Zr:Ti ratio. It may be noted that the very large difference in weak field permittivity (ε ~3000 $\rightarrow$ ε ~750) is completely lost at liquid helium temperature where all extrinsic contributions are frozen out, and that the data agree quite well with the intrinsic permittivity calculated from the average of the single domain values deduced from the thermodynamic theory for that composition and temperature.

LOWER LEVEL MODIFIERS (0 to 10 MOLE %)

'Donor' Additives	'Acceptor' Additives
Nb_2O_5 or $PbNb_2O_6$	Fe_2O_3
Ta_2O_5 or $PbTa_2O_6$	Al_2O_3
WO_3	Cr_2O_3
Bi_2O_3	MnO_2
Sb_2O_5	MgO
La_2O_3	NiO

V_3O_8

Other Low Level Additives:

Na_2O, K_2O, Ga_2O_3, In_2O_3, IrO_2, ThO_2

Figure 7.15: Common 'dopants' used in 'soft' donor doped and 'hard' 'acceptor' doped PZT compositions.

In the acceptor doped compositions there are very good explanations of how the domain structure (not the wall) is stabilized (Carl and Hardtl, 1978; Dederichs and Arlt, 1986; Pan et al., 1989). In essence the charged acceptor associates with an oxygen vacancy to produce a slowly mobile defect dipole. The vacancy is the only mobile defect in the perovskite at room temperature and the defect dipole orients by vacancy migration in the dipole field associated with the domain. Thus over time the existing domain structure (poled or unpoled) is stabilized and the walls are "stiffened." Bias phenomena in both poled and unpoled ceramics can be logically explained as can some facets of the aging behaviour and the time dependence of mechanical Q.

For donor doped samples, there are only "hand waving" arguments as to how or why the domain walls should become more mobile and indeed it is not clear whether the effects are from domain walls, phase boundaries, or are defect induced. Much more work is needed to determine the physics of the softening in these materials.

For valence conpensated additions the systems studied have included:

$Pb(Ni_{1/3}Nb_{2/3})O_3$:$PbTiO_3$:$PbZrO_3$
$Pb(Co_{1/3}Nb_{2/3})O_3$:$PbTiO_3$:$PbZrO_3$
$Pb(Mn_{1/3}Nb_{2/3})O_3$:$PbTiO_3$:$PbZrO_3$
$Pb(Cu_{1/3}Nb_{2/3})O_3$:$PbTiO_3$:$PbZrO_3$
$Pb(Mn_{1/3}Ta_{2/3})O_3$:$PbTiO_3$:$PbZrO_3$
$Pb(Zn_{1/3}Nb_{2/3})O_3$:$PbTiO_3$:$PbZrO_3$
$Pb(Ni_{1/3}Fe_{1/3}Nb_{1/3})O_3$:$PbTiO_3$:$PbZrO_3$

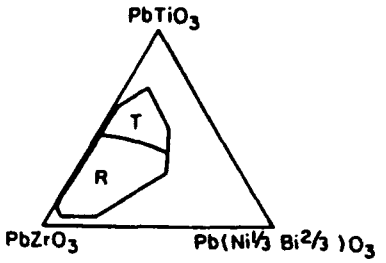

$Pb(Cu_{1/3}Nb_{2/3})O_3$:$PbTiO_3$
$Pb(Cd_{1/3}Nb_{2/3})O_3$:$PbTiO_3$
$Pb(Zn_{1/2}Te_{1/2})O_3$:$PbTiO_3$
$Pb(Mg_{1/2}Te_{1/2})O_3$:$PbTiO_3$

$Pb(Sb_{1/2}Nb_{1/2})O_3$:$PbTiO_3$:$PbZrO_3$
$Pb(Sn_{1/2}Nb_{1/2})O_3$:$PbTiO_3$:$PbZrO_3$
$Pb(Sb_{1/2}Nb_{1/2})O_3$:$PbTiO_3$
$Pb(Sn_{1/2}Nb_{1/2})O_3$:$PbTiO_3$

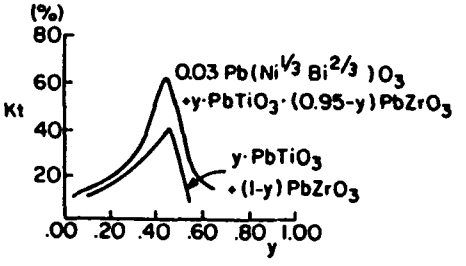

$Pb(Mg_{1/2}V_{1/2})O_3$:$PbTiO_3$:$PbZrO_3$
$Pb(Mn_{1/3}Sb_{2/3})O_3$:$PbTiO_3$:$PbZrO_3$
$Pb(Li_{1/4}Nb_{3/4})O_3$:$PbTiO_3$:$PbZrO_3$
$Pb(Sb_{1/2}Nb_{1/2})O_3$:$PbTiO_3$:$PbZrO_3$
$Pb(Fe_{1/2}Sb_{1/2})O_3$:$PbTiO_3$:$PbZrO_3$
$Pb(In_{1/2}Nb_{1/2})O_3$:$PbTiO_3$:$PbZrO_3$
$Pb(In_{1/2}Nb_{1/2})O_3$:$PbZrO_3$:$PbSnO_3$:$PbTiO_3$
$Pb(Mg_{1/2}V_{1/2})O_3$:$PbTiO_3$:$PbZrO_3$

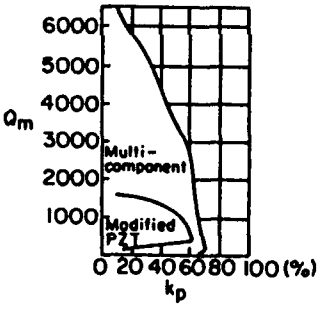

$(Ag_{1/2}Bi_{1/2})TiO_3$:$PbZrO_3$:$PbTiO_3$
$(Ag_{1/2}Bi_{1/2})ZrO_3$:$PbTiO_3$:$PbZrO_3$

Figure 7.16: Examples of systems using a relaxor additives to PZT.

A favorite pastime for empirical development has been the combination of PZTs with relaxor spin glass lead based compositions to produce improved "soft" high permittivity high coupling ceramics (Figure 7.16) and a vast range of compositions has been explored. In general the effect is to lower T_C, raise ε, raise k_t and k_p and d33. The typical ranges of advantage are given in 7.16. Usually the compositions used follow closely along the MPB into these 3 component phase diagrams.

7.5 Electrostrive Actuators

The poled ferroelectric domain structure of the normal piezoelectric PZT provides very useful actuators with field induced strain of order $1 \sim 2.10^{-3}$ at field levels of 10kV/cm. For systems which require a fiducial zero strain position however, aging and de-aging of the domain structure under high fields lead to uncomfortable changes of the zero field dimensions which are unacceptable in precise positioning applications.

For the electrostrictor (Figure 7.17) useful strain levels require very high levels of induced polarization i.e. high dielectric permittivity.

ELECTROSTRICTIVE ACTUATORS

Direct Electrical Control of shape (strain) in an Insulating solid.

Electrostriction.

$$x_{kl} = M_{ijkl} E_i E_j$$

$$\frac{\ell - \ell_o}{\ell_o} = M_{111} E_1^2$$

$$\boxed{x_{kl} = Q_{ijkl} P_i P_o}$$

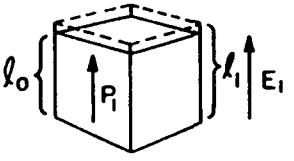

M values widely scattered in different insulators

Q values - much more limited range. Systematic change with elastic behavior.

Controlling dimensions in an electrostrictive requires control of polarization.

Figure 7.17: Actuation using the direct electrostrictive effect in a very high K ferroelectric type perovskite.

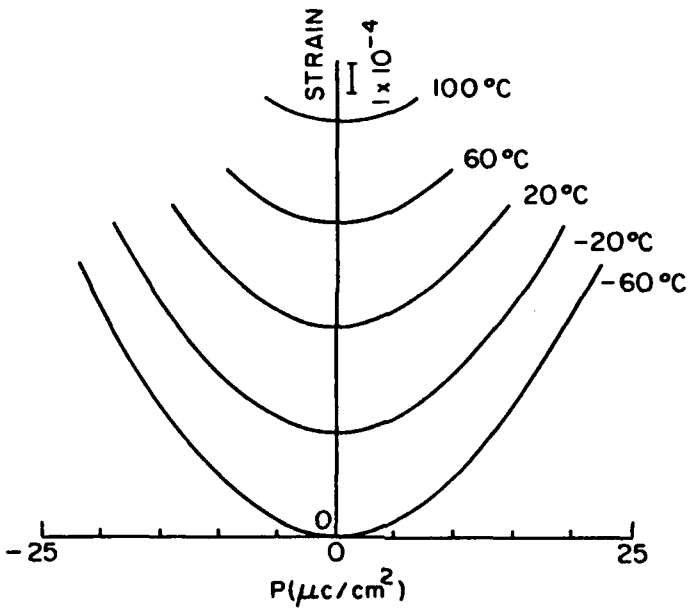

Figure 7.18: Typical polarization:strain curves in a PMN electrostriction actuator as a function of temperature.

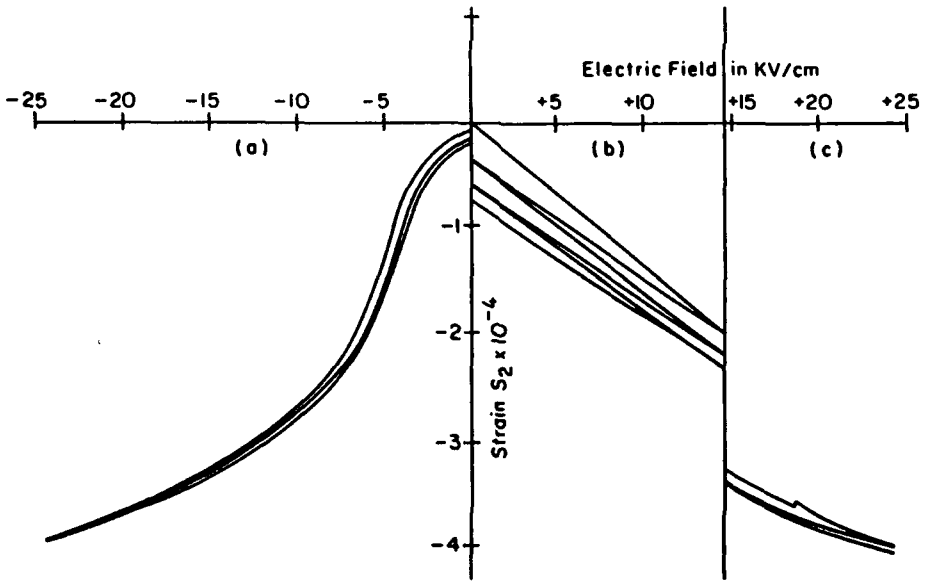

Figure 7.19: Contrasting the non linear but repeatable strain response in a PMN:PT relaxor with the walk-off in zero field strain which occurs in a PZT 8 formulation.

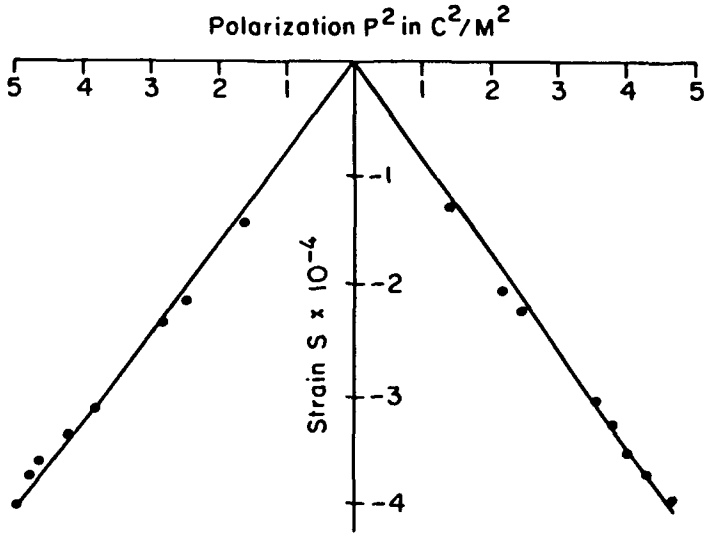

Figure 7.20: Quadratic electrostrictive response in a PMN:10%PT actuator composition.

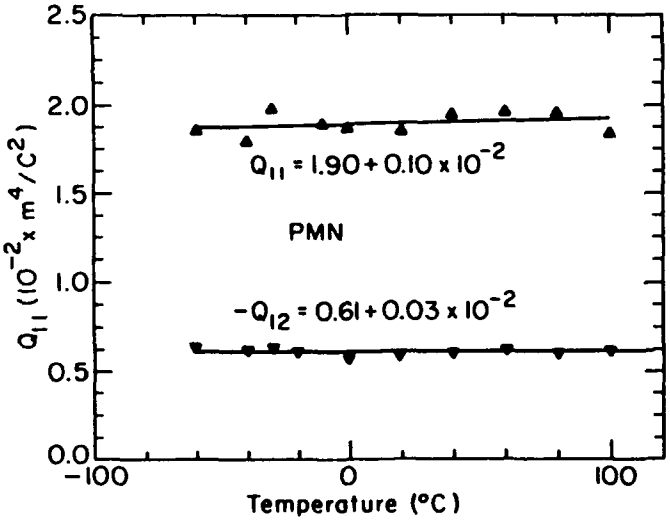

Figure 7.21: Electrostriction constants Q_{11} and Q_{12} vs. temperature in PMN:10% PT.

In the relaxor ferroelectric spin glass compositions like lead magnesium niobate (PMN), at temperatures above the freezing temperature large levels of polarization can be induced at realizable field levels and high quadratic levels of strain are possible (Figure 7.18). Reproducibility of the strain under cyclic E field is evident in Figure 7.19, and is compared to the "walk off" which occurs in a PZT8 due to de-aging. Figure 7.20 shows that the strain is truly quadratic when referenced to the polarization as would be expected in electrostrictors. It is interesting to note that the Q constants for PMN are essentially temperature independent over the range from 100 to -60°C (Figure 7.21). An unexpected bonus in the relaxors is that the steady accretion of polarization for temperatures below T_{Burns} leads to an expansion term of the form

$\Delta v \; \alpha(Q_{11} + 2Q_{12})P_{<111>}^2$

which tends to compensate for the normal thermal contraction. Thus over a range of temperatures near 20°C it is possible to mate PMN:10%PT with ULE glass so that dimension can be controlled electrically but do not drift thermally.

8 Piezoelectric Composites

Dielectric, piezoelectric and elastic properties of poled piezoelectric ceramics are tensor quantities and for many types of application it is possible to spell out a figure of merit for the material which often requires the enhancement of some of these tensor coefficients and the diminution of others.

A typical example is the requirement for sensing very weak hydrostatic pressure waves using large area sensors as in many Navy hydrophone needs (Figure 8.1). For hydrostatic pressure (Figure 8.2) the stress $X_{11} = X_{22} + X_{33} = -p$, so that the polarization change P_3 is given by

$$\begin{aligned} P3 &= d_{33}(-p) + d_{31}(-p) + d_{31}(-p) \\ &= (d_{33} + 2d_{31})(-p) \\ &= d_h(-p) \end{aligned}$$

where d_h is called the hydrostatic piezoelectric charge coefficient.

The voltage generated by the hydrophone, working into a very high impedance load will be give by

$$g_h = \frac{(d_3 + 2d_{31})}{\varepsilon_{33}}$$

and a figure of merit often used for hydrophone materials is the product $d_h g_h$

$$d_h g_h = \frac{(d_{33} + 2d_{31})^2}{\varepsilon_{33}} .$$

For high sensitivity PZTs, there is an unfortunate near cancellation such that

$d_{33} \simeq -2d_{31}$

so that $d_h << d_{33}$ or d_{31}, and PZT alone is not a good hydrophone materials.

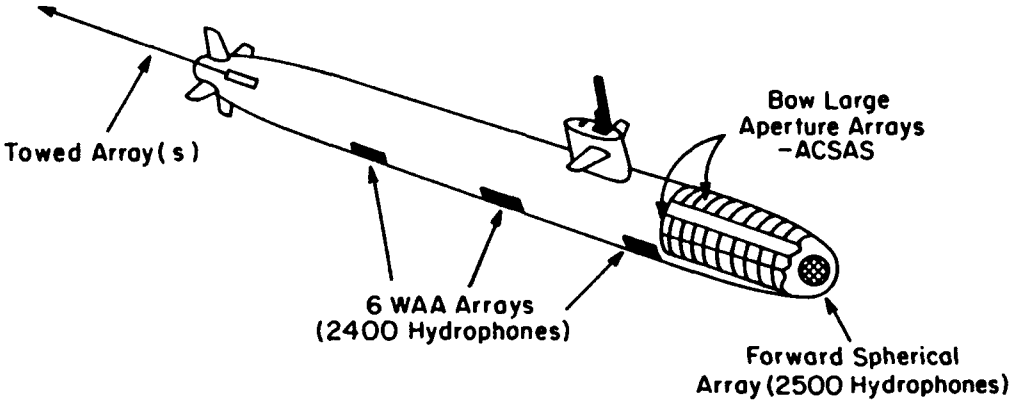

Figure 8.1: Examples of the need for large area hydrophone sensors in submarine acoustics.

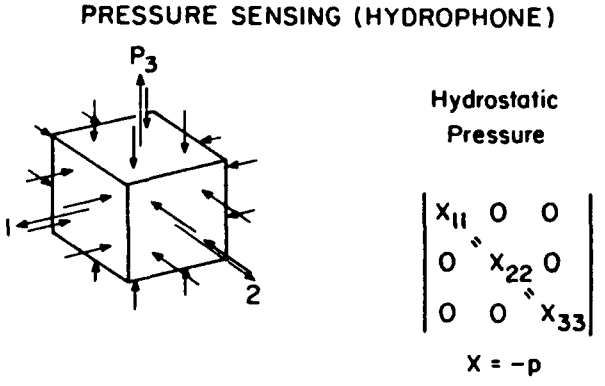

Figure 8.2: Stress system seen by the transducer under hydrostatic conditions.

In exploring composites for hydrophone applications it would be advantageous from the point of view of density and of flexibility to combine the ceramic with a dielectric polymer. Comparing the dielectric and elastic properties between two such phases, a fascinating juxtaposition is evident.

Dielectrically PZT is ultra soft (k ~ 3,000) whilst the polymer is quite stiff (k ~ 10) but in the elastic response, just the converse is true. The polymer is ultra soft (s_{11} ~ $30.10^{-11}M^2/N$) but the ceramic is very stiff (s_{11} ~ $2.10^{-11}M^2/N$) thus by careful control of the mode in which each phase is self-connected in the composite one can "steer" the fluxes and fields so as to enhance wanted coefficients and diminish unwanted coefficients so as to vastly improve the figure of merit.

Over some 12 years of intensive effort to design effective composites three important basic principles have emerged.

- Connectivity. The mode of self interconnection of the phases controls the fluxes and fields in the system enabling a tailoring of the tensor coefficients.
- Symmetry. Both the symmetry of the individual component phases and the macro symmetry of their arrangement in the composite can be used for additional control.
- Scale. The mode of averaging for the property coefficients depends upon the scale of the composite phases in relation to the wavelength of excitation. Unusual resonances can occur when λ and d are comparable.

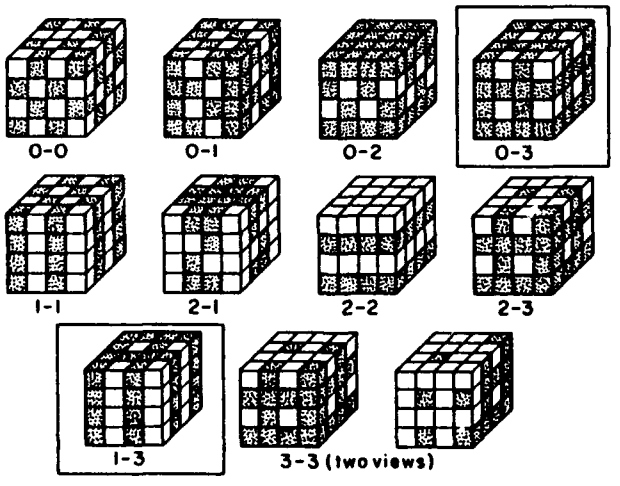

Figure 8.3: Simple 'cubes model' of connectivity patterns possible in a two phase piezoelectric ceramic polymer composite.

A major aid in thinking about the design of connectivity was the simple cubes model (Newnham et al., 1978) (Figure 8.3) and the associated notation, now internationally accepted

which describes the dimensionality of the connectivity for active and passive phases.

An indication of the many types of connectivities which have been used at Penn State for piezoceramic: polymer composites is shown in Figure 8.4 and a measure of the improvement in hydrophone figure of merit over pure PZT for some of these systems is shown in Figure 8.6.

The special case of the 1:2:3:0 composite which uses PZT rods in a foamed polymer matrix with transverse glass reinforcement is given in Figure 8.5.

For the 1:3 type composites a major impediment to evolution for large scale structures has been the problem of assembly. Recently Fiber Materials of Biddeford, Maine have applied their ultraloom technology originally evolved for thick section carbon:carbon composites to this problem. Using the ultraloom they are able to stitch PZT posts into a template structure which contains the transverse glass fiber reinforcement and make sections up to 4 feet in width and of almost any length.

The FMI composites are not only interesting for very large area hydrophones, but can also be used in an actuator mode. It is interesting to note that with only 5 vol% PZT and a resultant density of 2.2 gm/cm^3 the transverse coupling coefficient k_t at 0.70 is larger than that of solid PZT (Figure 8.7).

The 1:3 type concept has also been applied to transducers for medical ultrasonics (Shaulov, 1986; Gururaja et al., 1984; Smith, 1986). Here the required frequencies are much higher ~10MHz so that the scale is very much smaller and the rod structure can be cut from solid PZT (Figure 8.8). Beam characteristics, pulse shape and coupling factor are improved over solid PZT transducers.

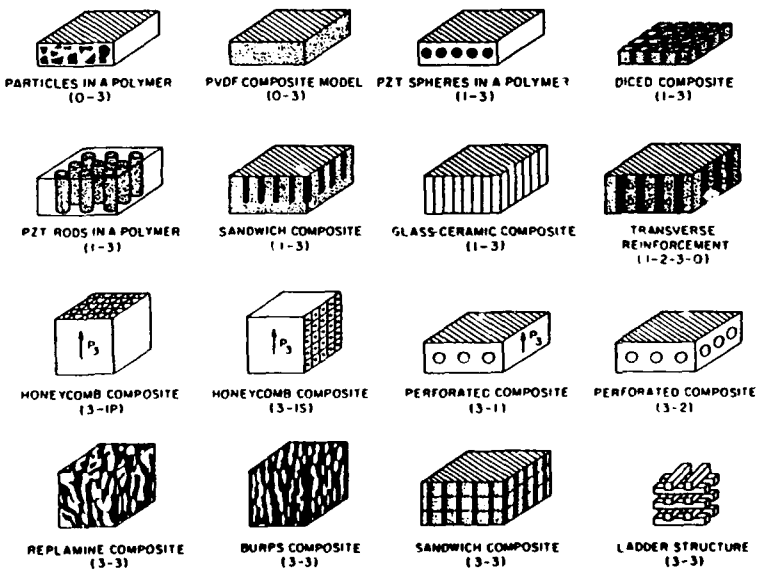

Figure 8.4: Examples of composite structures with different engineered connectivities.

TENSOR ENGINEERING IN ACTIVE COMPOSITES

NAVY HYDROPHONE

Up to 1975 Material lead zirconate titanate piezoelectric ceramic PZT

Power figure of merit $d_h g_h$

Product of hydrostatic voltage x hydrostatic charge

$d_h g_h$ in tensor form $\rightarrow \dfrac{(d_{333} + 2d_{311})^2}{\epsilon_{33}}$

$\boxed{d_h g_h \sim 100 \cdot 10^{-15}\ M^2/\text{Newton}}$ $\Longleftarrow$

PROBLEM $d_{333} \cong -2d_{311}$ ϵ_{33} very large

COMPOSITE SOLUTION

TRANSVERSE REINFORCEMENT
(1-2-3-0)

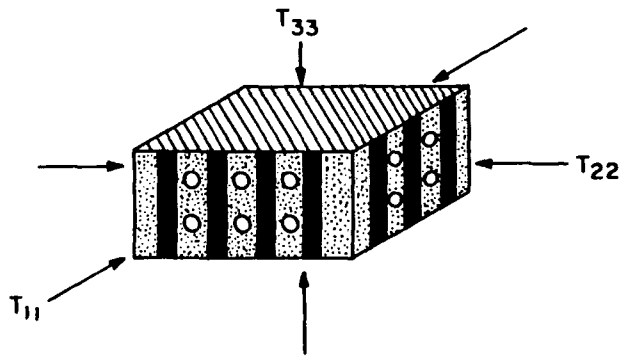

$$p = \begin{vmatrix} -T_{11} & 0 & 0 \\ 0 & -T_{22} & 0 \\ 0 & 0 & -T_{33} \end{vmatrix}$$

} Taken up on transverse reinforcement

— Enhanced on PZT
Polymer acts like a tent

ϵ_{33} much reduced by the polymer

Composite 10 v/o PZT 90% rubber

$\boxed{d_h g_h \cong 150{,}000 \cdot 10^{-15}\ M^2/\text{Newton}}$ $\Longleftarrow$

Figure 8.5: Figure of merit for a 1-2-3-0 transverse reinforced foamed polymer composite vs. performance of pure PZT.

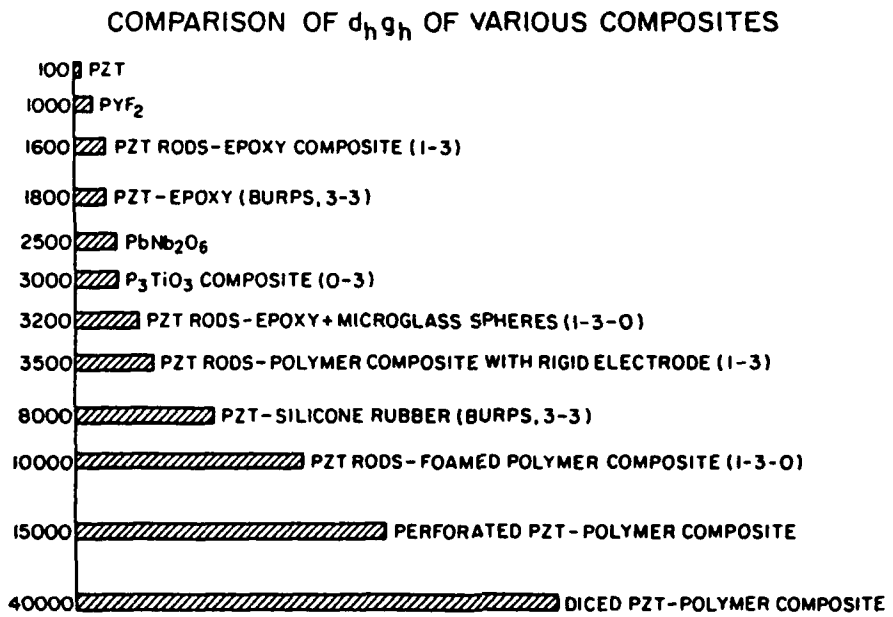

Figure 8.6: Hydrostatic figures of merit achieved using different connectivities.

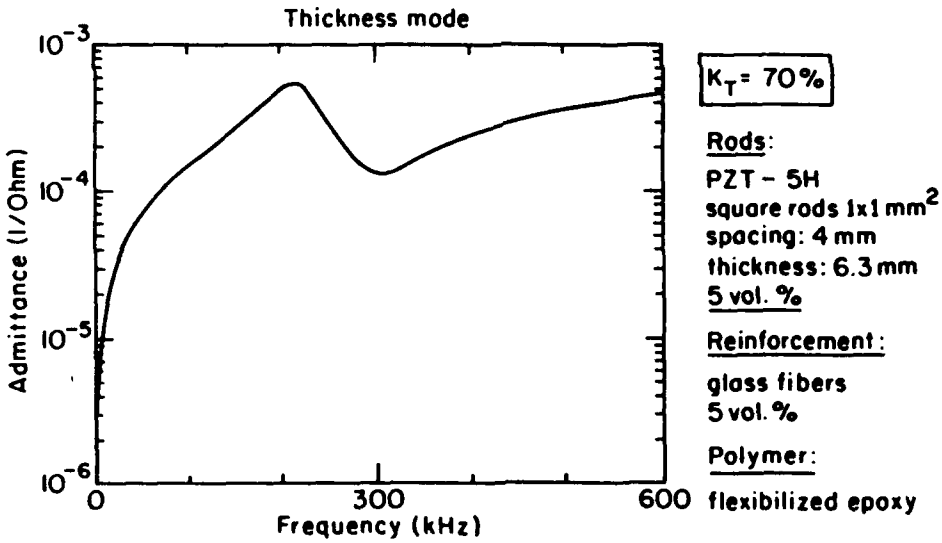

Figure 8.7: Thickness resonance curve for an FMI 1:3 composite containing 5 vol% of PZT rods.

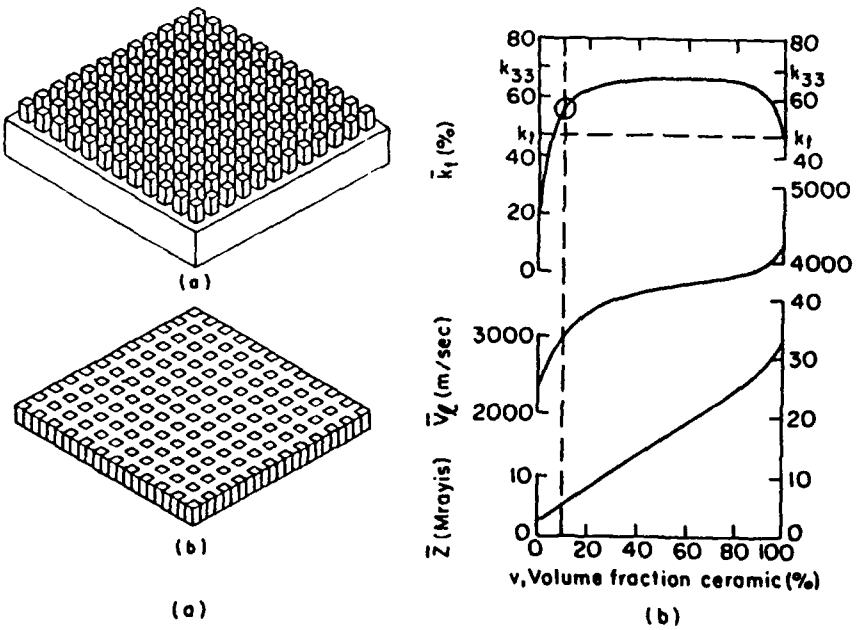

Figure 8.8: Piezoceramic:Polymer composites applied to electromedical transduction.
(a) The "dice and fill" method of construction.
(b) Transverse coupling k_t of the composite as a function of volume fraction PZT.

9 Piezoelectric Properties of Thin Films

In a perovskite structure ferroelectric in its tetragonal ferroelectric phase, symmetry 4mm, the non zero intrinsic piezoelectric constants of the single domain are:

$d_{31} = d_{32} = 2Q_{12}P_3\varepsilon_{33}$

$d_{33} = 2Q_{11}P_3\varepsilon_{33}$

$d_{15} = d_{24} = Q_{33}P_3\varepsilon_{11}$

where the Qij are the non zero electrostriction constants

P_3 is the spontaneous electric polarization.

ε_{ij} the components of the dielectric tensor.

For a bulk ceramic poled into conical symmetry (Curie group ∞ mm) we expect similar relations except that now the $\bar{Q}_{ij}$ are orientation averages, the P_3 is now P_r and ε_{33} is to be measured along the poling direction.

In the thin film it is probable that the Q constants are not significantly changed so that if we can achieve high values of P_r and of ε_{33} we might expect strong piezoelectricity. Initial measurements of the change of film thickness under field, using the Penn State MRL optical ultradilatometer (Zhang et al., 1988; Pan and Cross, 1989) show a clear piezoelectric effect (Figure 9.1). Measuring the slope of a sequence of strain: field curves like Figure 9.1 at different DC bias levels a maximum

d_{33} = 217 pC/N (is recorded in Figure 9.2).

For an undoped PZT of a similar 52/48 Zr:Ti composition

d_{33} = 223 pC/N .

To measure d_{31}, since the film is firmly bonded to a platinum film on the silicon substrate, it was necessary to use a monomorph bending mode excited in a thin silicon strip. Again the measured deflections yield a value for

d_{31} = -88.7 pC/N (Figure 9.3).

close to the value

d_{31} = -93.5 pC/N

quoted for the 52:48 Zr:Ti undoped composition.

Taking values for the elastic constants s_{11}^E, s_{33}^E, s_{12}^E similar to the bulk ceramic it is then possible to derive the piezoelectric coupling coefficients

K_{33} = 0.49

K_{31} = 0.22

K_p = 0.32.

As a preliminary exercise to explore the utility of the high piezoelectric constants and strong

electromechanical coupling for PZT films on silicon we have cooperated with MIT and Lincoln Labs to demonstrate a piezoelectric flexure wave micro-motor.

The concept is shown schematically in Figure 9.4. The silicon wafer is coated with a thick (2 μ meters) silicon oxynitride film, then etched from the back side to define a window 2.5 mm square. Titanium bonded platinum electrode is deposited upon the upper surface and a 4,500 Å 52:48 PZT sol gel film is spun on and processed on the upper surface.

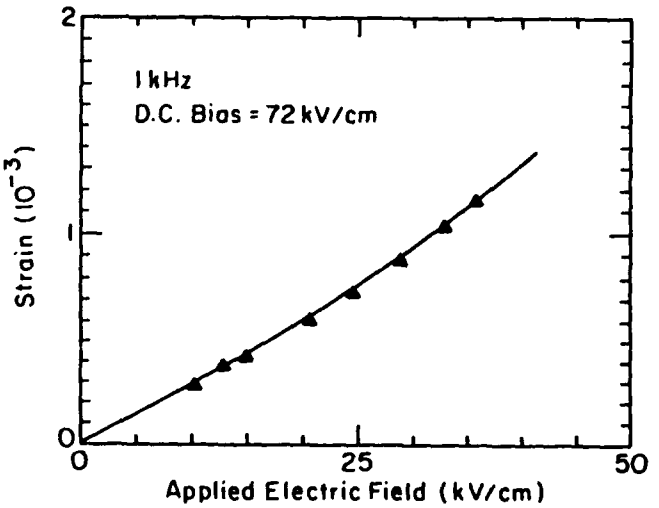

Figure 9.1: Thickness strain x3 measured as a function of applied DC field

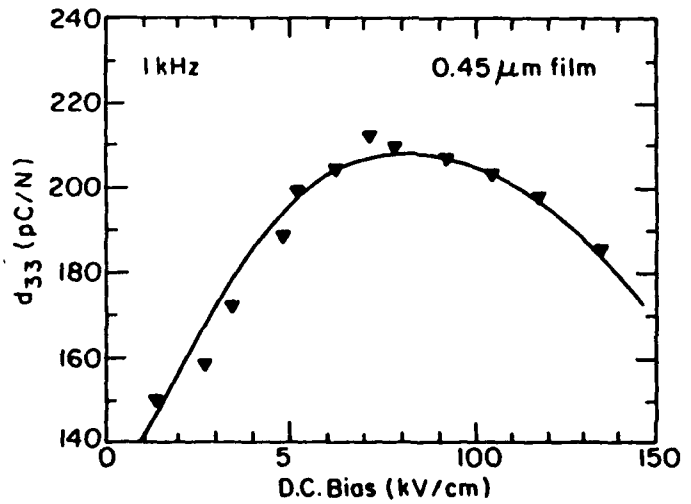

Figure 9.2: Piezoelectric constant d33 as deduced from a sequence of strain:field curves such as 9.1 under different static bias field levels.

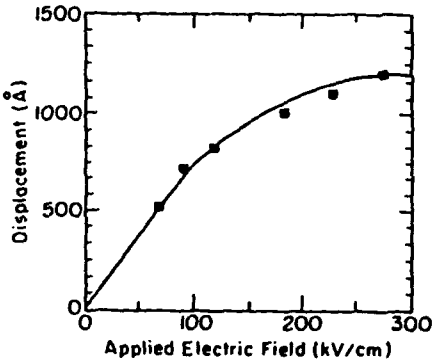

Figure 9.3: Strain measured from the flexure of a PZT 52/48 thin film monomorph on a silicon substrate.

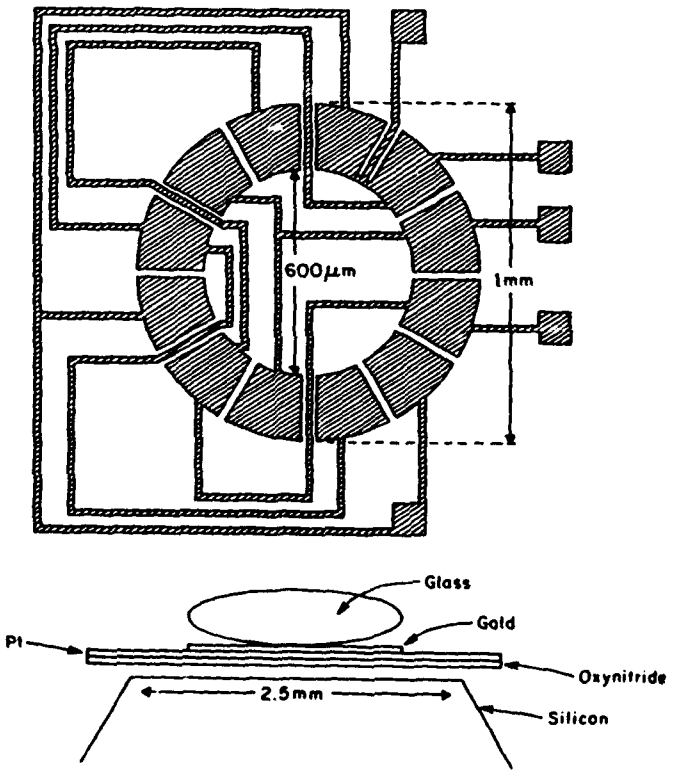

Figure 9.4: Schematic drawings of the electrode pattern for a PZT thin film micro-motor using a rotating flexure wave generated in a PZT film on a silicon oxynitride diaphragm. The rotating wave has been demonstrated to rotate a small (0.8 mm) glass lens at ~120 rpm.

The upper electrode pattern 1 mm in diameter is plated onto the upper surface of the PZT using a photo-resist technique.

To examine the surface flexure wave generated by sine:cosine fields applied to the electrodes a 0.8 mm diameter glass lens was centered on the electrode pattern. With a field of 2 volts applied it was possible to generate stable rotation of the lens at a speed ~ 120 rpm. The experiment was in the nature of a proof of concept, and the system is now being redesigned to better locate the pattern and to improve the electrode geometry and dielectric perfection.

From observation of the acceleration of the glass lens on switching on the fields, we project that torques of the order 10^{-9} Newton meters are realized even with this very primitive design. Such torques would not be unrealistic, given the high energy density and the strong coupling coefficient of the ferroelectric film.

References

Aizu, K., 1967: J. Phys. Soc. Jpn. **23**, 794.

Aizu, K., 1970: Phys. Rev. B **23**, 754.

Aizu, K., 1966: Phys. Rev. **146**, 423.

Aldrich, R. E., 1980: Ferroelectrics **27**, 19.

Alexandrov, K., 1976: Ferroelectrics **14**, 801.

Alexandrov, K., 1978: Ferroelectrics **20**, 61.

Alfness, R., 1986: Proc. ISAF 86, Lehigh University, 1.

Amin, A., and L. E. Cross, 1983: Ferroelectrics **50**, 237.

Amin, A., M. J. Haun, B. Badger, H. McKinstry and L. E. Cross, 1985: Ferroelectrics **65**, 107.

Arlt, G., D. Hennings and G. deWith, 1985: J. Appl. Phys. **58**, 1619.

Asadipour, P., 1986: *"Polarization Mechanisms in Relaxor Ferroelectrics"* MS Thesis, The Pennsylvania State University, May .

Axe, J. D., 1972: *Physics of Electronic Ceramics*, chapter 23. Marcel Decker, NY.

Buessem, W. R., L. E. Cross and A. K. Goswami, 1966: J. Am. Ceram. Soc. **49**, 33.

Carl, K., and K. H. Hardtl, 1978: Ferroelectrics **17**, 472.

Chen, J., 1991: "*Microstructure Property Relations in the Complex Perovskite Lead Maguesium Niobate*" PhD Thesis, Lehigh University.

Cross, L. E., and B. J. Nicholson, 1955: Phil. Mag. **46**, 452.

Cross, L. E., 1987: Ferroelectrics **76**, 241.

Cross. L. E., 1956: Phil. Mag ., Ser. 8 1, 76.

Cross. L. E., 1967: J. Phys. Soc. Japan **23**, 77.

Cummins, S. E., and L. E. Cross, 1967: Appl. Phys. Lett. **10**, 14.

Daniels, J., and K. H. Haerdtl, 1976: Philips Research Reports **31**, 489.

DeAlmedia, J., and D. Thouless, 1978: J. Phys. **A 11**, 983.

Dederichs, D., and G. Arlt, 1986: Ferroelectrics **68**, 281.

Devonshire, A. F., 1954: Adv. in Physics **3**, 85.

Devonshire, A. F., 1949: Phil. Mag. **740**, 1040.

Devonshire, A. F., 1951: Phil. Mag. **742**, 1065.

Dey, S. K., K. D. Budd and D. A. Payne, 1988: EEE Trans. UFFC **35**, 80.

Dey, S., 1991a: Private Communication.

Dey, S., 1991b: *Advance in Chemical Processing of Thin Films*, Arizona State University.

DiDomenico, Jr. M., and S. H. Wemple, 1969: J. Appl. Phys. **40**, 720.

Dudkevich, V. P., V. A. Bukreev, M. Mukhortov, I. Golovko, Yu G. Sindeev, M. Mukhortov, and G. Fesenko, 1981: Phys. Slat. Sol. **(a)65**, 463.

Fesenko, O. E., R. V. Kolesova and Yu G. Sindeyev, 1978: Ferroelectrics **20**, 177.

Galasso, F. S., 1969: *Structure, Properties and Preparation of Perovskite Type Compounds*, Pergamon Press, Oxford.

Gerson, R., and T. C. Marshall, 1959: J. Appl. Phys. **30**, 1650.

Gerson, R. J., 1960: Appl. Phys. **31**, 188.

Gerson, R., H. Jaffe., 1963: J. Phys. Chem. Solids **24**, 979

Glazer, M., 1975: Acta Cryst **B28**, 3384., 1972), ibid **A31**, 756.

Guenter, P., 1980: Ferroelectrics **24**, 35.

Gururaja, T. R., W. A. Schulz, L. E. Cross and R. E. Newnham, 1984: Proc. IEEE Ultrasonics Symp., 523.

Hagemann, H. J., D. Hennings and R. Wernicke, 1983: Philips Tech. Rev. **41** (3), 89.

Halemane, T. R., M. J. Haun, L. E. Cross and R. E. Newnham, 1985: Ferroelectrics **62**, 149.

Hanke, L., 1979: Seimens Forsch Ber. **8.4**, 209.

Harmer, M. P., A. Bhalla, B. Fox and L. E. Cross, 1984: Mat. Lett **2** (4A), 178.

Haun, M. J., E. Furman, H. A. McKinstry and L. E. Cross, 1989b: Ferroelectrics **99**, 27.

Haun, M. J., E. Furman, S. J. Jang and L. E. Cross, 1989a: Ferroelectrics **99**, 13.

Haun, M. J., E. Furman, S. J. Jang and L. E. Cross, 1989e: Ferroelectrics **99**, 55.

Haun, M. J., E. Furman, T. R. Halemane and L. E. Cross, 1989d: Ferroelectrics **99**, 55.

Haun, M. J., T. R. Halemane, R. E. Newnham and L. E. Cross, 1985: Japan J. Appl. Phys. **24**, 209.

Haun, M. J., Z. Q. Zhuang, E. Furman, S. J. Jang and L. E. Cross, 1989c: Ferroelectrics **99**, 45.

Herbert, J., 1985a: *Ceramic Dielectrics and Capacitors*, Electrocomponents Science Monographs, Vol 6, Gordon Breach, London.

Herbert, J., 1985b: *Ferroelectric Transducers and Sensors*, Electrocomponent Science Monographs ,Vol. 3. Gordon and Breach, London.

High Technology Ceramic News, 1990: **2**, 167.

Jaffe, H., and D. Berlincourt, 1965: Proc. IEEE **53**, 1372.

Jaffe, B., W. R. Cooke and H. Jaffe, 1971: *Piezoelectric Ceramics*, Figure 5.14. Academic Press, London.

Kato, J., Y. Yokotami, H. Kagata, H. Niwa, 1987: Jpn. J. Appl. Phys. **26**, 90.

Kazan, B., 1977: *Advances in Image Pickup and Display*, Academic Press, London.

Kinoshita, K., and A. Yamaji, 1976: J. Appl. Phys. **47**, 371.

Krupanidhi, S. B., M. Maffei, M. Sayer and K. ElAssad, 1983: J. Appl. Phys. **54**, 6601.

Landolt Bornstein, 1981: *Ferroelectrics Oxides*, New Series III, Vol. 16a. Springer Verlag, Berlin.

Levinson, L. M., 1988: *Electronic Ceramics*, Marcel Decker, NY.

Liu, T. S., 1976: Ferroelectrics **10**, 83.

Merz, W., 1953: Phys. Rev. **91**, 513.

Miyake, S., and R. Vedal, 1946: J. Phys. Soc. Jpn. **1**, 32.

Myers, E. R., and Angus I. Kingon, 1990: *Ferroelectric Thin Films*, Materials Research Symposium Proceedings, San Fransisco, **200**.

Newnham, R. E., D. P. Skinner and L. E. Cross, 1978: Mat. Res. Bull. **13**, 525.

Oliver, J. R., R. R. Neurgaonkar and L. E. Cross, 1989: J. Am. Ceram. Soc. **72**, 202.

Pan, W. Y., and L. E. Cross, 1989: Rev. Sci. Inst. **60** (8), 2701.

Pan, W. Y., C. Q. Dam, Q. M. Zhang and L. E. Cross, 1989: J. Appl. Phys. **66** (12), 6014.

Pan, W. Y., T. R. Shrout and L. E. Cross, 1989: J. Mat. Sci. Lett. **8**, 771.

Payne, D. A., and L. E. Cross, 1984: *Microstructure - Property Relations for Dielectric Ceramics II* , Science Press, Beijing.

Payne, D. A., 1973: "*The Role of Internal Boundaries Upon the Dielectric Properties of Polycrystalline Ferroelectric Materials*" PhD Thesis, The Pennsylvania State University.

Pohanka, R. C., R. W. Rice and B. E. Walker, 1976: Jr. J. Am. Ceram. Soc. **59**, 71.

Porter, S. G., 1981: Ferroelectrics **33**, 193.

Randall, C., D. Barker, R. Whatmore and P. Groves, 1987: Ferroelectrics **76**, 277.

Rosen, C. A., 1959: *Solid State Magnetic and Dielectric Devices*, chapter 5. John Wiley and Sons, NY.

Salvo, C. J., 1971: IEEE Trans Electron Devices, ED. 18, 748.

Schwarz, H., and A. Tourtellotte, 1969: J. Vac. Sci. Tech. **Vol. 6**, 373.

Shaulov, A. A., M. E. Rosar, W. A. Smith and B. M. Singer, 1986: Proc. ISAF 86, Leigh University, 231.

Shuvalov, L. A., 1970: J. Phys. Soc. Japan, 28 Suppl, 38.

Smith, W. A., 1986: Proc. ISAF 86, 249, Lehigh University.

Subbarao, E. C., 1962: J. Phys. Chem. Solids **23**, 665.

Tummala, R. R., and E. J. Rymaszewski, 1989: *Microelectronics Packaging Handbook*, Van Nostrand, Reinhold, NY.

Udayakumar, K. R. To be published.

VanderLinde, D., and A. M. Glass, 1975: Appl. Phys. **8**, 85.

Viehland, D., 1991a: "*The Glassy Polar Behaviour of Relaxor Ferroelectrics*" PhD Thesis, The Pennsylvania State University.

Viehland, D., S. J. Jang, L. E. Cross and M. Wuttig, 1991b: J. Appl. Phys. **68** (6), 2916.

Viehland, D., S. J. Jang, L. E. Cross and M. Wuttig, 1991c: J. Appl. Phys. **69** (1), 414.

Wainer, E., and S. Soloman, 1942: Titanium Alloy Manufacturing Co. Reports 8-9.

Wakino, K. *Early History of Barium Titanate Accessible through Murata Company*, Kyoto, Japan.

Watton, R., 1986: Proc. ISAF 86, Lehigh University, 172.

Whatmore, R. W., J. M. Herbert and F. W. Ainger, 1980 Phys. Status Solidi **A61**, 73.

Wul, B. M., and I. M. Goldman, 1945: Dokl Akad Nauk SSSR **46**, 154.

Yamaji, A., Y. Enomoto, K. Kinoshita and T. Murakami, 1977: J. Am. Ceram. Soc. **60**, 97.

Zhang, Z. M., W. Y. Pan and L. E. Cross, 1988: J. Appl. Phys. **63**, 2492.

L. Eric Cross, Evan Pugh Professor of Electrical Engineering, Materials Research Laboratory, The Pennsylvania State University, University Park, PA 16802-4801 USA.

RELAXOR FERROELECTRICS

APPENDIX 2

ADSORPTIVE SEPARATION. See ADSORPTION; ADSORPTION, GAS SEPARATION; ADSORPTION, LIQUID SEPARATION.

ADVANCED CERAMICS

ELECTRONIC CERAMICS

Electronic ceramics is a generic term describing a class of inorganic, nonmetallic materials utilized in the electronics industry. Although the term electronic ceramics, or electroceramics, includes amorphous glasses and single crystals, it generally pertains to polycrystalline inorganic solids comprised of randomly oriented crystallites (grains) intimately bonded together. This random orientation of small, micrometer-size crystals results in an isotropic ceramic possessing equivalent properties in all directions. The isotropic character can be modified during the sintering operation at high temperatures or upon cooling to room temperature by processing techniques such as hot pressing or poling in an electric or magnetic field (see CERAMICS AS ELECTRICAL MATERIALS).

The properties of electroceramics are related to their ceramic microstructure, ie, the grain size and shape, grain–grain orientation, and grain boundaries, as well as to the crystal structure, domain configuration, and electronic and defect structures. Electronic ceramics are often combined with metals and polymers to meet the requirements of a broad spectrum of high technology applications, computers, telecommunications, sensors (qv), and actuators. Roughly speaking, the multibillion dollar electronic ceramics market can be divided into six equal parts as shown in Figure 1. In addition to SiO_2-based optical fibers and

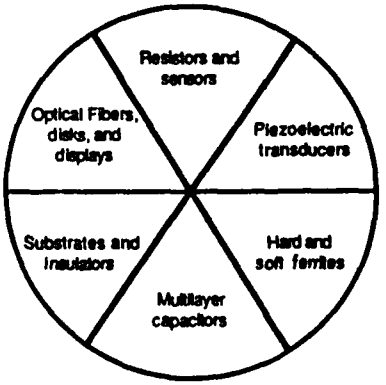

Fig. 1. Electronic ceramics market (1).

Table 1. Electronic Ceramic Functions and Products

Function	Material	Products[a]
insulators	porcelain, glass, steatite	high voltage insulation
packaging	Al_2O_3, BeO, AlN	IC substrates, packages (MMCs)
capacitors (energy storage)	$BaTiO_3$, $SrTiO_3$, TiO_2	multilayer and barrier layer capacitors
piezoelectrics	$Pb(Zr_{1-x}Ti_x)O_3$, SiO_2 *(quartz)*	vibrators, oscillators, filters, motors, and actuators
magnetics	$Mn_{1-x}Zn_xFe_2O_4$, $Ni_{1-x}Zn_xFe_2O_4$	inductors, transformers, memory devices
semiconductors	$(Ba,La)TiO_3$, V_2O_3, $Fe_{2-x}Ti_xO_3$, $ZnO–Bi_2O_3$, $MgCr_2O_4–TiO_2$, CdS, SiC	PTC, NTC-thermistors, varistors, pH sensor, humidity sensor, solar cells, electric heater
conductors	RuO_2, $NaAl_{11}O_{17}$, $Zr_{1-2x}Y_{2x}O_{2-x}$, $YBa_2Cu_3O_{7-\delta}$	resistors (thick film), solid electrolytes, oxygen sensors, superconductors

[a]MMC = multicomponent components; PTC = positive temperature coefficient; NTC = negative temperature coefficient.

displays, electronic ceramics encompass a wide range of materials and crystal structure families (see Table 1) used as insulators, capacitors, piezoelectrics (qv), magnetics, semiconductor sensors, conductors, and the recently discovered high temperature superconductors. The broad scope and importance of the electronic ceramics industry is exemplified in Figure 2, which schematically displays electroceramic components utilized in the automotive industry. Currently, the growth of the electronic ceramic industry is driven by the need for large-scale integrated circuitry giving rise to new developments in materials and processes. The development of multilayer packages for the microelectronics industry, composed of multifunctional three-dimensional ceramic arrays called monolithic ceramics (MMC), continues the miniaturization process begun several decades ago to provide a new generation of robust, inexpensive products.

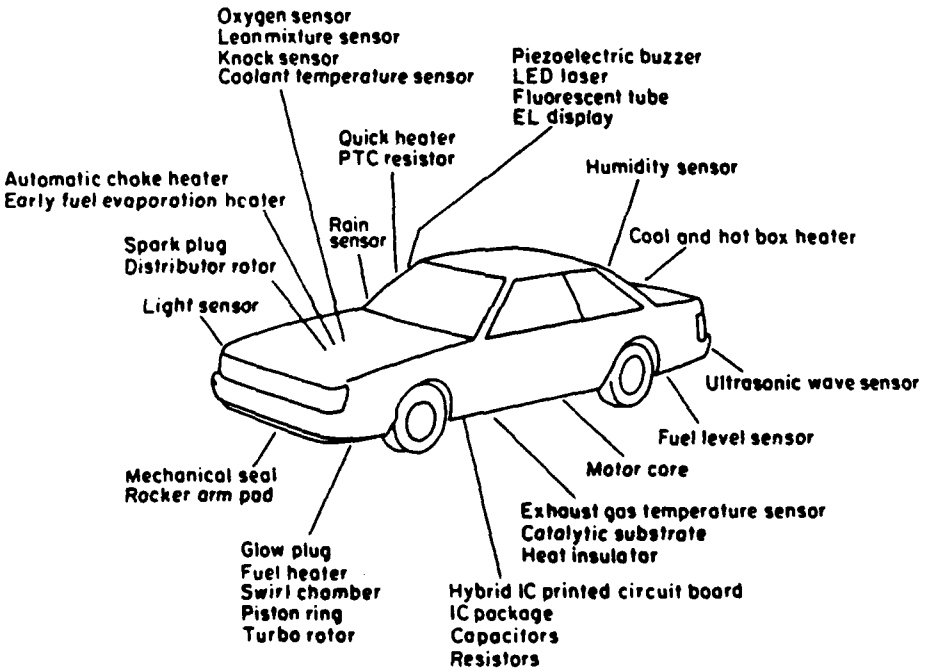

Fig. 2. Electronic ceramics for automotive applications. Courtesy of Nippon Denso, Inc.

Structure–Property Relations

An overview of the atomistic and electronic phenomena utilized in electroceramic technology is given in Figure 3. More detailed discussions of compositional families and structure–property relationships can be found in other articles. (See, for example, FERROELECTRICS, MAGNETIC MATERIALS, and SUPERCONDUCTING MATERIALS.)

Multilayer capacitors, piezoelectric transducers, and positive temperature coefficient (PTC) thermistors make use of the ferroelectric properties of barium

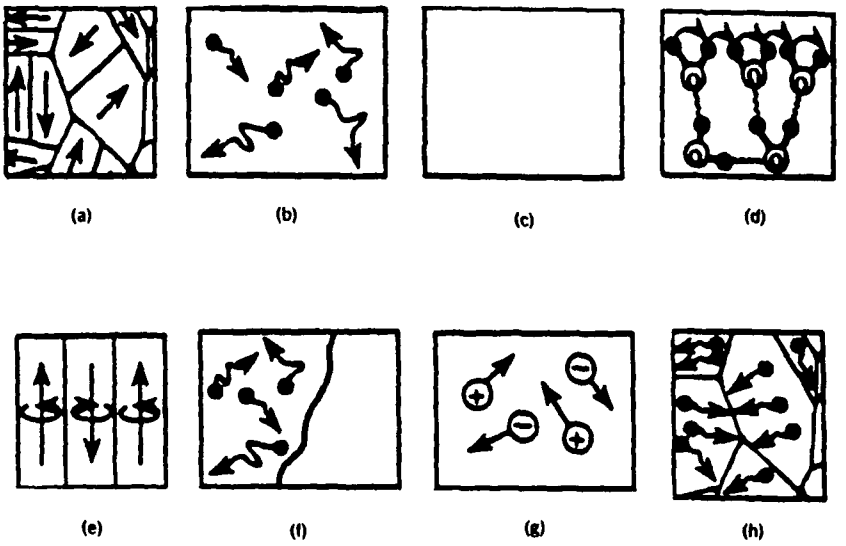

Fig. 3. An overview of atomistic mechanisms involved in electroceramic components and the corresponding uses: (**a**) ferroelectric domains: capacitors and piezoelectrics, PTC thermistors; (**b**) electronic conduction: NTC thermistor; (**c**) insulators and substrates; (**d**) surface conduction: humidity sensors; (**e**) ferrimagnetic domains: ferrite hard and soft magnets, magnetic tape; (**f**) metal–semiconductor transition: critical temperature NTC thermistor; (**g**) ionic conduction: gas sensors and batteries; and (**h**) grain boundary phenomena: varistors, boundary layer capacitors, PTC thermistors.

titanate (IV) [*12047-27-7*], $BaTiO_3$, and lead zirconate titanate [*12626-81-2*]. On cooling from high temperature, these ceramics undergo phase transformations to polar structures having complex domain patterns. Large peaks in the dielectric constant accompany the phase transitions where the electric dipole moments are especially responsive to electric fields. As a result, modified compositions of barium titanate (qv), $BaTiO_3$, are widely used in the multilayer capacitor industry and most piezoelectric transducers are made from lead zirconate titanate, $PbZr_{1-x}Ti_xO_3$, (PZT) ceramics. Applying a large dc field (poling) aligns the domains and makes the ceramic piezoelectric. The designation PZT is a registered trademark of Vernitron, Inc.

Similar domain phenomena are observed in ferrimagnetic oxide ceramics such as manganese ferrite [*12063-10-4*], $MnFe_2O_4$, and $BaFe_{11}O_{17}$, but the underlying mechanism is different. The unpaired spins of Fe^{3+} and Mn^{2+} ions give rise to magnetic dipole moments which interact via neighboring oxygen ions through a super-exchange mechanism. The magnetic dipoles are randomly oriented in the high temperature paramagnetic state, but on cooling through the Curie temperature, T_C, align to form magnetic domains within the ceramic grains. The peak in the magnetic permeability at T_C is analogous to the peak in the dielectric constant of ferroelectric ceramics. Domain walls move easily in soft ferrites (qv) like $MnFe_2O_4$ and γ-Fe_2O_3, which are used in transformers and magnetic tape. In barium ferrite [*11138-11-7*], the spins are firmly locked to the hexagonal axis, making it useful as a permanent magnet.

Several kinds of conduction mechanisms are operative in ceramic thermistors, resistors, varistors, and chemical sensors. Negative temperature coefficient (NTC) thermistors make use of the semiconducting properties of heavily doped transition metal oxides such as *n*-type $Fe_{2-x}Ti_xO_3$ and *p*-type $Ni_{1-x}Li_xO$. Thick film resistors are also made from transition-metal oxide solid solutions. Glass-bonded $Bi_{2-2x}Pb_{2x}Ru_2O_{7-x}$ having the pyrochlore [*12174-36-6*] structure is typical.

Phase transitions are involved in critical temperature thermistors. Vanadium , VO_2, and vanadium trioxide [*1314-34-7*], V_2O_3, have semiconductor–metal transitions in which the conductivity decreases by several orders of magnitude on cooling. Electronic phase transitions are also observed in superconducting ceramics like $YBa_2Cu_3O_{7-x}$, but here the conductivity increases sharply on cooling through the phase transition.

Ionic conductivity is used in oxygen sensors and in batteries (qv). Stabilized zirconia, $Zr_{1-x}Ca_xO_{2-x}$, has a very large number of oxygen vacancies and very high O^{2-} conductivity. β-Alumina [*12005-48-0*], $NaAl_{11}O_{17}$, is an excellent cation conductor because of the high mobility of Na^+ ions. Ceramics of β-alumina are used as the electrolyte in sodium–sulfur batteries.

Surface conduction is monitored in most humidity sensors through the use of porous ceramics of $MgCr_2O_4$–TiO_2 that adsorb water molecules which then dissociate and lower the electrical resistivity.

Grain boundary phenomena are involved in varistors, boundary layer capacitors, and PTC thermistors. The formation of thin insulating layers between conducting grains is crucial to the operation of all three components. The reversible electric breakdown in varistors has been traced to quantum mechanical tunneling through the thin insulating barriers. In a $BaTiO_3$–PTC thermistor, the electric polarization associated with the ferroelectric phase transition neutralizes the insulating barriers, causing the ceramic to lose much of its resistance below T_C. Boundary layer capacitors have somewhat thicker barriers which cannot be surmounted, and hence the ceramic remains an insulator. However, the movement of charges within the conducting ceramic grains raises the dielectric constant and increases the capacitance.

Lastly, the importance of electroceramic substrates and insulators should not be overlooked. Here one strives to raise the breakdown strength by eliminating the interesting conduction mechanisms just described. Spark plugs, high voltage insulators, and electronic substrates and packages are made from ceramics like alumina, mullite [*55964-99-3*], and porcelain [*1332-58-7*].

Electroceramic Processing

Fabrication technologies for all electronic ceramic materials have the same basic process steps, regardless of the application: powder preparation, powder processing, green forming, and densification.

Powder Preparation. The goal in powder preparation is to achieve a ceramic powder which yields a product satisfying specified performance standards. Examples of the most important powder preparation methods for electronic ceramics include mixing/calcination, coprecipitation from solvents, hydro-

thermal processing, and metal organic decomposition. The trend in powder synthesis is toward powders having particle sizes less than 1 μm and little or no hard agglomerates for enhanced reactivity and uniformity. Examples of the four basic methods are presented in Table 2 for the preparation of $BaTiO_3$ powder. Reviews of these synthesis techniques can be found in the literature (2,5).

The mixing of components followed by calcination to the desired phase(s) and then milling is the most widely used powder preparation method (2). Mixing/calcination is straightforward, and in general, the most cost effective use of capital equipment. However, the high temperature calcination produces an agglomerated powder which requires milling. Contamination from grinding media and mill lining in the milling step can create defects in the manufactured product in the form of poorly sintered inclusions or undesirable compositional modification. Furthermore, it is difficult to achieve the desired homogeneity, stoichiometry, and phases for ceramics of complex composition.

Coprecipitation is a chemical technique in which compounds are precipitated from a precursor solution by the addition of a precipitating agent, for example, a hydroxide (5). The metal salt is then calcined to the desired phase. The advantage of this technique over mixing/calcination techniques is that more intimate mixing of the desired elements is easily achieved, thus allowing lower calcination temperatures. Limitations are that the calcination step may once again result in agglomeration of fine powder and the need for milling. An additional problem is that the ions used to provide the soluble salts (eg, chloride from metal chlorides) may linger in the powder after calcination, affecting the properties in the sintered material.

Hydrothermal processing uses hot (above 100°C) water under pressure to produce crystalline oxides (6). This technique has been widely used in the formation process of Al_2O_3 (Bayer Process), but not yet for other electronic powders. The situation is expected to change, however. The major advantage of the hydrothermal technique is that crystalline powders of the desired stoichiometry and phases can be prepared at temperatures significantly below those required for calcination. Another advantage is that the solution phase can be used to keep the particles separated and thus minimize agglomeration. The major limitation of hydrothermal processing is the need for the feedstocks to react in a closed system to maintain pressure and prevent boiling of the solution.

Metal organic decomposition (MOD) is a synthesis technique in which metal-containing organic chemicals react with water in a nonaqueous solvent to produce a metal hydroxide or hydrous oxide, or in special cases, an anhydrous metal oxide (7). MOD techniques can also be used to prepare nonoxide powders (8,9). Powders may require calcination to obtain the desired phase. A major advantage of the MOD method is the control over purity and stoichiometry that can be achieved. Two limitations are atmosphere control (if required) and expense of the chemicals. However, the cost of metal organic chemicals is decreasing with greater use of MOD techniques.

Powder Processing. A basic guideline of powder manufacturing is to do as little processing as possible to achieve the targeted performance standards (see POWDERS, HANDLING). Ceramic powder fabrication is an iterative process during which undesirable contaminants and defects can enter into the material at any stage. Therefore, it is best to keep the powder processing scheme as simple as

Table 2. Methods Used to Prepare $BaTiO_3$ Electronic Ceramic Powders

Method	Reaction	Particle size
mixing/calcination[a]	$BaCO_3 + TiO_2 \xrightarrow{\Delta T} BaTiO_3 + CO_2\uparrow$	1 μm to 100s of μm
coprecipitation[b]	$Ba^{2+} + TiO^{2+} + 2\,C_2O_4^{2-} \xrightarrow{H_2O} BaTi(C_2O_4)_2{\cdot}4H_2O \xrightarrow{\Delta T}$ $BaTiO_3 + 4\,H_2O\uparrow + 4\,CO_2\uparrow$	if calcined, mean size of $\approx$0.5 μm after milling
hydrothermal[c]	$Ba^{2+} + TiO_2 + H_2O \xrightarrow[\Delta T, P]{OH^-} BaTiO_3 + 2\,H_2O$	nanosize to 50 μm
metal organic decomposition[c]	$Ba(i\text{-}OC_3H_7)_2 + Ti(OC_4H_9)_4 + 3\,H_2O \rightarrow BaTiO_3 + 2\,C_3H_7OH + 4\,C_4H_9OH$	5.0–35.0 nm, depending upon calcination conditions

[a]Ref. 2.
[b]Ref. 3.
[c]Ref. 4.

possible to maintain flexibility. Uncontrollable factors such as changes in the characteristics of as-received powders must be accommodated in the processing from batch to batch of material. Keeping the processing simple is not always possible: the more complex the material system, the more complex the processing requirements.

A fundamental requirement in powder processing is characterization of the as-received powders (10–12). Many powder suppliers provide information on tap and pour densities, particle size distributions, specific surface areas, and chemical analyses. Characterization data provided by suppliers should be checked and further augmented where possible with in-house characterization. Uniaxial characterization compaction behavior, in particular, is easily measured and provides data on the nature of the agglomerates in a powder (13,14).

Milling is required for most powders, either to reduce particle size or to aid in the mixing of component powders (15). Commonly employed types of comminution include ball milling, and vibratory, attrition, and jet milling, each possessing advantages and limitations for a particular application. For example, ball milling is well-suited to powder mixing but is rather inefficient for comminution.

Green Forming. Green forming is one of the most critical steps in the fabrication of electronic ceramics. The choice of green forming technique depends on the ultimate geometry required for a specific application. There are many different ways to form green ceramics, several of which are summarized in Table 3. Multilayer capacitors require preparation and stacking of two-dimensional ceramic sheets to obtain a large capacitance in a small volume. Techniques used to prepare two-dimensional sheets of green ceramic, including tape casting, (16–22) are discussed later under processing of multilayer ceramics. Manufacturing methods for ceramic capacitors have been reviewed (23).

Table 3. Green Forming Procedures for Electronic Ceramics

Green forming method	Geometries	Applications
uniaxial pressing	disks, toroids, plates	disk capacitors, piezo transducers, magnets
cold isostatic pressing	complex and simple	spark plugs, ZrO_2–O_2 sensors
colloidal casting	complex shapes	crucibles, porcelain insulators
extrusion	thin sheets (>80 μm), rods, tubes, honeycomb substrates	substrates, thermocouple insulator, catalytic converters, PTC thermistor heaters
injection molding	small complex shapes (<1.0 cm)	ZrO_2–O_2 sensors

Uniaxial pressing is the method most widely used to impart shape to ceramic powders (24). Binders, lubricants, and other additives are often incorporated into ceramic powders prior to pressing to provide strength and assist in particle compaction (25). Simple geometries such as rectangular substrates for integrated circuit (IC) packages can be made by uniaxial pressing (see INTEGRATED CIRCUITS).

More complex shapes can be made by cold isostatic pressing (CIP). CIP uses deformable rubber molds of the required shape to contain the powder. The application of isostatic pressure to the mold suspended in a pressure transfer media, such as oil, compacts the powder. CIP is not as easily automated as uniaxial pressing, but has found wide application in the preparation of more complex shapes such as spark plug insulators (26).

Slip or colloidal casting has been used to make complex shapes in the whiteware industry for many years (24). Other work has shown that colloidal casting can be used to produce electronic ceramic materials having outstanding strength because hard agglomerates can be eliminated in the suspension processing (27–29). Colloidal casting uses a porous mold in which the fine particles in a colloidal suspension accumulate because of capillary forces at the wall surface of the mold. Relatively dense packing of the particles, to approximately 60% of theoretical density, can be achieved. More importantly, hard aggregates can be eliminated from the colloid by suitable powder selection and processing. Drying of the resulting material may not be trivial and sections greater than about ~1.25 cm thick are sometimes difficult to obtain.

In addition to being the preferred forming technique for ceramic rods and tubes, extrusion processes are used to fabricate the thick green sheets used in many electronic components (24,30,31). The smallest thickness for green sheets prepared by extrusion techniques is about 80 μm. Organic additives similar to those used in tape casting are employed to form a high viscosity plastic mass that retains its shape when extruded. The extrusion apparatus, schematically shown in Figure 4, consists of a hopper for introduction of the plasticized mass, a deairing chamber, and either a screw-type or plunger-type transport barrel in which the pressure is generated for passage of the plastic mass through a die of the desired geometry. The plastic mass is extruded onto a carrier belt and passed through dryers to relax the plastic strain remaining after extrusion. The green sheet can be stamped or machine diced to form disks, wafers, or other platelike shapes.

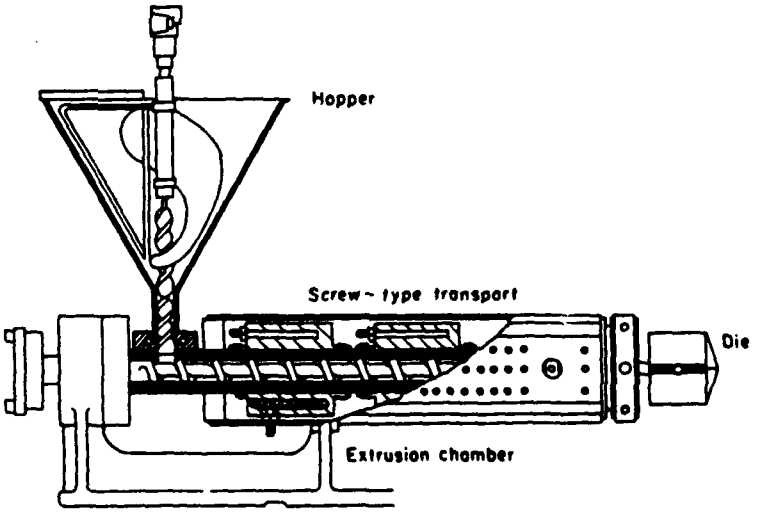

Fig. 4. Schematic of extrusion type apparatus for green sheet fabrication.

Injection molding is particularly suited to mass production of small complex shapes with relatively small (< 1.0 cm) cross sections (32–34). Powders are mixed using thermoplastic polymers and other organic additives. A molten mass composed of the ceramic and a thermoplastic binder system are injected via a heated extruder into a cooled mold of desired shape. The organic is burned out and the ceramic consolidated. Machining fragments from the green ceramic can be recycled because the thermoplastic polymers can be reversibly heated. Molds can be relatively expensive so injection molding is best suited to the preparation of a large number of single parts. Because of the high organic content required, organic removal is not trivial. Green sections greater than 1.0 cm thick require slow heating rates during burnout to avoid bloating and delamination of the green ceramic.

Densification. Densification generally requires high temperatures to eliminate the porosity in green ceramics. Techniques include pressureless sintering, hot-pressing, and hot isostatic pressing (HIP). Pressureless sintering is the most widely used because of ease of operation and economics. Hot-pressing is limited to relatively simple shapes whereas more complex shapes can be consolidated using HIP (35). Sintering is used for most oxide electronic ceramics. Hot-pressing and HIP, which employ pressure and high temperatures, are used to consolidate ceramics in which dislocation motion (leading to pore elimination) is sluggish. Both techniques are particularly useful for nonoxide materials such as silicon nitride [*12033-89-5*] and silicon carbide [*409-21-2*] (35,36) (see CARBIDES; NITRIDES).

Special precautions are often used in the sintering of electronic ceramics. Heating rates and hold times at maximum temperature are critical to microstructural development and grain size control. Sintering cycles may include intermediate temperature annealing or controlled cooling to relieve residual strains or avoid deleterious phase transformations. Atmosphere control may be important to prevent loss of volatile components or avoid reduction reactions. In continuous production, sequential burnout (organics) and sintering may take place in the same furnace, requiring complex temperature cycles even for relatively simple devices. Complex devices such as thick film circuits and monolithic multicomponent ceramics may require many sequential fabrication and sintering steps.

Processing of Multilayer Ceramics

Rapid advances in integrated circuit technology have led to improved processing and manufacturing of multilayer ceramics (MLC) especially for capacitors and microelectronic packages. The increased reliability has been the result of an enormous amount of research aimed at understanding the various microstructural–property relationships involved in the overall MLC manufacturing process. This includes powder processing, thin sheet formation, metallurgical interactions, and testing.

Presently, multilayer capacitors and packaging make up more than half the electronic ceramics market. For multilayer capacitors, more than 20 billion units are manufactured a year, outnumbering by far any other electronic ceramic component. Multilayer ceramics and hybrid packages consist of alternating layers of dielectric and metal electrodes, as shown in Figures 5 and 6, respectively.

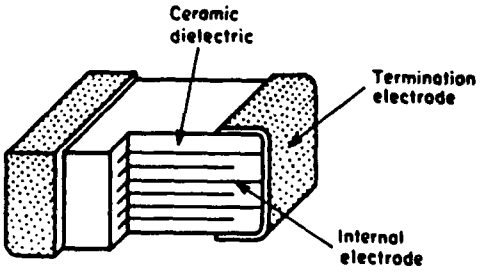

Fig. 5. Schematic cross section of a conventional MLC capacitor.

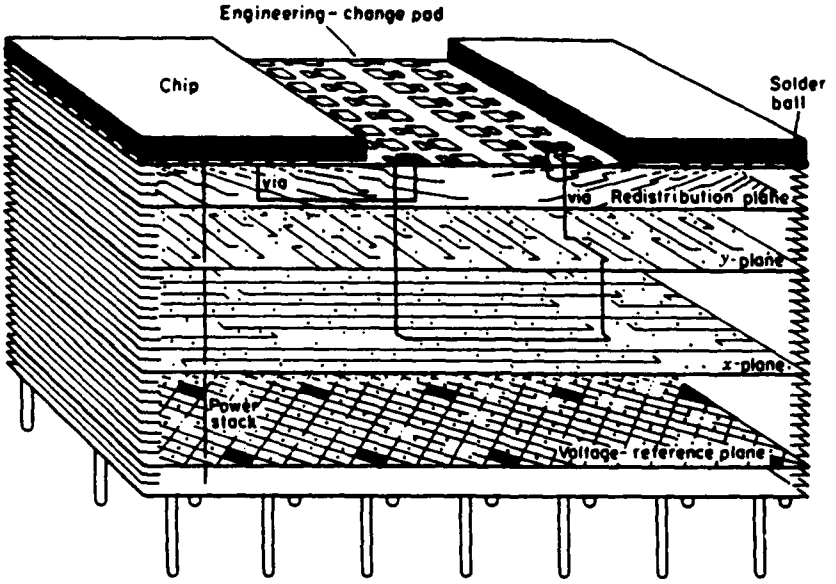

Fig. 6. Schematic of a MLC substrate for microelectronic packaging (37).

The driving force for these compact configurations is miniaturization. For capacitors, the capacitance (C) measured in units of farads, F, is

$$C = \frac{\epsilon_0 AK}{t}$$

where K is the dielectric constant (unitless); ϵ_0 the permittivity of free space = 8.85×10^{-12} F/m; A the electrode area, m^2; and t the thickness of dielectric layer, m. Thus C increases with increasing area and number of layers and decreasing thickness. Typical thicknesses range between 15 and 35 μm. Similarly, for substrate packages, the multilayer configuration incorporates transversely integrated conductor lines and vertical conducting paths (vias) allowing for numerous interconnects to components throughout the device system and power distribution in a relatively small space. MLC substrates capable of providing 12,000 electrical connections containing 350,000 vias are currently manufactured (38,39).

A number of processing steps, shown in Figure 7, are used to obtain the multilayer configuration(s) for the ceramic–metal composites. The basic process steps are slip preparation, green tape fabrication, via-hole punching (packages), printing of internal electrodes or metallization, stacking and laminating, dicing or dimensional control, binder burnout, sintering, end termination, and encapsulation. After each processing step, quality control in the form of nondestructive physical and electrical tests ensures a uniform end-product.

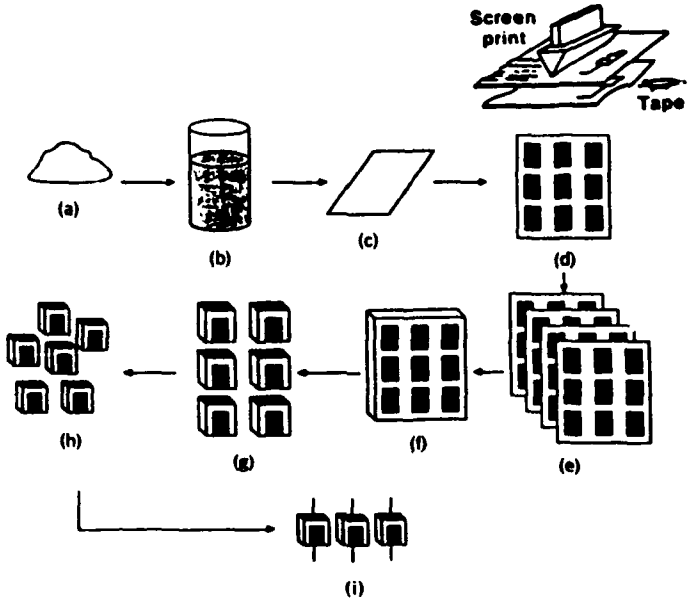

Fig. 7. Fabrication process for MLC capacitors. Steps are **(a)** powder; **(b)** slurry preparation; **(c)** tape preparation; **(d)** electroding; **(e)** stacking; **(f)** lamination; **(g)** dicing; **(h)** burnout and firing; and **(i)** termination and lead attachment.

The basic building block, the ceramic green sheet, starts using a mixture of dielectric powder suspended in an aqueous or nonaqueous liquid system or vehicle comprised of solvents, binders, plasticizers, and other additives to form a slip that can be cast in thin, relatively large area sheets. The purpose of the binder (20,000–30,000 molecular weight polymers) is to bind the ceramic particles together to form flexible green sheets. Electrodes are screened on the tape using an appropriate paste of metal powders. Solvents play a number of key roles, ranging from deagglomeration of ceramic particles to control the viscosity of the cast slip, to formation of microporosity in the sheet as the solvent evaporates. Plasticizers, ie, small to medium sized organic molecules, decrease cross-linking between binder molecules, imparting greater flexibility to the green sheet. Dispersants, typically 1,000 to 10,000 molecular weight polymer molecules, are added to slips to aid in the de-agglomeration of powder particles, allowing for higher green densities in the cast tape. Several review articles on the functional additives in tape cast systems are available (16,17,25,40–44). The resulting slip should have pseudoplastic rheological behavior so that the slip flows during high shear rate

casting operations, but displays little or no flow afterward, thus maintaining tape dimension (45).

There are several methods to make large ceramic sheets for MLC manufacturing (17–23). The methods include glass, belt and carrier film casting, and wet lay down techniques. The relative advantages and limitations of each technique have been reviewed (46). The two most commonly employed techniques, belt casting and doctor blading, are depicted schematically in Figure 8.

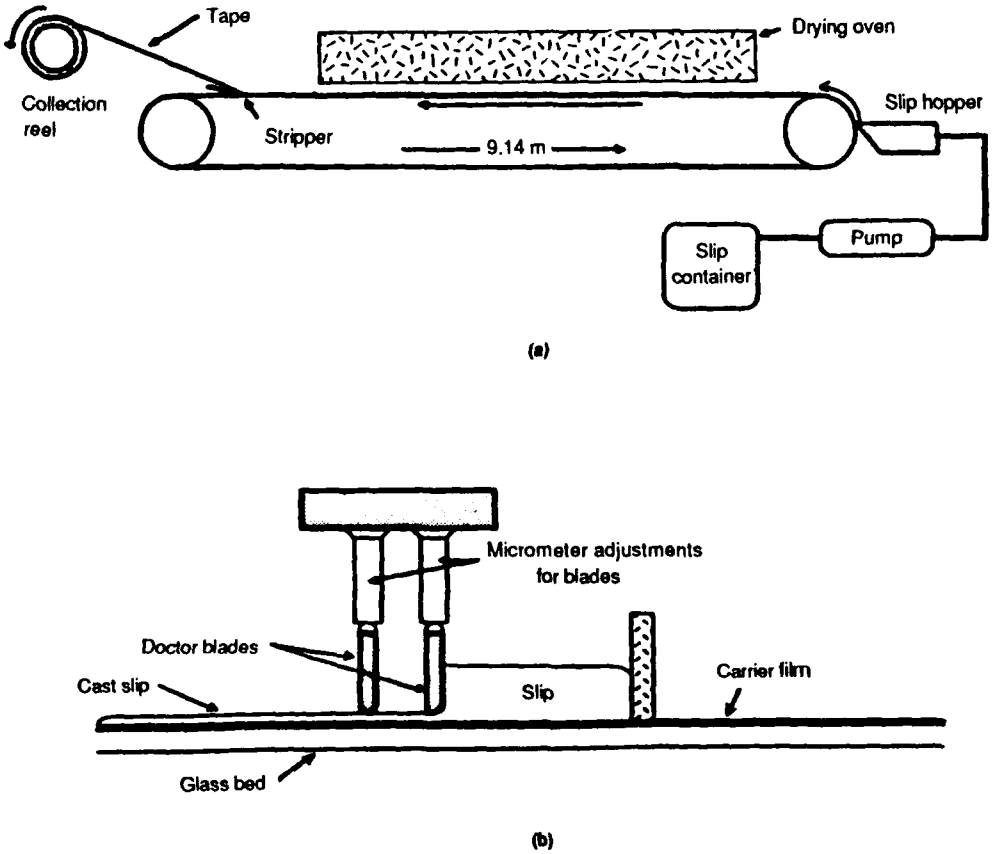

Fig. 8. Schematic of methods for MLC manufacturing; (a) belt casting; (b) carrier film casting using a doctor blade.

Metallization of the green sheets is usually carried out by screen printing, whereby a suitable metal ink consisting of metal powders dispersed in resin and solvent vehicles is forced through a patterned screen. Palladium [*7440-05-3*] and silver-palladium (Ag:Pd) alloys are the most common form of metallization; tungsten [*7440-33-7*] and molybdenum [*7439-98-7*] are used for high (>1500°C) temperature MLCs (47–52). Following screening, the metallized layers are stacked and laminated to register (align) and fuse the green sheets into a monolithic component. Proper registration is crucial to achieve and maintain capaci-

tance design (MLC capacitors) and for proper via-hole placement in MLC packages.

Sintering is the most complex process in MLC fabrication. Ideally, the binder burnout and sintering steps are performed during the same temperature cycle and in the same atmosphere. Most binders burn out by 500°C, well before pore closure in the densification of most ceramics. Sintering behavior of the many different MLC components must be reconciled to achieve a dense material. Internal metallization and the dielectric must co-fire in a single process. Firing temperatures are related to material composition and can be adjusted using additives. Densification rates are related both to the process temperature and to particle characteristics (size, size distribution, and state of agglomeration). Thus, the burnout and sintering conditions depend heavily on the system.

After densification, external electrode termination and leads are attached for MLC capacitor components, and pin module assembly and IC chip joining is carried out for MLC packages. The devices are then tested to ensure performance and overall reliability.

Thick Film Technology

Equally important as tape casting in the fabrication of multilayer ceramics is thick film processing. Thick film technology is widely used in microelectronics for resistor networks, hybrid integrated circuitry, and discrete components, such as capacitors and inductors along with metallization of MLC capacitors and packages as mentioned above.

In principle, the process is equivalent to the silk-screening technique whereby the printable components, paste or inks, are forced through a screen with a rubber or plastic squeegee (see Fig. 7). Generally, stainless steel or nylon

Table 4. Components of Thick Film Compositions[a]

Component	Composition
functional phase	
conductor	Au, Pt/Au
	Ag, Pd/Ag
	Cu, Ni
resistor	RuO_2
	$Bi_2Ru_2O_7$
	LaB_6
dielectric	$BaTiO_3$
	glass
	glass ceramic
	Al_2O_3
binder	glass: borosilicates, aluminosilicates
	oxides: CuO, CdO
vehicle	volatile phase: terpineol, mineral spirits
	nonvolatiles: ethyl cellulose, acrylates

[a]Ref. 53.

filament screens are masked using a polymeric material forming the desired printed pattern in which the composition is forced through to the underlying substrate.

Thick film compositions possess three parts: (*1*) functional phase, (*2*) binder, and (*3*) vehicle. The functional phase includes various metal powders for conductors, electronic ceramics for resistors, and dielectrics for both capacitors and insulation. Examples of typical components for thick film compositions are given in Table 4. The binder phase, usually a low (<1000°C) melting glass adheres the fired film to the substrate whereas the fluid vehicle serves to temporarily hold the unfired film together and provide proper rheological behavior during screen printing. Thick film processing for hybrid integrated circuits typically takes place below 1000°C providing flexible circuit designs.

Current and Future Developments in Multilayer Electronic Ceramics

Advances in the field of electronic ceramics are being made in new materials, novel powder synthesis methods, and in ceramic integration. Monolithic multicomponent components (*MMC*) take advantage of three existing technologies: (*1*) thick film methods and materials, (*2*) MLC capacitor processes, and (*3*) the concept of cofired packages as presented in Figure 9. Figure 10 shows an exploded view of a monolithic multicomponent ceramic substrate.

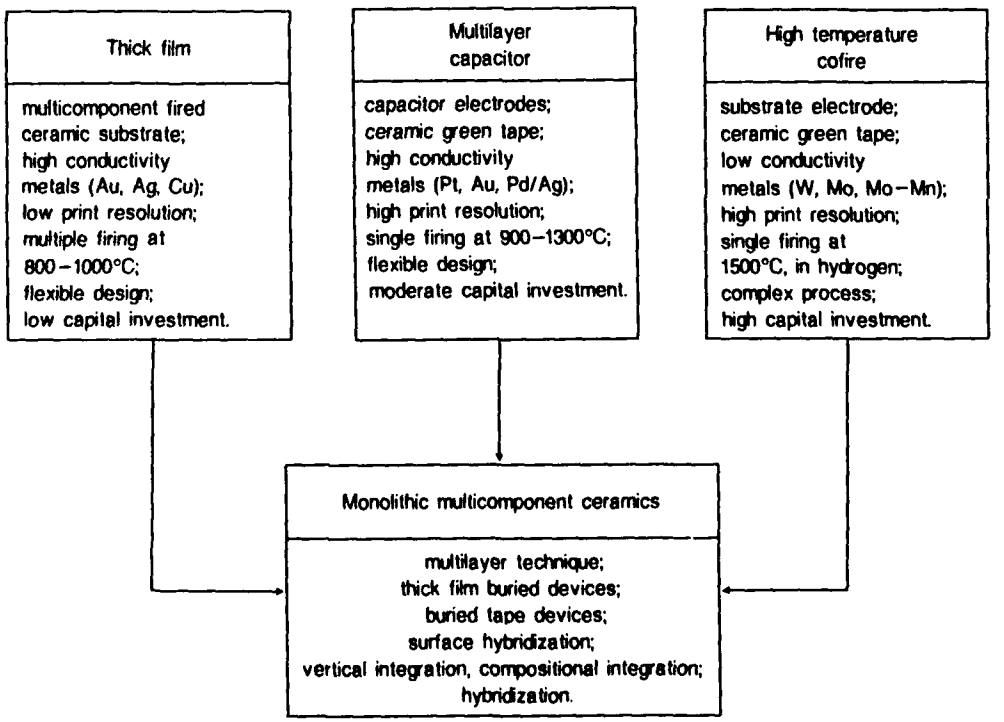

Fig. 9. Monolithic multilayer ceramics (MMCs) derived from multilayer capacitor, high temperature cofire, and thick film technologies.

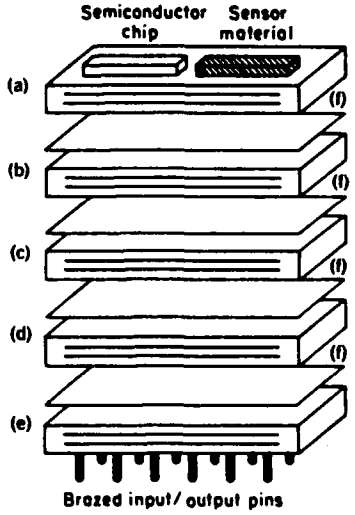

Fig. 10. Exploded view of a monolithic multicomponent ceramic substrate. Layers (a) signal distribution; (b) resistor; (c) capacitor; (d) circuit protection; and (e) power distribution are separated by (f) barrier layers.

New materials for packaging include aluminum nitride [*24304-00-5*], AlN, silicon carbide [*409-21-2*], SiC, and low thermal expansion glass-ceramics, replacing present day alumina packaging technology. As shown in Table 5, these new materials offer significant advantages to meeting the future requirements of the microelectronics industry. Properties include higher thermal conductivity,

Table 5. Properties of High Performance Ceramic Substrates[a]

Properties	AlN	SiC	Glass-ceramics	90% Al_2O_3
thermal conductivity, W/(m·K)	230	270	5	20
thermal expansion coefficient, RT – 400°C × 10^{-7}/°C[b]	43	37	30–42	67
dielectric constant at 1 MHz	8.9	42	3.9–7.8	9.4
flexural strength, kg/cm^2	3500–4000	4500	1500	3000
thin film metals	Ti/Pd/Au Ni/Cr/Pd/Au	Ti/Cu	Cr/Cu, Au	Cr/Cu
thick film metals	Ag–Pd Cu	Au Ag–Pd	Au, Cu, Ag–Pd	Ag–Pd Cu, Au
cofired metals	W	Mo	Au–Cu, Ag–Pd	W, Mo
cooling capability, °C/W				
air	6	5	60	30
water[c]	<1	<1	<1	<1

[a]Ref. 39.
[b]RT = room temperature.
[c]External cooling.

lower dielectric constant, cofire compatibility, and related packaging characteristics such as thermal expansion matching of silicon and high mechanical strength as compared to Al_2O_3.

Greater dimensional control and thinner tapes in multilayer ceramics are the driving forces for techniques to prepare finer particles. Metal organic decomposition and hydrothermal processing are two synthesis methods that have the potential to produce submicrometer powders having low levels of agglomeration to meet the demand for more precise tape fabrication.

As stated above, the development of multifunctional MLCs based on existing technologies offers excellent growth potential since MMCs combine the possibilities of both the high cofire (packaged) substrates and burial of surface devices (54–57). Burial of surface devices promises gains in both circuit density and device hermiticity, leading to increased reliability. Processing trade-offs are expected since current electronic materials for multilayer applications (capacitors, transducers, sensors) are densified at very different firing temperatures. Consequently, integrated components will likely be of lower tolerance and limited range, at least in the early developmental stages. Current efforts have been directed toward incorporation of multilayer capacitor-type power planes and burial of thick film components, including resistors and capacitors. The latter processing technology offers more immediate possibilities as it is developed to cofire at conventional thick film processing temperatures for which a wide range of materials exist.

The continuing miniaturization of electronic packaging should see the replacement of components and processes using such thin film technologies developed for semiconductors as sputtering, chemical vapor deposition, and sol–gel (see SOL–GEL TECHNOLOGY; THIN FILMS) (58,59). Sputtering is the process whereby a target material is bombarded by high energy ions which liberate atomic species from the target for deposition on a substrate. Chemical vapor deposition (CVD) involves a gaseous stream of precursors containing the reactive constituents for the desired thin film material, generally reacted on a heated substrate. The more recent process for thin films, sol–gel, uses a nonaqueous solution of metal–organic precursor. Through controlled hydrolyses, a thin, adherent film is pre-

Table 6. Current and Future Developments in Thin Film Electronic Ceramics[a]

Material	Application	Methods
PT, PZT, PLZT	nonvolatile memory, ir, pyroelectric detectors, electro–optic waveguide, and spatial light modulators	sol–gel, sputtering
diamond (C)	cutting tools, high temperature semiconductors, protective optical coatings	chemical vapor deposition (CVD)
SiO_2, $BaTiO_3$	capacitors	sol–gel, sputtering, chemical vapor deposition (CVD)
1:2:3 superconductors	squids, nmr, interconnects	

[a]Refs. 58 and 59.

pared by dip-coating or spin-coating. The dried "gel" film is then crystallized and densified through heat treatments. Both existing and future developments of thin film electronic ceramics and methods are presented in Table 6.

BIBLIOGRAPHY

1. *Japan Electronics Almanac,* Dempa Publications, Inc., Tokyo, 1986, p. 412.
2. D. W. Johnson in G. Y. Chin, ed., *Advances in Powder Technology,* American Society for Metals, Metals Park, Ohio, 1982, pp. 23–37.
3. K. Osseo-Asare, F. J. Arriagada, and J. H. Adair, "Solubility Relationships in the Coprecipitation Synthesis of Barium Titanate: Heterogeneous Equilibria in the $Ba-Ti-C_2O_4-H_2O$ System," in G. L. Messing, E. R. Fuller, Jr., and Hans Hausin, eds., *Ceramic Powder Science,* Vol. 2, 1987, pp. 47–53.
4. D. Miller, J. H. Adair, W. Huebner, and R. E. Newnham, "A Comparative Assessment of Chemical Synthesis Techniques for Barium Titanate," Paper, 88th Annual Meeting of the American Ceramic Society, Pittsburgh, Pa., April 27–30, 1987.
5. B. J. Mulder, *Am. Ceram. Soc. Bull.* **49**(11), 990–993 (1970).
6. E. P. Stambaugh and J. F. Miller, "Hydrothermal Precipitation of High Quality Inorganic Oxides," in S. Somiya, ed., *Proceedings of First International Symposium on Hydrothermal Reactions,* Gakujutsu Bunken Fukyu-kai (c/o Tokyo Institute of Technology), Tokyo, Japan, 1983, pp. 859–872.
7. K. S. Mazdiyasni, C. T. Lynch, and J. S. Smith, *J. Ceram. Soc.* **48**(7), 372–375 (1965).
8. R. R. Wills, R. A. Markle, and S. P. Mukherjee, *Am. Ceram. Soc. Bull.* **62**(8), 904–911 (1983).
9. R. West, X.-H. Zhang, I. P. Djurovich, and H. Stuger, "Crosslinking of Polysilanes as Silicon Carbide Precursors," in L. L. Hench and D. R. Ulrich, eds., *Science of Ceramic Chemical Processing,* John Wiley & Sons, New York, 1986, pp. 337–344.
10. K. K. Verna and A. Roberts in G. Y. Onoda, Jr., and L. L. Hench, eds., *Ceramic Processing Before Firing,"* John Wiley & Sons, Inc., New York, 1978, pp. 391–407.
11. J. H. Adair, A. J. Roese, and L. G. McCoy, "Particle Size Analysis of Ceramic Powders," in K. M. Nair, ed., *Advances in Ceramics,* Vol. 2, The American Ceramic Society, Columbus, Ohio, 1984.
12. J. W. McCauley, *Am. Chem. Soc. Bull.* **63**(2), 263–265 (1984).
13. G. L. Messing, C. J. Markhoff, and L. G. McCoy, *Am. Ceram. Soc. Bull.* **61**(8), 857–860 (1982).
14. D. E. Niesz and R. B. Bennett, in ref. 10, pp. 61–73.
15. C. Greskovich, "Milling" in F. F. Y. Wang, ed., *Treatise on Materials Science and Technology,* Vol. 9, Academic Press, New York, 1976.
16. R. E. Mistler, D. J. Shanefield, and R. B. Runk, in ref. 10, pp. 411–448.
17. J. C. Williams, "Doctor-Blade Process," in F. F. Y. Wang, ed., *Treatise on Materials Science and Technology,* Vol. 9, Academic Press, New York, 1976.
18. U.S. Pat. 3,717,487 (1973) (to Sprague Electric Company).
19. B. Schwartz and D. L. Wilcox, *Ceramic Age,* 40–44 (June 1967).
20. R. B. Runk and M. J. Andrejco, *Am. Ceram. Soc. Bull.* **54**(2), 199–200 (1975).
21. C. Wentworth and G. W. Taylor, *Am. Ceram. Soc. Bull.* **46**(12), 1186–1193 (1967).
22. R. E. Mistler, *Am. Ceram. Soc. Bull.* **52**(11), 850–854 (1973).
23. J. M. Herbert, *Methods of Preparation, Ceramic Dielectrics and Capacitors,* Gordon and Breach Science Publishers, New York, 1985, Chapt. 3.
24. F. H. Norton, *Forming Plastic Masses, Fine Ceramics: Technology and Applications,* Robert E. Krieger Publishing, Huntington, NY, 1978, Chapt. 10.

25. T. Morse, *Handbook of Organic Additives for Use in Ceramic Body Formulation*, Montana Energy and MHD Research and Development Institute, Inc., Butte, Mont., 1979.
26. D. B. Quinn, R. E. Bedford, and F. L. Kennard, "Dry-Bag Isostatic Pressing and Contour Grinding of Technical Ceramics," in J. A. Mangels and G. L. Messing, eds., *Advances in Ceramics*, Vol. 9 (Forming of Ceramics), 1984, pp. 4–31.
27. I. A. Aksay, F. F. Lange, and B. I. Davis, *J. Am. Ceram. Soc.* **66**(10), C190–C192 (1983).
28. F. F. Lange, B. I. Davis, and E. Wright, *J. Am. Ceram. Soc.* **69**(1), 66–69 (1986).
29. I. A. Aksay and C. H. Schilling, in ref. 26, pp. 85–93.
30. G. N. Howatt, R. G. Breckenridge, and J. M. Brownlow, *J. Am. Ceram. Soc.* **30**(8), 237–242 (1947).
31. J. J. Thompson, *Am. Ceram. Soc. Bull.* **42**(9), 480–481 (1963).
32. J. A. Mangels and W. Trela, in ref. 26, pp. 85–93.
33. T. J. Whalen and C. F. Johnson, *Am. Ceram. Soc. Bull.* **60**(2), 216–220 (1981).
34. M. J. Edirisinghe and J. R. G. Evans, *Int. J. High Technol. Ceram.* **2**(1), 1–31 (1986).
35. R. R. Wills, M. C. Brockway, and L. G. McCoy, "Hot Isostatic Pressing of Ceramic Materials," in R. F. Davis, H. Palmour III, and R. L. Porter, eds., *Materials Science Research*, Vol. 17 (Emergent Process Methods for High-Technology Ceramics), Plenum Press, New York, 1984.
36. M. H. Leipold, "Hot Pressing," in F. F. Y. Wang, ed., *Treatise on Materials Science and Technology*, Vol. 9 (Ceramic Fabrication Processes), Academic Press, New York, 1976.
37. A. J. Blodgett, Jr., *Sci. Am.* **249**(1), 86–96 (1983).
38. R. R. Tummala and E. J. Rymaszewski, *Microelectronics Packaging Handbook*, Van Nostrand Reinhold, New York, 1989.
39. R. R. Tummala, *Am. Ceram. Soc. Bull.* **67**(4), 752–758 (1988).
40. D. J. Shanefield and R. S. Mistler, *Am. Ceram. Soc. Bull.* **53**(5), 416–420 (1974).
41. D. J. Shanefield and R. S. Mistler, *Am. Ceram. Soc. Bull.* **53**(8), 564–568 (1974).
42. R. A. Gardner and R. W. Nufer, *Solid State Technol.* (May 8–13, 1974).
43. A. G. Pincus and L. E. Shipley, *Ceram. Ind.* **92**(4), 106–110 (1969).
44. N. Sarkar and G. K. Greminger, Jr. *Am. Ceram. Soc. Bull.* **62**(11), 1280–1284 (1983).
45. G. Y. Onoda, Jr., in ref. 10, pp. 235–251.
46. J. H. Adair, D. A. Anderson, G. O. Dayton, and T. R. Shrout, *J. Mater. Ed.* **9**(1,2), 71–118 (1987).
47. D. A. Chance, *Met. Trans.* **1**, 685–694 (March 1970).
48. I. Burn and G. H. Maher, *J. Mater. Sci.* **10**, 633–640 (1975).
49. U.S. Pat. 4,075,681 (Feb. 1978), M. J. Popowich.
50. T. L. Rutt and J. A. Syne, "Fabrication of Multilayer Ceramic Capacitor by Metal Impregnation," *IEEE Trans. Parts Hybrids Packag.*, **PHP-9**, 144–147 (1973).
51. D. A. Chance and D. L. Wilcox, *Met. Trans.* **2**, 733–741 (March 1971).
52. D. A. Chance and D. L. Wilcox, *Proc. IEEE* **59**(10), 1455–1462 (1971).
53. L. M. Levinson, *Electronic Ceramics*, Marcel Dekker, Inc., New York, 1988, Chapt. 6.
54. K. Utsumi, Y. Shimada, and H. Takamizawa, "Monolithic Multicomponent Ceramic (MMC) Substrate," in K. A. Jackson, R. C. Pohanka, D. R. Ulhmann, and D. R. Ulrich, eds., *Electronic Packaging Materials Science*, Materials Research Society, Pittsburgh, Pa., 1986, pp. 15–26.
55. W. A. Vitriol and J. I. Steinberg, "Development of a Low Fire Cofired Multilayer Ceramic Technology," 1983, pp. 593–598.
56. H. T. Sawhill and co-workers, "Low Temperature Co-Firable Ceramics with Co-Fired Resistors," International Society of Hybrid Microelectronics Proceedings, 1986, pp. 473–480.
57. C. C. Shiflett, D. B. Buchholz, and C. C. Faudskar, "High-Density Multilayer Hybrid Circuits Made with Polymer Insulating Layers (Polyhic's)," Society of Hybrid Microelectronics Proceedings, 1980, pp. 481–486.

58. S. L. Swartz, "Topics in Electronic Ceramics," *IEEE Trans. Elect. Insul.* Digest on Dielectrics **25,** 935–987 (Oct. 1990).
59. C. P. Poole, Jr., T. Datta, and H. A. Farach, *Copper Oxide Superconductors,* John Wiley & Sons, New York, 1988.

General references

R. C. Buchanan, ed., *Ceramic Materials for Electronics,* Marcel Dekker, Inc., New York, 1986.
L. M. Levinson, ed., *Electronic Ceramics,* Marcel Dekker, Inc., New York, 1988.
B. Jaffe, W. R. Cook, Jr., and H. Jaffe, *Piezoelectric Ceramics,* Academic Press, New York, 1971.

ROBERT E. NEWNHAM
THOMAS R. SHROUT
Pennsylvania State University

APPENDIX 3

The Pennsylvania State University

The Graduate School

THE GLASSY BEHAVIOR OF RELAXOR FERROELECTRICS

A Thesis in

Solid State Science

by

Dwight D. Viehland

Submitted in Partial Fulfillment
of the Requirements
for the Degree of

Doctor of Philosophy

May 1991

ABSTRACT

A spin-glass-like model for the relaxor ferroelectric has been developed. The glassy behavior is shown to be reflected in the dielectric, polarization, and electromechanical responses. The glassy behavior is believed to arise due to correlations, both dipolar and quadrupolar, between superparaelectric sized moments.

The complex susceptibility was measured over the frequency range of 10^2 to 10^7 Hz. The frequency dispersion of the temperature of the permittivity maximum was modelled with the Vogel-Fulcher relationship, predicting a characteristic freezing temperature which coincided with the collapse of a stable remanent polarization. The imaginary component was also found to be nearly frequency independent below this temperature, phenomenologically scaling to the Vogel-Fulcher relationship. The relaxation time distribution was then calculated by analogy to spin-glasses, and shown to extend from microscopic to macroscopic periods near freezing reflecting the onset of nonergodicity. The deviation from Curie-Weiss behavior was also investigated. At high temperatures, the dielectric stiffness was found to follow the Curie-Weiss relationship. A local (glassy) order parameter was calculated from the deviation at lower temperatures, by analogy to spin-glasses. The dependence of the complex susceptibility on an applied electric field and the degree of chemical long range ordering was then investigated using these techniques.

The remanent polarization was investigated for various electrical and thermal histories. The field-cooled and zero-field-cooled behaviors were both studied. The magnitude of both polarizations was found to be equal above a critical temperature. A macroscopic polarization developed under bias in the zero-field-cooled state, with the temperature of the maximum charging current decreasing with increasing bias.

This decrease was modelled using the deAlmedia-Thouless relationship, which predicted an average moment size freezing of approximately $3x10^{-25}$ C-cm. The time dependence of the remanent polarization was also investigated. The square-to-slim-loop hysteresis transition, measured using a standard Sawyer-Tower circuit, was phenomenologically modelled by modifying Neel's equation for the magnetization of a superparamagnet to a similar relationship for a superparaelectric. A temperature dependent internal dipole field was included to account for correlations. The slim loop polarization curves were also found to scale to $E/(T-T_f)$.

The electromechanical behavior was investigated using a nonlinear internal friction technique. The linear elastic response was found to stiffen at all bias levels with the maximum electroelastic coupling occurring near the Vogel-Fulcher freezing temperature. A strong frequency dependence of the kinetics of the anelastic relaxation was found at low measurement frequencies. These data are compared to recent high frequency results. The existence of an inhomogeneous internal strain was found from the line broadening of the (220) and (321) diffraction peaks. On application of an electrical field the internal strain is relieved by the development of a macrostrain which is shown to be the electrostrictive strain. Strong elastic nonlinearities, both an elastic softening and hardening under stress, have also been observed. These results are interpreted as a stress activation of the internal deformation process.

APPENDIX 4

The Pennsylvania State University

The Graduate School

Program in Solid State Science

FERROELECTRIC PROPERTIES OF LEAD BARIUM NIOBATE COMPOSITIONS NEAR THE MORPHOTROPIC PHASE BOUNDARY

A Thesis in

Solid State Science

by

Ruyan Guo

Submitted in Partial Fulfillment
of the Requirements
for the Degree of

Doctor of Philosophy

December 1990

ABSTRACT

Ferroelectric properties, electrooptic properties, and the polarization mechanisms of the tungsten bronze ferroelectric lead barium niobate $Pb_{1-x}Ba_xNb_2O_6$ (PBN(1-x)%) solid solution system with emphasis on the morphotropic phase boundary (MPB) compositions ($1-x\sim0.63$) are the primary contents of this thesis. This study is directed toward (i) the potential applications of the PBN single crystals of the morphotropic phase boundary compositions as electrooptic devices and (ii) the improved understanding of the polarization mechanisms in lead-containing tungsten bronze ferroelectric crystals near a morphotropic phase boundary.

Ferroelectric single crystal and ceramic samples of $Pb_{1-x}Ba_xNb_2O_6$ ($0.25\leq1-x\sim0.84$) were prepared and examined during this thesis work. Single crystals were grown by the Czochralski method. It is shown that in the Ba-rich PBN (prototype point symmetry 4/mmm) the polarization vector is along the c-axis, while in the Pb-rich side of the phase diagram, the polarization vector is in the a-b plane parallel to the $<110>$ direction. However, over the range where the $PbNb_2O_6$ content is 60 to 66 mole percent, it is evident from the X-ray studies that the two structures coexist in polycrystalline samples and appear nearly equal in ratio at 63 mole percent of $PbNb_2O_6$. Dielectric constant maximum and the ferroelectric-paraelectric phase transition temperature minimum are observed at the morphotropic phase boundary composition where $1-x=0.63$.

Ferroelectric phase relations for the $PbNb_2O_6$-$BaNb_2O_6$ solid solution system are studied by measuring the dielectric and the thermal expansion properties. Ferroelectric-paraelectric phase transition in Ba-rich composition (ferroelectric 4mm $\leftrightarrow$ paraelectric 4/mmm) is found to be diffuse near-second order type with small thermal hysteresis. However, the phase transition in Pb-rich compositions (ferroelectric m2m $\leftrightarrow$ paraelectric 4/mmm) is predominantly diffuse first order type with large thermal hysteresis ($\sim$30°C). Thermal hysteresis is more prominent in

compositions near the morphotropic phase boundary. It is found by using high temperature X-ray diffraction that in single crystal PBN61.5 two phase transitions take place. The lower temperature phase transition (at ~125°C) corresponds to the phase transition across the MPB between the orthorhombic m2m and the tetragonal 4mm phases and the higher temperature phase transition (at ~290°C) is the ferroelectric-paraelectric phase transition between tetragonal 4mm and 4/mmm phases. Very large thermal hysteresis (~70°C) is observed for the lower temperature phase transition. The phase diagram of PBN solid solution is updated by including our experimental data into the previously reported phase diagram (Subbarao 1959) with a curved morphotropic phase boundary into the Ba-rich side between ferroelectric m2m and ferroelectric 4mm.

A qualitative thermodynamic model is suggested to account for the large thermal hysteresis observed at the phase transition across the MPB. Such a model is also useful in understanding the phase transition induced by an electric field. Very large thermal hysteresis observed for the phase transition near the morphotropic phase boundary is an indication that the two ferroelectric phases are very similar in their free energies.

Low temperature (10~300K) dielectric and pyroelectric properties of morphotropic phase boundary PBN ferroelectric single crystals have been investigated and characterized to understand the strong "Debye-like" dielectric dispersion along a nonpolar direction (perpendicular to the *polarization direction*) by using dielectric spectrum techniques and a direct charge measurement method, respectively. Significant dielectric relaxation phenomena have been encountered for MPB PBN single crystals in nonpolar directions at low temperatures ($T < 210K$) and over a broad frequency range ($10^2 \sim 10^6$Hz). A small "frozen-in" polarization component has been detected in a nonpolar direction at corresponding temperatures. There is no evidence found for ferroelectric phase transitions at low temperature in the PBN system. The low temperature relaxation effects can be successfully explained by the concept of internal-reorientation type polarization perturbation and a thermally agitated local dipole fluctuation model.

Optic and electrooptic properties of PBN single crystals are studied by using various techniques. Preliminary study using ellipsometry technique on the dispersion behavior of the PBN crystals shows the crystals are transparent in the visible range without noticeable absorption bands.

By studying the conoscopic interference pattern and the transition temperature dependence on the bias electric field, it is demonstrated for the first time that an external electric field can induce ferroelectric phase switching in the morphotropic phase boundary compositions from one ferroelectric phase to the other. One of the most interesting results is that the electrically controlled optical bistable states are possible to obtain in MPB PBN single crystals.

Optic indices of refraction have been measured using the minimum deviation technique to reveal the details of a morphotropic phase transition in a single crystal. Optical birefringence as a function of temperature has been measured using different techniques, particularly the Senarmont method, and has enabled the calculation of RMS value of spontaneous polarization which is otherwise difficult to obtain for PBN single crystals of high transition temperature (> 270°C). The highest spontaneous polarization evaluated in this way for morphotropic phase boundary composition PBN61.5 is of the value $47\mu C/cm^2$ at room temperature.

Transverse linear electrooptic coefficients and half-wave voltages have been measured for different PBN compositions. Morphotropic phase boundary compositions show both high r_c and r_{42} coefficients ($r_{c2} = 311 \times 10^{-12}$ V/m, $r_{42} = 862 \times 10^{-12}$ V/m in PBN61.5), primarily because the dielectric constants perpendicular and parallel to the c-direction are both large and insensitive to temperature. In the ferroelectric tetragonal phase, the transverse electrooptic coefficient r_{51} ($r_{51} = 1524 \times 10^{-12}$ V/m in PBN57) is large and in the ferroelectric orthorhombic phase the r_c ($r_{c2} = 216 \times 10^{-12}$ V/m in PBN65) is large. Both can be attributed to the large transverse dielectric constants.

The g-coefficients were derived from the electrooptic measurements including half-wave voltage and the birefringence. Positive $g_{33} = 0.0603m^4/C^2$ and negative $g_{13} = -0.0152m^4/C^2$ are obtained, in agreement with theoretical predictions. Overall, the g-coefficients are smaller than Pb-free perovskites, indicating considerable electronic polarization contribution from Pb^{2+}.

Preliminary study on the electrooptic response behavior of PBN single crystals shows that PBN has fast electrooptic response of the order ~100nsec ($\delta t_{10/90}$ = 50nsec has been obtained) and is therefore a potential candidate for electrooptic modulator applications.

The transmission electron microscope study reveals the manner in which the polarization manifests itself in the various ferroelectric symmetries. There exist only 180° ferroelectric domains in tetragonal 4mm; in orthorhombic m2m, both 90° twin-like domains and 180° domains in the a-b plate are present. The domain microstructures are deduced for PBN compositions across the phase diagram. TEM study in the temperature range from -180°C to ~80°C revealed the presence of incommensurate ferroelastic domains in PBN solid solution similar to those discovered in the other tungsten bronzes BNN and SBN. The degree of incommensurability varies with temperature and compositions. These incommensurations exist at room temperature in both tetragonal and orthorhombic ferroelectric phases; however, the discommensuration density is much lower and better defined on the orthorhombic side of the phase diagram. The large thermal hysteresis at the ferroelectric-paraelectric phase transition in a Pb-rich orthorhombic composition can be understood by taking the incommensurate phase transition into consideration. The discommensuration structures, however, seem to be independent of the ferroelectric domains in the m2m phase, which indicates that the lock-in phase transition takes place at a higher temperature than the ferroelectric phase transition.

In general, the dielectric constant, pyroelectric coefficients, and linear electrooptic coefficients are found to be enhanced near the MPB compositions. The transverse linear electrooptic coefficients (r_{51} = 1524x10^{-12} V/m for PBN57) are among the highest known in oxide ferroelectric materials (e.g., r_{51} = 1600x10^{-12} V/m in $BaTiO_3$). More importantly, in the morphotropic phase

boundary compositions, the enhanced physical properties are relatively temperature insensitive at ambient temperatures (much lower than their Curie temperatures), which is of great advantage for electrooptic and photorefractive device applications.

APPENDIX 5

The Pennsylvania State University

The Graduate School

Program in Solid State Science

OPTICAL AND ELECTROOPTICAL PROPERTIES OF LEAD MAGNESIUM NIOBATE - LEAD TITANATE

A Thesis in

Solid State Science

by

Dean A. McHenry

Submitted in Partial Fulfillment
of the Requirements
for the Degree of

Doctor of Philosophy

May 1992

ABSTRACT

The optical and electrooptical properties of a relaxor ferroelectric Lead magnesium niobate, $Pb(Mg_{1/3},Nb_{2/3})O_3$ (PMN), and its solid solution with Lead titanate, $PbTiO_3$ (PT) to form (1-x) $Pb(Mg_{1/3},Nb_{2/3})O3$ - (x) $PbTiO_3$ (PMN-PT) have been examined in hopes of realizing its potential usefulness as an electrooptic material. A better insight into the underlying nature of optical phenomena in this and other relaxor ferroelectric solid solution systems was also a goal of this effort. Fundamental optical property measurements such as spectral transmission, refractive index, birefringence, thermooptic and electrooptic coefficients were undertaken in order to characterize compositional and structural relationships for PMN-PT.

Spectral transmission measurements for these perovskite structure materials indicate an optical bandgap of about 3.35 eV corresponding to the onset of transmission in the near UV near 380 nm. Increasing transmission of light (near 60%) for thin polished ceramic samples of PMN-PT occurs out into the infrared regime without significant absorption to wavelengths greater than 5μm and then decreasing transmission to become totally absorbing at 10μm.

Refraction of light as a function of frequency for many PMN-PT compositions was examined by the minimum deviation method. For this system the refractive index increases nearly linearly from PMN (n_d = 2.5219) by 2.415 x 10^{-3}/ mole % $PbTiO_3$ added. The optical dispersion was successfully modeled upon a single term Sellmeier oscillator equation even

for these Pb^{2+} A-site perovskite compounds which have a Pb $6s^2$ electronic energy level in the region of the lowest conduction band modifying the predominant B-O oxygen-octahedra interactions.

Thermooptic properties, n(T), were undertaken over a temperature range sufficient to ascertain the ferroelectric polarization contribution to the refractive index. Birefringence measurements sensitive to long range polar order were also performed as a complement to the n(T) measurements. The n(T) curves for the compositions with small amounts of $PbTiO_3$ were shown to exhibit relaxor effects exemplified by a purely paraelectric linear high temperature regime and then a gradual departure from linear behavior at a temperature well above (~300°C) the dielectric constant maximum temperature. This reduction of the refractive index is explained by the existence of short range ordered regions of local polarization (superparaelectric behavior). The average polarization remains zero in this regime but the nonzero root mean square polarization biases the refractive index by the quadratic electrooptic effect. Only below the freezing temperature T_f of the interacting and coalescing polar regions is there a measurable optical anisotropy $\Delta n(T)$ observed from uniformly distorted macroscopic scale domains. The field induced birefringence for .80PMN-.20PT of .005 is comparable to other perovskite materials.

For this system of relaxor ferroelectrics the response to simultaneous optical and electrical fields as an electrooptic media has been demonstrated to be based on other solid-state features such as their dielectric, polarization, and ferroelectric properties. Electrooptic and polarization hysteresis loops were measured as a function of electric field and temperature. The measured quadratic electrooptic R coefficients at room

temperature (e.g 14.1 x 10^{-16} m^2/V^2 for .90PMN-.PT with λ = 632.8nm) were such that several halfwaves of retardation could be produced for modest fields. Electrooptic shuttering experiments indicated that switching speeds of the order 700nsec could be readily achieved in .93PLMN-.07PT bulk ceramic samples. Polarization optic coefficients were found to be of order .01m^4/C^2 and in common with many other Pb perovskite relaxors an order of magnitude smaller than non Pb materials. In addition to electrically controllable birefringence, longitudinal electrooptic light scattering and spectral filtering effects were also observed.

Because of their large electrooptic coefficients, photorefractive effects have been shown to be readily induced by the excitation of free carriers caused by illumination from near bandgap (375 nm) radiation. Photoassisted domain switching (PDS) has been observed during measurement of polarization -electric field hysteresis loops. Photorefractive induced birefringence (>10^{-4}) under simultaneous UV illumination and electric field has been demonstrated in polycrystalline ceramics of composition .90PMN-.10PT. This photorefractive index pattern storage was demonstrated to be maintainable at least for several hours, reversible under the action of an electric field of opposite polarity, and erasable by thermal treatment or broadband illumination.

The large quadratic electrooptic coefficients in polycrystalline ceramics of PMN-PT, comparable to any previously measured electrooptic ceramics, and linear electrooptic coefficients demonstrated in near morphotropic phase boundary single crystals such as .70PMN-.30PT may prove to be of significant interest for applications involving electrooptic modulation and photorefractive effects.

APPENDIX 6

The Pennsylvania State University

The Graduate School

AN INVESTIGATION OF THE LEAD SCANDIUM TANTALATE-LEAD TITANATE SOLID SOLUTION SYSTEM

A Thesis in

Solid State Science

by

Jayne R. Giniewicz

Submitted in Partial Fulfillment
of the Requirements
for the Degree of

Doctor of Philosophy

December 1991

ABSTRACT

The unique characteristics of the solid solution $(1-x)Pb(Sc_{1/2}Ta_{1/2})O_3$-$(x)PbTiO_3$ make it an interesting system from both a theoretical and practical point of view. A variety of compositionally and thermally "adjustable" states of structural ordering, Curie temperatures, and material properties are accessible for these materials, making them attractive for many device applications as well as a useful model system for further exploring the fundamental nature of relaxor ferroelectrics. Selected compositions from the system have been prepared as ceramics, characterized, and subjected to various property measurements. Two structural phase boundaries have been identified between three main lower symmetry ferroelectric phase regions. Materials from each of these regions possess different states of structural ordering and exhibit distinctive ferroelectric behaviors. Structure-property relationships are highlighted for compositions representing each region and a preliminary evaluation of the material for pyroelectric device application is presented.

The $(1-x)Pb(Sc_{1/2}Ta_{1/2})O_3$-$(x)PbTiO_3$ ceramics were prepared by a conventional mixed-oxide method involving the use of high-purity starting compounds, a precursor-phase formulation, and controlled lead atmosphere sintering. Compositions were selected from across the entire range so as to represent all phase regions occurring in the system. Each composition was calcined at 900°C for four hours and then at 1000°C for one hour with an intermediate comminution step. Compacted specimens of all compositions were then subjected to firing at 1400°C for one hour within sealed crucibles containing $Pb(Sc_{1/2}Ta_{1/2})O_3$ / $PbZrO_3$ source powders. Specimens with compositions [$x \leq 0.1$] required a second higher temperature sintering at temperatures in the range [1500-1560°C] depending on the composition. Those specimens for which the degree of ordering could be varied by post-sintering heat-treatment were annealed in a sealed

system with a controlled lead atmosphere so as to allow negligible lead loss during the ten-hour period required to order the material.

Four distinct phase regions were identified in the system: (1) a high-temperature cubic phase, below which there exist, (2) a rhombohedral (pseudocubic) region of variable order/disorder [VOD] in the composition range [x=0-0.075], (3) a structurally invariable rhombohedral (pseudocubic) region in the range [x=0.1-0.4], and (4) a tetragonal region extending from [x=0.45] to [x=1.0]. Boundary regions separating the three lower symmetry phase regions were defined where the VOD phase boundary was determined to lie in the composition range [x=0.075-0.1] and the morphotropic phase boundary [MPB] between [x=0.4] and [x=0.45]. It was noted that the extent of the VOD phase region and, hence, the position of the VOD phase boundary may well depend upon the annealing conditions imposed and, therefore, the structural features reported for the system in this compositional range reflect only the nature of materials produced under the preparation conditions applied in this study.

A range of ferroelectric behaviors was observed for materials representing each of the three non-cubic phase regions, each of which was correlated with the coherence length of the ordering present as determined by means of electron and x-ray diffraction. It was thereby shown that all three of the nanostructure-property classes defined in the classification scheme of Pb-based perovskites described in Section 1.1.3 are represented in this system.

Preliminary investigation of the nanoscale ordering occurring in as-fired specimens by means of electron diffraction indicated the presence of short coherence length (20-800Å) long-range ordering up to [x=0.3] as evidenced by the presence of the "F-type" reflections associated with the ordered superstructure. The steady decrease observed in the intensity of these spots with increasing x reflects a decrease in the coherence length of the ordering. Estimation of the order domain sizes in annealed VOD

materials by means of x-ray diffraction utilizing the Scherrer expression (Equation 1.11; Section 1.3.1) yielded average order domain sizes greater than 1000Å for all of the annealed specimens.

Dielectric hysteresis was observed for all compositions [x=0-0.4]. As-fired materials from the composition range [x=0-0.4] were observed to display relaxor-type dielectric behavior which becomes more normal on approaching the MPB [x=0.4-0.45] beyond which the response is essentially that of a first-order ferroelectric. Both relaxor and normal first-order type dielectric responses were found to occur for VOD compositions with the as-fired materials showing the characteristic diffuse and dispersive responses typical of a relaxor and the annealed specimens exhibiting more sharp, first-order type behaviors. The dielectric behaviors exhibited by as-fired and annealed samples under a biasing field of 5 (KV/cm) were also observed to be those typically associated with relaxor-type ferroelectrics and normal first-order ferroelectrics respectively. The general features of the temperature dependences of the remanent polarization, P_r, and the 100 KHz reduced RMS polarization, $P_{(100K)}$, observed for the VOD compositions highlight the nature of the polarization as it relates to the degree of positional ordering present; it becomes evident that even for the annealed samples, for which relatively high degrees of long-range ordering are achieved and near-normal first-order dielectric responses displayed, some "glassy" polarization character is retained. The depolarization curves of the remanent, P_r, and 100 KHz reduced RMS, $P_{(100K)}$, polarizations for compositions [x=0.1-0.4] showed relaxor-type tendencies with a trend towards a more normal first-order type response on approaching the MPB region.

A preliminary evaluation of the pyroelectric response has been conducted in this investigation for selected $(1-x)Pb(Sc_{1/2}Ta_{1/2})O_3$-$(x)PbTiO_3$ compositions in order to determine the most promising materials for thermal imaging applications and to roughly establish the optimum operating conditions for those which exhibit the highest figures of

merit (defined in Section 6.1). The relatively high dielectric constant coupled with the moderate values of the pyroelectric coefficient below T(max) for all the compositions considered results in a low voltage response [F_V] making them not particularly well-suited for large area device applications. These materials do, however, show detectivities [F_D] adequate for potential use as point detectors. The VOD compositions, in particular, appear to be promising candidates for field-stabilized pyroelectric devices.

The detectivities for as-fired and annealed [x=0.025] and [x=0.05] compounds were evaluated under a DC biasing field of 5 (KV/cm). Some enhancement of F_D was observed at this field strength for the as-fired specimens which even under unbiased conditions exhibited stable responses over an extremely broad temperature range [T ≈0-70°C; Figure 6.8]. The peak F_D of the annealed [x=0.025] material [F_D(max)≈16 ($10^{-5}Pa^{-1/2}$); Figure 6.9(a)] was observed to occur at ≈20°C and showed a much more marked enhancement under DC bias than its as-fired counterpart [F_D(max)≈2.5 ($10^{-5}Pa^{-1/2}$); Figure 6.8(a)]. The effect of the biasing field on the annealed [x=0.05] material was less dramatic with respect to the peak F_D attained [F_D(max)≈6.3 ($10^{-5}Pa^{-1/2}$); Figure 6.9(b)]; however, similar to the as-fired materials, this material exhibited an enhanced detectivity over a broad temperature range above T(max). These preliminary results, obtained under modest field conditions, have indicated that the materials from the VOD composition range are highly variable in their performance, both with respect to the maximum response achieved and the breadth of the temperature range over which a stable response is obtained.

APPENDIX 7

Glassy polarization in the ferroelectric tungsten bronze $(Ba,Sr)Nb_2O_6$

A. S. Bhalla, R. Guo, and L. E. Cross
Materials Research Laboratory, The Pennsylvania State University, University Park, Pennsylvania 16802

G. Burns and F. H. Dacol
IBM T. J. Watson Research Center, P.O. Box 218, Yorktown Heights, New York 10598

R. R. Neurgaonkar
Rockwell International Science Center, Thousand Oaks, California 91360

(Received 17 June 1991; accepted for publication 19 February 1992)

We report accurate temperature dependent measurements of optic indices of refraction, the birefringence, and the strain in the ferroelectric tungsten bronze crystals $Ba_{0.25}Sr_{0.75}Nb_2O_6$ and two compositions of $(Ba_{2-x}Sr_x)_2(K_{1-y}Na_y)_2(NbO_3)_{10}$. These results are compared to our previous results in $Ba_{0.4}Sr_{0.6}Nb_2O_6$. From the experimental data, it appears that far above the ferroelectric T_c, up to a temperature T_d, these crystals possess a local, randomly oriented polarization, P_d, with similar T_d values, irrespective of their chemical composition and T_c. Various aspects of our understanding of the polarization behavior and other effects in this ferroelectric system are discussed.

I. INTRODUCTION

In a previous paper[1] we reported measurements, as a function of temperature, of the optic indices of refraction, $n(T)$, and elements of the strain tensor, x_{ij} of the tetragonal tungsten bronze ferroelectric $Ba_{0.4}Sr_{0.6}Nb_2O_6$ (BSN40, $T_c \simeq 75$ °C). BSN40, as well as other mixed system ferroelectrics, show crystalline ferroelectric behavior but with a glassy polarization phase transition above the ferroelectric transition temperature T_c up to a dipole temperature (T_d). Some aspects of materials with these properties have been reviewed.[2] Particularly noteworthy in our previous work[1] is that analysis of the $n(T)$ and x_{ij} data yields essentially the same T_d values as well as essentially the same temperature dependent dipole polarization $[P_d \equiv (\overline{P_3^2})^{1/2}]$ which merges with the ferroelectric reversible polarization (P_r) below T_c.

In this paper we extend our previous measurements to several related crystals. These are $Ba_{0.25}Sr_{0.75}Nb_2O_6$ (BSN25, $T_c \simeq 56$ °C) and $(Ba_{2-x}Sr_x)_2(K_{1-y}Na_y)_2(NbO_3)_{10}$ (BSKNN) with several ratios of atoms. In particular, for these materials we report measurements of P_r, n_3, n_1, and the optical birefringence, as well as some components of the strains. These results are compared to those obtained from BSN40 and aspects of our understanding of these results are discussed.

II. STRUCTURE

A unit cell of the tetragonal tungsten bronze structure is shown in Fig. 1. Above T_c it has a center of symmetry (space group D_{4h}^5-$P4/mbn$). Below T_c it remains tetragonal (space group C_{4v}^2-$P4bm$) but develops a reversible polarization along the c axis (3 axis). Figure 1 shows the primitive unit cell viewed along the c axis. The chemical formula can be thought of as $(Ba_{1-x}Sr_x)_5(NbO_3)_{10}$ since there are ten niobium octahedra in this unit cell and the Ba and Sr atoms randomly occupy the two α and four β positions.[3,4] However, there are six such positions and only five Ba + Sr atoms; thus the structure automatically has defects. The small, four γ sites tend to be occupied only by smaller ions (such as Li). In fact, none of the tungsten bronze ferroelectrics actually are ordered compounds,[5] they all have defect structures.[2,6]

III. THEORETICAL CONSIDERATIONS

A. Thermal expansion

In the tungsten bronze type crystals, the prototype point symmetry is $4/mmm$ so that the thermal expansion is anisotropic with components x_3 along the fourfold axis and x_1 in the perpendicular plane. The ferroelectric point symmetry is 4 mm and the very high dielectric anisotropy at T_c shows that fluctuations are confined to the fourfold axis (i.e., the ferroelectricity is uniaxial). For these cases, the polarization fluctuation induced strains will be given by[1]

$$x_3 = \Delta c/c_0 = Q_{33}\overline{P_3^2}, \tag{1}$$

$$x_1 = \Delta a/a_0 = Q_{13}\overline{P_3^2}, \tag{2}$$

where Q, the electrostrictive coefficient, is a fourth ranl tensor written in contracted notation.

B. Optical refractive index

In the bronze family, there is a standing birefringenc in the uniaxial tetragonal prototype (i.e., $n_3 \neq n_1$) and birefringence Δn_{31}. Since all polarization occurs along th ferroelectric (c, or 3) axis, then in contracted notation, w have, for the indices of refraction,

$$\Delta n_3 = -g_{33}(n_3^0)^3\overline{P_3^2}/2, \tag{3}$$

$$\Delta n_1 = -g_{13}(n_1^0)^3\overline{P_3^2}/2, \tag{4}$$

where n^0 is the index of refraction if there were no pola ization of any sort present, whether along the c axis (n_3^0) perpendicular to it (n_1^0) and g_{ij} are the quadratic electr optic constants. The change of optical birefringen $\delta(\Delta n_{31})$ will be given by (for $n_3^0 \simeq n_1^0 \simeq n_0$):

 0021-8979/92/115591-05$04.00

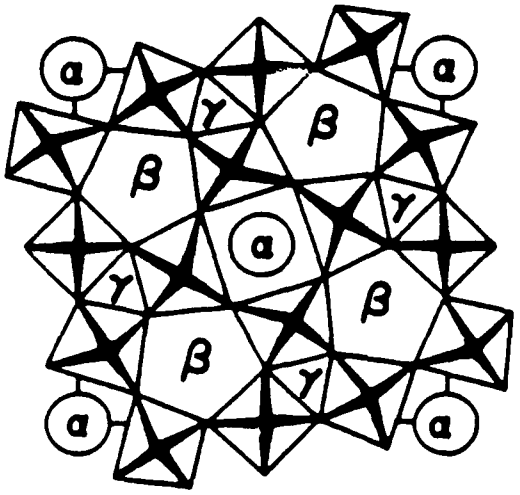

FIG. 1. A unit cell of the tetragonal tungsten bronze structure.

$$\delta(\Delta n_{31}) = -\tfrac{1}{2}n_0^3(g_{33}-g_{13})\overline{P_3^2}. \tag{5}$$

IV. EXPERIMENTAL TECHNIQUE

The reversible polarization, P_r, was obtained by the integration of the pyroelectric current versus temperature measured by a method developed by Byer and Roundy.[7] The poled single-crystal sample was heated in an air oven with automatic heating rate control. The pyroelectric current was measured by a picoammeter.

Thermal expansion measurements were carried out from room temperature to about 500 °C by using a high sensitivity linear variable differential transformer (LVDT) dilatometer. Heating/cooling rate of 0.5 °C/min was chosen and regulated by a microprocessor based temperature controller. Single-crystal rods cut with length parallel to either c or a axis were mounted inside a fused silica holder which is set upright in a vertical furnace, and the thermal expansion or contraction was recorded on an X–Y recorder.

The indices of refraction parallel to $P_r(n_3)$ and perpendicular to $P_r(n_1)$ were measured by the minimum deviation technique.[8] Oriented single-crystal prisms were used in an oven in conjunction with various lasers as light sources.

The birefringence, Δn_{31}, was also directly measured. An a-cut plate was polished into a wedge shape with a known wedge angle (5°–7°). Δn_{31} was measured using a polarizing microscope with a hot stage and the sodium D lines as a light source ($\lambda = 589.3$ nm). The birefringence was determined by

$$\Delta n_{31} = \lambda/d \sin\theta, \tag{6}$$

where θ is the wedge angle, and d is the separation between the interference fringes resulting from the varying thickness of the wedge.

TABLE I. Values of the Q and g coefficients used for calculation of $(\overline{P_3^2})^{1/2}$.

Electrostrictive constant (m^4/C^2)	$Q_{31} = -0.71 \times 10^{-2}$
	$Q_{33} = 3 \times 10^{-2}$
Quadratic electro-optic coefficient (m^4/C^2)	$(g_{33} - g_{13}) = 0.068$

V. RESULTS AND DISCUSSION

Room-temperature values of several physical constants derived experimentally and used for the calculations of $(\overline{P_3^2})^{1/2}$ are summarized in Table I.

Figure 2(a) shows the indices of refraction both parallel and perpendicular to the tetragonal c axis of single-crystal BSN25. As can be seen, the changes in n_3 are considerably larger than those perpendicular to the tetragonal axis (n_1). Continuous change in values of both n_1 and n_3 rather than a classical soft mode behavior can be seen.

Figure 2(b) shows birefringence, Δn_{31}, as a function of temperature for the same BSN25 single crystal. As is evident from Fig. 2(b), Δn_{31} decreases with temperature, goes through zero for $\lambda = 589.3$ nm at a temperature well above T_c and the crystal changes from optically positive to negative.

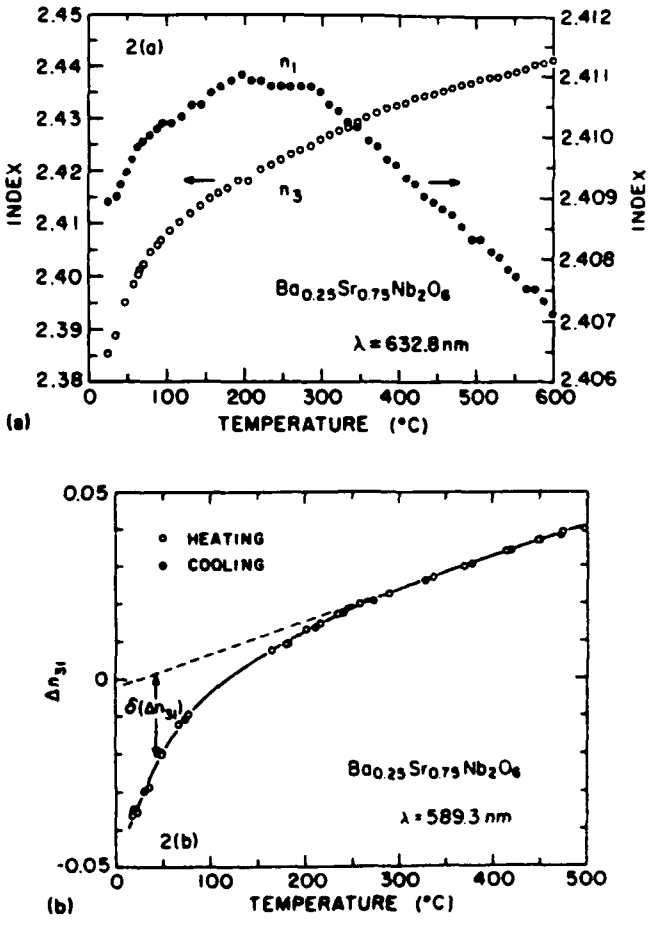

FIG. 2. (a) The measured n_1 and n_3 for BSN25 single crystal at 632.8 nm (b) Optical birefringence Δn_{31} for a BSN25 at 589.3 nm. The results for heating and cooling overlap.

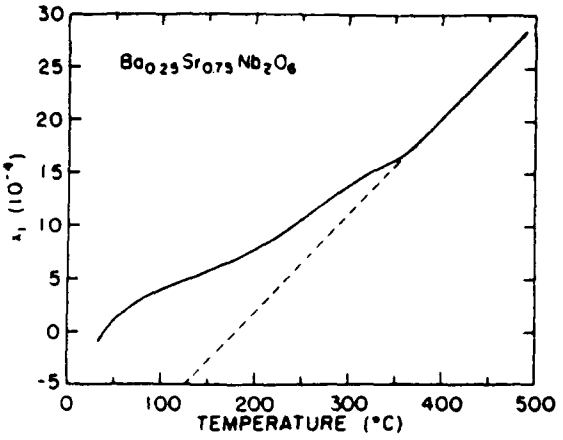

FIG. 3. Thermal strain for BSN25 along the a axis.

Figure 3 shows the thermal strain data, $x_1 = \Delta a/a$, measured by LVDT for a BSN25 single crystal. Using an extrapolation of the high-temperature curve, it is possible to calculate the arrest of the change which is due to the onset of $(\overline{P_3^2})^{1/2}$. As can be seen from Fig. 3, the deviation from the linear high-temperature behavior occurs at a temperature ($\sim$360 °C) approximately.

Temperature dependence of the pyroelectric coefficient p and the integrated reversible polarization P_r of single-crystal BSN25 are plotted in Fig. 4. BSN25 is a typical relaxor-type ferroelectric in which a ferroelectric–paraelectric phase transition is frequency dependent.[9]

The Q and g coefficients for BSN25 have not been measured. However, those for BSN40 have been measured[10,11] (Table I) and they have been used for deducing the data of BSN25 (and for BSKNN, discussed later). Due to the similarity of these materials, this should cause little error. Then, using these Q and g values (Table I), Fig. 5 summarizes the value of $(\overline{P_3^2})^{1/2}$, obtained from independent measurements. That is, P_d or $(\overline{P_3^2})^{1/2}$ is obtained from the n_3, n_1, Δn_{31}, and $\Delta a/a$ experimental results, using the

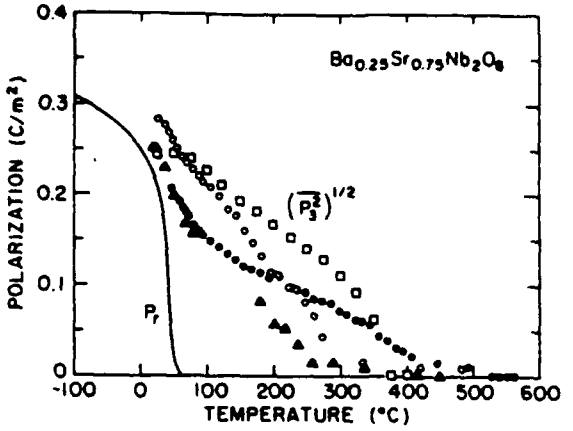

FIG. 5. $(\overline{P_3^2})^{1/2}$ vs T for BSN25, as calculated from n_3 vs T (in solid circles), n_1 vs T (in open circles), Δn_{31} vs T (in solid triangles), and $\Delta a/a$ vs T (in open rectangles). P_r vs T, from p vs T, is also shown.

corresponding equations (1) through (5). Also plotted is the reversible polarization data P_r from Fig. 4. It is evident that the polarization calculated from the $(\overline{P_3^2})^{1/2}$ is larger than P_r and extends several hundred degrees above T_c. However, note that below T_c both P_d and P_r appear to merge.

It has been known[9] that the ferroelectric–paraelectric phase transition becomes more diffuse when the Sr:Ba ratio increases. Figure 6 shows the results[1] of similar measurements performed on BSN40. BSN25 shows more pronounced relaxor behavior for which the $(\overline{P_3^2})^{1/2}$ decays slowly with temperature compared to BSN40. Nevertheless, both BSN40 and BSN25 show similar T_d value, even though there are differences in their compositions. It has been reported that T_d of (PLZT) $[Pb_{1-x}La_x(Zr_yTi_{1-y})_{1-x/4}O_3]$ is approximately equal to T_c of PZT[8] and T_d of $Pb(Ti_{1-x}Sn_x)O_3$ is found[12] to be equal to T_c of $PbTiO_3$. In BSN crystals, there is no end member from which an estimate of T_d can be made. How-

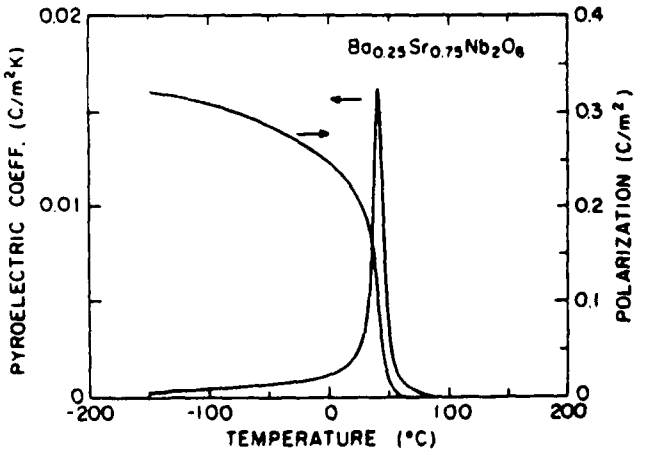

FIG. 4. Temperature dependence of the pyroelectric coefficient p and reversible spontaneous polarization P_r for a BSN25 single crystal.

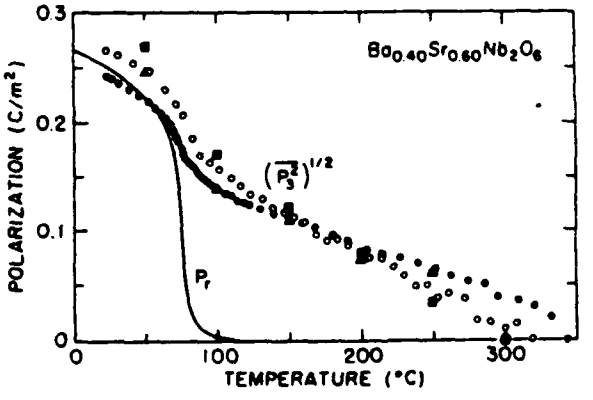

FIG. 6. $(\overline{P_3^2})^{1/2}$ vs T for BSN40, as calculated from n_3 vs T (in solid circles), n_1 vs T (in open circles), Δn_{31} vs T (in solid triangles), and $\Delta c/c$ vs T (in solid rectangles). P_r vs T, from p vs T, is also shown as the solid line.

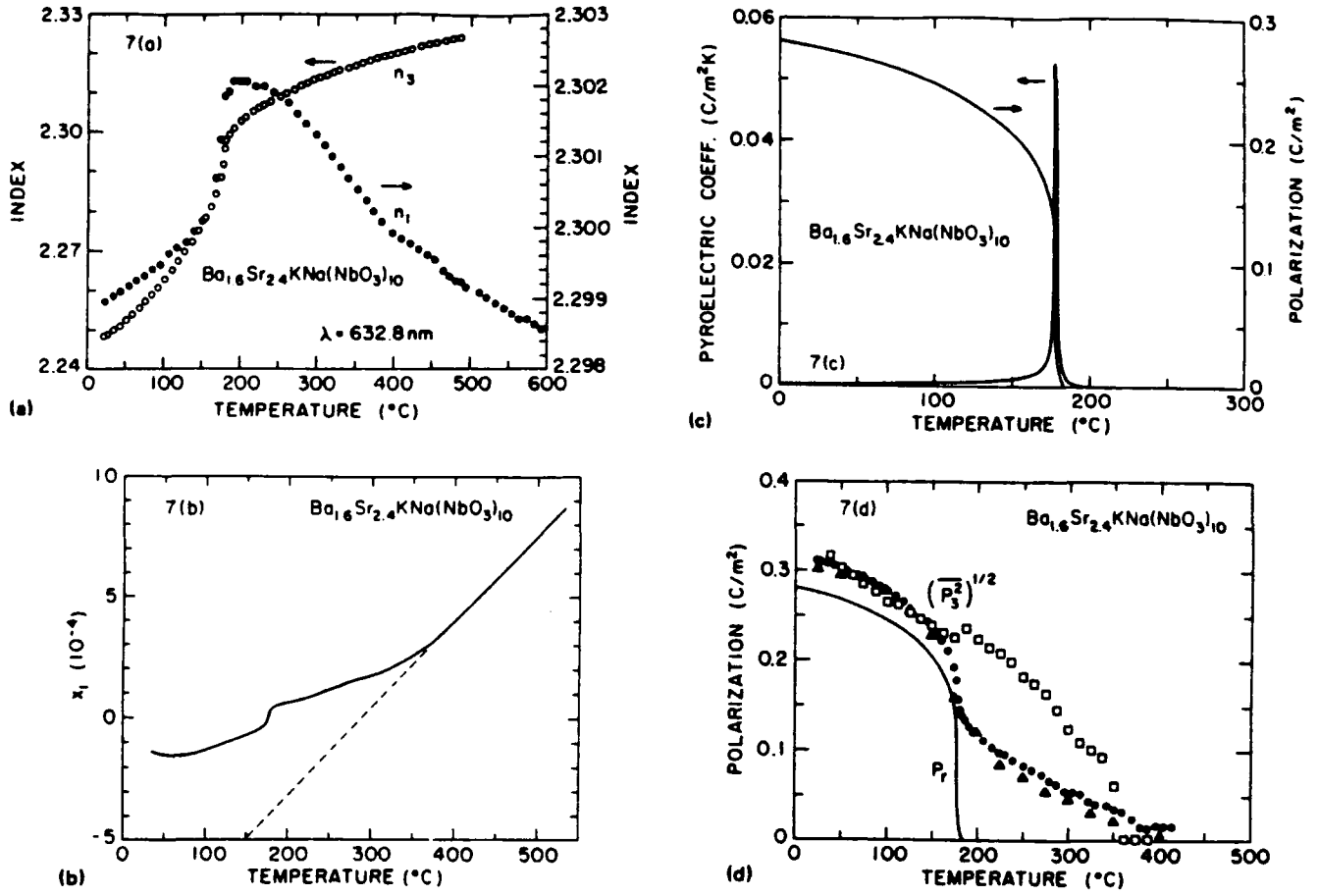

FIG. 7. (a) The indices of refraction both parallel and perpendicular to the tetragonal c axis at $\lambda = 632.8$ nm; (b) the thermal strain $\Delta a/a$ measured by LVDT dilatometry method; (c) the temperature dependence of the pyroelectric coefficient p and the integrated reversible spontaneous polarization P_r; and (d) a summary of the values of $(\overline{P_3^2})^{1/2}$ obtained from n_3 (in solid circles), Δn_{31} (in solid triangles), and $\Delta a/a$ (in open rectangles) of a single crystal BSKNN(1). P_r is also shown.

ever, a T_d that is approximately compositional insensitive does seems to exist in this system.

We have carried out similar studies on related "stuffed" tungsten bronze crystals with the formula $(Ba_{2-x}Sr_x)_2(K_{1-y}Na_y)_2(NbO_3)_{10}$ or BSKNN as well as rare-earth doped BSKNN. These stuffed tungsten bronzes have six atoms for the six $\alpha + \beta$ sites (Fig. 1). However, since the various atoms occupy both the α and β sites, the fundamental randomness in this structure is maintained. We have measured two such stuffed crystals with the formulas, abbreviations, and T_c values listed here:

$Ba_{1.6}Sr_{2.4}KNa(NbO_3)_{10}$ BSKNN(1) $T_c \approx 175$ °C

$Ba_3SrK_{1.5}Na_{0.5}(NbO_3)_{10}$ BSKNN(2) $T_c \approx 220$ °C.

Figure 7(a) shows the indices of refraction both parallel and perpendicular to the tetragonal c axis of single-crystal BSKNN(1) for $\lambda = 632.8$ nm. Figure 7(b) shows the thermal strain $\Delta a/a$ measured by LVDT for BSKNN(1) single crystal. The temperature dependence of the pyroelectric coefficient p and the reversible spontaneous polarization P_r of single crystal BSKNN(1) are plotted in Fig. 7(c). A summary of the $(\overline{P_3^2})^{1/2}$, or P_d, results for BSKNN(1) are shown in Fig. 7(d). Similar to the results for BSN (Figs. 5 and 6), for BSKNN(1) P_d obtained from the index and strain measurements extended to $T_d \sim 350$–400 °C. This T_d value is several hundred degrees above the ferroelectric T_c (≈ 175 °C) indicating glassy polarization behavior over this range. This T_d value is similar to those found for the BSN25 and BSN40 crystals (Figs. 5 and 6). Also note that below T_c, P_d is approximately equal to the reversible polarization P_r indicating a common origin of both of these properties.

Figure 8 shows plots of $(\overline{P_3^2})^{1/2}$ (determined from birefringence data) versus the temperature for several related BSKNN compositions, as indicated. BSKNN(2) shows a sharper drop of the P_d at the T_c while BSKNN(1) shows a slow decay of it. Although T_c for BSKNN(1) and BSKNN:Nd are 175 and 145 °C, respectively, their T_d values are almost the same.

The results reported here for BSN25, and several BSKNN materials, are similar to those found earlier[1] for BSN40. It appears that a local nonreversible polarization P_d starts to become observable below a dipole temperature T_d. The latter is several hundred degrees above the ferroelectric transitions. Related measurements have been re-

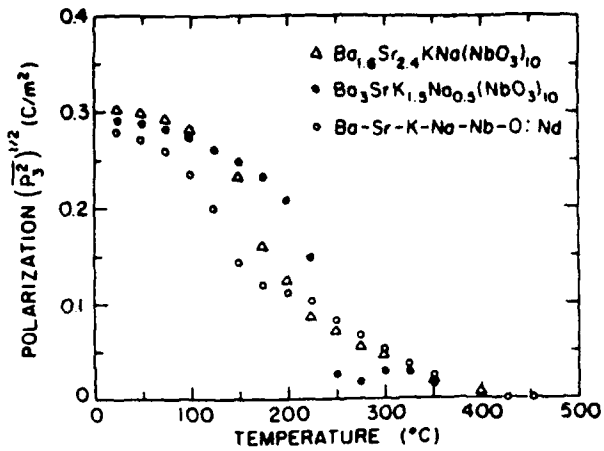

FIG. 8. $(\overline{P_3^2})^{1/2}$ data derived from optical birefringence measurements for BSKNN(1), BSKNN(2), and Nd doped BSKNN.

ported[13] in the tungsten bronze ferroelectric system $K_2Sr_4(NbO_3)_{10}$.

The optic index of refraction (Δn) and the strain (Δx) measurements yield similar P_d and T_d results. Experimentally, the optic index of refraction results are totally independent of strain measurements, each being interpreted by different coefficients (Table I). Thus, the qualitative and quantitative agreement [Figs. 5, 6, and 7(d)] for P_d and T_d in the ferroelectric systems measured here gives strong support to the interpretation that local, randomly orientated (along the $\pm c$ axis) polarization exists in these crystals far above T_c. Similar agreement was found previously.[1] We note, however, that the agreement of the Δn and Δx measurements results from general symmetry considerations and not from any detailed microscopic model. The fact that we expect $\Delta n \propto P^2$ and $\Delta x \propto P^2$ comes from the expectation that the high-temperature phase can be treated as centrosymmetric and any polarization (local or macroscopic) can be treated as an expansion about $P = 0$. Thus, the first term in an expansion will be a P^2 term.

Discussion of these and similar results in related materials has been reviewed.[2] Basically the effects have been discussed in terms of two microscopic models. Smolenskii[14] has emphasized compositional fluctuations with a dimension ~ 1 μm in order to understand these materials. On the other hand, Burns *et al.*[2,13,15] have emphasized compositional fluctuations on the scale of the dimension of a unit cell, and using these ideas, some of these types of results can be significantly understood with fluctuations on this (~ 4 Å) scale.[13,15] Work by Setter and Cross[16,17] support the small-scale fluctuations idea. They[16,17] studied $Pb(Sc_{1/2}Ta_{1/2})O_3$ and varied the degree of order on the B site (Sc^{3+} and Ta^{5+}) to obtain sharp or diffuse phase transitions by annealing and quenching the crystals. Since in their work the B site ions would be expected to diffuse a distance of only one or two unit cells, their results support the ideas of Burns *et al.*

It was suggested that dynamic polarization fluctuations in normal nonglassy uniaxial ferroelectrics will exist above T_c as a general property.[18] One can therefore, expect some perturbations to properties related to P_3^2 term. However, here we are considering a somewhat complicated situation as, for this type of glassy polarization fluctuation that is the implication of local chemical inhomogeneity, the correlated effective-field theory of ferroelectricity from which the nonglassy type polarization fluctuations are determined does not apply to the system as a whole. In tungsten bronze BSN solid solution family as addressed earlier, the chemical composition is homogeneous locally that allows the local symmetry to be lower than the global symmetry and prevents the establishment of short range correlations in chains along the incipient polar axis beyond the dimension of the local area. Sizes of these polar local regions are such that the orientations of the polarization are thermally reversible,[17] analogous to superparamagnetism.[19] The polarization fluctuation depends on the local polar island dimension distribution and hence is found prominent in broad temperature region well above the average Curie temperature, T_c. For T approaches to T_c, a polarization vector dynamic freezing-in model has been suggested[17] based upon the experimental evidence of the temperature dependence of the electrostrictive coefficients Q_{33} and Q_{13} measured on BSN60,[20] as both Q_{33} and Q_{13} are markedly temperature dependent and approach zero near T_c while Q_{11} is essentially independent of temperature to T_c.

To summarize, in these materials it appears that a local, nonreversible polarization can appear, below a temperature T_d that is far above the ferroelectric transition temperature (T_c). In the tungsten bronze crystals discussed here, T_d is in the 350–400 °C neighborhood and only weakly depending on the particular composition. The similarity of these T_d values probably is related to the similarity of the orientation sizes of the NbO_6 octahedra that play the fundamental polarization role.

[1] A. S. Bhalla, R. Guo, L. E. Cross, G. Burns, F. H. Dacol, and R. R. Neurgaonkar, Phys. Rev. B 36, 2030 (1987).
[2] G. Burns and F. H. Dacol, Ferroelectrics 104, 25 (1990); G. Burns, Phase Transitions 5, 261 (1985).
[3] S. C. Abrahams, P. B. Jamieson, and J. L. Bernstein, J. Chem. Phys. 54, 2355 (1971), and the references quoted there to their earlier papers.
[4] M. E. Lines and A. M. Glass, *Principles and Applications of Ferroelectrics and Related Materials* (Clarendon, Oxford, 1977).
[5] B. A. Scott, E. A. Giess, B. L. Olson, G. Burns, A. W. Smith, and D. F. O'Kane, Mater. Res. Bull. 5, 47 (1970).
[6] G. Burns, *Solid State Physics* (Academic, New York, 1985).
[7] R. L. Byer and C. B. Roundy, Ferroelectrics, 3, 333 (1972).
[8] G. Burns and F. H. Dacol, Phys. Rev. B 28, 2527 (1983); Jpn. J. Appl. Phys. 24, Suppl. 24-2, 85 (1986).
[9] A. M. Glass, J. Appl. Phys. 40, 4699 (1969).
[10] T. Shrout, Ph.D. thesis, Penn. State Univ., 1981.
[11] P. Asadipour, M. S. thesis, Penn State Univ., 1986.
[12] G. Burns and F. H. Dacol, Solid State Commun. 58, 567 (1986).
[13] G. Burns and F. H. Dacol, Phys. Rev. B 30, 4012 (1984); G. Burns, *ibid.* 13, 215 (1976).
[14] G. H. Smolenskii, Proceedings 2nd IMF, Kyoto, 1969. Phys. Soc. Jpn. 26 (1970).
[15] G. Burns and B. A. Scott, Solid State Commun. 13, 423 (1973).
[16] N. Setter and L. E. Cross, J. Appl. Phys. 51, 4356 (1980).
[17] L. E. Cross, Ferroelectrics 76, 241 (1987).
[18] M. E. Lines, Phys. Rev. B 5, 3690 (1972).
[19] L. Neel, Compt. Rend. Acad. Sci. 228, 664 (1949).
[20] C. Sundius, M. S. thesis, Penn State Univ., 1984.

APPENDIX 8

Microstructure-property relations in tungsten bronze lead barium niobate, $Pb_{1-x}Ba_xNb_2O_6$

C. A. Randall, R. Guo, A. S. Bhalla, and L. E. Cross
The Pennsylvania State University, Materials Research Laboratory, University Park, Pennsylvania 16802

(Received 4 January 1991; accepted 10 April 1991)

Transmission electron microscopy (TEM) has been used to explore details of the structural phase transitions and corresponding microstructural features in the solid solution of $Pb_{1-x}Ba_xNb_2O_6$ (PBN) tungsten bronze ferroelectrics at compositions embracing the morphotropic phase boundary between orthorhombic and tetragonal ferroelectric phases. In addition to the ferroelectric domain structures that were consistent with the expected symmetries, incommensurate ferroelastic phases were observed. The "onset" and "lock-in" transition temperatures are a function of the Pb/Ba ratio, and for lead-rich compositions it appears that the incommensurate distortion may occur above the ferroelectric Curie temperature in the paraelectric phase.

I. INTRODUCTION

The tungsten bronze structure and phase transitions

The tungsten bronze structure family is probably the second largest family of known oxygen octahedron based ferroelectrics.[1] The structure that has tetragonal symmetry in the paraelectric phase is defined by corner linked oxygen octahedra, and the section normal to the tetragonal c axis is shown in Fig. 1.[2,3] Chemically, it may be described by a formula of the form $[A1(A2)_2C_2][B1(B2)_4]O_{15}$, where combinations of larger monovalent (K^+, Na^+, Rb^+), divalent (Pb^{2+}, Ba^{2+}, Sr^{2+}, Ca^{2+}), and trivalent (La^{+3}, Eu^{+3}, Gd^{+3}) and similar ions occupy the square and pentagonal shaped tunnels, A1 and A2 sites (Fig. 1). Only very small ions such as Li^+ can occupy the small triangular channels, C-sites, and small but highly charged cations such as Nb^{5+}, Ta^{5+}, Ti^{4+}, Zr^{4+}, etc. occupy the octahedral B1 and B2 sites. Frequently, in consistence with charge balance, not all sites are occupied, and the very large variation in cation radii leads to many complex end member compounds and innumerable solid solutions, which satisfy the conditions to support ferroelectric phases.[4,5]

In spite of the immense chemical flexibility in the tungsten bronze structure systems, only two types of ferroelectric phases are known. In terms of the point symmetries the paraelectric prototype form is always in point group $4/mmm$. In the orthorhombic ferroelectric form the spontaneous polarization P_s is along one of the twofold axes $\langle 001\rangle_P$ (of point group $mm2$) or $\langle 110\rangle_P$ (denoted as point group $m2m$) where the suffix indicates that the orientation refers to the original prototypic axial system (see Fig. 1). In the tetragonal ferroelectric form the symmetry is $4mm$ and two domain states have P_s oriented along $[001]_P$ and $[00\bar{1}]_P$. Both orientation states are fully consistent with the group theoretical prediction of Aizu and Shuvalov.[6,7] The tetragonal states exhibit only 180° domain walls, while in the orthorhombic ferroelectric states both 180° and 90° walls occur.

In 1981, Schneck *et al.* reported incommensurate satellite reflections in the tungsten bronzes $Ba_2NaNb_5O_{15}$ (BNN) and $Sr_2KNb_5O_{15}$ (SKN).[8-11] At present many crystals are known to have incommensurate phases. These incommensurate phases are periodic but their periodicity is not fixed by a three-dimensional lattice.

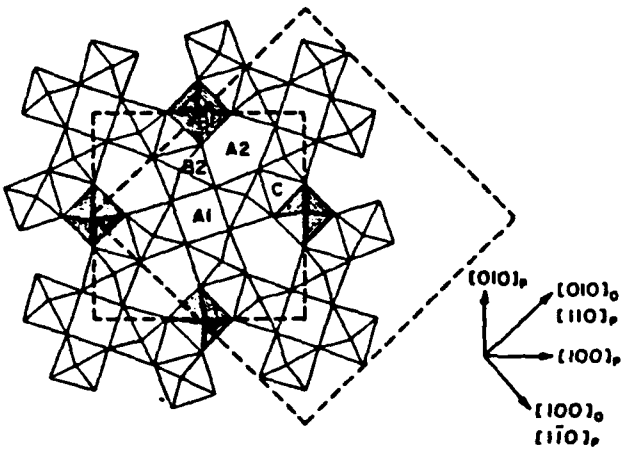

	Crystallographical Site	Number of Coordinations	Number of Positions
□	A1	12	4
⬠	A2	15	2
◈	B1	6	2
◈	B2	6	8
△	C	9	4

FIG. 1. The generalized crystallographic structure of tungsten bronze compositions with the indicated A, B, and C sites.

Incommensurate periodicity can be due to a number of different phenomena such as atomic displacements or occupancy of cations or anions.[11] The origin of incommensurability in the tungsten bronze family is presumably associated with the displacive structural change owing to ferroelastic octahedral tilting.[10–18]

Many of the displacive incommensurate structures 'lock-in' to low temperature commensurate superstructures.[15,19] The degree of incommensurability, δ, reduces to zero at the lock-in transition temperature. The incommensurability parameter, δ, is defined as the ratio of the difference between the distance of two adjacent superlattice reflections $(x - y)$ parallel to $\langle 100 \rangle_p$ divided by the total distance between those points $(x + y)$.

$$\delta = \frac{x - y}{x + y} \tag{1}$$

Thus at lock-in there is an equal and rational spacing between these superlattice reflections and matrix reflections giving $\delta = 0$. Corresponding microstructural changes also take place in the crystals close to the lock-in transition; commensurate domains within the crystal begin to grow. These commensurate domains can be out-of-phase with each other, and at a place where two domains join, a wall known as a discommensuration may be formed. The discommensuration density, D, is inversely related to the magnitude of the incommensurability parameter, δ; i.e., as $\delta \rightarrow 0$, $D \rightarrow \infty$.[12] However, there are some exceptions to this behavior where the incommensurability locks-in to a so-called 'quasi-commensurate' state, and the tungsten bronze family appears to be of this type. In the case of the tungsten bronzes BNN, SKN, and SBN $[(Sr, Ba)Nb_2O_6]$, incommensurability reduces to about $\delta \approx 1\%$ but does not go to zero; a quasi-commensurate structure exists along with a low density of discommensurations. Reasons for this are still not clear, but point defect pinning the motion of the discommensuration walls during growth is a popular suggestion.[15]

The majority of the detailed work on the incommensurate tungsten bronze phases has been on $Ba_2NaNb_5O_{15}$ (BNN).[12,15,17,18] The suggested sequences of phase transitions in this crystal are summarized in Table I.

Table I shows a generalized summary of much of the work on BNN, but many uncertainties remain. There is, however, agreement that two incommensurate phases exist, namely $1q$ and $2q$. The $1q$ phase is an orthorhombic phase with a modulation existing along a single direction, whereas the $2q$ phase corresponds to a tetragonal symmetry and there exist modulations in two perpendicular directions. These $1q$ and $2q$ phases are well illustrated in a study on BNN by Barre *et al.*[15] The $1q$ phase is stable over $2q$ for the lower temperatures in the incommensurate phase range. The $2q$ phase is more stable at the higher temperatures. At the lock-in temperature, $T_L \approx 250$ °C, there is a reduction of the incommensurability parameter, δ, to develop a quasi-commensurate low temperature state. The lower temperature phases are not fully understood at this time and are still topics of debate.[18]

TABLE I. Phase transitions in BNN.

Paraelectric	
4/mmm	
Paraelastic	
	+580 °C
Paraelastic	
4mm	
Ferroelectric	
	+300 °C
Ferroelectric + mixed incommensurate ferroelastic phases $1q$ and $2q$	
	+250 °C
Quasi-commensurate ferroelastic	
Ferroelectric (*mm2*)	
Other phases reported[18]	

The $Pb_{1-x}Ba_xNb_2O_6$ tungsten bronze compositions studied here are of special interest owing to their potential application in a bistable optical switching device. The ferroelectric phases are tetragonal ($4mm$) or orthorhombic ($m2m$), depending on the composition.[19,20] As can be observed from the phase diagram,[21] Fig. 2, the Ba-rich side is tetragonal and the Pb-rich side is orthorhombic. These two phases meet at a morphotropic phase boundary close to PBN: $1 - x = 0.63$. This morphotropic phase boundary is curved, allowing a first order tetragonal → orthorhombic phase transition to occur for a few restricted compositions close to this boundary. In these crystals the phase change can b

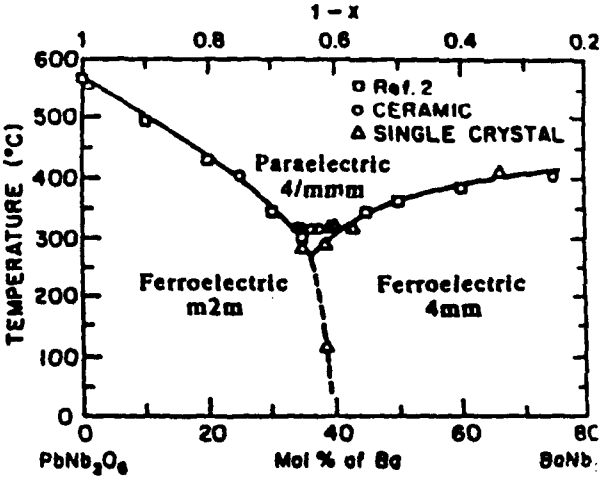

FIG. 2. Phase diagram of the tungsten bronze solid solu $Pb_{1-x}Ba_xNb_2O_6$ over the range $0.2 \leq 1 - x \leq 1.0$.[20]

effected either by changing temperature or by applying an appropriately oriented electric field. Hence, it is possible to electrically switch an optical indicatrix from uniaxial to biaxial symmetry.

Until recently these tetragonal and orthorhombic phases were believed to be the only ferroelectric phases existing within the tungsten bronze family; however, a study of dielectric and pyroelectric properties at low temperatures has shown additional anomalies.[22,23] These anomalies, as shown in Fig. 3, are very reminiscent of the relaxor anomalies found in many of the complex lead perovskites such as $Pb(Mg_{1/3}Nb_{2/3})O_3$.[24] These anomalies were found in the PBN single crystal plates of the compositions close to the morphotropic phase boundary at temperatures well below the paraelectric → ferroelectric phase transition. The dielectric constant measurements were made perpendicular to the polar axis. The present understanding of these relaxor anomalies in the PBN are small thermal agitations of the polar vector about the polar direction, but this still has to be substantiated. In addition to these transitions we also have reported the presence of incommensurate phases within the PBN.[21]

The aim of this paper is to study and classify the various domain microstructures existing in the PBN tungsten bronze system. The incommensurate ferroelastic phases are described and are found to vary with composition and temperature. The microstructural and crystallographic features of these ferroic phases within the PBN are related to macroscopic anomalies in dielectric and optical properties.

II. EXPERIMENTAL PROCEDURE[25]

Ceramic specimens were prepared from high purity chemicals using conventional techniques of milling, prefiring, crushing, pressing, and firing. The specimens were prepared in the form of disks ~10 mm in diameter and ~1.2 mm thick. The final sintering times and temperatures, which depended on composition, were between 1280 °C and 1320 °C for 1 to 6 h. To compensate for PbO loss during the calcination, 3 wt.% of excess PbO was added. Well-reacted PBN ceramics with 94–99% theoretical density and 3 to 6 μm grain size were produced. The composition chosen for TEM study was $Pb_{1-x}Ba_xNb_2O_6$, where $(1-x) = (0.75, 0.65, 0.61, 0.60, \text{and } 0.25)$.

Single crystal specimens were prepared by the Czochralski growth technique. Starting from high purity chemicals, the charge was heated in a Pt crucible by RF induction up to the melting temperature. Each crystal was then withdrawn at a rate of 1 to 2 mm/h along with constant rotation of the crucible and the crystal boules. The crystal was slowly cooled to room temperature in a time period of 48 h. Single crystals several millimeters in size and of optical quality were achieved even though some cracking of the boule occurred during the cooling procedure, probably when the crystal passed through the paraelectric to ferroelectric phase transition.

TEM thin sections were prepared by grinding and polishing to ~50 μm and then ion-beam thinning of the samples after being mounted on 3 mm copper grids. Transmission electron microscopy was performed on a Philips 420 STEM, and a double-tilt liquid nitrogen cold stage made by Gatan was used for low temperature analysis, $-168\ °C \leqslant T \leqslant 80\ °C$.

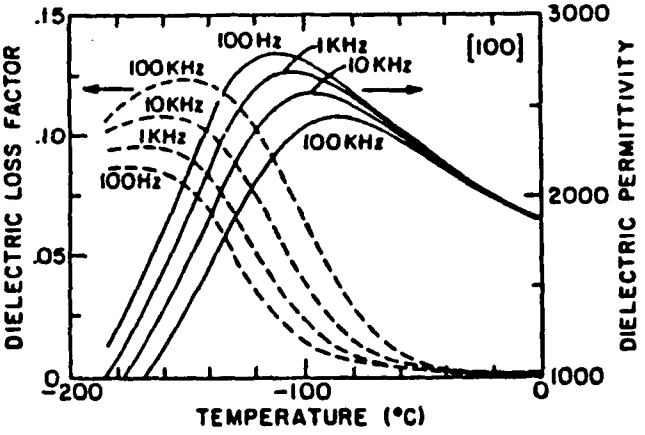

FIG. 3. Typical low temperature anomaly in the dielectric constant perpendicular to the polar direction in PBN single crystals with compositions close to the morphotropic phase boundary ($1-x = 0.57$). Note the strong frequency dependence in dielectric permittivity and loss.

III. RESULTS

The tetragonal ferroelectric $Pb_{0.25}Ba_{0.75}Nb_2O_6$ (PBN: $1-x = 0.25$) was studied at room temperature to liquid nitrogen temperatures. Typical 180° or inversion domain boundaries are observed with dark-field imaging of the diffraction vector, $\mathbf{g} = (001)_P$, as seen in Figs. 4(a) and 4(b). The contrast of the 180° regions in neighboring domains is the result of the noncentrosymmetric nature of the crystals. The diffraction intensities of hkl and $\overline{hkl}$ are not equal, and hence there is a contrast difference.[26]

The orthorhombic phase ($m2m$) compositions $Pb_{1-x}Ba_xNb_2O_6$ (PBN: $1-x = 0.65$ and 0.75) were studied. The orthorhombic symmetry is the result of Nb–O displacements in the $\langle 110\rangle_P // \langle 010\rangle_O$ directions. This gives rise to 90° twin ferroelectric domains on $\{100\}_P // \{110\}_O$ habit planes and also 180° domains with no fixed habit plane. Selected area diffraction of the 90° twin domains shows electron spot splitting parallel to the diffraction vector $\mathbf{g} = (110)_O$, as observed in the inset of Fig. 5(b). Also, α-fringe contrast is observed in Fig. 5(b), marked "a", and these correspond to an inclined 180° domain wall.[25]

Compositions of PBN near the morphotropic phase boundary were also chosen for study with PBN:

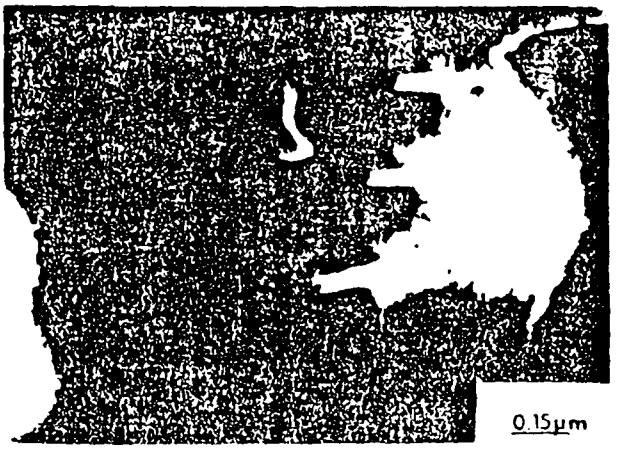

(a)

(b)

FIG. 4. (a, b) Dark-field micrograph using $\mathbf{g} = (100)_p$, revealing 180° domains in PBN ($1 - x = 0.25$) at room temperature.

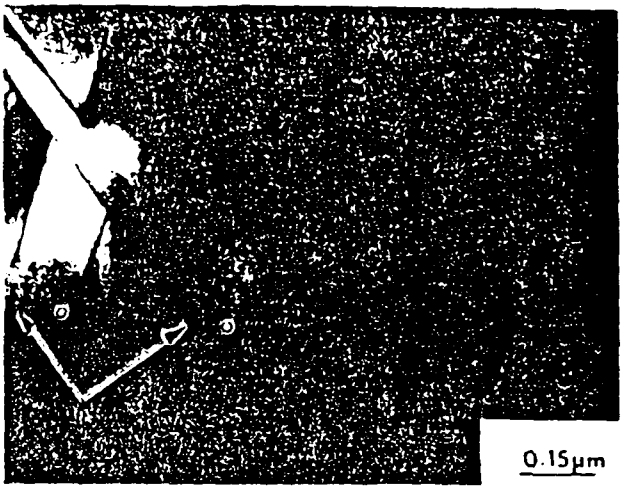

(a)

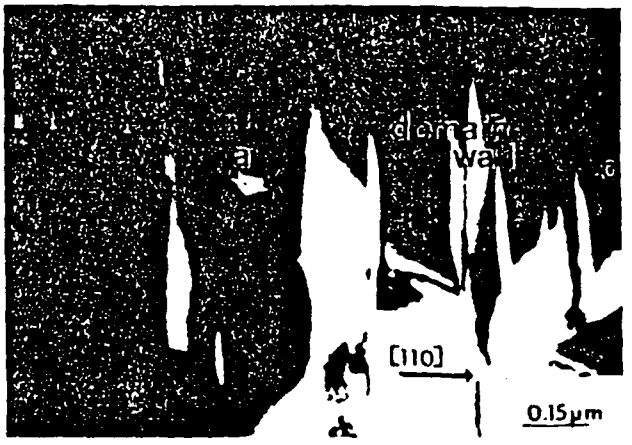

(b)

FIG. 5. (a, b) Electron micrographs of orthorhombic PBN: $1 - x = 0.75$ and 0.65, respectively. Both show a complex configuration of ferroelectric 180° and 90° domains. Figure (b) has an inset that reveals spot splitting perpendicular to the 90° twin walls and also an α-fringe marked "a". The α-fringe is an inclined 180° domain wall.

$1 - x = 0.61$ and 0.60. For the compositions studied here, PBN: $1 - x = 0.60$, the ferroelectric is on the tetragonal side of the phase boundary and 180° domains are observed; see Fig. 6(a). The fine-scale texture of a discommensuration structure is also observed in the background; this will be discussed in more detail below. Cooling this sample to liquid nitrogen did not induce the orthorhombic ferroelectric phase, so we assume the morphotropic phase boundary does not cross this composition. Changes in Pb-stoichiometry (owing to high volatility) under the electron beam and during thin foil preparation may also be a problem and hence could explain why the tetragonal → orthorhombic phase transition was not observed. This is especially true when subtle changes in composition strongly affect the nature of the phase transition, as is the case near the morphotropic phase boundary.

Comparisons of the selected area electron diffraction patterns in $\langle 001 \rangle_p$ orientation show the presence of a set of commensurate superlattice reflections $(h + 1/2, k + 1/2, 0)_p$. However, the relative strength of this superlattice varies with composition. The PBN: $1 - x = 0.75$, orthorhombic crystals/grains have a strong $(h + 1/2, k + 1/2, 0)_p$ superlattice, Fig. 7(a). But, the more Ba-rich composition PBN: $1 - x = 0.25$ does not. Figure 7(b) shows (001) zone axis electron diffraction patterns at room temperature for PBN: $1 - x = 0.25$ for comparison; the superlattice is weak and diffuse even at the lower temperatures. The $\{h + 1/2, k + 1/2, 0\}_p$ superlattice has also been observed by Bursill and Peng in tungsten bronz

(a)

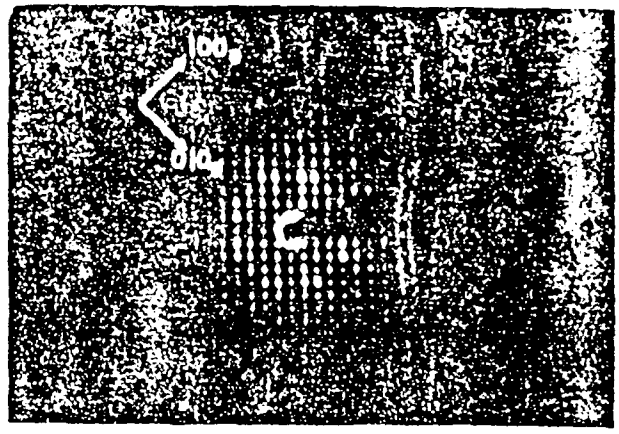

(c)

(b)

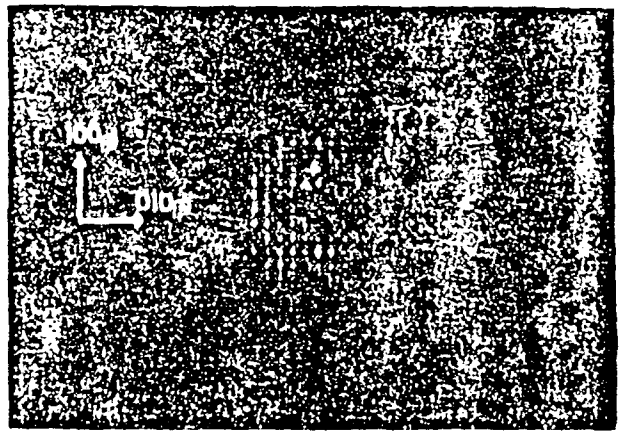

(d)

[illegible] Micrographs of domain structures in PBN [illegible] PBN at room temperature. Bright-field and (b) [illegible] a mixture of [illegible] ferroelectric domains and a fine textured discommensurate structure [illegible] a.

[illegible] tured $Sr_{1-x}Ba_xNb_2O_6$. In their study they found additional superlattice reflections appearing at lower temperatures (~ 150 °C), no such superlattice reflections were found in this study on PBN at any composition, [illegible] 2.8 < x < 0.75, and to temperatures as low as -170 °C.

At the onset we stated that PBN compositions close to the morphotropic phase boundary have an additional low temperature relaxor like anomaly in dielectric and pyroelectric studies [illegible]. In this TEM study no evidence of domain superlattices or satellites could be associated with this phenomenon. The reason for this is most likely that the temperature region studied by TEM was not sufficiently low to freeze in the more polar regions [illegible].

In addition to the incommensurate superlattice reflections [illegible] there are incommensurate superlattices also present in the PBN compositions

These incommensurate superlattices [illegible] degrees of incommensurability as determined by the δ parameter and the dark field images of the incommensurate structures. Figures [illegible] of these room temperature [illegible] diffraction patterns for compositions PBN [illegible] 0.60 and 0.75 respectively. The respective room temperature incommensurability parameter is [illegible] and 2. Hence the orthorhombic PBN [illegible] Ladderich composition is at room temperature in a quasi-incommensurate state. This can also be observed from corresponding dark field images of the incommensurate spots. The dark boundaries in [illegible] are discommensuration structures in Fig. [illegible]. We will discuss these in more detail below.

For PBN [illegible] single crystal [illegible] and δ parameter changes from [illegible] increase to 4 at -140 °C. The [illegible]

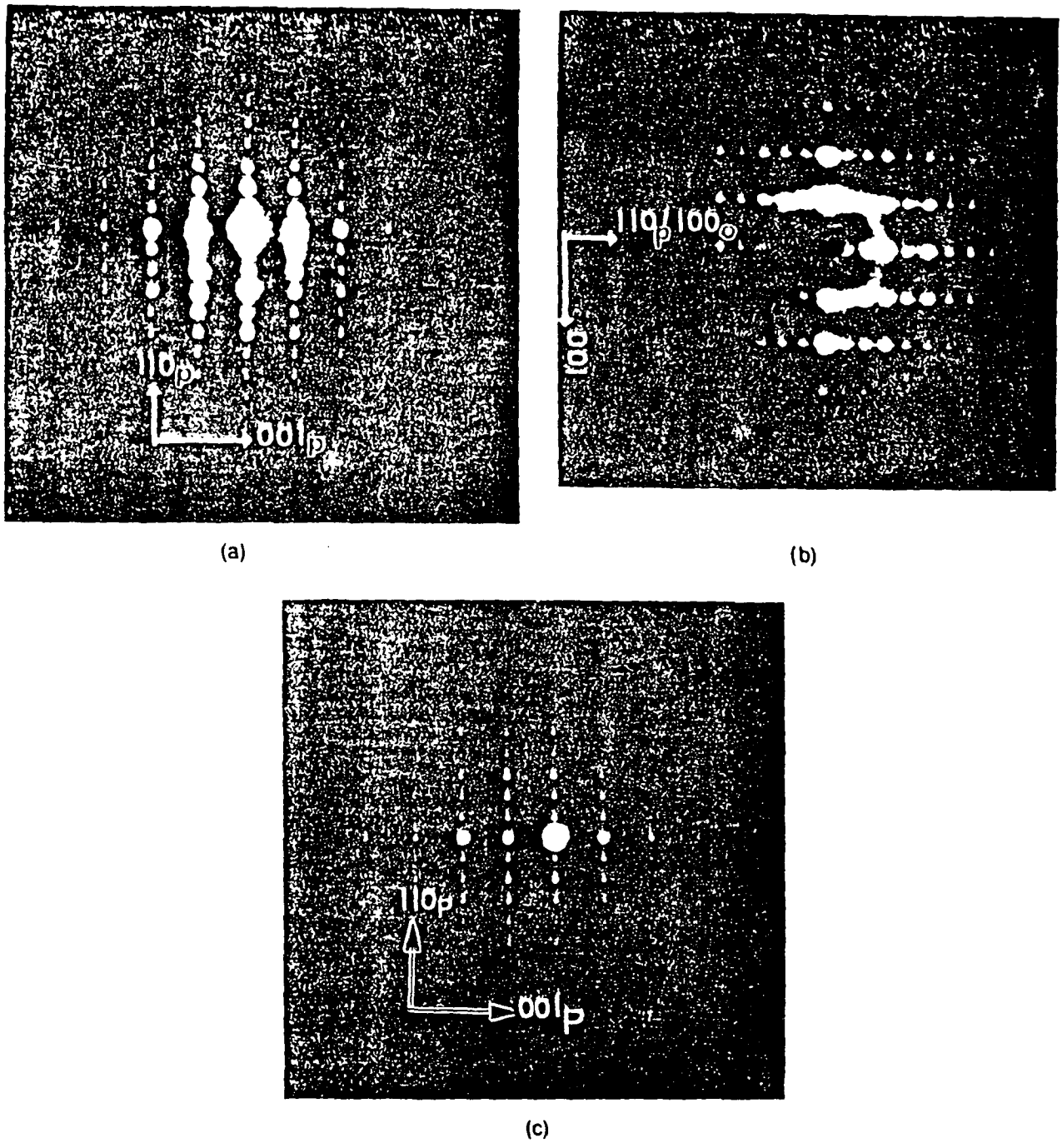

FIG. 8. Comparison of PBN (110) electron diffraction patterns at room temperature. PBN: $1 - x$ = (a) 0.25, (b) 0.60, and (c) 0.75, respecti

discommensurate microstructure is shown in Fig. 9(a), and is similar to discommensurate structures in the mixed $2q$ and $1q$ phase, as observed by Barre *et al.*, in BNN.[15] The discommensurate microstructures in PBN compositions change easily close to the morphotropic phase boundary. It is easy to switch to a finely textured discommensurate microstructure during the electron microscopic observations, as seen in Fig. 6(b). This ferroelastic switching is obtained by local heatin the electron beam that gives rise to strain grad owing to thermal expansion. These strain grad are believed to be strong enough to switch the f elastic domains. Figures 6(a) and 6(b) show f aligned discommensurate structures co-existing 180° ferroelectric domains. The aligned discomm rates are parallel to the diffraction vector $\mathbf{g}$ = (1

(a)

(a)

(b)

FIG. 9. (a) Room temperature discommensuration structure of single crystal PBN $1 - x = 0.61$. (b) shows the dark-field diffraction condition and also evidence of streaking of the incommensurate superlattice reflections (see inset).

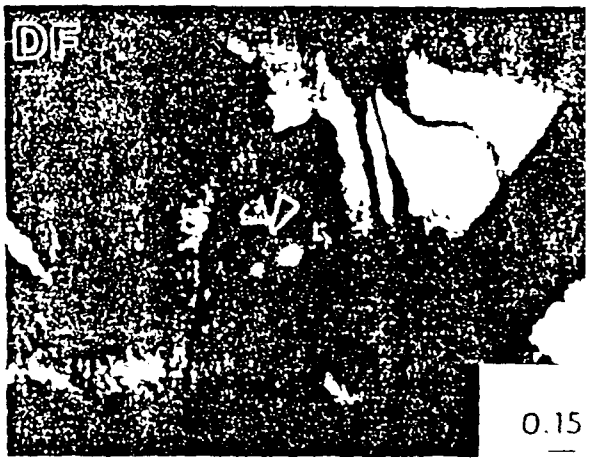

(b)

FIG. 10. (a) Discommensuration and ferroelectric microstructure PBN $1 - x = 0.75$. Note that the discommensuration microstru are independent of the ferroelectric domains. (b) shows discon suration node structure.

or $(100)_0$. The diffuse streaking along $(100)_c$ in the diffraction pattern Fig. 9(b) is thought to be related to the fine textured discommensurates, as it is perpendicular to their habit and observed only when they are present.

Returning to Fig. 10, a number of important features are to be noted. The discommensurate structures are aligned parallel to $(010)_o$. Also, the discommensurations are continuous across 90° and 180° domains. This implies to us that the 'lock-in' incommensurate transition was independent of the ferroelectric transition. This complex domain configuration and phase mixing can be possible only by the lock-in transition occurring in the paraelectric phase, which is not the case with other tungsten bronze phases. Also, from the discommensurate configurations a phase shift of $\pi/2$ in the modulation can be determined by the fourfold node lines, this is similar to findings in BNN and 2H $TaSe_2$.[14,20]

IV. DISCUSSION

The PBN solid-solution shows a complex ing of ferroelectric and incommensurate ferroe phase domains. The incommensurate phase and electric phases are sensitive to composition. Dif incommensurate parameters, δ, are found at temperature along with different discommensu structures and densities.

One of the most surprising results deduced co the lock-in transition in the orthorhombic PBN c sitions. With the discommensurate structures sh continuity through the ferroelectric 180° and 90° d structures, one has to conclude the quasi-commer lock in occurred before the paraelectric → ferroe transition. This is not the case with the prev

studied SBN and BNN tungsten bronzes, which have the sequence of transitions found in Table II.

To confirm our conclusions about the departure from the previous trends of phase sequences known in tungsten bronze, we made an additional study on the temperature dependence of the birefringence in PBN single crystals.[25] Figure 11 shows the transmitted intensity variation as a function of temperature during a cooling run for PBN: $1 - x = 0.65$ of orthorhombic symmetry. Besides a first-order-like phase transition (at ~213 °C during a cooling run) that corresponds to the ferroelectric orthorhombic $m2m$ to tetragonal paraelectric $4/mmm$ phase transition, a continuous or rather smooth but unambiguous phase transition can be detected at temperatures near 322 °C during both cooling and heating runs. No prominent dielectric anomaly other than a small kink has been observed in this temperature region. We thus suggest that this anomaly is the incommensurate transition as inferred by the TEM domain microstructural observations. As we know that incommensurate phase transition is always a second order,[30] it is not surprising to us that the birefringence, being a polar second rank tensor property, is more sensitive to the onset of incommensurate modulations than other techniques such as dielectric measurements. Further results regarding the optical studies will be found in later papers.[31] For the Ba-rich compositions the incommensurate lock-in phase transition is below the paraelectric-ferroelectric transition and corresponds more closely to the phase sequences in BNN and SBN tungsten bronzes.

The dielectric and x-ray characterization of the PBN agrees well with the TEM observations, as reported earlier.[21,23,25] However, no evidence was found for domains/polar regions being associated with the low temperature relaxor-like anomalies close to the morphotropic phase boundary. The reason for this is probably that lower temperature observations would be required to eliminate electron beam heating contributions from thermal excitations, preventing a freezing-in of the domains.

V. CONCLUSIONS

Solid solutions of tungsten bronze lead barium niobate, $Pb_{1-x}Ba_xNb_2O_6$, have been studied by TEM techniques. Ferroelectric 180° domains have been characterized in the tetragonal part of the phase diagram.

TABLE II. Phase sequences in tungsten bronze BNN and SBN.

(4/*mmm*)		(4*mm*)		(*mm*2)
Paraelastic		Paraelastic		Ferroelastic
Paraelectric	→	Ferroelectric	→	Ferroelectric

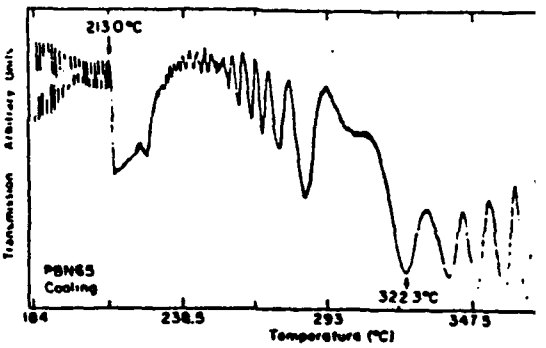

FIG. 11. Transmitted intensity recorded as a function of te in a cooling run for PBN = 0.65 sing crystal i the birefringence. The light (λ = 633 nm) pro ted per to both the $[010]_p$ and the $[001]_p$ directions.

With the orthorhombic compositions 90°-tw 180° inversion ferroelectric domains were o A ferroelastic incommensurate phase is found throughout the phase diagram. The degree of mensurability varies with temperature and com Discommensuration structures are observed an phase modulation is deduced from the micr From the combined TEM and birefringenc of PBN it is suggested that the quasi-comm 'lock-in' transition occurs within the par phase in compositions $(1 - x) \geq 0.63$, mak orthorhombic PBN different from previous ferr incommensurate behavior in the tungsten bronze

ACKNOWLEDGMENTS

We wish to acknowledge and thank the f for their support: ONR and DARPA. Also, than Dr. Steven Markgraf and Dr. Thomas Shrout f useful discussions regarding tungsten bronzes. also to J. Baney for typing this manuscript.

REFERENCES

1. E. Lines and A.M. Glass, *Principles and Appl electrics and Related Mate* (Oxford Unive Oxford, 1977).
2. S.C. Subbarao, G. Shirane, and F. Jona, Acta Cry (1960).
3. P.B. Jamieson, S.C. Abrahams, and J.L. Bernstein Phys. 48, 5048 (1968).
4. Landolt-Bornstein, *Ferroelectric and Antiferroelectri* (Springer-Verlag, New York, 19
5. I. Vainshtein, V.M. Fridkin, and V.L. Indebo *tallography II* (Springer-Verlag, Berlin, Heide York, 1982).
6. K. Aizu, Phys. Rev. 140 (2A), A590 (1965).
7. L.A. Shuvalov, J. Phys. Soc. Jpn. 28S, 38 (1970).
8. J. Schneck and F. Denoyer, Phys. Rev. B 23, 383 (1
9. J. Schneck, J.C. Toledano, R.W. Whatmore, and F Ferroelectrics 36, 327 (1981).
10. C. Manolikas, Phys. Status Solidi (a) 68, 653 (1981
11. L.A. Bursill and J.L. Peng, Philos. Mag. B 54 (2),

12. T. Janssen and A. Janner, Adv. Phys. 36 (5), 519 (1987).
13. C. Manolikas, J. Schneck, J.C. Toledano, J.M. Kiat, and G. Calvin, Phys. Rev. B 35 (16), 8884 (1987).
14. X.Q. Pan, H.S. Hu, M.H. Yao, and D. Feng, Phys. Status Solidi (a) 91, 57 (1985).
15. S. Barre, H. Murka, and C. Roneau, Phys. Rev. B 38 (13), 9113 (1988).
16. J.L. Peng and L.A. Bursill, Acta Cryst. B 43, 504 (1987).
17. M. Vermerft, G. Van Tendeloo, J.V. Landupt, and S. Amelinckx, Ferroelectrics 88, 27–36 (1988).
18. W.F. Oliver and J.F. Scott, 1st USA-USSR Meeting on Ferroelectrics, Colorado (1989).
19. M.H. Francombe, Acta Cryst. 13, 131 (1960).
20. E.C. Subbarao, G. Shirane, and F. Jong, Acta Cryst. 13, 226 (1960).
21. R. Guo, A.S. Bhalla, C.A. Randall, Z.P. Chang, and L.E. Cross, J. Appl. Phys. 67 (3), 1453 (1990).
22. L.E. Cross, Ferroelectrics 76, 241 (1987).
23. R. Guo, A.S. Bhalla, C.A. Randall, and L.E. Cross, J. Appl. Phys. 67 (10), 6405 (1990).
24. G.A. Smolenskii, J. Phys. Soc. Jpn. 28 (Suppl.), 26 (1970).
25. R. Guo, Ph.D. Thesis, The Pennsylvania State University, University Park, PA (1990).
26. R. Gevers, H. Blank, and S. Amelinckx, Phys. Status Solidi 13, 449 (1966).
27. C.A. Randall, D.J. Barber, and R.W. Whatmore, J. Microsc. 45, 275 (1987).
28. C.A. Randall, D.J. Barber, R.W. Whatmore, and P. Groves, Ferroelectrics 76, 265 (1987).
29. K.K. Fung, S. McKernan, J.W. Steeds, and J.A. Wilson, J. Appl. Phys. C 14, 5417 (1981).
30. D. Weigel, Phase Transitions 16/17, 341 (1989).
31. R. Guo, D.A. McHenry, A.S. Bhalla, and L.E. Cross (in preparation).

APPENDIX 9

Ferroelectrics, 1991, Vol. 118, pp. 77–83
Reprints available directly from the publisher
Photocopying permitted by license only

PYROELECTRIC PROPERTIES OF LEAD BARIUM NIOBATE SINGLE CRYSTALS

R. GUO, A. S. BHALLA and L. E. CROSS
Materials Research Laboratory, The Pennsylvania State University, University Park, PA 16802 USA

(Received February 18, 1991)

The temperature dependence of the pyroelectric coefficients of lead barium niobate $Pb_{1-x}Ba_xNb_2O_6$ (PBN) single crystals were investigated using the Byer-Roundy technique. Pyroelectric coefficients were found to be enhanced in single crystals of the near-morphotropic phase boundary (MPB) compositions. High pyroelectric coefficients (336 $\mu C/m^2$-K, $1 - x = 0.684$) and switchable polarization vectors between the two perpendicular crystallographic directions ([001] and [110]) in crystal of near-morphotropic phase boundary composition ($1 - x = 0.615$) were found to be of interest for pyroelectric device applications.

INTRODUCTION

A most interesting solid solution in the family of tungsten bronze ferroelectrics is that between $PbNb_2O_6$ and a hypothetical end member $BaNb_2O_6$, namely, lead barium niobate, $Pb_{1-x}Ba_xNb_2O_6$ (PBN[1 − x]%).[1-7] Ferroelectric PBN has recently regained its intriguing importance because it is a lead-containing tungsten bronze type ferroelectric relaxor with a morphotropic phase boundary (MPB) and has potential in electrooptic applications. The morphotropic phase boundary in this solid solution system separates a tetragonal ferroelectric phase 4*mm* (with polarization vector along ⟨001⟩) and an orthorthombic ferroelectric phase m2m (with polarization vector along ⟨110⟩).[5] Since there is no coupling between the fourfold ([001]) and the twofold (⟨100⟩ or ⟨110⟩) axes in the prototype 4/mmm tetragonal symmetry, the two polarization modes adjacent to the morphotropic phase boundary are unrelated and have separate Curie-Weiss temperatures as well as distinct ferroelectric characteristics. Large dielectric,[8] piezoelectric,[9] and pyroelectric (in polycrystalline samples by Lane *et al.*)[10] properties of PBN compositions were reported and enhanced properties in near the MPB compositions were expected.

The earlier research (before 1980s) on PBN were based on measurements on the polycrystalline ceramic form, primarily due to the lack of single crystals. It was reported that pyroelectric coefficient p showed sharp maxima at compositions close to the morphotropic phase boundary[10] with $p = 270$ $\mu C/m^2$-K (measured by radiation heating method) for $Pb_{0.6}Ba_{0.4}Nb_2O_6$ ceramic sample. Pyroelectric coefficients of PBN single crystals of several compositions were also reported[9]; however, the pyroelectric properties in relation to the MPB and the crystallographic phase transition have not yet been studied.

A comprehensive investigation of the phase relations and the polarization mechanisms of PBN solid solution in the near morphotropic phase boundary compositions has been carried out by this group.[11] It was discovered that close to the

morphotropic phase boundary in a Pb-rich composition ($1 - x = 0.615$) the sample actually goes through a phase transition (at $T \sim 125°C$ via heating) from the ferroelectric orthorhombic phase to the ferroelectric tetragonal phase during which the polarization axis switches from the ⟨110⟩ direction to the c-axis. A PBN phase diagram is shown in Figure 1 in which a curved morphotropic phase boundary into the Ba-rich side is indicated.[11] It was also demonstrated optically that such morphotropic phase transition can be induced electrically.[12] This behavior of the sample should be studied in view of its pyroelectric properties to further understandings of the polarization mechanisms and the potential applications of the PBN single crystals.

In the present paper the results of pyroelectric property study will be reported and interpreted in relation to the crystallographic structure and phase transitions of the PBN solid solution system. High remanent polarization and pyroelectric coefficients in compositions near the MPB were found to be particularly intersting for pyroelectric device applications.

SPECIMEN PREPARATION

Single crystal specimens used for this investigation were prepared by the Czochralski pulling technique. Starting from high purity chemicals, the charge was heated in a Pt crucible by RF induction heating to the melting temperature. Crystal was withdrawn at a rate of 1 to 2 mm/hour along with rotations of crucible (at -5 rpm) and the crystal boule (at $10 \sim 15$ rpm). After the growth run was completed, the crystal was slowly cooled to room temperature in 48 hours. Transparent single crystals of the size of several millimeters of optical quality were thus obtained even though some cracking problems occurred during the slow cooling probably when the crystal passed through the paraelectric to ferroelectric phase transition. After annealing at 550°C for 5 hours, crystals were cleaned in acetone and then sputtered with Au electrodes on both faces for pyroelectric measurements.

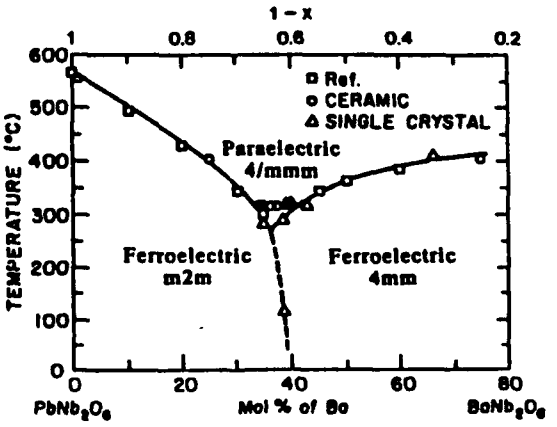

FIGURE 1 Phase diagram of $Pb_{1-x}Ba_xNb_2O_6$ solid solution system with the phase transition temperatures marked as they would appear during heating. The reference in the figure refers to Subbarao *et al.* (1960), Reference 7.

The composition quoted in the text, tables, and figures as PBN[(1 − x)%] where (1 − x)% is the mole percent of $PbNb_2O_6$ in $Pb_{1-x}Ba_xNb_2O_6$ composition, refers to the post-growth analytical composition as determined by electron microprobe analysis. The crystal orientations used in this paper are based on the prototype tetragonal 4/mmm symmetry unless otherwise specified.

MEASUREMENT TECHNIQUES AND PROCEDURE

A method developed by Byer and Roundy[13] for measuring pyroelectric coefficients was used in this work. Essentially, a prepoled or on-site poled specimen was mounted inside a specially designed sample holder in an air oven and short circuited during the measurement. The pyroelectric current I was measured using a high sensitivity (10^{-2} pA) picoammeter (model 4140B, Hewlett-Packard, Palo Alto, Ca.). The heating rate dT/dt was carefully programmed and controlled by computer interfacing to maintain constant (usually 2 to 4°C/min) while liquid nitrogen gas was used as cooling media.

The pyroelectric coefficient p was calculated from the pyroelectric current using the following equation:

$$p(T) = \frac{I}{A(dT/dt)} \text{ (C/m}^2\text{-K)}$$

where A is the electrode area and dT/dt is the rate of heating.The polarization can be calculated by integrating the pyroelectric current:

$$P = \int p\,dT = \frac{1}{A(dT/dt)} \int I\,dT(\text{C/m}^2)$$

In this study, all specimens were poled inside the sample holder before measurement. The poled sample was short circuited at the starting temperature of the measurement for at least 10 minutes to eliminate surface charges. In the case of the highest temperature measured being lower than the phase transition temperature, ΔP rather than P was obtained.

RESULTS AND DISCUSSION

For ferroelectric tetragonal single crystal PBN34, the polar vector is parallel to the [001] direction, therefore large pyroelectric coefficient was observed in the [001]-cut crystals as shown in Figure 2. For ferroelectric orthorhombic single crystal PBN68.4, as evinced in Figure 3, the spontaneous polarization is parallel to the [110] direction therefore pyroelectric measurement on the [010] direction yielded large pyroelectric coefficient. As of the single crystal PBN61.5, it has orthorhombic symmetry at room temperature with polar vector parallel to the [110] direction and tetragonal symmetry at temperatures higher than ~125°C with the polarization along the [001] direction, therefore measurements on two principle directions can give a general picture of the polarization sense in the material. Measured along the [010] direction, Figure 4, the spontaneous polarization first went through a

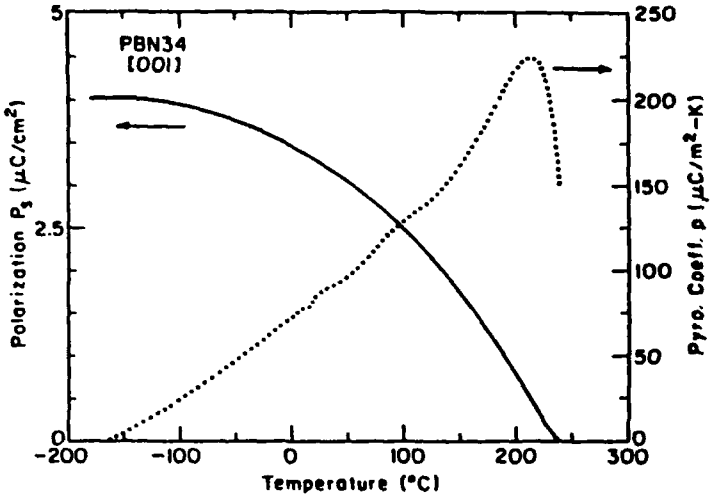

FIGURE 2 Change of the spontaneous polarization and the pyroelectric coefficient versus temperature for tetragonal PBN34.

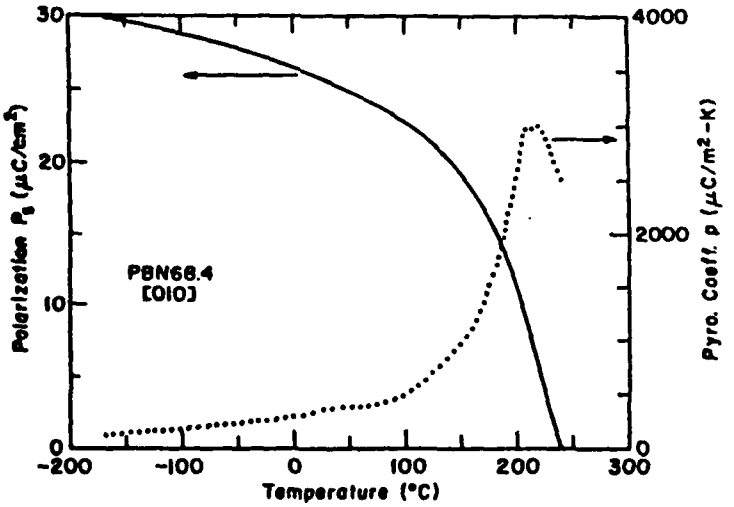

FIGURE 3 Change of the spontaneous polarization and the pyroelectric coefficient versus temperature for orthorhombic PBN68.4.

sharp depoling at the orthorhombic-tetragonal phase transition (the total amount of charge released at this phase transition corresponded to the strength of the orthorhombic polar vector and was of the magnitude of 18 $\mu C/cm^2$) and then became relatively constant, decreasing slowly with temperature. Measured along the [001] direction for the same crystal PBN61.5, as shown in Figure 5, polarization started to build up at the temperature above the orthorhombic-tetragonal phase transition, along with the sign change of the pyroelectric coefficient. Figures 4 and 5 demonstrated the polarization characteristics in this material at compositions close to the morphotropic phase boundary.

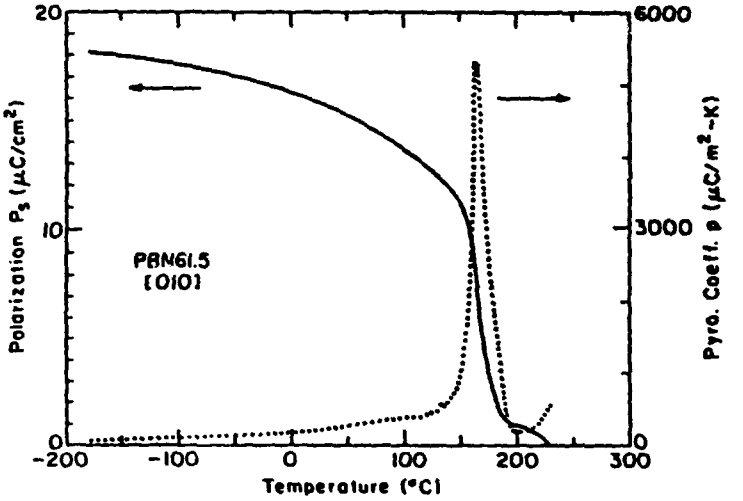

FIGURE 4 Change of the spontaneous polarization and the pyroelectric coefficient versus temperature for the MPB composition PBN61.5 measured parallel to the [010] direction.

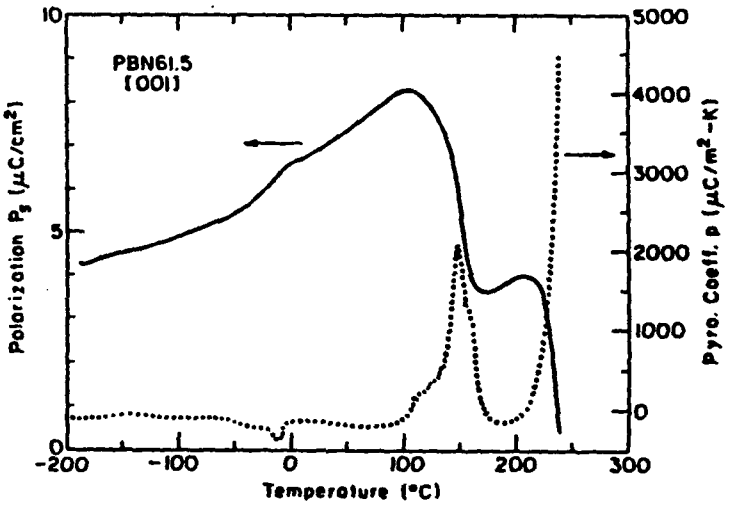

FIGURE 5 Change of the spontaneous polarization and the pyroelectric coefficient versus temperature for the MPB composition PBN61.5 measured parallel to the [001] direction.

The pyroelectric coefficients p of PBN single crystals of different compositions at room temperature (20°C) obtained using Byer-Roundy method are summarized in Table I (signs of the pyroelectric coefficients are omitted in the Table). The p values obtained for single crystal samples are substantially higher than those for ceramic samples from the earlier reports.[10]

The decrease of polarization with temperature was also calculated from the pyroelectric data. However, no absolute values of the spontaneous polarization are given because the phase transition temperatures are higher than the maximum temperature attained in the measurements.

TABLE I

Pyroelectric coefficient of PBN compositions measured using Byer-Roundy method

$Pb_{1-x}Ba_xNb_2O_6$ Composition 1-x	Symmetry	Pyro. Coefficient (at 20°C) ($\mu C/m^2$-K)	Pyro. Coefficient Maximum Value Obtained ($\mu C/m^2$-K)
0.34	Tetragonal	p_3=82	p_3=221 at 213°C
0.57	Tetragonal	p_3=134	p_3=1250 at 240°C
0.615	Orthorhombic/Tetragonal	p_2=196 p_3=142	p_2=5432 at 149.8°C p_3=4468 at 240°C
0.684	orthorhombic	p_2=336	~310 at 219.4°C
*$Pb_{0.86}Ba_{0.19}Nb_{1.98}O_6$	Orthorhombic	210	

* Results of Shrout et al. (1987), Reference 9.

Pyroelectric coefficients for PBN single crystals in polar directions increase as the compositions approach to the morphotropic phase boundary. However, the maximum value of pyroelectric coefficient (336 $\mu C/m^2$-K) was observed in composition close to the MPB but in the orthorhombic side of the phase diagram (PBN68.4) in which the dielectric constant and the piezoelectric coefficient are not the highest[9,11] in the solid solution system.

In PBN61.5, polarization vector switches its direction as the crystal goes through the morphotropic phase transition. Pyroelectric coefficients in either [001] or [110] direction can be high at room temperature which is unique among ferroelectric single crystals and can be very interesting for device applications.

The reasons for the maximized pyroelectric coefficients in the near-morphotropic phase boundary compositions may be discussed as follows:

The appearance of an MPB can usually be related to the instability of one ferroelectric phase against another ferroelectric phase upon critical composition change. It is logical to expect that the two phases separated by the MPB are energetically very similar but differ slightly in composition. The mechanical restraints to preserve one phase against the other may very well be relaxed, or softened, because of the structural instability. Hence, many physical properties will be either greatly enhanced or suppressed in near the morphotropic phase boundary compositions. Remanent polarization P_r, for instance, may increase due to the increase in magnitude of dipole displacement arising from the softening of the structure or the increase in the number of possible polarization directions. Spontaneous polarization of a polar state in the tetragonal phase can have two polar directions ([001] and [00$\bar{1}$]), and four directions ([110], [1$\bar{1}$0], [$\bar{1}$10], and [$\bar{1}\bar{1}$0]) in an orthorhombic phase. In a MPB composition, spontaneous polarization hence can have total six possible polar states therefore high values of remanent polarization and pyroelectric coefficients. Unlike a ferroelectric-paraelectric phase transition, in which the phase transition is a function of temperature and the physical properties such as dielectric constants and the polarization change drastically with

temperature, morphotropic phase transition can take place at temperatures much lower than the Curie-Weiss temperature and hence moderate dielectric constants can be preserved through the phase transition over a broad temperature region. Such a feature is considered very useful particularly in pyroelectric and electrooptic device applications.

Spontaneous polarization and the pyroelectric coefficient in the temperature range 10K to 300K were also studied using direct charge measurement technique. Details on low temperature pyroelectric property studies of PBN single crystals can be found in our earlier publication.[14]

SUMMARY

Physical properties of the MPB compositions have been reported in many solid solutions of perovskite structure.[15] The morphotropic phase boundary in PBN solid solution, separating two ferroelectric phases with mutually orthogonal polarization directions has been found so far only in tungsten bronze solid solution family. Current studies on temperature dependence of pyroelectric coefficients of PBN single crystals showed that the pyroelectric property is optimized in PBN crystals of the near-MPB compositions and large pyroelectric coefficients in either perpendicular or parallel to the c-axis can be obtained in PBN61.5 composition. The MPB PBN compositions are therefore interesting for pyroelectric device applications.

ACKNOWLEDGEMENT

We would like to express our thanks to Dr. Z. P. Chang of the same group for his help in single crystal growth, and the Office of Naval Research and the Defence Advanced Research Project Agency for their financial support.

REFERENCES

1. V. A. Isupov and V. I. Kosiakov, *Soviet Phys. Tech. Phys.*, **3**, 2002 (1958).
2. G. A. Smolenskii, V. A. Isupov, and A. I. Agranovskaya, *Soviet Phys. Solid State*, **1**, 400 (1959).
3. E. C. Subbarao, *J. Amer. Ceram. Soc.*, **42**, 448 (1959).
4. P. Baxter and N. J. Hellicar, *J. Amer. Ceram. Soc.*, **43**, 578 (1960).
5. M. H. Francombe, *Acta Cryst.*, **13**, 131 (1960).
6. I. G. Ismailzade, *Soviet Phys. Cryst.*, **4**, 618 (1960).
7. E. C. Subbarao, G. Shirane and F. Jona, *Acta Cryst.*, **13**, 226 (1960).
8. T. R. Shrout, L. E. Cross and D. A. Hukin, *Ferroelectric Letters*, **44**, 325 (1983).
9. T. R. Shrout, H. Chen and L. E. Cross, *Ferroelectrics*, **74**, 317 (1987).
10. R. Lane, D. L. Mack and K. R. Brown, *Trans. J. Brit. Ceramic Soc.*, **71**, 11 (1972).
11. R. Guo, A. S. Bhalla, C. A. Randall, Z. P. Chang and L. E. Cross, *J. Appl. Phys.*, **67**(3), 1453 (1990).
12. R. Guo, A. S. Bhalla and L.E. Cross, *Applied Optics*, **29**(7), 904 (1990).
13. R. L. Byer and C. B. Roundy, *Ferroelectrics*, **3**, 333 (1972).
14. R. Guo, A. S. Bhalla, C. A. Randall and L. E. Cross, *J. Appl. Phys.*, **67**(10), 6405 (1990).
15. B. Jaffe, W. R. Cook, Jr. and H. Jaffe, *Piezoelectric Ceramics* (Academic Press, London and New York, 1971).